

# **Functionalisation of CVD Graphene for Gas Sensing**

By

**Abdullah Aladim**

A thesis presented for the degree of

Doctor of Philosophy



Mathematics, Statics and Physics

Newcastle University

United Kingdom

March 2023

**Abstract:**

Due to several of its physical properties, graphene is well suited to use within gas sensing devices. The extremely large surface-to-volume ratio and atomic thinness means any adsorbate on the graphene surface will strongly modify the electrical properties. Also, graphene typically presents high carrier mobilities and a low density of states close to its Dirac point further improving its sensor characteristics. In combination, these factors have given rise to extensive research into graphene as a candidate for gas sensing, it has been found that even at the modest charge exchange, interaction between a graphene sheet and adsorbates can produce a measurable variation in the graphene's conductivity and shift in the Dirac point of the graphene channel.

This work reports upon gas sensing performance of monolayer graphene grown by Chemical Vapour Deposition (CVD). The electrical properties are characterised during exposure to gaseous analytes via analysis of their electrical behaviour as graphene field effect transistor (GFET) devices. Results are presented for adsorption of NH<sub>3</sub> and NO<sub>2</sub> gas leading to electron donation and withdrawing effects respectively. Both Fermi level shift and charge mobility change upon the gas adsorption is used to fingerprint sensor response for these two analytes. We present results that indicate atmospheric adsorption is responsible for strong changes in graphene sensor recovery and that this effect is reversible with exposure to high vacuum conditions.

In addition, this work illustrates the potential for improvement upon current graphene gas sensing devices via wet chemical oxygen functionalisation. The oxygen functionalised CVD graphene is characterised using Raman Spectroscopy, X-ray Photoelectron Spectroscopy, and Atomic Force Microscopy. The electrical properties are then characterised before and after oxidation via analysis of gate dependent GFET measurements and the during gas exposure by resistivity measurements. It is demonstrated that even for a relatively low concentration of introduced oxygen groups ( $\sim 1.65 \times 10^{10} \text{ cm}^{-2}$ ) the oxygen functionalised CVD graphene sensors show a response of up to 600x that of the comparable non-functionalised sensor. The response time for oxidised CVD graphene is also measured and found to be two times faster than pristine CVD graphene and is shown to be capable of detecting low gas concentrations of NO<sub>2</sub> with a limit of detection of  $\sim 41$ ppb.

## **Acknowledgements**

First, I would like to express my thanks and appreciation to my primary supervisor, Dr. Toby Hallam for his guidance, encouragement and help to complete my academic research. He was always ready to help and give advice, which made me learn a lot more in my research.

I would like to thank my secondary supervisor, Dr. Johannes Gausden, for his time, help and training me in the lab. Without his advice and guidance, I would not use the equipment correctly.

I must also thank Dr. Konstantin Vasilevskiy, who has invested a lot of time in training me to use the fabrication equipment. Also, for his help in ordering the chemical material. I am also thankful to Mr. Paul Sterling for his help in ordering all the gas cylinders.

I would like to thank Dr. Elisabetta Arca for her help in the XPS measurements and training.

I must also thank Jouf University for giving me this opportunity to complete my PhD. Also, I am grateful for their funding and support. In addition, Saudi Arabian Cultural Bureau (SACB) for their support.

I would like to thank Talha Qamar and Merve Yakut for their help in the lab and support.

I am deeply grateful for my wife, Nisrein Amarabeh, who has been patient during my study time. Thank her for her support and encouragement throughout my PhD. In addition, I am thankful to my kids, Laila, Abdulaziz, and Abdurrahman, for their understanding and patience throughout my study. I must thank my parents Mrs. Minwa Almarabeh and Mr. Kareem Aladim, for their support and encouragement in me to complete my PhD. I want also to thank all my sisters and brothers for their support. Finally, I must thank my aunt Mrs. Hafidhah Almarabeh, for her support and encouragement throughout my PhD.

## **COVID-19 Impact**

In 2021, the lockdown had a massive impact on my ability to work in the lab. As a result of the closure of the lab for 12 months, my project, which relied heavily on experiments, was greatly affected. The inability to conduct experiments and obtain results was a major setback. Additionally, the delivery of experiment parts ordered online was challenging due to the circumstances, and the workshop at the university postponed the production of other essential experiment components. These factors combined impeded my experimental progress significantly. Despite planning to conduct extensive experiments during the summer, COVID-19 prevented me from doing so, and I was unable to obtain any results in 2021.

In 2022, I was granted a six-month extension in the lab to finish my experiments, but even with this extra time, I was unable to complete all of the planned experiments. The impact of the lockdown on my mental health and anxiety cannot be overstated. The sudden and prolonged disruption to my work in the lab, which I had invested a considerable amount of time and effort into, was extremely distressing. The uncertainty and lack of control over the situation caused significant stress and anxiety, which affected not only my work but also my overall well-being.

The isolation and social distancing measures implemented during the lockdown further exacerbated these feelings of anxiety and stress. The inability to socialize with colleagues or engage in activities outside of work made it challenging to cope with the situation.

Furthermore, the uncertainty regarding the future of my project and whether I would be able to complete it as planned caused a great deal of worry and anxiety. The extension of time provided some relief, but it also added to the pressure to perform and complete the work within a limited timeframe.

Overall, the impact of the lockdown on my mental health and anxiety was significant and cannot be ignored. It was a challenging and stressful time that required a great deal of resilience and support to overcome.

## Contents

1	Introduction .....	1
1.1	Gas Sensing.....	1
1.2	Types of Gas Sensors.....	5
1.2.1	Metal Oxide Gas Sensors .....	6
1.2.2	Field Effect Transistor (FET) Sensors.....	8
1.2.3	Electrochemical Gas Sensor .....	9
1.2.4	Catalytic Gas Sensor.....	10
1.2.5	Nondispersive Infrared Radiation Gas Sensor.....	11
1.3	Graphene based Gas Sensors .....	12
2	Literature Review.....	14
2.1	Graphene Gas Sensors.....	14
2.2	Density Functional Theory (DFT).....	14
2.3	Pristine Graphene Gas Sensors.....	19
2.4	Graphene Oxide Gas Sensors.....	22
2.4.1	Oxidation Methods .....	23
2.4.2	Sensitivity.....	24
2.4.3	Recovery.....	28
2.5	Graphene Gas Sensors Benefits and Challenges .....	29
3	Theory.....	31
3.1	Graphene.....	31
3.1.1	Atomic Structure of Graphene.....	31
3.1.2	Electronic Band Structure of Graphene .....	32
3.2	Graphene Oxide.....	34
3.3	Graphene Growth .....	36
3.3.1	Top-down Synthesis .....	36
3.3.1.1	Micro-Mechanical Exfoliation .....	36
3.3.1.2	Liquid Phase Exfoliation .....	36
3.3.2	Bottom-up Synthesis.....	37
3.3.2.1	Epitaxial Growth on Silicon Carbide .....	38
3.3.2.2	CVD on Transition-metal films.....	38
3.4	GFET Electrical Transport.....	40
3.5	Graphene Sensors .....	40
4	Methods.....	43
4.1	Sensor Fabrication .....	43

4.1.1	CVD Graphene Growth.....	43
4.1.2	Graphene Transfer.....	44
4.1.3	GFET Fabrication.....	46
4.1.4	Graphene Oxidation.....	48
4.2	Sensor Measurement.....	49
4.2.1	Electronic Characterisation.....	49
4.2.2	Gas Machine .....	51
4.3	Analysis Methods .....	55
4.3.1	Atomic Force Microscopy.....	55
4.3.2	Raman Spectroscopy.....	57
4.3.3	X-Ray Photoelectron Spectroscopy.....	60
5	Pristine Graphene Gas Sensors.....	63
5.1	GFET Device Cleanliness.....	64
5.1.1	Higher Resolution Microscopy and SEM.....	64
5.1.2	AFM.....	66
5.1.3	Raman Spectroscopy.....	67
5.1.4	XPS.....	69
5.1.5	Electric Characterisation .....	70
5.2	NO <sub>2</sub> Sensor Characteristics.....	72
5.2.1	NO <sub>2</sub> Saturation Measurement.....	73
5.2.2	NO <sub>2</sub> Repeatability Measurement.....	76
5.2.3	NO <sub>2</sub> Cycles Measurement .....	78
5.2.4	Repeated Device Test after 9 Months.....	82
5.3	NH <sub>3</sub> Sensor Characteristics.....	84
5.3.1	NH <sub>3</sub> Saturation Measurement.....	84
5.3.2	Mass Spectrometry.....	85
5.4	GFET Sensing and Field Effect Gating.....	86
5.4.1	NO <sub>2</sub> Cycles Measurement .....	87
5.4.2	Gating Sensitivity Test.....	89
6	Functionalised Graphene Gas Sensors.....	95
6.1	Functionalised GFET Device.....	96
6.1.1	High Resolution Microscope .....	96
6.1.2	Raman Spectroscopy.....	98
6.1.3	XPS.....	100
6.1.4	Electric Measurements for Functionalised Graphene FET (GFET).....	103
6.2	NO <sub>2</sub> Functionalised Sensor Characteristics .....	106

6.2.1	NO <sub>2</sub> Saturation Measurement .....	107
6.2.2	NO <sub>2</sub> Repeatability Measurement.....	111
6.2.3	NO <sub>2</sub> Cycles Measurement .....	112
6.2.4	Repeated Device Test without Vacuum Condition .....	118
6.2.5	Specificity Measurement.....	120
7	Conclusion and Future Work.....	123
7.1	Future Work.....	124

## List of Figures

Figure 1.1: Shows the interaction between gas molecule and receptor leads to the signal generated by the transducer.....	2
Figure 1.2: Demonstrates the mechanism of the MOs gas sensor. The green layer represents the MOs sensing film, the brown layer represents the depletion region, the yellow region represents the Au electrode, the blue layer represents the substrate, and the orange layer represents the heating element. At the operating temperature, the sensing layer interacts with oxygen, and the oxygen is adsorbed on the surface. When the CO reducing gas interacts with the adsorbed oxygen, it forms CO <sub>2</sub> by taking one oxygen. As a result, the electron injects back to MOs surface which changes the resistance. ....	6
Figure 1.3: Shows the shape of the FET, which has a P-type sensing layer between two electrodes (source and drain), silicon is coated with silicon oxide and voltage is applied to substrate. As an oxidising gas e.g. oxygen interacts with the sensing layer, some electrons from the conduction band are captured on the surface. On the other hand, reducing gas like carbon monoxide interacts with the sensing layer and result in freeing electrons back to the conduction band. ....	9
Figure 1.4: Shows the CO oxidised through the chemical reaction on the working electrode. This results in generated H <sup>+</sup> and current flow to the counter electrode through the electrolyte. Also, the generated e <sup>-</sup> flow through the external circuit to the counter electrode. ....	10
Figure 1.5: Schematic of catalytic gas sensor. ....	11
Figure 1.6: Schematic of Nondispersive infrared radiation gas sensor. ....	12
Figure 2.1: Shows the change in sensitivity of the graphene sensor upon exposure to different types of gases. Region I: the device is in vacuum before its exposure; II: exposure to a 5 l volume of a diluted chemical; III: evacuation of the experimental set-up; and IV: annealing at 150 °C. Adapted from reference [77]. ....	20
Figure 2.2: Transfer curves characteristics of a back-gated CVD graphene FET in air while exposed to NO <sub>2</sub> and NH <sub>3</sub> . Inset shows the changes in conductance of CVD graphene with the flow of 20 ppm NO <sub>2</sub> and 550 ppm NH <sub>3</sub> . The gas carrier used in the experiment during the exposure is N <sub>2</sub> . Adapted from reference [80]. ....	21
Figure 2.3: a) Represent the response of the GO sensors to NO <sub>2</sub> , NH <sub>3</sub> , and H <sub>2</sub> . The inset shows the change in the response curve to the gases. b) demonstrate the response curve to different concentration range from 1 -5 ppm of NO <sub>2</sub> , and the inset shows linear response vs gas concentration. Adapted from reference [64]. ....	25

Figure 2.4: Demonstrates the change in resistance for pristine graphene (black) and graphene oxide by ozone treatment (red) upon exposure to different concentrations of NO<sub>2</sub> (0.2ppm to 200 ppm). The inset shows the response change for both pristine and treated graphene to different NO<sub>2</sub> concentrations. Adapted from reference [69]. .....26

Figure 3.1: Shows the graphene honeycomb lattice and its Brillouin zone. The lattice on the left demonstrates a structure of graphene, which is made of two interpenetrating triangular lattices. The  $a_1$  and  $a_2$  are the vectors of the lattice unit, and  $\delta_i, i=1, 2, 3$  are the closest neighbour vectors. The right lattice corresponds to the Brillouin zone, where the Dirac points are located at the K and K' points. Copied from reference [103]. .....31

Figure 3.2: Energy dispersion in the graphene lattice. Left: energy spectrum in units of  $t$  for finite values of  $t$  and  $t'$ , with  $t=2.7$  eV and  $t'=-0.2t$ . Right: zoom in on of the energy bands close to one of the Dirac points. Copied from reference [103]. .....32

Figure 3.3: Shows the calculated resistance for shifting the Fermi level in graphene using gate voltage. Adapted from reference [106]. .....34

Figure 3.4: Graphene oxide structure. Adapted from reference [117]. .....34

Figure 3.5: Demonstrate the general four used methods for graphene production; a) micromechanical cleavage, b) liquid phase exfoliation, c) epitaxial growth on SiC. d) chemical vapour deposition. Adapted from reference [118]. .....37

Figure 3.6: Represent the epitaxial growth of graphene on silicon carbide wafer. Adapted from reference [128]. .....38

Figure 3.7: Schematic diagrams of the possible distribution of C isotopes in graphene films based on different growth mechanisms for sequential input of C isotopes. (a) Graphene with randomly mixed isotopes such as might occur from surface segregation and/or precipitation. (b) Graphene with separated isotopes such as might occur by surface adsorption. Copied from X. Li et al [141]. .....39

Figure 4.1: A schematic of the CVD furnace reactor used for graphene growth. ....43

Figure 4.2: Shows the synthesis process of the graphene sheet. ....45

Figure 4.3: Shows an image of fabricated GFET in this project. The GFET consists of a 10 nm Cr/ 60 nm Au electrode on top of a silicon substrate capped with 300 nm silicon dioxide. The transferred graphene is outlined by the white dashed line for easy visualisation. ....46

Figure 4.4: Demonstrates a fabrication process from the spin of the photoresist to the transfer of the graphene to create GFETs. ....48

Figure 4.5: Demonstrates an oxidation process of graphene for the creation of GFETs. ....49

Figure 4.6: a) Shows the I-V curve of the graphene channel with a metal electrode. b) the typical transfer curve of the graphene field effect transistor. Dirac point on the forward sweep is located at 9 V and at 13 V on the backward sweep. c) the forward/backward sweep of the  $g_m$  as a function of gate voltage. Blue and green circles highlight the  $g_m$  values for the holes and electrons, which can be substituted in equation 4.4. ....51

Figure 4.7: Shows an image of the GFETs device preparation for the gas sensitivity test. 9. a) represent the GFETs devices wired for the measurements, b) thermal cable used to read the temperature inside the chamber, and c) Gaps junction connected to the junction box for the measurements. The right represents the enlarged image of the GFETs device. ....53

Figure 4.8: a) Diagram description of the user inputs into the apparatus. All the set up with black arrows must be used while the blue arrows are optional. b) An image of the gas controller chamber. Which show the setup in order from top to bottom, MFCs, the junction box which connect the device to the instrument, pressure sensor which gives the reading from the pressure inside the chamber, chamber, the regular vacuum pumps are at the back of the unit, and the turbopump at the bottom. C) Schematic of the LabVIEW setup with measurement inputs/outputs and gas control. ....54

Figure 4.9: Display the force relationship between the tip to sample and distance separation. Adapted from reference [190]. ....56

Figure 4.10: Display the force relationship between the tip to sample and distance separation. Adapted from reference [191]. ....57

Figure 4.11: Demonstrates the three Raman scattering processes of Rayleigh, Stokes, and Anti-Stokes under the light-material interaction. The upward and downward shift in energy is due to obtaining or losing energy from a phonon to a phonon or unsteady state in the material. ....58

Figure 4.12: a) Shows a single-layer graphene structure, b) a measured dispersion phonon relation, and Raman spectra taken from the edge of graphene showing the characteristic D, G, 2D, D, Raman peaks. d) represent the photon-phonon interactions which give most of the spectral peaks on Raman spectroscopy. Adapted from reference [200]. ....59

Figure 4.13: Represents ID/IG ratio for CVD graphene, CVD graphene with low oxidation level and CVD graphene with higher oxidation as presented on red and blue graphs, respectively. ....60

Figure 4.14: Represent a diagram of XPS. ....60

Figure 4.15: Shows the XPS result for the binding energies of Carbon and Oxygen and their intensity which relate to the atomic percentage of each element in the sample. ....62

Figure 5.1: Images displaying the graphene sheet after being transferred to SiO<sub>2</sub>/Si substrate, a and c), show the 10 μm area of the middle of the graphene sheet and edge of the graphene sheet, respectively, with a black, blue, red, and green arrow pointing to folding, residues, tear, and multilayer graphene, respectively. b and d), the same images of a and c) after converting the dark field for residues analysed.....65

Figure 5.2: a and b) Represent the SEM image that has been taken for the graphene sheet after transfer to SiO<sub>2</sub>/Si with red, blue, black, and orange arrow pointing to tears, residuals, fold, and back side graphene, respectively. The transfer handling procedure causes a large tear on the bottom right side of Figure a) with a tweezer. ....66

Figure 5.3: Shows an AFM image of transferred graphene to SiO<sub>2</sub>/Si substrate with blue, black, and yellow pointed to residues, wrinkles, and dirt, respectively.....67

Figure 5.4: Demonstrates the Raman spectra for the graphene where G and 2D peaks are presented at 1580 cm<sup>-1</sup> and 2670 cm<sup>-1</sup>, respectively. The laser excitation wavelength is 532 nm.....68

Figure 5.5: C1s core-level XPS spectrum recorded from graphene on Si substrate coated with 295 nm SiO<sub>2</sub>. ....70

Figure 5.6: Shows typical transfer curve of graphene field effect transistor. Dirac point on the forward sweep locate at 35 V and on the backward sweep at 62V.....71

Figure 5.7: a and b) Response of graphene device D1 and D2 for 1000 ppb of NO<sub>2</sub> gas, respectively. Graphene in devices D1 and D2 were transferred using NC as a supporting layer. The measurement is done at room temperature with a flow of N<sub>2</sub> during the recovery process.....74

Figure 5.8: a and b) Show the rate fitting curves for the exposure curves for 1000 ppb of NO<sub>2</sub>. ....76

Figure 5.9: a and b) Show the repeatability of the devices for 1000 ppb of NO<sub>2</sub> gas exposure on three cycles of 180s each at room temperature. During recovery, N<sub>2</sub> was purged into the system. c and d) demonstrate the change in resistance response for devices D1 and D2 as a function of the sequence obtained from Figures a and b. ....77

Figure 5.10: a and b) Show the sensor's response for five steps measurements under different concentrations of NO<sub>2</sub> at room temperature. The change in resistance increase with NO<sub>2</sub> concentration. The columns represent the time of exposure to NO<sub>2</sub>. ....80

Figure 5.11: Shows the response percentage for the two devices during exposure to different NO<sub>2</sub> concentrations. The black and red lines are related to devices 1 and 2, respectively.....80

Figure 5.12: Represents the response percentage versus the recovery percentage for NO<sub>2</sub> for the pristine graphene devices presented within this work by a blue cross, compared to the pristine devices in the literature as presented by a red cross. ....81

Figure 5.13: Shows both resistance response for the device after prepared and after 9 months which are presented by black and red curves, respectively. The change in resistance increase with NO<sub>2</sub> concentration. The columns represent the time of exposure to NO<sub>2</sub>. ....83

Figure 5.14: Shows the response percentage for the device before and after 9 months upon exposure to different NO<sub>2</sub> concentrations. The black and red lines are related to device measurements as prepared and after 9 months, respectively. ....83

Figure 5.15: a and b) Response of graphene device D1 and D2 for 10 ppm of NH<sub>3</sub> gas, respectively. The measurement is done at room temperature with a flow of N<sub>2</sub> during the recovery process. ....85

Figure 5.16: Shows the mass spectrum result of nitrogen (N<sub>2</sub>), methanol (CH<sub>3</sub>OH), and ammonia (NH<sub>3</sub>) gases. ....86

Figure 5.17: Shows both resistance response for the devices D3 and D4 which are presented by black and red curves, respectively. The change in resistance increase with NO<sub>2</sub> concentration. The columns represent the time of exposure to NO<sub>2</sub>. ....88

Figure 5.18: shows the response percentage for the device D3 and D4 upon exposure to different NO<sub>2</sub> concentrations. The black and red lines are related to device measurements of D3 and D4, respectively. ....88

Figure 5.19: a and b) Demonstrate the conductance vs gate voltage under different concentration of NO<sub>2</sub> and NH<sub>3</sub>, respectively. c) the carrier charge density increase with NO<sub>2</sub> adsorption, and d) the carrier charge density decrease with NH<sub>3</sub> adsorption. ....91

Figure 5.20: a and b) Demonstrate the Dirac point shift vs gas concentration of NO<sub>2</sub> and NH<sub>3</sub>, respectively. a and c) the resistance response upon NO<sub>2</sub> and NH<sub>3</sub> adsorption, respectively. ....92

Figure 5.21: a and c) Represent the linear factor calculated from inverse of mobility versus gate voltage. b and d) the summation of the linear factor versus the summation of gate voltage. ....93

Figure 6.1: Images displaying the graphene sheet before a) and after being immersed in 3.6 mol of sulphuric acid (H<sub>2</sub>SO<sub>4</sub>) for 120 minutes c). a and c) show the 10 μm area of the graphene sheet with a black, blue, red, and green arrow pointing to folding, residues, tear, and multilayer graphene, respectively. b and d) the same image after converting to the dark field for residue analysing. ....97

Figure 6.2: a) Raman spectra taken from CVD graphene before and after oxidation for 0, 30, 60, 90, and 120 as indicated by black, red, blue, green, and grey spectra, respectively. b) magnified view of the D peak before and after oxidation.....99

Figure 6.3: a) Demonstrate the intensity ratio  $I_D/I_G$  as the function of time of exposure  $H_2SO_4$ . b) The calculated defect density as the function of the time of exposure. Both intensity ration and defect intensity increases linearly with time of oxidation..... 100

Figure 6.4: Demonstrates C1s core-level XPS spectrum collected from pristine CVD graphene..... 102

Figure 6.5: Demonstrates C1s core-level XPS spectrum collected from oxidised CVD graphene. a) oxidised sample for 30 min in  $H_2SO_4$  and b) oxidised sample for 120 min in  $H_2SO_4$ ..... 102

Figure 6.6: Shows the atomic percentage of carbon-to-carbon bonding (C-C), carbon-to-hydroxyl or epoxy oxygen bonding (C-OH, C-O), and carbon-to-carbonyl bonding (C=O) plotted versus the oxidation time. .... 103

Figure 6.7: a) Shows the Dirac point shifted toward positive voltage as the time of exposure to the  $H_2SO_4$  increases. Dirac point before exposure to the  $H_2SO_4$  located at 4 V. After 30, 60, 90, and 120 minutes of exposure to the  $H_2SO_4$ , Dirac point shifted to 9, 1, 13.8, and 14 V respectively. b) shows both holes and electrons mobility as a function of time of exposure. .... 105

Figure 6.8: Shows the carrier charge density increase with increasing the exposure time to  $H_2SO_4$ ..... 105

Figure 6.9: a and b) Response of graphene device D1 and D2 for 1000 ppb of  $NO_2$  gas before and after each oxidation step, respectively. The black, red, blue, green, and grey curves represent the response result optioned from device after 0, 30, 60, 90, and 120 minutes of oxidation, respectively. The measurement is done at room temperature with a flow of  $N_2$  during the recovery process. .... 108

Figure 6.10: a and b) Show the rate fitting curves of device D1 and D2 for the exposure curves for 1000 ppb of  $NO_2$  before and after each oxidation steps. The black, red, blue, green, and grey curves represent the response result optioned from device after 0, 30, 60, 90, and 120 minutes of oxidation, respectively. .... 109

Figure 6.11: a and b) Show the repeatability of the devices for 1000 ppb of  $NO_2$  gas exposure on three cycles before and after oxidation steps at room temperature. During recovery,  $N_2$  was purged into the system. The black, red, blue, green, and grey curve represent the response optioned from devices after 0, 30, 60, 90, and 120 minutes of oxidation,

respectively. c and d) demonstrate the change in resistance response for devices D1 and D2 as a function of the sequence obtained from Figures a and b. .... 112

Figure 6.12: a and b) Show the sensor's response for five steps measurements under 200, 400, 600, 800, and 1000 ppb of NO<sub>2</sub> at room temperature. All the measurements were taken for each step of 0, 30, 60, 90, and 120 minutes of oxidation. The black, red, blue, green, and grey curves represent the response obtained from device D1 and D2 after 0, 30, 60, 90, and 120 minutes of oxidation, respectively. .... 114

Figure 6.13: Shows the response percentage for four device measurements taken after each oxidation step to the devices during exposure to different NO<sub>2</sub> concentrations. The black, red, blue, green, and grey lines are related to the data obtained from device after oxidation of 0, 30, 60, 90, and 120 minutes, respectively. .... 115

Figure 6.14: Shows the response percentage per ppb for the oxidise devices for 60 minutes presented in this work, which is presented by the blue cross, and the response percentage data from the published oxidise devices data presented by the red cross. .... 117

Figure 6.15: Shows both resistance responses for the device with the vacuumed condition and without vacuumed condition, which are presented by black and red curves, respectively. The change in resistance increase with NO<sub>2</sub> concentration, and the columns represent the time of exposure to NO<sub>2</sub>. .... 119

Figure 6.16: Shows the response percentage for the device with the vacuumed condition and without vacuumed condition upon exposure to different NO<sub>2</sub> concentrations. The black and red lines are related to measurements for the device with vacuum conditions and without vacuum conditions, respectively. .... 119

Figure 6.17: a and b) Response of graphene device D1 and D2 for CH<sub>3</sub>OH gas before and after each oxidation step, respectively. The black, red, blue, green, and grey curves represent the response result obtained from device after 0, 30, 60, 90, and 120 minutes of oxidation, respectively. The measurement is done at room temperature with a flow of N<sub>2</sub> during the recovery process. .... 121

## List of Tables

Table 2.1: Summary of oxidised graphene gas sensors process and presented response, recovery, and detection limit for NO <sub>2</sub> and NH <sub>3</sub> .....	17
Table 5.1: Represent the average electron and hole mobility for field-effect transistor devices. ....	72
Table 5.2: Represent the LOD and the response percentage for NO <sub>2</sub> for all measured devices. ....	81
Table 5.3: Represent the data obtained from the linear factor fitting. ....	94
Table 6.1: Represent the average Raman defect and charge residual carrier before and after each oxidation step for field-effect transistor devices. ....	106
Table 6.2: Represent both constant of adsorption (k <sub>a</sub> ) and desorption(k <sub>d</sub> ) rates extracted from fitted curves for devices D1 and D2 before and after oxidation. ....	110
Table 6.3: Summary of pristine and oxidised graphene gas sensors response percentage for NO <sub>2</sub> .....	117
Table 6.4: Summary of the detection limit for the devices with different oxidation times for NO <sub>2</sub> .....	117

## **Publications and Conferences**

### **List of Publications**

1. Abdullah K. Aladim, Toby Hallam, Graphene field effect transistor gas sensors, “in Proceedings of the 2nd Ed. of the Sensors Technologies International conference - Sensors 2022 Oct to 28 Oct 2022 Athens – Greece- October 26- 28, 2022, pp. 1-6
2. Abdullah K. Aladim, Toby Hallam. (2023). Functionalised CVD graphene FET sensors for detection of NO<sub>2</sub> in preparation.

### **List of Conferences**

1. UK Semiconductors 2022 Conference, 6-7 July 2022, Sheffield Hallam University, Howard Street, Sheffield S1 1WB, UK. (Poster presentation)
2. Graphene week 2022 Conference, 5-9 September 2022, Munich, German. (Poster presentation)
3. SMS 2022 / Nano Med 2022 / Sensors 2022 / EGF 2022 Joint International Conferences, 26-28 October 2022, Athens, Greece. (Poster presentation)

## **Chapter 1**

### **1 Introduction**

Chemiresistor gas sensors play an important role in environmental and industrial monitoring. They work by the changing electrical resistance due to the interaction between the sensor material and the gas molecule. Chemiresistor gas sensors can be used to detect the existence of harmful gas as a part of safety systems to detect poisonous and flammable gas mixtures in the air. Gas detectors are very important in the medicine and aviation industries to detect the decrease or increase of oxygen. Industrial emissions, such as NO<sub>2</sub> and NH<sub>3</sub>, are increasingly monitored and are a significant contributor to air pollution, which is harmful to human health and the environment.

#### **1.1 Gas Sensing**

Gas sensors can be used for the detection and determination of the concentration of toxic and hazardous gases in the environment. For some toxic gases, even small changes in the percentage of these gases can cause health problems and can negatively affect the human body [1]. Various research has reported the influence of these pollutant gases, such as NO<sub>2</sub>, CO and NH<sub>3</sub>, on serious diseases, such as ischemic heart disease, lung cancer, chronic obstructive pulmonary disease, and strokes [1]. A report from the World Health Organization stated that globally, environmental pollution was the cause of around 9 million deaths in 2022 [2].

A gas sensor normally possesses two major principal functions, receptor function, and transducer function [3]. The receptor function is the interaction between the analyte gas and sensor device, such as adsorption, chemical reaction, or an electrochemical reaction [3, 4]. Transducer function is the change in the receptor which translates to a signal that can be measured and quantified to express the concentration of the gas. This transduction might take the form of a change in electrical resistance, colour, or reflectivity. Figure 1.1 demonstrates how gas molecules interact with the receptor and lead to a signal being generated by the transducer. The performance of gas sensors is assessed based on several key characteristics including sensitivity, selectivity, response time, recovery, adsorption capacity, and energy consumption [5, 6]. We discuss these characteristics in the section below.

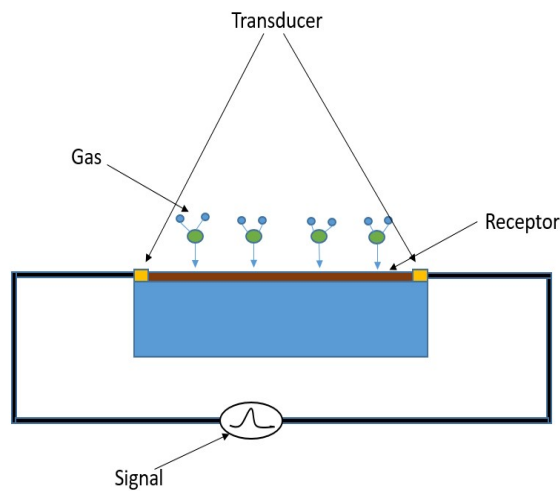


Figure 1.1: Shows the interaction between gas molecule and receptor leads to the signal generated by the transducer.

- **Sensitivity**

The sensitivity is the ability of the sensor to determine the concentration of the target gas. Different levels of sensitivity may be needed for different sensing applications. For example, measuring oxygen content in air (at 21%) requires a lower sensitivity device than measuring the concentration of certain atmospheric pollutants (like NO<sub>2</sub> at 40 ppb) [7]. The sensitivity is determined as the ratio of the signal level (for example resistance) before and after the sensor is exposed to a target gas and is denoted by  $S$ . It takes the general form of,

$$S = \frac{\Delta a}{\Delta b}$$

Where  $\Delta a$  is the change in the output, and  $\Delta b$  is the change of the input of the sensors.

In chemiresistor gas sensors, the sensitivity determined by the change in resistance and therefore can be written as,

$$S = \frac{\Delta R}{\Delta t}, [8]$$

Where  $\Delta R$  is the resistance change of the gas sensors at a particular target gas concentration and  $\Delta t$  is the time taken for the sensor to change resistance.

- **Selectivity**

Selectivity is the ability of the sensor to distinguish between types of gases. It is described as the proportion of the output signal change generated by the target gas at the sensor interface. It is important that sensors are able to differentiate between gases as sensors are usually used to detect a specific type of gas in a mixture of other gasses (for example oxygen in air). Some sensors can show sensitivity towards several different gasses. Here, the gas sensors cannot identify the target gas in the gas mixture, and show the same response for all of the different types of gases. Selectivity of gas sensors can be variable dependant on the conditions of the environment, creating great challenges for sensing gases in certain settings, such as in presence of humidity and extreme temperatures [9]. Increasing the selectivity is essential to improve the function of gas sensors and decrease false-positive responses. To increase selectivity, the gas sensor can be modified physically or chemically [10]. Physical modification is used to change the gas sensor's physical properties (such as physical structure) or physical barriers (like using a microchannel filter to only allow the target gas to reach the sensing channel) [11-13], or using sensor arrays which can sense the target gas molecule. Chemical modification occurs by adding additional material to the sensing channel which is attracts the target gas molecule. Materials are usually chosen based on their chemical properties, which allow them to recognise specific gas molecules by adsorption or reaction. In general, higher selectivity can be achieved by chemical modification than physical modification [14, 15].

- **Response Time**

Response time is the time it takes for a sensor to correctly report gas concentration. Described as the time required to change from sensor resistance in air, to the resistance expected after target gas exposure [9]. Similarly, for FET-mediated gas sensing, the response is explained as the change in current (or resistance) under the target gas compared to in air [10]. Reception and transduction processes take some time to complete, and thus all gas sensors have a characteristic response time to make a measurement. This time should be as short as possible, as some gases cause an impact on health or the environment in short exposure times. For example, short exposure to ammonia ( $\text{NH}_3$ ) at a concentration level of 35 ppm can cause serious health problems [11]. Also, exposure to nitrogen dioxide ( $\text{NO}_2$ ) of 5 ppm concentration is hazardous at short exposures, as reported by Occupational Safety and Health Administration (OSHA) [12]. Several parameters can affect the response speed, such as temperature, pressure,

and humidity. For example, metal oxide sensors requires high operating temperature to show a fast response [13], and graphene sensors are disturbed by humidity, which increases the response time [14]. Several techniques have been reported to improve sensor sensitivity, such as changing the nanostructure morphology, using conducting polymers, temperature modulating, and 2D metal dichalcogenides, all with limited achievement [15-18]. Despite these methods for increasing sensitivity, it remains difficult to reduce response time, as a trade-off between selectivity and response time exists due to device geometry at the nanoscale. Achieving high selectivity requires functionalisation of the sensor's material, which often increases the response time. Therefore, achieving a fast response time needs less sensor material's functionalisation, and this reduces selectivity.

- **Recovery**

Recovery is the ability of the sensing material to recover to the initial condition after detecting some concentration of gas. If gas sensors are to be installed for a long periods of time, they must be capable of measuring many gas events. Therefore, to maintain sensitivity over a long period of time, it needs to be able to respond identically to the same stimuli (gas concentration) over the device's whole lifetime. This is important for the reliability and long life of a device.

- **Adsorption Capacity**

Adsorption capacity is the amount of the available adsorption sites to host gas molecules. A large capacity increases the ability to adsorb a large amount of gas before the device reaches saturation. This is particularly important for sensors that might be exposed to very high concentrations of gases while still needing to maintain sensitivity. For example, in semiconductor metal oxide gas sensors, the limitation of low detection limit is attributed to the immunity of the interface capacity [19]. Several studies have been done to overcome this challenge, such as introducing oxygen vacancy, or surface decoration with nanoparticles to the sensing material [9, 20-23]. M. Epifani et al. demonstrated that a tin (IV) oxide ( $\text{SnO}_2$ ) nanocrystal sensor doped with oxygen vacancy increased the electrostatic adsorption capacity for  $\text{NO}_2$  detection [24]. The sensor exhibited a high sensitivity to  $\text{NO}_2$ , which resulted from high charge carrier transport induced by oxygen vacancy.

Another publication shows an increase in sensitivity to  $\text{NO}_2$  of CVD graphene sensors decorated with Polystyrene (PS) beads compared to CVD graphene alone [25]. The graphene

sensor was prepared by CVD and transferred to a Si wafer coated with 300 nm SiO<sub>2</sub> to form a graphene-based field effect transistor gas sensor. After that, the PS beads were drop-coated on the graphene layer. The increase in sensitivity in graphene/ PS was due to the increase in the adsorption sites provided by the PS for the target gas, resulting in a large amount of electron charge transfer [25].

- **Energy Consumption**

Energy consumption is the power used by the device to sense the gas. A gas sensor such as a metal oxide or catalytic sensor needs a high temperature to operate, which causes an increase in energy use [26-28]. Therefore, an improvement is needed for these sensors toward reduced operating temperature. Many methods have been investigated to overcome this problem by using other materials, such as decorating metal oxide with nanoparticles [29], or introducing oxygen vacancy [30]. On the other hand, graphene chemiresistor gas sensors can operate at room temperature, reducing energy use and operating costs. H. Choi et al. demonstrated the use of CVD graphene gas sensors for NO<sub>2</sub> detection at room temperature, the sensors showed sensitivity to sub-ppm scale with low power operation [31].

## **1.2 Types of Gas Sensors**

Given the change in receptor and transducer described in the section above, gas sensors require further enhancement to have the best performance while operating sustainably at low power. That is why it is important to review the advantages and disadvantages of different gas sensors when considering which sensor is best suited to a particular application. Variations exist in the way sensors are affected by environmental conditions, cost of the production of the sensor, and power consumption, all of which are dependent on the type of technology and sensors used. Various common sensors can be used, such as catalytic gas sensors, electrochemical, thermal, metal oxide gas sensors, field-effect transistor-based gas sensors, optical gas sensors, and Nondispersive infrared radiation gas sensor [32-35]. Each sensor type cannot detect all types of harmful gases on its own, so the sensor type and capabilities must fit the specific sensing needs of the system.

### 1.2.1 Metal Oxide Gas Sensors

One subtype of semiconductor gas sensors is the thin film metal oxide (MO) sensor, in which the MO acts as the sensing layer [4, 36, 37]. The surface structure of the MO is polycrystalline, meaning it has many grains. Grains usually have random crystallographic orientation. This means that each orientation of crystal is different to the adjoining grains. The interfaces separating the grains from each other are called grain boundaries. These grain boundaries act as defective sites and decrease the conductivity of the material, but corrosion or oxidation is more easily achieved at grain boundaries [4, 37], which is favorable for gas adsorption, and therefore detection.

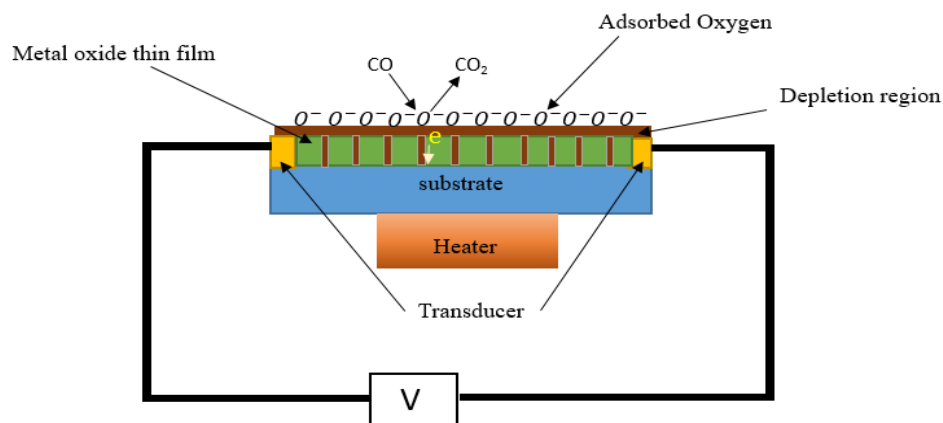


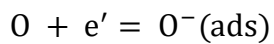
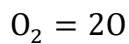
Figure 1.2: Demonstrates the mechanism of the MOs gas sensor. The green layer represents the MOs sensing film, the brown layer represents the depletion region, the yellow region represents the Au electrode, the blue layer represents the substrate, and the orange layer represents the heating element. At the operating temperature, the sensing layer interacts with oxygen, and the oxygen is adsorbed on the surface. When the CO reducing gas interacts with the adsorbed oxygen, it forms CO<sub>2</sub> by taking one oxygen. As a result, the electron injects back to MOs surface which changes the resistance.

The MO sensing layer works by adsorbing the oxygen from the atmosphere at the surface as shown in Figure 1.2. When an oxygen atom from the atmosphere reacts with the surface of MO, it takes an electron from the outer surface of MO to form an oxygen ion (O<sup>-</sup>). This leads to a decrease in the conductivity of the MO sensing layer. The decrease in conductivity occurs as the electron that is taken by the oxygen is no longer free, creating a depletion region (insulating layer), and therefore an energy barrier, around the grain boundaries. This causes the conduction band to bend as the electron cannot move freely due to the barrier, if the electron wants to move, it must have a certain amount of energy to cross the barrier.

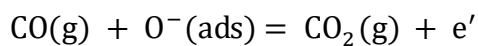
Temperature plays an important role in the MO gas sensor's sensitivity. The sensors cannot show fast response and recovery in the atmosphere at room temperature due to the low adsorption of  $O^-$  on the surface of the MO layer [26, 38]. Increasing the temperature makes  $O^-$  dominant at the surface of the MO sensing layer, which increases the interaction between gas species and adsorbed  $O^-$  on the MO sensing layer. Most MO sensors operate at high temperatures ranging between 150 and 450 °C depending on the type of MO material. For example, tin oxide ( $SnO_2$ ) operates at 200 °C and zinc oxide ( $ZnO$ ) operates at 150 °C [26, 27].

The sensing mechanism can be written chemically, separated into two reactions as follows:

a) Adsorption of the oxygen on the surface of MOs.



b) When the sensor is exposed to the oxidising gases in the air, the gas species will act as an electron donor or acceptor leading to a decrease in resistance for p-type or an increase in resistance for n-type, respectively [36]. For example, when absorbing carbon monoxide (CO), a reducing gas, the chemical reaction is as follows [39, 40],



As a result of the gas species interaction with chemisorbed oxygen on the surface, the electron that is held by the oxygen on the surface is injected back to the MO's material and therefore becomes free. Which leads to an increase or decrease of the conductivity for p-type or n-type material, respectively.

As described above MO sensor is suitable for detecting oxidizing and reducing gases. But the high operating temperature means it is not cost-effective in real applications. Therefore, many methods have been investigated to enhance the MO sensor and reduce the operating temperature, such as doping with nanoparticles and oxidation [41, 42].

### 1.2.2 Field Effect Transistor (FET) Sensors

A field-effect transistor sensor consists of a sensing channel placed between two electrodes (source and drain) with a gate contact to modulate the electronic response of the channel [43, 44]. The flow of the current is adjusted by applying a voltage to the gate, which changes the conductivity between the source and drain. FETs operate by using electrons or holes as charge carriers by applying a positive or negative voltage to the gate.

The adsorption or desorption of the gas molecules on the surface of the sensing layer of a FET will modify its channel conductivity. The conductivity depends on the mobility and concentration of free charge carriers. When used as a gas detector, the main mechanism is the adsorption of the gas molecules, which causes the change in the mobility and concentration of the charge carriers via charge transfer interactions between the adsorbed species and FET channel.

In the case of the p-type sensing layer, charge carrier concentration increases under the adsorption of the oxidizing gas molecules, which causes some of the free electrons in the conduction band to be captured on the device surface by the adsorbed species. In contrast, under a reducing gas, the charge carrier concentration decreases, as some captured electrons on the surface are released into the conduction band.

There are a variety of sensing mechanisms for the FETs, one of which is described in Figure 1.3. The figure below illustrates the mechanism of the p-type sensing layer, which interacts with the oxidizing gas oxygen ( $O_2$ ), and reducing gas carbon monoxide (CO). The  $O_2$  interacts with the sensing layer leading to electron-withdrawal at the surface. As a result, charge carrier (hole) concentration and therefore, device conductance, are increased.

Adversely, when the CO interacts with the sensing layer, it is oxidised by  $O^-$ . This results in electrons being released back into the conduction band, which then recombine with holes. This interaction causes the charge carrier concentration and device conductance to decrease.

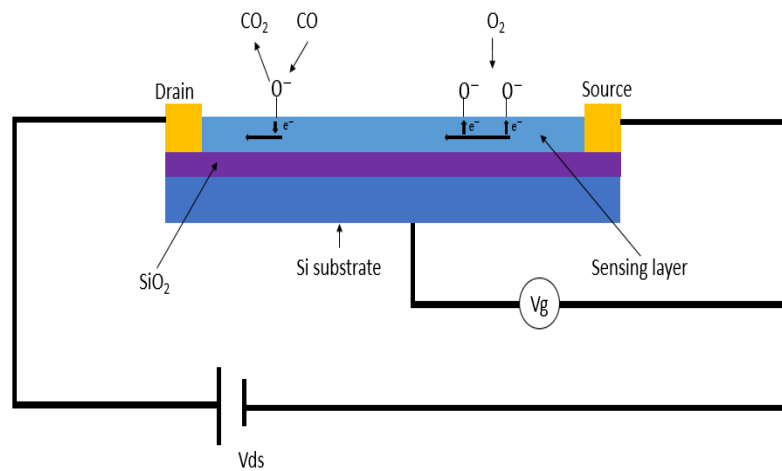


Figure 1.3: Shows the shape of the FET, which has a P-type sensing layer between two electrodes (source and drain), silicon is coated with silicon oxide and voltage is applied to substrate. As an oxidising gas e.g. oxygen interacts with the sensing layer, some electrons from the conduction band are captured on the surface. On the other hand, reducing gas like carbon monoxide interacts with the sensing layer and result in freeing electrons back to the conduction band.

### 1.2.3 Electrochemical Gas Sensor

Electrochemical gas sensors consist of a working electrode, an electrolyte, and a counter electrode [45, 46]. Both the working and counter electrodes work as sensing layers. The electrolyte acts as a thin channel that separates the two electrodes while allowing ions to pass from the working electrode to the counter electrode. An ammeter is connected to the working electrode and the counter electrode through an external circuit to measure the current that results from the electrochemical reaction between the target gas and the working electrode.

When gas molecules interact with the working electrode, ions and electrons are generated. These generated charge carriers will flow from one electrode to the other through the electrolyte channel. The generated electrons (current) produced due to this mechanism flow through the external circuit, as demonstrated in Figure 1.4. During oxidation, the generated charge flows from the working electrode to the counter electrode, and during reduction, the flow of the generated charge will be from the counter electrode to the working electrode. The number of generated electrons is measured by the ammeter, and is proportional to the target gas concentration. For example, CO gas molecules interact with the working electrode as shown in Figure 1.4, where the CO interacts with water vapour on the working electrode and is oxidised [47]. The chemical reaction can be written as follows.



This interaction results in the charge carriers  $H^+$  and  $e^-$  being generated.

Electrochemical gas sensors are suitable for the detection of toxic and oxygen gases. They require low power to operate, but the sensors have some problems which limit their performance. For example, electrochemical gas sensors are sensitive to changes in humidity and temperature, which deteriorate their response [48, 49].

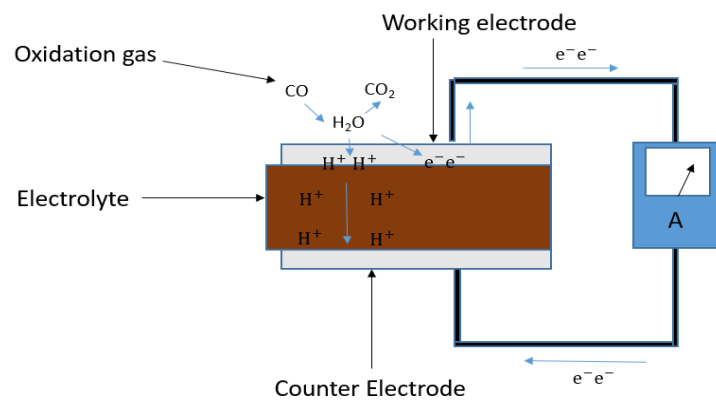


Figure 1.4: Shows the CO oxidised through the chemical reaction on the working electrode. This results in generated  $H^+$  and current flow to the counter electrode through the electrolyte. Also, the generated  $e^-$  flow through the external circuit to the counter electrode.

### 1.2.4 Catalytic Gas Sensor

Catalytic gas sensors can be used to detect flammable gas [33, 50]. They consist of two platinum wire coils, each embedded in an alumina bead as presented in Figure 1.5, connected to form a Wheatstone bridge circuit. The alumina bead is then covered with a thick film catalyst which is made of metal. The first sensor (detector coil) acts as the active resistance which oxidises in the presence of gas, and the second acts as a reference resistance which is encapsulated to avoid oxidation.

When the flammable gas molecule oxidises on the detector coil, the temperature will increase causing a change in the resistance, while the temperature and resistance on the reference coil stay unchanged. Consequently, the presence of the gas, and therefore its oxidation on the

detector coil, can be detected by monitoring the variation in resistance compared to the reference resistance.

Catalytic gas sensors are simple and operate at low energy. However, they require oxygen to operate and can easily be contaminated by chlorine [51]. Which lead to the failure in their sensitivity.

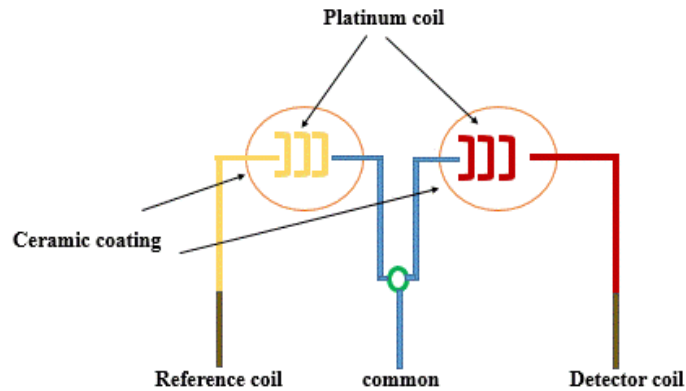


Figure 1.5: Schematic of catalytic gas sensor.

### 1.2.5 Nondispersive Infrared Radiation Gas Sensor

Nondispersive infrared radiation gas sensor is used to detect gas molecules and measure their concentration [52, 53]. As shown in Figure 1.6, it comprises of a chamber with an infrared light source on one side and an infrared detector on the other. An optical filter is placed in front of the infrared detector to filter out all light except frequencies absorbed by gas molecules. It operates by directing an infrared beam through the chamber which may contain the target gas molecules. In the presence of the gas, the infrared beam is absorbed proportionally to the concentration of gas present - this causes the detector signal to be attenuated as less light remains to hit the detector, and thus the gas concentration is determined [53].

This type of gas sensor is usually used to detect carbon dioxide and combustible gases in the absence of oxygen in the surrounding environment. It can also operate in inert atmospheres.

However, only gases that absorb infrared radiation can be detected in this manner, which limits their potential application to only certain target gases.

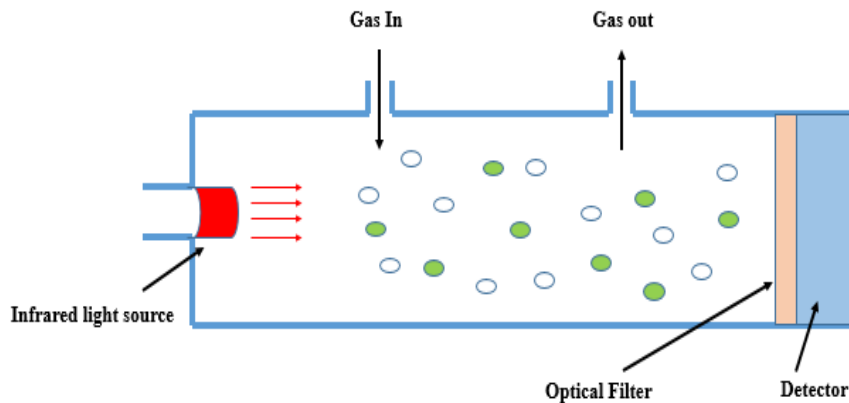


Figure 1.6: Schematic of Nondispersive infrared radiation gas sensor.

### 1.3 Graphene based Gas Sensors

In recent years, graphene has been demonstrated to provide good characteristics for sensing application. Such as its large surface area to volume ratio, high conductivity, and low electrical noise [54-56]. Graphene can operate as a sensor at room temperature, which greatly reduces energy consumption compared to other key sensing technologies[57]. The unique feature of graphene is its high surface area to volume ratio and atomic thickness, which means that any adsorbed gas molecules on the surface influence the entire depth of the graphene channel. This means that graphene interacts strongly with its surrounding environment. Also, graphene has high electrical mobility of  $1304 \text{ cm}^2\text{V}^{-1}\text{s}^{-1}$  even within low-quality of prepared devices [58]. These properties make graphene an ideal candidate for gas sensor material, and it is used widely in gas sensors today [59]. However, graphene sensors suffer from issues such as slow response time, baseline drift, and taking a long time to reach saturation [60-63].

Graphene oxide (GO) sensors with functional oxygen groups have been revealed to overcome device issues and improve the sensitivity and stability [64, 65]. Functional oxygen groups

significantly influence the graphene sensor's performance. The inclusion of oxygen groups within the graphene lattice causes larger electron transfer from adsorbates and thus yields an improved sensing signal. However, a high percentage of oxygen groups on graphene can degrade the graphene sensitivity and stability and ultimately make graphene electrically insulating [66]. Therefore, oxidation of graphene needs to be controlled to improve electrical characteristics for gas sensors use. Reduced graphene oxide sensors have been used to overcome this problem and device performance improved in comparison to graphene oxide [64, 67]. The sensitivity and stability for the device at room temperature are enhanced after oxygen groups are reduced [64, 67]. Introducing oxygen groups to CVD graphene (oxidised CVD graphene) sensors by the chemical method has been demonstrated and found to possess the same properties as the reduced graphene oxide [68]. In addition, the amount of introduced oxygen can be controlled during the oxidation process without the need for further reduction steps. Devices based on oxidised CVD graphene have higher sensitivity and stability in the ambient environment than pristine graphene and GO [66, 69, 70].

## Chapter 2

### 2 Literature Review

#### 2.1 Graphene Gas Sensors

Graphene is widely used as a semiconductor today. It is made of a hexagonal lattice of carbon atoms in a single layer. Graphene has attracted attention from researchers due to its ultimately high surface area to volume ratio, of  $2000 \text{ m}^2/\text{m}^3$  [54], high conductivity, and low electrical noise [55, 56]. Graphene can operate as a gas sensor at room temperature, which greatly reduces energy consumption compared to other key sensing technologies, such as MO sensors operating at temperatures ranging between 150 and 450 °C [26, 27, 57]. The distinctive features of graphene are its high surface area to volume ratio and atomic thickness, which means that any physisorbed gas molecules on the surface influences the entire depth of the graphene channel. This means that graphene should interact strongly with its surrounding environment. Additionally, graphene has high electrical mobility. These properties make graphene an ideal gas sensor material, and it is used widely in gas sensors today[59].

Moreover, if graphene is modified with functional oxygen groups, such as epoxy, hydroxyl, carbonyl, and carboxylic groups, it can significantly improve the graphene sensor's performance. The increasing in adsorption strength provided by oxygen groups causes larger electron transfer from adsorbates to the sensor, and an improved sensing signal.

In the following section, literature about unmodified/modified graphene gas sensors is reviewed. Also, density functional theory (DFT) was reviewed for the sake of understanding the charge transformation between the adsorbent and the graphene and oxygen graphene oxide (GO).

#### 2.2 Density Functional Theory (DFT)

The low density of states around the graphene Dirac-Point, tied with atomic thinness of graphene, make it easy for graphene to be influenced by adsorbed gas species, because any adsorbed species will interact with the entire depth of the graphene channel, and the physisorb-related charge-transfer should have a non-negligible impact on the graphene-channel charge-carrier-density [71]. Therefore, controlling the type and the density of charge carriers of the graphene via doping makes graphene a very promising material for selective gas detection. The

adsorption of the atoms or molecules can easily influence the graphene-channel charge-carrier density [72].

The detection of the  $\text{NH}_3$  and  $\text{NO}_2$ , as archetypal electron donors and acceptors, respectively, have been widely studied, theoretically [72-75].

O. Leenaerts et al. used first-principles calculations, and showed that the charge transfer between adsorbed  $\text{NO}_2$  molecules and the graphene surface is independent of the adsorption site [73], but is dependent on adsorbate orientation on the graphene surface [73]. Their work also shows that  $\text{NO}_2$  strongly p-dopes graphene by  $-0.1e$ , if it adsorbed on lowest unoccupied molecular orbital (LUMO) position below the Dirac point. In contrast, in the mixed orientation of the highest occupied molecular orbital (HOMO) and LUMO orbital, there is a small charge transfer to the graphene surface ( $\pm 0.039e$ ). On the other hand, the charge transfer from  $\text{NH}_3$  to the graphene surface is about  $0.03e$  in the HOMO orbital orientation. While in the LUMO and HOMO orbitals orientation, the charge transferred from the LUMO orbital is opposite to the HOMO orbital, and therefore they cancel each other. They result in zero charges transferred.

T. Wehling et al., used local density approximation (LDA) and gradient-corrected exchange-correlation functionals (GGA) to study the charge transfer from  $\text{NO}_2$  and  $\text{NH}_3$  to graphene [72]. According to their calculation, the electron transfer from graphene to  $\text{NO}_2$  is found to be  $0.1e$ . While in the case of  $\text{NH}_3$ , the electron being donated to graphene and the calculation predicted donated electrons to be between  $0.03$  and  $0.04e$ . Which is comparable with values identified by Leenaerts.

DFT has also been used to investigate the charge transferred between adsorbates and graphene oxide (GO) with oxygen functional groups [74]. S. Tang and Z et al. used the first-principles calculation to study the adsorption of  $\text{NO}_x$  ( $x=1,2,3$ ) on graphene and GO [74]. They show that the adsorbed  $\text{NO}_2$  on graphene results in  $-0.07e$  charge transfer from  $\text{NO}_2$  to the graphene surface, which is a similar value to that identified by Leenaerts. On the other hand, the charge transfer by adsorption of  $\text{NO}_2$  on the GO with the oxygen functional groups C-OH (hydroxyl), C-O-C (epoxy), C=O (carbonyl), and R-COOH (carboxyl) is different. The adsorption of  $\text{NO}_2$  on the -OH site is found to have a larger charge transfer of  $-0.2e$  compared to  $-0.1$ ,  $-0.07$ , and  $0.19 e$  charge transferred on graphene. This improvement of the charge transformation is attributed to the strong binding between the hydrogen bond and the oxygen from  $\text{NO}_2$ . In addition, the binding energy depends on the orientation of  $\text{NO}_2$ , which can also form weak covalent nitrogen bonds with carbon [74]. The study shows that the existence of hydroxyl and

carbonyl functional groups on GO increases the charge transfer resulting in NO<sub>2</sub> being adsorbed on GO chemically. The –OH and –COOH are favourable energetically for NO<sub>2</sub> adsorption. As the concentration of the hydroxyl group decreases on the GO, the charge transfer between the adsorbate and GO increases. This gives rise to the importance of controlling or reducing the amount of oxygen functional groups on GO, which then improve the sensitivity for the GO [74]. Epoxy and carbonyl group are not favourable energetically by NO<sub>2</sub> but also does not affect the adsorption on –OH and -COOH site.

Other publications investigate NH<sub>3</sub> adsorption at the vacancy of carbon atom on the graphene layer and epoxy group, via DFT, and show that both adsorption results in a small electron charge transformation [75]. Matterson et al. used the QUANTUM ESPRESSO package and LDA to perform the calculation. They found that the adsorption of NH<sub>3</sub> on pristine graphene was found to have a small charge transferred of -0.001e. At the same time, the interaction between NH<sub>3</sub> and the carbon vacancy site (C-OH, C=O) on graphene was found to be reactive with an adsorption energy of -1.71eV. Moreover, the adsorption on the epoxy group is energetically favourable by NH<sub>3</sub> with an adsorption energy of -0.37eV. This binding leads to the dissociation of the NH<sub>3</sub> to NH<sub>2</sub> and OH, resulting in chemisorption formation. The carbonyl and hydroxyl groups provides an active site for the adsorption of NH<sub>3</sub> through the hydrogen bond to oxygen or N to the H in hydroxyl [75]. However, adsorption of NH<sub>3</sub> on carbonyl and hydroxyl groups are more likely to occur due to the high binding energy than epoxy groups. Therefore, carbonyl and hydroxyl groups are favoured energetically for NH<sub>3</sub> adsorption.

Y. Peng et al reported that epoxy and hydroxyl groups enhance the adsorption of NH<sub>3</sub> on GO compared to pristine graphene [76]. They used the DFT calculation to study the molecular adsorption on GO. The result of the calculation revealed that the binding energy of the adsorption on pristine graphene (0.114 eV) is smaller than that for hydroxyl (0.175 eV) and epoxy (0.145) groups and is not affected by the adsorbent orientation. The increased binding energy of hydroxyl groups is favourable for the NH<sub>3</sub> adsorption and results in enhancing the adsorption compared to epoxy groups and pristine graphene. Also, the charge transfer from the NH<sub>3</sub> molecule to the graphene surface is 0.001e, which is smaller than the charge transfer of 0.018e and 0.003e from hydroxyl and epoxy groups, respectively. The enhancement in the charge transferred is attributed to the high binding energy provided by the oxygen groups [76]. The adsorption of the NH<sub>3</sub> in hydroxyl groups is higher than that in epoxy groups. This can be explained by the N atom from adsorbed NH<sub>3</sub> being bonded to the H atom from the hydroxyl group, resulting in high charge transfer. While the adsorption on epoxy groups happens by the

H atom from NH<sub>3</sub> being bonded to the O atom, resulting in low charge transferred. Therefore, the enhancement of the adsorption and charge transferred provides high sensitivity to the GO sensors.

Table 2.1: Summary of oxidised graphene gas sensors process and presented response, recovery, and detection limit for NO<sub>2</sub> and NH<sub>3</sub>.

Oxidation Method	Response to NO <sub>2</sub> (-%)/concentration (ppb)	Response to NH <sub>3</sub> (+%)/concentration (ppb)	Recovery NO <sub>2</sub> (%)	Recovery NH <sub>3</sub> (%)	LOD (ppb)	Temperature (°C)	Reference
Graphene (Micromechanical cleavage of graphite)	5/1000 (0.005)	3.8/1000 (0.0038)	0	3	-	room temperature	[77]
Graphene (epitaxial graphene on SiC)	2/50 (0.04)	0.1/50000 (0.000002)	5	-	-	room temperature	[78]
CVD Graphene	10/2000 (0.005)	19/2000 (0.0095)	-	-	100 (NO <sub>2</sub> ) 500 (NH <sub>3</sub> )	room temperature	[79]
CVD Graphene	21/20000 (0.00105)	10/550000 (0.000018)	70	80	-	-	[80]
CVD Graphene	0.2/5000 (0.00004)	0.1/500000 (0.0000002)	0	0	-	room temperature	[64]
Hummers GO	17/5000 (0.0034)	2.5/500000 (0.000005)	83	3	650 (NO <sub>2</sub> )	room temperature	[64]
rGO(1)	16/5000 (0.0032)	-	50	-			
rGO(2)	7/5000 (0.0014)	-	23	-			
(rGO was obtained by annealing the GO at 200 °C)							
Hummers (0.2 mg/mL GO dropped cast on Pt)	32/5000 (0.0064)	9/50000 (0.00018)	92	-	0.21 (NO <sub>2</sub> )	150	[70]

IDEs/SiO <sub>2</sub> /Si substrate and left for 10 min at 100 °C to dry)							
Hummers (suspension GO was spray coated on heated SiO <sub>2</sub> /Si substrate at 80 °C by Fengda BD-208 airbrush)	-	30/500000 (0.00006)	-	49	-	25	[65]
rGO (GO was reduced by thermal annealing in argon (Ar) flow at 300 °C for 1 h)	156/2000 (0.078)	-	80	-	-	room temperature	[81]
rGO (GO was reduced by laser irradiation )	5/50000 (0.0001)	0.04/50000 (0.0000008)	85	-	10000 (NO <sub>2</sub> )	25	[82]
rGO ( The reduction of GO was performed using aniline)	-	37.1/50000 (0.000742)	-	100	-	-	[67]
rGO ( The reduction of GO was performed using pyrrole)	-	10/1000 (0.01)	-	100	1 (NH <sub>3</sub> )	room temperature	[83]
rGO ( The reduction of GO was performed using n-hexanol )	19.6/60000 (0.000326)	-	20	-	-	room temperature	[84]
rGO (GO was reduced by hydrazine and then annealed at 300 °C for 4 h )	5/10000 (0.0005) 6/10000 (0.0006) 7/10000 (0.0007)	8/20000 (0.0004) - -	45 - 78	37 - -	- - -	25 60 100	[85]
rGO nanofibers (the reduction was hydriodic acid with acetic acid (HI–AcOH))	18/4500 (0.004)	-	70	-	-	100	[86]
CVD G	8/200000 (0.00004)	-	70	-	-	room temperature	[69]
CVD GO (CVD G oxidised by ozone treatment for 70 s)	20/200000 (0.0001)	-	80	-	1.3 (NO <sub>2</sub> )		

CVD GO (CVD G oxidised by oxygen plasma treatment)	-	60/475000 (0.000126)	-	100	-	room temperature	[87]
CVD GO/G composite (CVD G oxidised by oxygen plasma treatment)	-	13/200000 (0.000065)	-	95	750 (NH <sub>3</sub> )	room temperature	[88]
CVD GO (CVD G oxidised by 65% concentrated nitric acid (HNO <sub>3</sub> ))	9/100000 (0.00009)	41/100000 (0.00041)	-	80	27 (NH <sub>3</sub> )	25	[89]
CVD GO (CVD G oxidised by hydrogen peroxide (H <sub>2</sub> O <sub>2</sub> ) under UV light)	-	-	-	-	-	-	[90]
CVD GO (CVD G oxidised using 20% of sulphuric acid solution(H <sub>2</sub> SO <sub>4</sub> ))	-	-	-	-	-	-	[68]

### 2.3 Pristine Graphene Gas Sensors

Graphene gas sensors have been used to detect a different type of gas such as NH<sub>3</sub> and NO<sub>2</sub> [77]. These types of gas sensors have many advantageous features, such as working at room temperature, thus consuming less power, and costing less [78, 91]. Generally, oxidising/reducing gas adsorption on the graphene surface causes a reduction or increase in the response of the sensors, respectively.

In 2007, Schedin et al. fabricated a sensor using micromechanical exfoliation of graphite for detecting gas molecules [77]. In the sensitivity measurements, the response of graphene to 1 ppm ammonia (NH<sub>3</sub>), nitric oxide (NO), water vapor, and carbon monoxide (CO) was measured by recording the change in resistance of the sensor [77]. Figure 2.1. represents the change in resistance upon exposure to different types of gases. The sensor showed an increase in resistance upon exposure to the reducing gases, NH<sub>3</sub> and CO. This increase in resistance is attributed to the electron transfer from these gases into to the graphene layer after adsorption on the surface of graphene, which causes a decrease in the device's conductivity and therefore an increase in resistance. Because the device is within the hole-transporting regime as the Dirac point is located to the right of 0 volts. By adding electrons, the number of charge carriers available is decreased. The inverse can be observed for

oxidising gases such as water vapor and NO<sub>2</sub>. The response for the sensor was 0.005% for NO<sub>2</sub> and 0.0038% for NH<sub>3</sub>, as presented in Table 2.1. Also, the recovery after NO<sub>2</sub> was not achievable as the sensor did not recover at all at room temperature; meanwhile, after NH<sub>3</sub> exposure, the recovery was very low and was found to be 3% at room temperature. In order to achieve full recovery sensors was annealed at 150 °C.

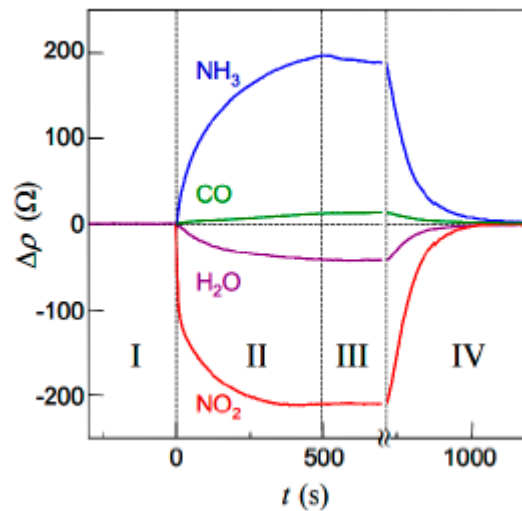


Figure 2.1: Shows the change in sensitivity of the graphene sensor upon exposure to different types of gases. Region I: the device is in vacuum before its exposure; II: exposure to a 5 l volume of a diluted chemical; III: evacuation of the experimental set-up; and IV: annealing at 150 °C. Adapted from reference [77].

In 2016, S. Novikov et al. fabricated sensors based on epitaxial graphene on SiC for detecting low concentrations of NO<sub>2</sub> [78]. The sensors show n-type behaviour due to electron donation from the SiC substrate to the graphene layer. This n-type behaviour is in contrast to the typically p-type behaviour of transferred CVD graphene. In the experiment, the sensors were annealed at 110 °C before exposure to different concentrations (20 and 50 ppb) of NO<sub>2</sub> for 100 seconds and 300 seconds of exposure to 50 ppm of NH<sub>3</sub>. The sensors show high sensitivity to sub ppb of NO<sub>2</sub> with response of 0.04% and 0.00002% for NO<sub>2</sub> and NH<sub>3</sub> respectively as presented in Table 2.1. The sensor only recovered 5% after exposure to NO<sub>2</sub> at room temperature and did not recover after NH<sub>3</sub> exposure. However, 100% of recovery was achieved after annealing the sensors at 110 °C.

Another publication by F. Yavari et al. showed that GFETs fabricated using CVD graphene show a response of 0.005% and 0.0095% for 2 ppm of NO<sub>2</sub> and NH<sub>3</sub>, respectively, at room temperature [79]. The exposure time was 50 and 360 minutes for NO<sub>2</sub> and NH<sub>3</sub>, respectively. The response behaviour is similar to Novikov's results, which show that the graphene is more sensitive to NO<sub>2</sub> than NH<sub>3</sub>, which is comparable to the DFT identification [72, 73]. The

detection limit was calculated for the sensor and found to be 100 ppb and 500 ppb for NO<sub>2</sub> and NH<sub>3</sub>, respectively. However, the recovery was not achievable at room temperature, and the device recovered to almost 95% of the baseline resistance after being heated on a hot plate at 200 °C.

A. Singh et al. also demonstrated NO<sub>2</sub> and NH<sub>3</sub> sensing at 20 ppm and 550ppm, respectively, using GFETs based on CVD graphene [80]. Two different measurement regimes were used to determine the sensitivity of the device – one regime involved sweeping back gate voltage and monitoring the change of Dirac point, the second regime was carried out by modulation via back gate bias and measuring the resulting channel conductivity [80]. Figure 2.2, demonstrates the response and change in Dirac point upon exposure to different gases [80]. As the device is exposed to oxidising gas (NO<sub>2</sub>) the Dirac point moves to positive voltage, whereas exposing it to reducing gases causes the Dirac point to move toward negative voltage. The shift toward positive voltage or downshift of the Fermi level is attributed to NO<sub>2</sub> being an electron trap, which results in increasing the hole density in the graphene. While the shift in the Dirac point toward negative voltage or upshift to the Fermi level is due to the NH<sub>3</sub> donating electrons to graphene, increasing the electron density in the graphene layer. The inset figure, in Figure 2.2, shows the response to 20ppm NO<sub>2</sub> and 550ppm NH<sub>3</sub>. The response for the sensor is 0.00105% and 0.000018% for NO<sub>2</sub> and NH<sub>3</sub>, respectively. Correspondingly, the sensor response direction changes upon gas exposure, which increases with NO<sub>2</sub> and decreases with NH<sub>3</sub> as the GFETs initially poses p-type behaviour. The sensor recovered to 70% after NO<sub>2</sub> and 80% after NH<sub>3</sub> exposure.

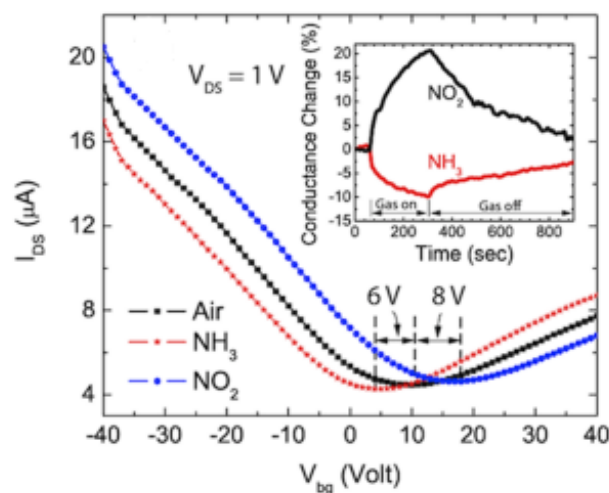


Figure 2.2: Transfer curves characteristics of a back-gated CVD graphene FET in air while exposed to NO<sub>2</sub> and NH<sub>3</sub>. Inset shows the changes in conductance of CVD graphene with the flow of 20 ppm NO<sub>2</sub> and 550 ppm NH<sub>3</sub>. The gas carrier used in the experiment during the exposure is N<sub>2</sub>. Adapted from reference [80].

In separate study, Wei et al. demonstrated change in Dirac point upon exposure to nitrogen dioxide (NO<sub>2</sub>) and ammonia (NH<sub>3</sub>) in ambient conditions [58]. The device sensitivity was determined by the Dirac point shift upon gas exposure to NO<sub>2</sub> and NH<sub>3</sub>. The Dirac point is initially located at a positive voltage, indicating that graphene is p-doped. The shift in Dirac point was observed toward more positive voltage as the concentration of NO<sub>2</sub> increased from 50 ppm to 400 ppm, whilst the opposite shift was observed for NH<sub>3</sub>. The shift in Dirac point is attributed to the increase or decrease in the charge carrier concentration after gas adsorption as the NO<sub>2</sub> withdrew an electron from the device leading to an increase of hole charge carrier concentration and resulting in a downshift to the Fermi level; meanwhile, upon exposure to NH<sub>3</sub>, the opposite happens with an upward shift to the Fermi level. Which is similar to the Dirac shift observed by Singh.

Another publication by H. E. Romero et al. showed that Dirac shifts in GFETs toward negative gate voltages as the device exposes to 10% NH<sub>3</sub>. This change is due to the electron transferred to the pristine graphene surface which increase the electron charge carrier density [92].

In the literature above, it was shown that the lack of surface modification in the unmodified graphene gas sensors limits their performance to detect gas concentration of sup ppb. This results in in low sensitivity and selectivity which are inherent to the devices in these experiments. Another related issue associated with these sensors is not being able to show stable operation, reproducibility, or recovery at room temperature. It was shown that increasing the temperature (100 -150 °C) improved recovery, but this was at the cost of increased energy consumption [93]. To overcome these issues, various methods have been investigated to modify the surface of graphene gas sensors with an aim to improve and achieve the desired sensitivity, recovery and selectivity. One route to enhance the selectivity of graphene gas sensors is by modifying the surface of the graphene via oxidation, which provides defect sites on graphene for gas adsorption.

## **2.4 Graphene Oxide Gas Sensors**

Pristine graphene gas sensors are not favourable for gas adsorption and desorption as they do not possess high sensitivity and fast response time. Also, these gas sensors have limitations in their sensitivity, as explained in section 2.3 and the result presented in Table 2.1, which is seen as low response at room temperature. Moreover, these pristine graphene gas sensors do

not have a high response. The response percentage achieved was around 0.005% and 0.0038% per ppb after adsorption to NO<sub>2</sub> and NH<sub>3</sub>, respectively, as presented in Table 2.1. Therefore, variations on pristine graphene gas sensors have been introduced to overcome this problem via oxidation [69, 88, 89]. Graphene oxide (GO) gas sensors with oxygen functional groups on graphene surfaces (C-OH (hydroxyl), C-O-C (epoxy), C=O (carbonyl), and R-COOH (carboxyl)) have high selectivity, sensitivity, and recovery, making them good at differentiating between chemically similar and diverse compounds.

The oxidation to graphene surface was studied many years ago [70, 81, 85]. Chemical oxidation to CVD graphene has been recently studied and oxidised CVD graphene has been found to interact much more strongly with the target gases than pristine graphene [64, 68, 69, 82, 85, 87, 89]. Many oxidation methods are used to oxidise graphene, such as chemically [68, 89], reduced graphene oxide [84, 85], laser [82], Oxygen plasma [87, 88], and UV [90].

#### **2.4.1 Oxidation Methods**

One possible chemical method involves a simplified Hummers method which consists of the oxidation of graphite by using a mixture of a potent oxidising agent such as sulphuric acid (H<sub>2</sub>SO<sub>4</sub>), nitric acid (HNO<sub>3</sub>) and hydrogen peroxide (H<sub>2</sub>O<sub>2</sub>) to produce oxygen functional groups on the graphene surface [64, 68, 83, 89, 90]. The amount of oxidation on graphene cannot be well controlled during the oxidation process by Hummers method in comparison with other chemical oxidation methods. As the Hummers oxidation cannot be controlled, further reduction is required, to lower the amount of oxygen groups on GO by chemical, thermal, and laser irradiation, to produce reduced graphene oxide (rGO) [64, 81, 82].

Y. R. Choi et al. and N. Hu et al. have used XPS to evaluate the oxidation percentage change from GO to rGO as the GO has 30.03% to 35 % of C-O compare to 30% to 11.29 % on rGO [64, 83]. Reduced graphene oxide has low oxygen groups concentration with low percentage compared with GO by Hummers method. Also, the carbon to carbon bond (C-C) improves after reduction from 55% for GO to 79% for rGO.

Another method to chemically oxidise CVD graphene is via the use of strong nitric acid or sulphuric acid [68, 89]. The oxidation to CVD graphene was confirmed by taking the Raman I<sub>D</sub>/I<sub>G</sub> ratio to evaluate the defect percentage before and after oxidation. For oxidised CVD graphene, the Raman I<sub>D</sub>/I<sub>G</sub> ratio was found to be depending on oxidation time as I<sub>D</sub>/I<sub>G</sub> ratio ranged from 0.14% for pristine CVD graphene to 1.10%, 3.44%, and 4.16% for oxidation time of 30, 60, and 160 minutes respectively [68]. The I<sub>D</sub>/I<sub>G</sub> is used to estimate the number

of the introduced defects in the graphene as it increases with defect. The  $I_D/I_G$  ratio is very small for the pristine graphene as there is small vacancy defect, while oxidising graphene increases the vacancy defect on graphene is proportional to it.

Yet another method of oxidising CVD graphene is through the use of oxygen plasma to introduce oxygen defects on the graphene surface [87]. The defects introduced on graphene was determined by Raman measurements which show the ratio of  $I_D/I_G$  increased after oxidation from 0.05 for pristine CVD graphene to 2.5 for oxidise graphene. The increase in the  $I_D/I_G$  ratio attributed to the carbon atom having  $sp^2$ -bound after treatment with oxygen plasma. Ozone treatment has also been used to introduce oxygen groups defect on CVD graphene, and the amount of oxidation can be control by the time of exposure and the intensity of UV light during the exposure as Raman  $I_D/I_G$  ratio was changed from 0.035% for pristine graphene to 0.11% and 0.25% after 70 and 80 s of treatment [69], which confirms the defect being formed on graphene. Overall the best method for controlling the oxidation percentage and type of introduced oxygen groups is through chemical oxidation to graphene.

#### **2.4.2 Sensitivity**

GO gas sensors' sensitivity at room temperature is much higher than pristine CVD graphene (CVD G) upon exposure to  $NO_2$  and  $NH_3$  gases [64]. As presented in Table 2.1, the pristine CVD G sensor shows a response percentage of 0.00004% and 0.0000002% to  $NO_2$  and  $NH_3$  gases, respectively, while the GO sensor has a sensitivity of 0.0034% and 0.000005% to  $NO_2$  and  $NH_3$ , respectively. Figure 2.3 a) illustrates the change in response of a graphene oxide device upon exposure to different gases; when the sensors are exposed to oxidising gases ( $NO_2$ ), the response decreases, and adversely, when exposed to reducing gases ( $NH_3$ ), the response increases. The sensor's response changed linearly with changing the  $NO_2$  concentration, as shown in the inset Figure 2.3 b) The limit of the detection of these sensors was estimated to be 650 ppb. The enhancement in sensitivity for the GO sensor over the CVD G sensor to  $NO_2$  was attributed to the hydroxyl groups, which serve as adsorption sites on graphene sensors.

J. Park et al studied the use of GO sensors at 150 °C operating temperature for  $NO_2$  and  $NH_3$  detection [70]. The response of the sensors was found to be very high, with 0.0064% to  $NO_2$  and 0.00018% to  $NH_3$ . The lower limit of detection for the sensors was found to be close to

0.21ppb for NO<sub>2</sub>. This high sensitivity is thought to be the result of the acid washing condition, which removes epoxide groups leading to low adsorption energy [70].

G. Bannov et al. demonstrated graphene oxide chemiresistive gas sensors for ammonia (NH<sub>3</sub>) gas detection that operate at 25 °C [65]. The sensors show a change in response with 0.00006% during the exposure to NH<sub>3</sub> under humidity of 65%. However, in dry air, the GO sensors show a change in response of 0.00001% to NH<sub>3</sub>, which is lower than the response under humidity. the improvement in sensitivity in the relatively high humidity is attributed to the enhancement of NH<sub>3</sub> adsorption on sensors in wet air as the carboxylic and sulfonic groups increases. In wet air, the ammonia adsorbed on the GO through the physical adsorption as the chemical interaction with oxygen groups is weak. Also, the sensors showed the highest sensitivity toward ammonia compared to CH<sub>4</sub> and H<sub>2</sub> due to the increases of the adsorption site on the GO in high humidity (carboxylic and sulfonic groups), which improved the selectivity as the increased oxygen groups being energetically favoured by NH<sub>3</sub> [65].

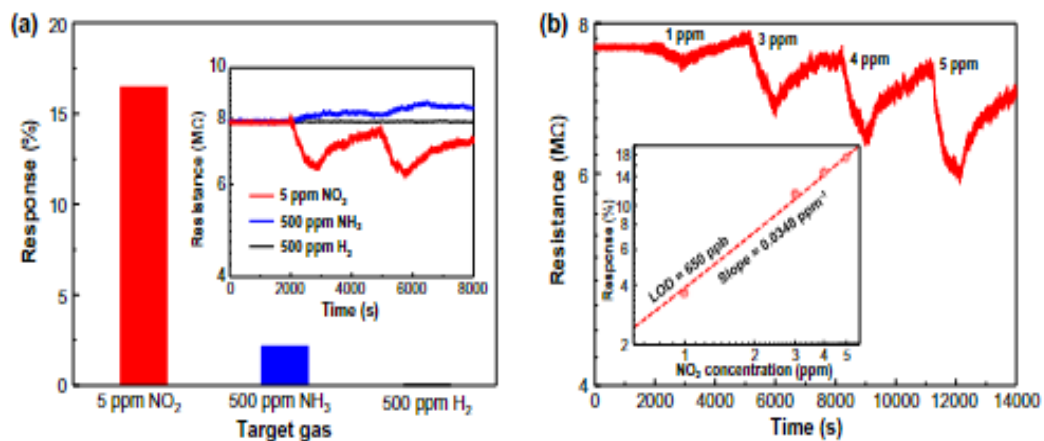


Figure 2.3: a) Represent the response of the GO sensors to NO<sub>2</sub>, NH<sub>3</sub>, and H<sub>2</sub>. The inset shows the change in the response curve to the gases. b) demonstrate the response curve to different concentration range from 1 -5 ppm of NO<sub>2</sub>, and the inset shows linear response vs gas concentration. Adapted from reference [64].

Thermally reduced graphene oxide sensors have a higher sensitivity compared to rGO reduced by chemical and laser methods, GO, and pristine graphene sensors as presented in Table 2.1. rGO sensors reduced by thermal method show a response of 0.078% to NO<sub>2</sub> while for chemically reduced graphene oxide sensors the response range between 0.004% to 0.0007% [67, 81, 83-86]. The response for rGO sensors by laser irradiation is 0.0001% to NO<sub>2</sub> [67]. An increase of ~100x in response for thermally reduced graphene compared to the

response for reduced graphene oxide by chemical or laser irradiation methods. Device response was enhanced by the oxygen reduction, attributed to the recovery of the double-bonded carbon atoms, as the amount of C-O defective site needs to be lower than the C-C bond to achieve a fast and high response. Also, the sensitivity to  $\text{NH}_3$  by rGO sensors was observed to be higher for sensors reduced by using pyrrole compared to other reducing GO methods [83-85]. The response was found to be 0.01% for  $\text{NH}_3$ , while for other reduction methods response was found to range from 0.0004% to 0.0000008%, as in Table 2.1. Enhancement in response to  $\text{NH}_3$  attributed to the increasing of epoxy (C-O) and carboxylic acid (C=O) on the rGO sensors, which interact with  $\text{NH}_3$  gas molecules [67]. This result in charge transfer from rGO to adsorbed  $\text{NH}_3$  molecule leads to an increase in the response.

Two different CVD graphene sensors that oxidised by two different methods, which are ozone treatment and nitric acid, show a response of 0.0001% and 0.00009%, respectively, to  $\text{NO}_2$  [69, 89]. The lower limit of detection was estimated to be 1.3 ppb for the device oxide by ozone. The sensor, which was treated with ozone for 70 s, was exposed to  $\text{NO}_2$  concentration range from 200 ppb to 200000 ppb and showed good sensitivity, as shown in Figure 2.4 [69]. The pristine graphene sensor did not show any sensitivity to  $\text{NO}_2$  concentration below 180000 ppb, while graphene treated by ozone exhibited high sensitivity with a low limit of detection of 200 ppb. The response of oxidising CVD G device is 0.0001%, and the pristine CVD G device is 0.00004%. This shows that the oxidised device's response is enhanced 50 times more than the pristine one.

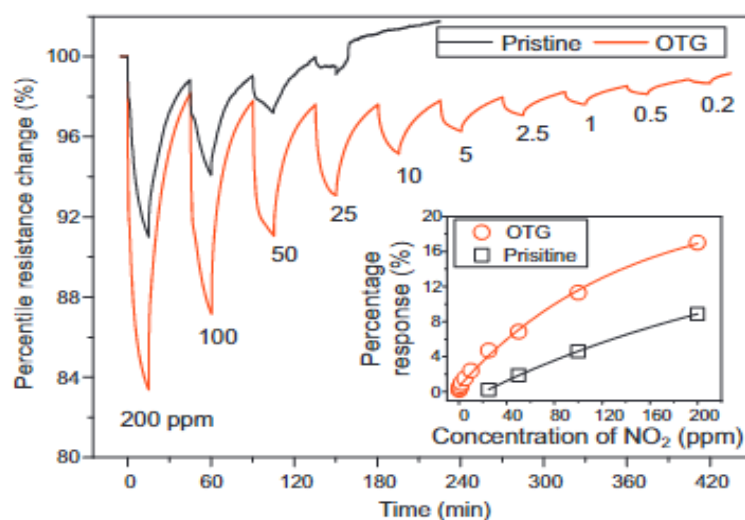


Figure 2.4: Demonstrates the change in resistance for pristine graphene (black) and graphene oxide by ozone treatment (red) upon exposure to different concentrations of  $\text{NO}_2$  (0.2 ppm to 200 ppm). The inset shows the response change for both pristine and treated graphene to different  $\text{NO}_2$  concentrations. Adapted from reference [69].

The enhancement in response to  $\text{NO}_2$  by CVD graphene oxide through ozone treatment resulted from the oxygen functional groups (C-OH) created on the graphene. Which then provides favourable sites for gas adsorption on the graphene surface. In contrast, the sensitivity for CVD G oxide by chemical method (nitric acid) is low due to the oxygen group introduced ( $-\text{NO}_2$ ) not being favoured energetically for  $\text{NO}_2$  adsorption. Also, CVD G sensors oxidised by nitric acid have a response of 0.00041% to  $\text{NH}_3$  with a limit of detection 27 ppb [89]. The enhanced sensitivity for the device treated with nitric acid is attributed to the interaction of the C-N bond and nitro ( $-\text{NO}_2$ ) functional groups introduced to the graphene surface, which provides an active site for the adsorption of the  $\text{NH}_3$  on graphene. While for the CVD G treated with oxygen plasma, the response was 0.000065%, which is 50 times less than the device treated with nitric acid. The improvement in the sensitivity of CVD G oxide by nitric acid compared to CVD G oxide by ozone treatment or oxygen plasma is attributed to the C-N and  $-\text{NO}_2$  induced by nitric acid being energetically favoured for  $\text{NH}_3$  adsorption.

As described above, the oxygen functional groups defects on graphene are favourable for gas adsorption, and the selectivity of the graphene gas sensors can be tailored through the appropriate choice of said functional group. Moreover, the sensitivity of the GO sensors depends on the number of oxygen functional groups on the graphene oxide, with a delicate balance having to be considered between the increase of favourable gas adsorption sites and the reduction of graphene's intrinsic favourable electronic properties. Problems associated with GO produced by the Hummer method, ozone treatment for CVD G, and oxygen plasma treatment for CVD G is the difficulty in controlling the amount of oxygen functional group formed on the GO during oxidation. The high amount of oxygen functional groups on GO reduces their electrical properties, which makes GO an insulating material. Also, to overcome this problem, the reduction method is used to reduce the oxygen group concentration and improve the sensitivity, but the process is hard to control. However, the oxidation to CVD G through the chemical method can be controlled via the exposure time and result in a low concentration of oxygen groups introduced to graphene without causing any damage to the graphene surface, which enhances the sensitivity toward gas adsorption. Also, the introduced oxygen groups (C-OH, C-O, C=O, and  $-\text{NO}_2$ ) could be controlled by using a specific type of acid solution (nitric acid or sulfuric acid). However, the type of introduced oxygen groups cannot be controlled for other oxidation methods.

### 2.4.3 Recovery

The recovery at room temperature for pristine graphene gas sensors and functional graphene sensors with oxygen moieties changes depending on the quality of the graphene and the percentage of oxidation. Whilst oxidation of graphene improves the sensitivity by providing favourable sites to increase the adsorption on the graphene surface, it can also negatively impact recovery behaviour by providing sites for chemisorption, which is less easily reversed than physisorption [94]. This leads to two different recovery behaviours that originate from physisorbed (fast recovery) and chemisorbed desorption (slow recovery) gas molecules [95].

The recovery percentage for pristine graphene gas sensors and functionalised graphene gas sensors are presented within Table 2.1. The GO gas sensors (Hummer's methods) show a recovery of 83% at room temperature, while the recovery for pristine CVD G gas sensors found to be 70%. The GO sensors show a recovery of 10% higher than the pristine device. The increase in recovery is attributed to the adsorption site provided by oxygen functional groups [69]. However, increasing the concentration of oxygen groups on graphene reduces the recovery by providing chemisorption sites that are hard to reverse at room temperature. The functional oxygen groups have a variety of chemical binding with different high energy levels (40-800 kJ/mol) and orientations on the graphene surface, which, as the cycle repeats of the gas adsorption and desorption, causes gas species to become more permanently adsorbed on these energetically favourable sites, which makes recovery slow down [69]. On the other hand, the recovery of CVD G gas sensors was 80% after exposure to  $\text{NH}_3$ , which was attributed to the  $\text{NH}_3$  being physisorbed on the graphene rather than chemisorbed due to the very low amount of defect on the graphene surface. Compared to the CVD G device, GO gas sensors show a low recovery of 49% as  $\text{NH}_3$  adsorbed chemically to the oxygen functional groups on the graphene oxide surface. However, the amount of the oxygen functional groups on graphene devices effect their recovery. So, high amount of oxidation make the device recovery slow compared to the lightly oxidised one.

As can be seen in Table 2.1, the recovery percentage for rGO gas sensors by laser irradiation is 85%, which is 13% and 2% higher than the pristine CVD G and GO sensors, respectively. This recovery improvement by the rGO sensor is attributed to the removal of oxygen functional groups (C-O), which enhance the adsorption of the  $\text{NO}_2$  molecule by changing of rotational motion of C-OH groups and relaxation to the original cause of the desorption of the  $\text{NO}_2$  [64]. Also, compared to the laser irradiation method, other methods of reducing graphene oxides, such as thermal annealing and chemical reduction, have shown low recovery percentages of

80% and 20%, respectively. These reduction methods are speculated to remove a large amount of hydroxyl groups from the graphene surface, making a recovery slower [84]. Therefore, maintaining the amount of hydroxyl groups is important for higher recovery. Nevertheless, the rGO gas sensors by chemical reduction process have a higher recovery of almost 100% after  $\text{NH}_3$  desorption than the GO device. This result of high recovery is attributed to the use of an IR lamp during the measurement, which increases the heating on the device and leads to faster desorption as the higher repulsive force is created by exciting the molecules' vibration [83].

The CVD GO gas sensors oxidised by oxygen plasma show high recovery after exposure to  $\text{NO}_2$  gas, compared to pristine, chemical, and thermal rGO sensors. The CVD GO sensors showed an 80% recovery at room temperature as in Table 2.1. Further, the CVD GO sensors that were oxidised by oxygen plasma and chemical methods showed a recovery percentage of 100% and 80% after the desorption of  $\text{NH}_3$ . Oxidised graphene provides more sensitivity due to the high energy sites provided by oxygen functional groups causing larger charge transfer between graphene and adsorbates [88, 89]. However, GO is worse at recovery at room temperature than pristine graphene or reduced graphene oxide. This is because oxygen functional groups (C-OH, C-O, and C=O) provide preferential binding sites for incident gases, but the binding energy of gases on these groups makes it more difficult to get rid of the gases post-exposure. Therefore, carefully controlled graphene oxidation should provide a route towards increased sensitivity without sacrificing too much recovery behaviour.

## 2.5 Graphene Gas Sensors Benefits and Challenges

Benefits:

Graphene possesses an exceptional surface-to-volume ratio due to its 2D structure. It is the thinnest material and has excellent electron mobility, making it promising for use as a gas sensor [55, 96]. These properties allow small gas molecules to adsorb easily on the graphene surface. Moreover, graphene is a good conductor for both electricity and heat. All these properties make graphene a good candidate for gas sensing. In particular, graphene's atomic thickness means that any adsorbate on the graphene will have the effect of doping the entire graphene channel thickness [55, 72]. In addition, graphene possessing a low density of states close to its Dirac point [97]. This is important as a small change in the number of charge carriers upon gas adsorption significantly changes the electronic state. Taken in combination, these factors make graphene an ideal candidate for gas sensing, as even modest charge exchange interactions between the graphene sheet and adsorbates should produce a

measurable change in the graphene's conductivity [58, 80] and shift in the Dirac point of the graphene channel [58, 79, 80]. Graphene gas sensors can be used to detect flammable gases such as hydrogen and ethanol at low concentrations [98]. In addition, it can detect toxic and explosive gases, including nitrogen dioxide, ammonia, carbon monoxide, and sulfur dioxide [70, 80]. It can operate at room temperature which leads to low consumption of energy [80], and can be fabricated easily and without high costs [98]. Also, GO with low amount of defects can be used as a gas sensor to improve gas detection [70] as oxygen introduces defects to the graphene which makes it favorable to the gas adsorption.

#### Challenges:

Graphene has no band gap, which makes it not useful for transistors devices [99] as it is difficult to switch between conducting and insulating states. Because of this, the on/off ratio is very high making it very unfavorable. In addition, the recovery time of the graphene gas sensor is very long and can never fully recover at room temperature. As a result, currently, the temperature of the sensor is increased to improve the sensitivity and recovery time, which in turn increases the power consumption. It also shows cross sensitivity to different gases [100, 101].

Pristine graphene is not favorable for gas adsorption, so defects have to be introduced to form adsorption sites and allow graphene to act as a good sensor. The oxidation method is a common way to make the sensor favorable to gas adsorption. However, the percentage of the oxygen on graphene surface is difficult to control during the oxidation process. Too much oxygen on the surface can turn the graphene into an insulator and prevent sensing.

## Chapter 3

### 3 Theory

#### 3.1 Graphene

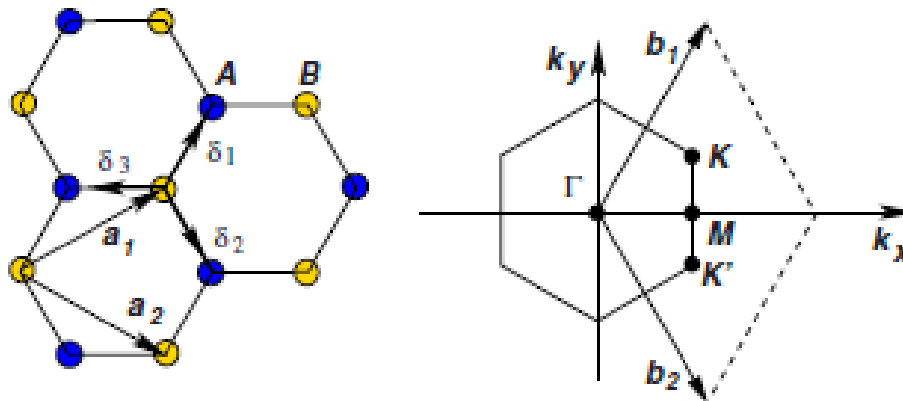


Figure 3.1: Shows the graphene honeycomb lattice and its Brillouin zone. The lattice on the left demonstrates a structure of graphene, which is made of two interpenetrating triangular lattices. The  $a_1$  and  $a_2$  are the vectors of the lattice unit, and  $\delta_i$ ,  $i=1, 2, 3$  are the closest neighbour vectors. The right lattice corresponds to the Brillouin zone, where the Dirac points are located at the  $K$  and  $K'$  points. Copied from reference [103].

Graphene is a two-dimensional (2D) material. It is considered to be one atom thick, and extends in length and width dimensions. This single atom layer of carbon atoms forms a hexagonal lattice structure, as shown in Figure 3.1. Pure carbon allotropes with different orientations join together to form blocks of graphene, for example, graphite (3D), polycyclic aromatic, fullerenes (0D), and carbon nanotube (1D). For all of the allotropes, each carbon bonded to the three adjacent neighbouring carbons in the form of a  $sp^2$  hybridized carbon. This bonding leads to a flexible structure and formation of  $\pi$  and  $\pi^*$  state bands [102], which exist over the layer of carbons. Graphene is a bipolar conductor with high electrical conductivity, and high electron/hole mobility. Graphene was first isolated by Novoselov and Geim in 2004, and since then has drawn attention due to its exceptional electronic, optical, and thermal properties [71].

##### 3.1.1 Atomic Structure of Graphene

The graphene lattice consists of two carbon atoms per unit cell [103]. Figure 3.1 represents the shape of the single-layer graphene lattice. The two vectors of the graphene lattice are presented by Equation 3.1.

$$a_1 = \frac{a_{\text{carbon-carbon}}}{2} (3, \sqrt{3}), \quad a_2 = \frac{a_{\text{carbon-carbon}}}{2} (3, -\sqrt{3}) \quad (3.1)$$

Where the carbon-carbon distance is measured and found to be about 1.42 Å. A reciprocal lattice of graphene vectors can then be written as in Equation 3.2 [103].

$$b_1 = \frac{2\pi}{3a} (1, \sqrt{3}), \quad b_2 = \frac{2\pi}{3a} (1, -\sqrt{3}) \quad (3.2)$$

For the physical properties of graphene, the most critical parameter is the Dirac points, K and K'. These two Dirac points are located at the corners of the graphene Brillouin zone (BZ). The importance of Dirac points will be explained shortly, their location and momentum are described in Equation 3.3.

$$K = \left( \frac{2\pi}{3a}, \frac{2\pi}{3\sqrt{3}a} \right), \quad K' = \left( \frac{2\pi}{3a}, -\frac{2\pi}{3\sqrt{3}a} \right) \quad (3.3)$$

### 3.1.2 Electronic Band Structure of Graphene

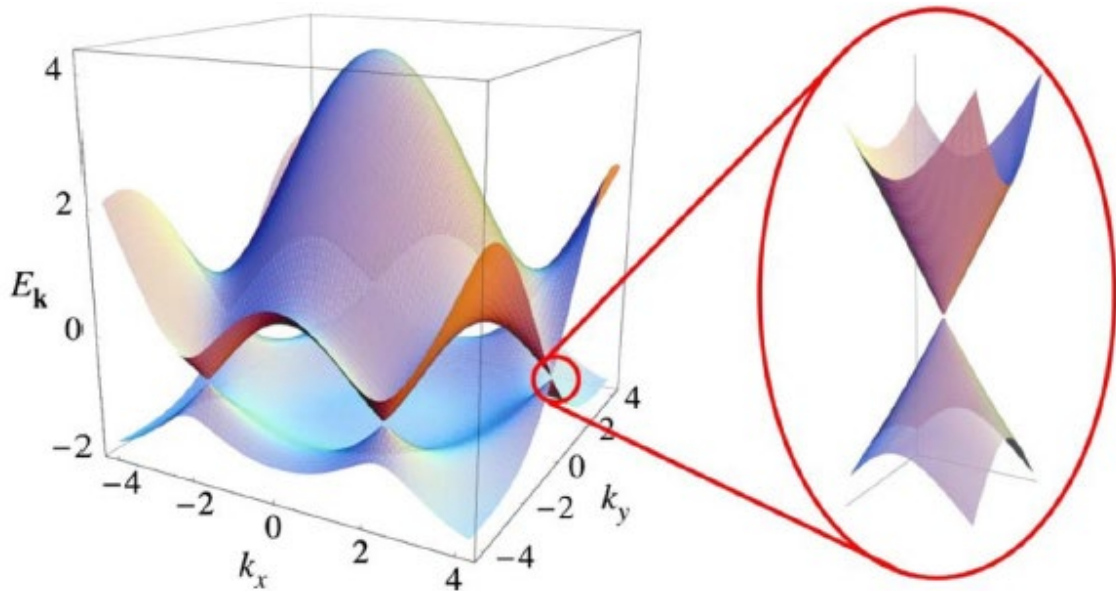


Figure 3.2: Energy dispersion in the graphene lattice. Left: energy spectrum in units of  $t$  for finite values of  $t$  and  $t'$ , with  $t=2.7$  eV and  $t'=-0.2t$ . Right: zoom in on of the energy bands close to one of the Dirac points. Copied from reference [103].

The carbon atom has four valence electrons. Only three electrons per carbon atom are involved in creating strong covalent sigma bonds. The electron that is not involved produces a pi bond, which is responsible for the material's electronic properties at low energy. Meanwhile, the covalent sigma electrons generate energy bands formed far from the Fermi level. The conduction band and valence band in graphene meet at the K, K' points, making it a zero-band-gap semiconductor. By considering the interaction that happens at the closest of neighbouring atoms, the energy can be expressed as [103, 104],

$$E(K_x, K_y) = \pm \gamma_0 \left[ 1 + 4 \cos \frac{\sqrt{3} k_x a}{2} \cos \frac{k_y a}{2} + 4 \cos^2 \frac{k_y a}{2} \right]^{1/2} \quad (3.4)$$

Where  $K_x$  and  $K_y$  are vectors for the wave in X and Y directions.  $\gamma_0$  is the integral transfer between the closest neighbour. The energy dispersion in the graphene lattice is demonstrated in Figure 3.2 [103]. The upper and lower half of the curve are named  $\pi^*$  and  $\pi$  band, respectively, which degenerate at the Dirac points (K and K'). As the density of states becomes zero, the energy dispersion (Fermi level) also goes to zero close to K and K' points. The Dirac points are vital for the purpose of studying the electronic properties of graphene. The linear dispersion exists at the areas near the Dirac points and can be explained by the Dirac equation as follows,

$$E_{\pm}(K) \approx \pm v_F |K| + O\left[\left(\frac{|K|}{K}\right)^2\right] \quad (3.5)$$

Where  $v_F$  is the Fermi velocity.

The linear dispersion near the Dirac points makes the charge carriers function as massless particles. This causes suspended graphene to have high mobilities of up to  $250,000 \text{ cm}^2 (\text{Vs})^{-1}$  [105]. The absence of band gap in graphene makes it possible to apply an external electrical field to shift between holes and electrons. By shifting the Fermi energy ( $E_f$ ) away from the Dirac point, holes or electrons become the majority charge carriers with applied positive and negative voltage, as demonstrated in Figure 3.3 [106].

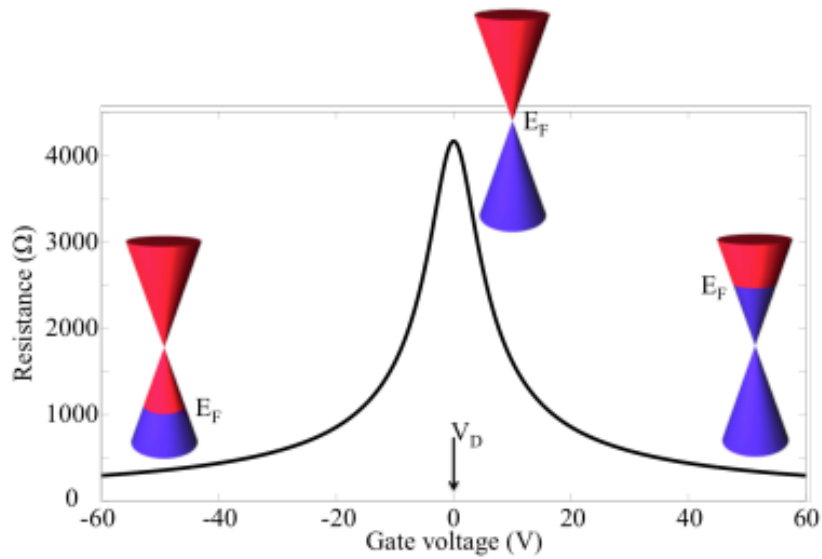


Figure 3.3: Shows the calculated resistance for shifting the Fermi level in graphene using gate voltage. Adapted from reference [106].

### 3.2 Graphene Oxide

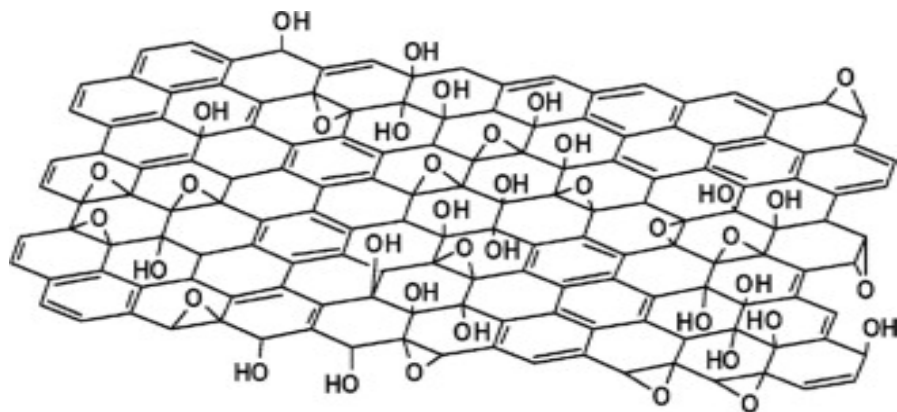


Figure 3.4: Graphene oxide structure. Adapted from reference [117].

The pristine graphene has a zero-band-gap at the Dirac point, meaning the Fermi level stays in the middle of the conduction and valence bands. The absence of the bandgap limits pristine graphene's utility in electronic logic devices [107], which requires precise control over electron transport. In contrast, the absence of the bandgap makes it difficult to control the electron transport. Therefore, shifting the fermi level with respect to the Dirac point by introducing

electronic charge in the pristine graphene is needed for its application as a semiconductor. Many methods have been implemented to overcome this issue, such as graphene metal oxide composite, polymer decorating, and oxidising graphene [25, 108, 109]. Decorating graphene with metal oxide nanoparticles alters the majority carrier concentration, and hence the resistance. In the case of p-doped graphene, graphene composites with p-type metal oxide nanoparticles will increase the number of majority hole carriers, while n-type metal oxide nanoparticles will decrease the number of majority hole carriers. Decorating the graphene with polymer is also used to open the band gap by causing charge transfer at the interface between graphene and polymer layer, which increases the charge carrier concentration [109].

Another way of opening a band gap in graphene is oxidation; many procedures have been used to oxidise graphene, such as Hummer's method, oxygen plasma, and ozone treatment [69, 110, 111]. The most common method for producing GO is known as the modified Hummer's method, which has the advantage of mass producibility [111-113] and its ability to be performed on graphite from mining, a cheap and plentiful material resource [114].

L. S. Hui et al. reported that oxygen plasma etching procedures introduce oxygen defects on CVD graphene [110]. The process was carried out by placing the CVD graphene sheet in the centre of the chamber of the plasma PDC-001 system at 29.6W; however, the high-power plasmas completely remove the graphene rather than oxidising it. Then the chamber was then evacuated to pressure below 100 mTorr, and oxygen flowed into the chamber for etching graphene. They found oxygen formed on the graphene surface after plasma etching.

In a separate study, M. G. Chung et al. demonstrated a method of introducing oxygen groups on CVD graphene by ozone exposure [69]. The graphene was exposed to ozone in the ambient atmospheric pressure. The ozone used in the experiment was generated by ultraviolet (UV) lamp irradiation with an intensity of 20 mW/cm<sup>2</sup>. This result in oxygen being introduced to a graphene sheet. However, low UV intensity does not cause oxidation [115, 116].

The processes mentioned earlier in the oxidation of the graphene layer lead to the creation of various oxygen-based functional groups. These functional groups include epoxy, hydroxyl, carbonyl, and carboxylic groups, as demonstrated in Figure 3.4 [117]. These oxygen groups on the pristine graphene increase the bonding between oxygen functional groups and carbon, causing large electron transfers from the graphene to the oxygen groups on the surface. This leads to a shift in Fermi level with respect to Dirac point.

### **3.3 Graphene Growth**

In 2004, Novoselov and Geim reported the first measurement of the electrical properties of graphene [71]. The measured graphene was obtained via micro-mechanical exfoliation of graphite. In 2010 Novoselov and Geim were awarded the Noble prize in physics for their successful work. Graphene that is produced by micro-mechanical exfoliation is of very high quality, but this process is difficult to perform and is not scalable. Hence, many alternative methods are now used for large-scale graphene production. Methods can be divided into two different categories, top-down and bottom-up synthesis.

#### **3.3.1 Top-down Synthesis**

In top-down syntheses, Graphene is formed by reducing the bulk material -graphite - to a small amount of nanostructure, as in micro-mechanical exfoliation and liquid phase exfoliation process which are demonstrated in Figures 3.5 a) and b) [118].

##### **3.3.1.1 Micro-Mechanical Exfoliation**

Micro-mechanical exfoliation is performed using adhesive tape to separate material from bulk crystal. A thin layer of graphene film is produced via repeated peeling of material from bulk graphite, which is then stuck to a target substrate for use in the experiments. Other methods can be used to exfoliate graphene such as transfer printing technique [119], etc. Micro-mechanical exfoliation is the first method used to separate graphene from graphite by Novoselov and Geim [71]. The produced graphene has high quality with low defect formation [120]. However, large scale production of graphene is still hard to achieve using micro-mechanical exfoliation.

##### **3.3.1.2 Liquid Phase Exfoliation**

Liquid phase exfoliation is the process used to convert a bulk laminar material (3D) into single or few-layer 2D material. In this method, the bulk material is placed into a liquid, which intercalates between the material layers and separate them [121]. The liquid usually used in this method is water or a polar solvent [122]. The high scalability of Liquid phase exfoliation drew attention for experimental use. However, 2D flakes obtained from this method are typically laterally small, and the dispersion of graphite in the liquid is difficult due to the high tension between graphite materials [123].

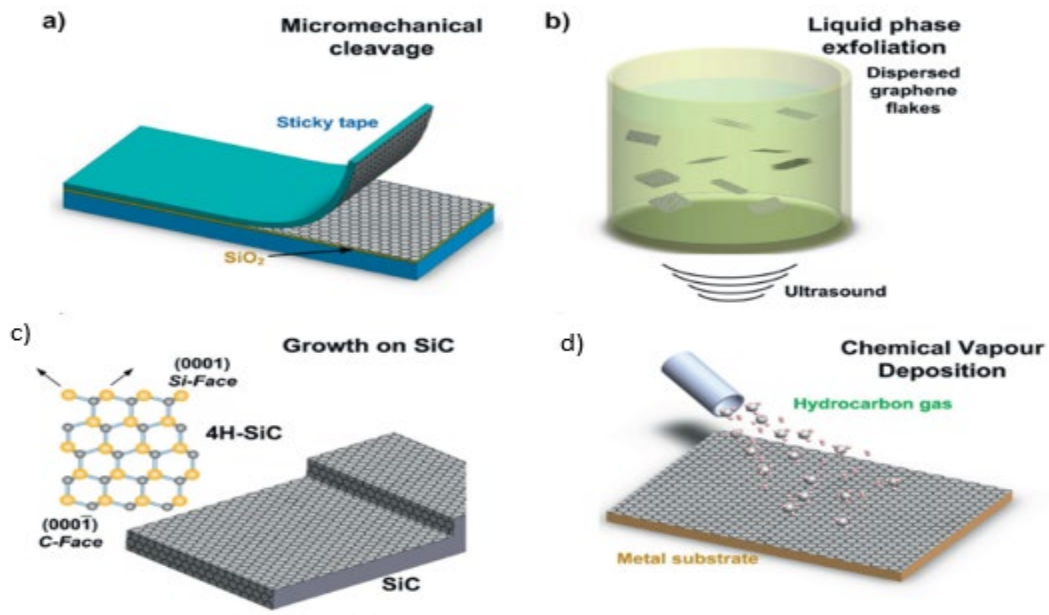


Figure 3.5: Demonstrate the general four used methods for graphene production; a) micromechanical cleavage, b) liquid phase exfoliation, c) epitaxial growth on SiC. d) chemical vapour deposition. Adapted from reference [118].

To overcome these issues graphene oxide (GO) is used, as it's interfacial energy does not prevent the suspension in liquids [124], resulting in the GO layer being obtained. However, a reduction process on the GO, to form reduced graphene oxide (rGO), is required to regain the properties of graphene. Additionally, it is not possible to avoid the introduction of defects via the GO to rGO route, even after the reduction of GO. For this reason, rGO is considered to be distinct material [125]. The first graphene dispersion from graphite using the liquid phase exfoliation was reported by Hernandez et al [126]. They placed the graphite bulk material in N-methyl-pyrrolidone in a sonicator to disperse the graphene. This method also suffers from difficulty in solvent removal.

### 3.3.2 Bottom-up Synthesis

The bottom-up synthesis is the method used to form a desired layer by sticking atoms onto each other. The most frequently used methods for bottom-up graphene synthesis are epitaxial growth on silicon carbide (SiC) and chemical vapour deposition (CVD), which are illustrated in Figure 3.5. c) and d). The highest quality of large-scale graphene production in terms of electronic properties is generally produced by bottom-up synthesis processes, as reported by X. Wu et al, who found that this graphene has charge carrier motilities of  $4000 \text{ cm}^2 \text{ V}^{-1} \text{ s}^{-1}$  [127].

### 3.3.2.1 Epitaxial Growth on Silicon Carbide

One method to produce large scale graphene layers is by the thermal decomposition of SiC. When the SiC wafer is annealed at high temperature above 1400 °C in a vacuum, silicon atoms evaporate from the surface of the wafer leaving behind graphitic layers [128]. Figure 3.6 illustrates graphene growth on SiC wafer via evaporating the silicon atoms, This leads first to the formation of a buffer- or 0-layer, which covalently bonds to the underlying SiC substrate, followed by free-standing graphene layers [128].

Graphene produced via epitaxial growth on SiC was found to be grown on both terminated faces, Si - (001) and C-(00 $\bar{1}$ )[129]. The growth speed for graphene on SiC (00 $\bar{1}$ ) was found to be faster than on SiC (001). Also, the number of grown layers is affected by the terminated faces of SiC. The single layer was found to be grown on the Si face and is identical to freestanding graphene [130]. On the other hand, the multilayer of graphene is grown on the C face and was found to be defective [131, 132].

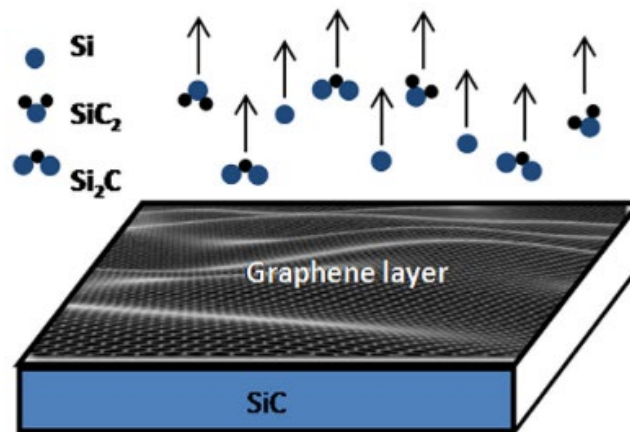


Figure 3.6: Represent the epitaxial growth of graphene on silicon carbide wafer. Adapted from reference [128].

### 3.3.2.2 CVD on Transition-metal films

CVD is a technique used to deposit high-quality thin films in a vacuum. The deposition is carried out by heating the chamber to the desired temperature to make the precursors react and bind to the surface of a substrate [133]. This method is the most common method for producing large-scale monolayer or bilayer graphene [134, 135]. For graphene growth, the common hydrocarbon precursor used is methane. However, high-quality graphene growth requires a high working temperature for methane-based graphene CVD [136]. Other precursor's material have been used to reduce the working temperature for graphene growth such as ethanol [137],

and solid sources [138]. But graphene obtained from these methods is of lower quality compared to graphene grown with methane.

Transition metal foil is used as a supporting substrate in most CVD graphene growth. As well as providing the substrate for growth, it also works as catalyst to speed up the precursor dissociation. The most common catalysts and supporting substrates used in CVD graphene growth are copper (Cu) and nickel (Ni). The growth of graphene on these catalysts differs as the carbon solubility within copper substrate (0.01%) is lower than a nickel substrate (0.18%) [139-142]. Figure 3.7 demonstrates the two different growth methods a) on nickel and b) on copper [141]. Copper has low carbon solubility, which means that carbon fragments are only adsorbed to the surface of the copper substrate. Resulting in promoting the growth of large-scale monolayer graphene [141, 143-146]. In contrast, the high solubility of carbon in the nickel substrate results in the carbon species dissolved into the nickel before penetrating out to coat the surface. Which then leads to producing high-quality graphene that has large multilayer regions [141, 142]. Copper is the preferred substrate grow large monolayer graphene and is known to produce graphene with high electronic properties. Hence, copper was chosen for CVD graphene growth in this project.

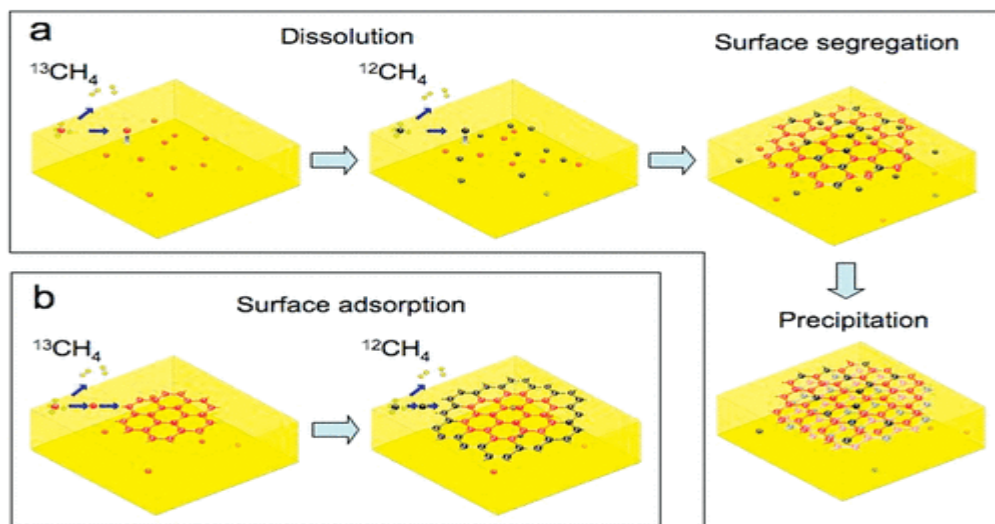


Figure 3.7: Schematic diagrams of the possible distribution of C isotopes in graphene films based on different growth mechanisms for sequential input of C isotopes. (a) Graphene with randomly mixed isotopes such as might occur from surface segregation and/or precipitation. (b) Graphene with separated isotopes such as might occur by surface adsorption. Copied from X. Li et al [141].

### 3.4 GFET Electrical Transport

Recently, graphene has attracted the attention due to its electronic properties which provide the high carrier velocity. Graphene transferred to silicon dioxide coated silicon substrate has low field carrier mobility, limited to  $2 \times 10^4/Vs$  [147, 148]. Many researchers have studied the mobility of graphene and changing the conductivity by doping [149-151]. The main problem causing the mobility degradation is the surrounding charge impurities to 2DEG. To overcome these charge impurities, suspending graphene has been reported to have high mobility [152, 153]. K. I. Bolotin et al, demonstrated that suspended graphene on SiO<sub>2</sub>/Si has low scatter impurities which enhance the carrier mobility at a temperature of 5 K to in excess of  $12 \times 10^4/Vs$  [152]. The improvement in mobility is attributed to the cleanliness of suspended graphene.

Suspended graphene has been measured at room temperature and found to have electron mobility in excess of  $1 \times 10^5/Vs$  [152]. This high mobility makes graphene the fastest semiconductors at room temperature. Moreover, high mobility is achievable in graphene field effect transistors (GFET) on SiO<sub>2</sub>/Si substrates at over  $10,000 \text{ cm}^2/Vs$  [90]. The mobility of electrons can be determined by the saturation velocity in GFETs [154, 155]. As graphene possesses bipolar behaviour GFETs can operate in either electron- or hole+ transporting regimes, at  $V_g < \text{or} > V_{\text{dirac}}$ , respectively [156].

### 3.5 Graphene Sensors

Graphene has attracted the attention of researchers due to its high surface to volume ratio, high conductivity, high electric mobility, adsorption ability, and low density of states near the Dirac point [55, 77, 97, 98, 157]. Graphene can operate as a gas sensor at a much lower temperature than metal oxide gas sensors which consumes no power to heat the sensor [158] compared to the operating temperature of metal oxide (200 °C- 500 °C) [28]. This results in reduced energy consumption in comparison to other key sensing technologies [159].

Graphene is well suited to use within gas sensing devices, due to its large surface-to-volume ratio [55] and thinness [160]. In particular, graphene's atomic thickness means that any adsorbate on the graphene will have the effect of doping the entire graphene channel thickness [55, 72]. In addition, graphene possess a low density of states close to its Dirac point [97]. Taken in combination, these factors make graphene an ideal candidate for gas sensing, as even modest charge exchange interactions between the graphene sheet and

adsorbates should produce a measurable change in the graphene's conductivity [58, 80] and shift in the Dirac point of the graphene channel [58, 79, 80]. Generally, graphene gas sensors are fabricated based on field effect transistor structure. GFET's mobilities depend on their cleanliness. Therefore the cleaner GFETs mean the greater sensitivity [161].

The conductivity of graphene is influenced by the analyte species, for instance,  $\text{NO}_2$  and  $\text{NH}_3$  as an electron acceptor and donor respectively [58, 79]. However, as graphene has low defect density, gas species are adsorbed on graphene through physisorption interactions. Also, the chemisorption interaction is low in graphene due to the low density of chemically active sites. Leenarets et al. reported that the charge exchanged between  $\text{NO}_2$  and graphene is 0.1e per  $\text{NO}_2$  molecule [73].  $\text{NO}_2$  is a polar gas that is physisorbed to graphene. Therefore, the gas sensor's device sensitivity is affected by the quality of graphene used within the sensors. As defects, enhance the small charge transfer between physisorbed gases and graphene.

On the other hand, the gas species that are chemisorbed to graphene have charge exchange between graphene and chemisorbed species of 1e. This enhancement in the adsorption is attributed to chemisorbed species being ionically or covalently bonded to graphene. One method, which is attracting a lot of interest in the field, is enhancing CVD graphene-based sensor sensitivity and selectivity through the oxidation of graphene [64, 69, 81, 83, 162-164]. The principle relies on the increase of the adsorption sites on the graphene layer, provided by a functional oxygen group, which leads to increases in the interaction strength of chemisorption.

Many methods have been used to oxidise graphene, aiming to improve the sensitivity and selectivity toward the oxidising and reducing analyte gases. As an example,  $\text{NO}_2$  detection at 2 ppm was reported at room temperature by G. Lu et al. through the use of partially thermally reduced graphene oxide prepared from graphite using the Hummers method [81]. Even higher sensitivity to  $\text{NO}_2$  was demonstrated by Y. R. Choi et al., who reported detection of 650 ppb of  $\text{NO}_2$  through the use of the modified Hummers method [64]. Moreover, the lowest detection to 200 ppb of  $\text{NO}_2$  was reported at room temperature by M. G. Chung et al., through ozone treatment to CVD graphene [69]. R. Ghosh et al. demonstrated a detection limit of 200 ppm of  $\text{NH}_3$  by reducing graphene oxide, which was prepared by the Hummers method and then reduced by  $\text{NaBH}_4$  solution for 90 min [162]. Improved detection to 1 ppb of  $\text{NH}_3$  was reported by N. Hu et al. through reduced graphene oxide [83]. More examples of

NO<sub>2</sub> [14, 165-168], NH<sub>3</sub> detection [169-171], hydrazine hydrate vapor detection [164], H<sub>2</sub> detection [172], NO<sub>2</sub> detection [173], and ethanol detection [163] show that graphene oxides have great impact as gas sensors, highlighting the high potential impact of developing a controllable method of oxidising graphene.

In this work, a similar oxidation approach is adopted from the Hummer method, which involves using sulphuric acid. However, we modified the method by using a diluted concentration of sulphuric acid and applying it to CVD graphene instead of graphite. This modification lets us separate the impact of aggressive chemical exfoliation from introducing oxygen groups. As a result, we can investigate the enhancement of the sensing response of graphene to low oxidation levels, specifically for NO<sub>2</sub> and NH<sub>3</sub>. Also, using vacuum pre-condition significantly impacts the device sensitivity as it increases 10 times compared to a non-vacuumed device.

## Chapter 4

### 4 Methods

#### 4.1 Sensor Fabrication

##### 4.1.1 CVD Graphene Growth

Graphene was grown on copper foil using a hot-wall CVD reactor. The heating element provided energy to the reactor, increasing the reaction zone's temperature. This process requires high energy to achieve stable, consistent heating during the reaction [174, 175], which is important for the growth reproducibility and for obtaining continuous graphene sheets.

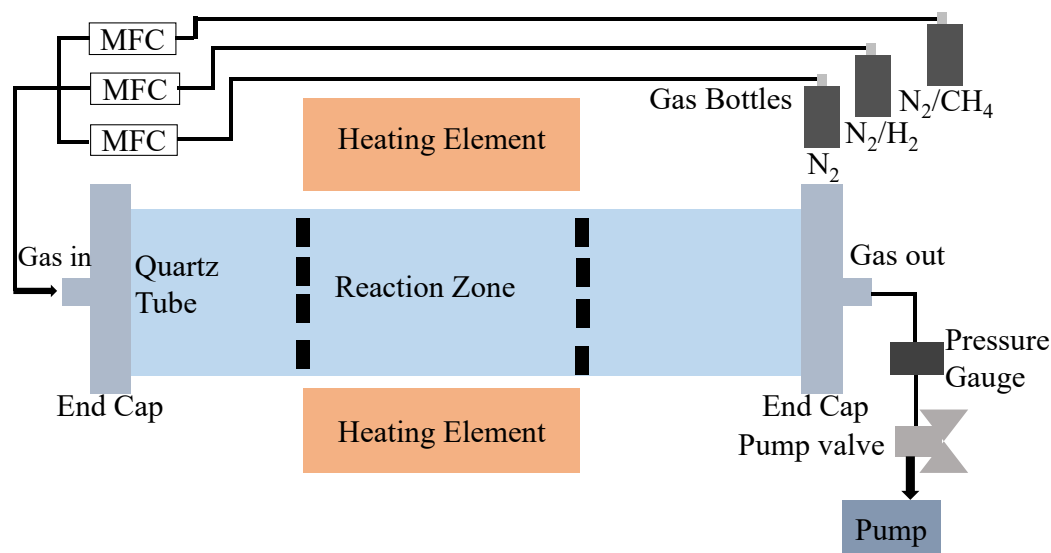


Figure 4.1: A schematic of the CVD furnace reactor used for graphene growth.

A schematic of the CVD reactor and its set-up is represented in Figure 4.1. The reactor is constituted of a three-zone Carbolite furnace, a quartz tube, a mass flow controller (MFC), an end cap, and a pressure gauge. The three-zone Carbolite furnace was placed in the middle of the two-meter quartz tube length with an external diameter of 54 mm and an internal diameter of 50 mm. Two Eurotherm 2132 temperate controllers controlled the Carbolite furnace end zones. Meanwhile, the middle zone was controlled by Eurotherm 32116 temperature controller. A nitrile O-ring was placed at both ends of the caps between the quartz tube and KF fittings to create a seal, which kept the reaction zone isolated from the ambient atmosphere. Both ends of the cap were checked for leaks and found to have a leak rate of  $1.38 \times 10^{-3}$  mBar.Ls<sup>-1</sup>. A MKS G-series mass-flow-controller was used to regulate the gas flow into the reactor. Three

gas lines were used in this operation, each with a control input. The flow rate of the MFCs used in this project was 200 standard cubic centimetres per minute (sccm) on the Nitrogen/Methane line and 1000 sccm on the Nitrogen and Nitrogen/Hydrogen lines. The flow rate used in this project was chosen to provide a large graphene domain and continuous sheet growth. The MFCs were set up to provide Hydrogen: Methane with a ratio of 10:1.

Using this setup, graphene was grown on a copper (Cu) substrate with a thickness of 25  $\mu\text{m}$  via CVD. After loading the Cu substrate into the CVD reactor, the reactor was heated to 1050°C under a constant flow of 100 sccm of Nitrogen ( $\text{N}_2$ ). Once 1050°C was reached, the copper substrate was annealed for 30 minutes under a flow of 100 sccm of  $\text{N}_2$  at 1050°C. Following the annealing, 100 sccm of 2% Methane/Argon ( $\text{CH}_4/\text{Ar}$ ) and 1000 sccm of 2% Hydrogen/Argon ( $\text{H}_2/\text{Ar}$ ) were introduced in the chamber for 30 minutes to grow the graphene. Finally, the chamber was cooled to below 100°C, and the  $\text{CH}_4$  and  $\text{H}_2$  flow was reduced to 20 sccm and 1000 sccm respectively, during the cooling process.

#### 4.1.2 Graphene Transfer

After the graphene was grown on the copper catalyst using the above protocol, it was then transferred from the metal growth substrate to the insulating substrate. This allows us to characterise the quality of the graphene and make the sensor.

The insulating substrate used in this project is thermally grown  $\text{SiO}_2$  on Si, with thicknesses of  $295 \pm 10$  nm, chosen as it provides the optimum contrast for optical imaging for the monolayer graphene placed on it [176].

A polymer was used to assist the graphene transfer from the copper growth substrate to the  $\text{SiO}_2/\text{Si}$  substrate. Using a procedure that kept graphene safe during the handling process was essential as a single layer of graphene is one atom thick and easy to damage. The polymer supports and protects the graphene structurally during the delicate transfer process from the growth substrate. In this project, two different supporting layers were used to transfer graphene to investigate the impact on the graphene's electrical measurements. The first supporting layer used to transfer graphene is PMMA as reported by Li et al. [141], a process used widely for graphene transfer. The other supporting layer used is nitrocellulose, as reported by Hallam et al. [177], who found that nitrocellulose produces less residue on the graphene than PMMA.

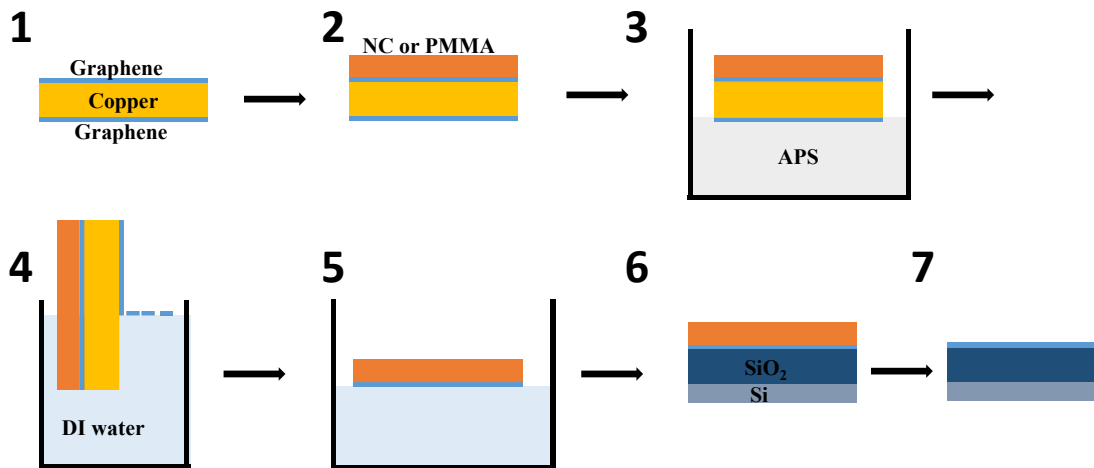


Figure 4.2: Shows the synthesis process of the graphene sheet.

Figure 4.2 shows the entire process of graphene transformation, which is described stepwise below:

1. Graphene is grown on both sides of the copper foil via CVD.
2. As mentioned earlier, two different methods are used to transfer graphene to investigate the impact of left residues on the electric properties of graphene.
  - a. A 280 nm layer of PMMA is spin cast from a 4% solution on the desired side of the graphene grown on copper. The spin coating speed is 700 rpm for 15 s, followed by 2000 rpm for 45 s.
  - b. A 200 nm nitrocellulose (NC) layer is spin-cast on the graphene. The NC was bought from Sigma Aldrich, item number 09817, and it is a 2% solution in ethyl acetate.

It is important to note that the NC will be used in the following sentence as a supporting layer. Nevertheless, keep in mind that PMMA supporting layer is also used in the other transferred followed the same process as NC supporting layer.

3. Ammonium persulphate (APS) (0.5 M) is used to etch the copper growth substrate. The NC supporting graphene/copper/graphene floats on the APS solution where the NC side up on the copper etching[177].
4. The NC/graphene/copper/graphene is gently handled and dipped in the fresh beaker filled with deionised (DI) water ten times to remove the one grown on the other side of copper before returning to the APS etchant for 90 seconds. This process was repeated

- 10 times, then the NC/graphene/copper was left in the etchant for 2 hours to ensure complete removal of the graphene grown on the other side of copper.
5. The NC/graphene was then gently transferred using a clean microscope slide to a beaker filled with DI water. The NC/graphene was left floating on the DI water for 5 minutes to rinse graphene of APS residue.
  6. Once the rinsing on DI water is done, the NC/graphene is transferred onto the target substrate and left to dry overnight.
  7. After that, the NC/graphene/substrate is placed into a dish of acetone to dissolve the NC or PMMA supporting layer for 2 hours.
  8. The graphene/substrate is taken from the acetone, placed on the wipe, and sprayed with isopropyl alcohol.
  9. Finally, the graphene/substrate is dried with a compressed air gun.

#### 4.1.3 GFET Fabrication

The graphene devices in this project were fabricated as graphene field effect transistor device (GFETs). Before graphene transfer, the substrates must be prepared, they are pre-patterned with Chromium/Gold (10 nm/60 nm) electrodes via thermal evaporation, as shown in Figure 4.3. The displayed configuration provides 11 graphene channels per chip, with the underlying Si acting as a global back gate.

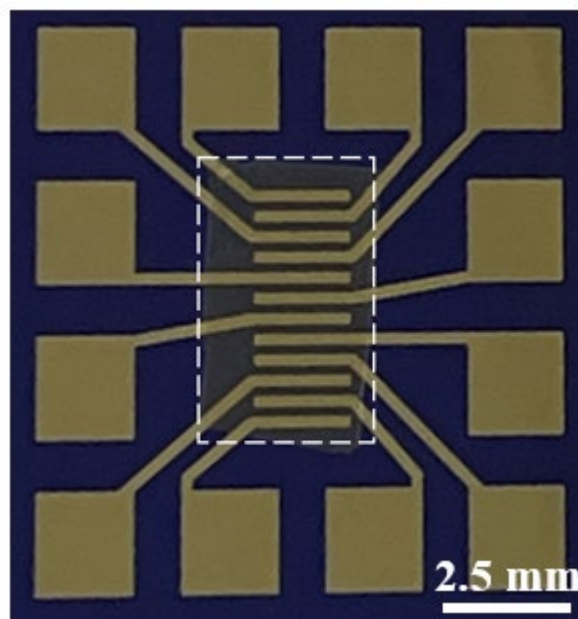


Figure 4.3: Shows an image of fabricated GFET in this project. The GFET consists of a 10 nm Cr/ 60 nm Au electrode on top of a silicon substrate capped with 300 nm silicon dioxide. The transferred graphene is outlined by the white dashed line for easy visualisation.

The electrodes were patterned using positive photolithography with AZ5214 photoresist and then exposed to the UV light through the shadow mask. After that, a thermal evaporator was used to deposit contact electrodes using 10 nm Chromium (Cr) and 60 nm Gold (Au).

Chromium was used to improve the adhesion between gold and the substrate. Also, the low contact resistance between the gold and graphene makes gold a suitable choice for this project [178]. The process of electrode deposition is demonstrated in Figure 4.4 with an explanation explained below:

1. Use SiO<sub>2</sub>/Si wafer.
2. Clean the wafer in a petri dish filled with acetone in a sonicator for 5 minutes, followed by 5 minutes sonication in isopropyl, and dry with a compressed air gun. Then prebake the wafer in an oven for 5 minutes for extra drying at 90 °C.
3. A layer of photoresist of ~ 1.5 μm is created on the wafer by spinning a photoresist (AZ5214). A spinner speed was set at 4000 rpm for the 60s, and soft baking for 10 minutes in the oven at 90 °C.
4. The shadow mask is placed the photoresist/wafer. Then send the UV light through the shadow mask for 12s to make the exposed photoresist area soluble.
5. The petri dish is filled with a photoresist developer (Microchem AZ 326 MIF Developer) and the sample is immersed to dissolve the exposed areas of photoresist.
6. 10 nm Cr / 60 nm Au metal contacts are deposited over the entire patterned area. The thicknesses of the metal film are determined and controlled by quartz crystal monitoring.
7. The remaining photoresist is dissolved in acetone using a sonicator, lifting away excess metallisation.
8. After the desired electrode pattern, a small sheet of NC/graphene/copper is transferred to cover all electrodes area using the method explained earlier in part 2.

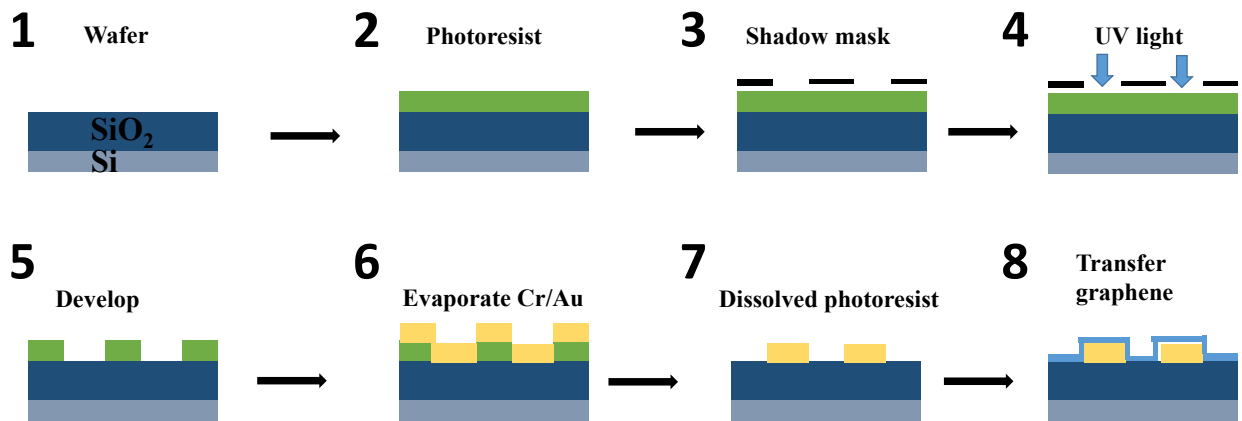


Figure 4.4: Demonstrates a fabrication process from the spin of the photoresist to the transfer of the graphene to create GFETs.

#### 4.1.4 Graphene Oxidation

Sulphuric acid (H<sub>2</sub>SO<sub>4</sub>) was used in diluted concentrations to introduce a mixture of oxygen groups to the GFET (Carboxyl, Hydroxy, Epoxy) [68]. The amount of the defect of the oxygen moieties was found to be dependant on the immersion time in the H<sub>2</sub>SO<sub>4</sub>. In order to have different oxidation levels, various immersion times were used for GFET in sulphuric acid. The oxidation process schematic has been demonstrated in Figure 4.5. The oxidation process used in this project is described below:

1. Use Au/Cr/graphene/SiO<sub>2</sub>/Si wafer described in part 3.
2. Anneal Au/Cr/graphene/SiO<sub>2</sub>/Si at 120 °C for 1 hour to evaporate any water residue from the sample. Annealing is more effective in avoiding graphene removal during the oxidation process.
3. 3.6 mole (M) of sulphuric acid is prepared by adding 21 ml of H<sub>2</sub>SO<sub>4</sub> to 79 ml of DI water, then leaving for 15 minutes to cool down.
4. The Au/Cr/graphene/SiO<sub>2</sub>/Si is immersed in the 3.6 M solution for 30 minutes.
5. Clean the sample with DI water to remove the H<sub>2</sub>SO<sub>4</sub> residue, and spray with isopropyl alcohol.

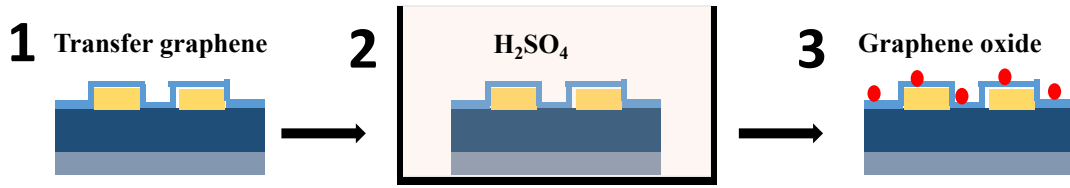


Figure 4.5: Demonstrates an oxidation process of graphene for the creation of GFETs.

## 4.2 Sensor Measurement

### 4.2.1 Electronic Characterisation

Electrical measurement provides information about the performance of the GFETs as functional devices, and the location of the Dirac point. The graphene channel's doping concentration and mobility ( $\mu$ ) are calculated to provide information on how the GFETs behave. In this work, the quality of the transferred graphene is studied and determined by the gradual channel approximation [179, 180].

The measurements were carried through a cascade probe station (CPS) that connected to a Keithley 4200A analyser to record the current ( $I_{ds}$ ) vs gate voltage ( $V_g$ ) sweeps. Figure 4.6.a. displays I-V curve characteristics of GFETs measured from -5 V to +5 V to investigate the electrical contact between the graphene channel and Cr/Au electrode. As can be seen, the current increases linearly with increased voltage, which proves that the electrical contact between graphene and Cr/Au electrode is similar to a p-type semiconductor [81, 89]. Figure 4.6.b. demonstrates a typical transfer curve of GFETs device measured in this work. It is compatible with previously reported graphene results [181-184]. The V-shaped transfer characteristic indicates that GFETs have ambipolar behaviour. The minimum point of the transfer curve is related to the Dirac point. The intentional doping of the graphene channel can be calculated by using Equation 4.1[184].

$$n_0 = \frac{(V_g - V_{Dirac}) \cdot C_{ox}}{e} \quad (4.1)$$

Where  $n_0$  is the carrier density of the graphene device,  $V_g$  is the gate voltage,  $V_{Dirac}$  is the Dirac point voltage,  $C_{ox}$  is the capacitance for the dielectric layer, and  $e$  is the electron charge.

The electron and hole mobilities can be calculated using the gradual channel approximation shown in Equation 4.2 [39].

$$I_{ds} = \frac{W}{L} \mu C_{ox} ((V_g - V_t) V_{ds} - \frac{V_{ds}^2}{2}) \quad (4.2)$$

Where  $I_{ds}$ ,  $W$ ,  $L$ ,  $\mu$ , and  $C_{ox}$  are the drain-source current, width of the channel, length of the channel, hole/electron mobility, and capacitance of dielectric layer, respectively,  $V_g$  is the gate voltage,  $V_t$  is the threshold voltage,  $V_{ds}$  the bias of the source-drain. Equation 4.2 differentiated by  $V_g$ , and the result displayed in Equation 4.3:

$$\frac{\delta I_{ds}}{\delta V_g} = \frac{W}{L} \mu \cdot C_{ox} \cdot V_{ds} \quad (4.3)$$

Where  $dI_{ds}$  and  $dV_{gs}$  are the derivatives of the source current and gate voltage, respectively.

Equation 4.3 can be written after substituting  $g_m = \frac{dI_{ds}}{dV_{gs}}$  as displayed in Equation 4.4:

$$\mu = \frac{g_m L}{W \cdot V_{ds} \cdot C} \quad (4.4)$$

The hole/electron mobility value can be extracted from the  $g_m$  vs  $V_g$  plot as displayed in Figure 4.6.c. The value of  $g_m$  is obtained from the maximum curve value and then substituted in equation 4.4 to calculate hole ( $\mu_h$ )/electron ( $\mu_e$ ) mobility values. Each forward and backward sweep has values for hole/electron mobility, as noted on the plot.

The gradual channel approximation is useful method to extract the quality information of GFET transfer. Also, conceding the charge trapped effect which make the device does not saturated. As well, the electric field between the drain and source is much smaller than electric field between gate and source [180]. The gradual channel approximation is best chosen for the GFET application. However, it does not take the contact resistance into account for charge carrier mobility calculation which limits its use. Therefore, to calculate an accurate charge carrier mobility threshold voltage is required, which is not applicable for this project. Many researchers used the gradual channel approximation to calculate the charge carrier mobility as they do not have hall measurements [185-187]. This means that the result obtained in this project by gradual channel approximation is comparable with the result published in litterateurs.

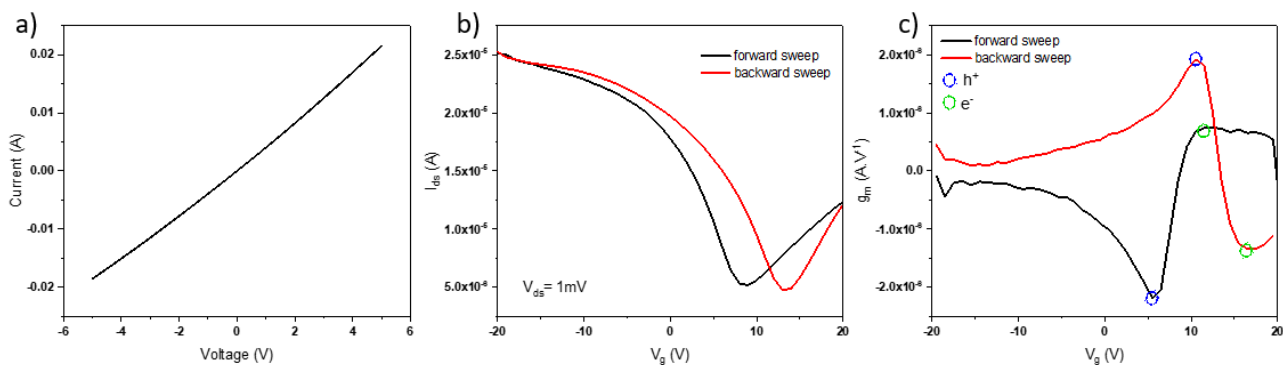


Figure 4.6: a) Shows the I-V curve of the graphene channel with a metal electrode. b) the typical transfer curve of the graphene field effect transistor. Dirac point on the forward sweep is located at 9 V and at 13 V on the backward sweep. c) the forward/backward sweep of the  $g_m$  as a function of gate voltage. Blue and green circles highlight the  $g_m$  values for the holes and electrons, which can be substituted in equation 4.4.

## 4.2.2 Gas Machine

Sensitivity measurements give information about the performance of the GFET devices fabricated within this work under different types of gases. Also, it provides details on the GFET's selectivity, recovery, and repeatability. It is vital to know how the GFET device behaves under different gas conditions for comparison and practical use. A self-built gas machine chamber (GMC) was used to perform these measurements. This uses a program that constantly measures the change in the GFET device's conductivity during changing chamber conditions. A labVIEW program was built by Callum Rigby and used to modulate the quad voltage source to MFCs and save the data obtained during the measurement from Sourcemeter in a PC file. In this measurement, the GFETs device was wired to provide four-sense measurement, as presented in Figure 4.7. The four-sensing technique gives more accurate measurements by minimizing the impact of lead resistance, as it is commonly used in resistance measurements. The device holder has a metal substrate to which the device is adhered and a thermal cable to monitor the temperature inside the chamber. The Keithley 2450 Sourcemeter was used to record the conductivity as it is able to measure even slight signal changes during the interaction of the small gas concentration with the GFETs device. Also, the MKS 600 Series Pressure controller and LakeShore 331 Temperature Controller controlled the pressure and temperature inside the chamber. An image of GMC was taken after all the equipment was set-up, as displayed in Figure 4.8. The set-up process is explained below:

1. The fabricated GFET device is wired to the supported sample holder tray, which has three junctions at the end, two used for electrical measurement and a third for thermal measurements.
2. Three lines of MFCs used in this work for Nitrogen ( $N_2$ ), 10 parts per million (ppm), Nitrogen dioxide/Nitrogen ( $NO_2/N_2$ ), and 10 ppm Ammonia/Nitrogen ( $NH_3/N_2$ ). The flow rate for each MFCs is 200 sccm. The gas concentration of the  $NO_2$  or  $NH_3$  is reduced by mixing with  $N_2$  gas to the desired concentration within the chamber.
3. The junction box connects the GFET device to the measuring instrument to continuous recording of the change in the resistance/current throughout the measurement.
4. All the gas interaction with GFET device takes place in the chamber.
5. A valve and pressure sensor connected to the pressure controller are used to modulate the pressure inside the chamber to a fixed pressure point. This then regulates the pressure by opening/closing the valve to evacuate the excess gas during the test measurement.
6. Two vacuum pumps are used. The first vacuum pump is used to evacuate the chamber from all gases until the pressure reaches to  $1.5 \times 10^{-3}$  mbar, and then the turbo pump is used to reach high vacuum level, which gets below  $1 \times 10^{-6}$  mbar. The second vacuum pump is used during the gas test measurement to evacuate and carry the excess gas out of the chamber.

The GFET device was put under a high vacuum overnight before the measurement started in order to remove as much atmospheric gas as possible from the chamber as well as from the GFET device itself. The overnight vacuuming of the device and the chamber step is required before each measurement of the gas, the device, and the chamber as the GFET device does not fully recover after gas exposure.

The gas interaction with the device was carried in a cycle as follows:

1. The pressure modulator is set at 799.9 mbar during the measurement.
2. The sample settles under only in  $N_2$  for 600 seconds.
3. 200 ppb of ( $NO_2$  or  $NH_3$ )/ $N_2$  is introduced to fill the chamber for 180 seconds. Using  $NO_2$  concentration of 1ppm and mixing with  $N_2$  in a ratio of 1:5, a concentration of 200 ppb is achieved, with the help of MFC.

- The chamber was refilled with  $N_2$  for 600 second for another cycle to begin again for different concentrations. The concentration used in this project for  $NO_2$  is 200 ppb to 1000 ppb, in steps of 200 ppb, and for  $NH_3$  is 2 ppm to 10 ppm, in steps of 2 ppm.

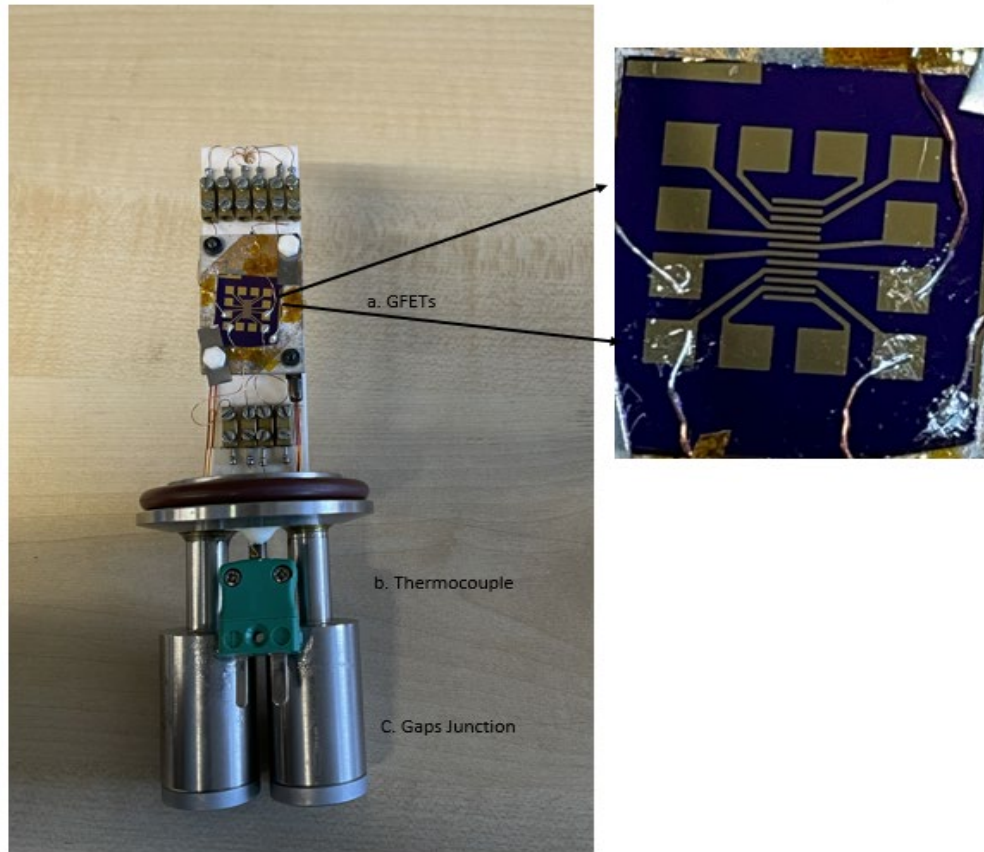


Figure 4.7: Shows an image of the GFETs device preparation for the gas sensitivity test. 9. a) represent the GFETs devices wired for the measurements, b) thermal cable used to read the temperature inside the chamber, and c) Gaps junction connected to the junction box for the measurements. The right represents the enlarged image of the GFETs device.

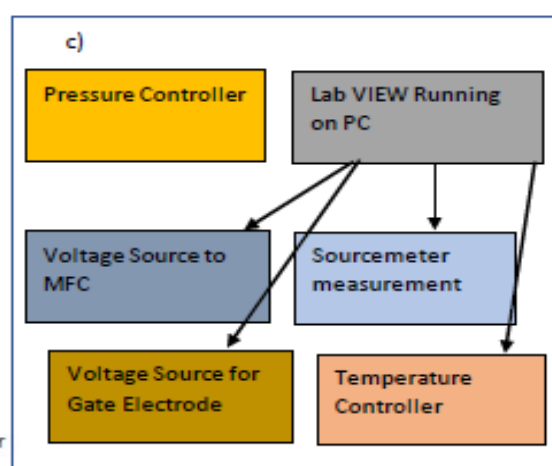
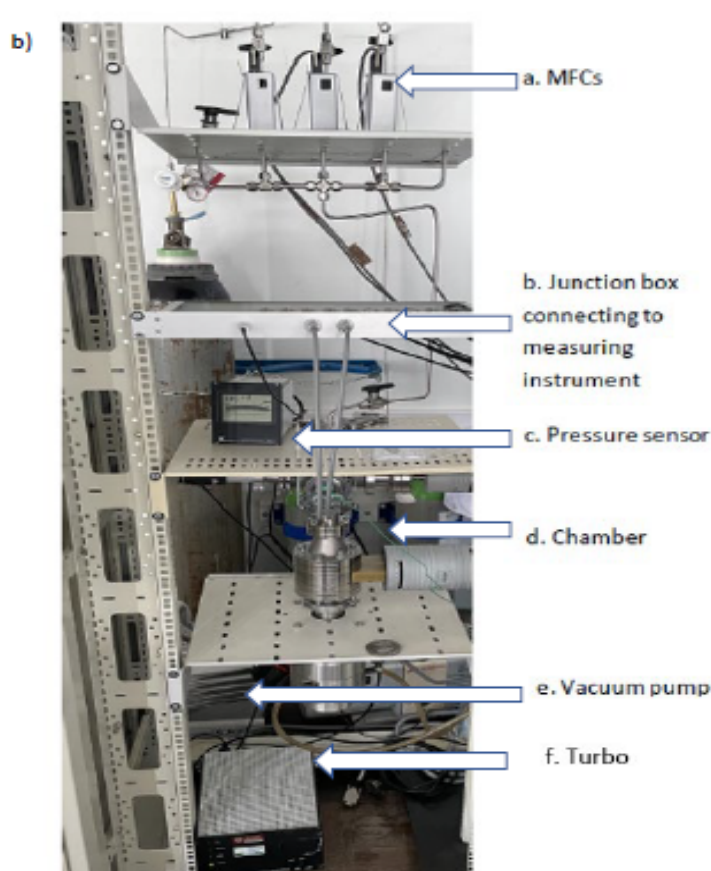
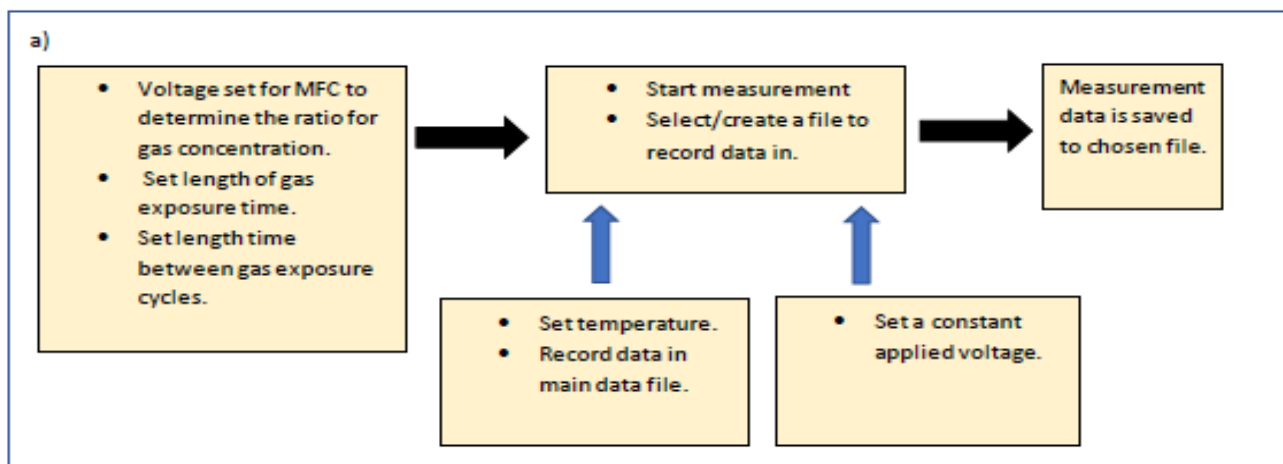


Figure 4.8: a) Diagram description of the user inputs into the apparatus. All the set up with black arrows must be used while the blue arrows are optional. b) An image of the gas controller chamber. Which show the setup in order from top to bottom, MFCs, the junction box which connect the device to the instrument, pressure sensor which gives the reading from the pressure inside the chamber, chamber, the regular vacuum pumps are at the back of the unit, and the turbopump at the bottom. C) Schematic of the LabVIEW setup with measurement inputs/outputs and gas control.

## 4.3 Analysis Methods

### 4.3.1 Atomic Force Microscopy

Atomic force microscopy (AFM) has been used for characterizing nanomaterials since 1986 [188, 189]. AFM works by mapping the surface of the sample in X and Y directions. The mapping is done by a cantilever, which has a sharp tip mounted at the end to produce the measurement, as demonstrated in Figure 4.9 [190]. During the movement on the surface of the sample, a laser is reflected by the cantilever which is then collected by the photodiode detector. The interaction between the tip and the surface of the material is on an atomic scale, while the movement of the cantilever is on a micrometre scale. Information of the measurement is collected by a photodiode detector, which converts the reflected laser light from the moving cantilever to an electric signal. When the cantilever is kept at a short distance from the surface of the sample during the mapping, such as in contact mode, the force between the tip and the sample is repulsive due to the electrostatic forces between the tip and the sample [188]. Alternatively, non-contact mode can be used, where the distance between the cantilever and the surface of the sample is relatively large, the oscillation of the cantilever in this case is disrupted by van der-Waals forces above the surface of the material rather than the material itself. Figure 4.10 demonstrates how the force between the tip and sample varies with the distance separation between the tip and sample [191]. As seen in this figure, the force regimes where contact and noncontact mode is operated are presented.

The topography measurements of AFM can be measured using three main modes: contact, non-contact, and tapping mode. In contact mode the topography of the surface of the sample is measured by the cantilever deflection. Resulting from the force between the tip and the sample being electrostatically repulsive. Within contact mode the forces between the tip and sample kept constant during the mapping. Variations in the height of the surface of the sample cause the cantilever to bend and therefore the laser spot position change on the photodiode detector upon cantilever bending. Contact mode mapping measurements provide high z resolution, but the large shear force applied by the cantilever is capable of damaging the sample or the tip. Also, as the tip in contact mode moves extremely close to the surface, opportunities for the sample or recording tip to be contaminated are significant.

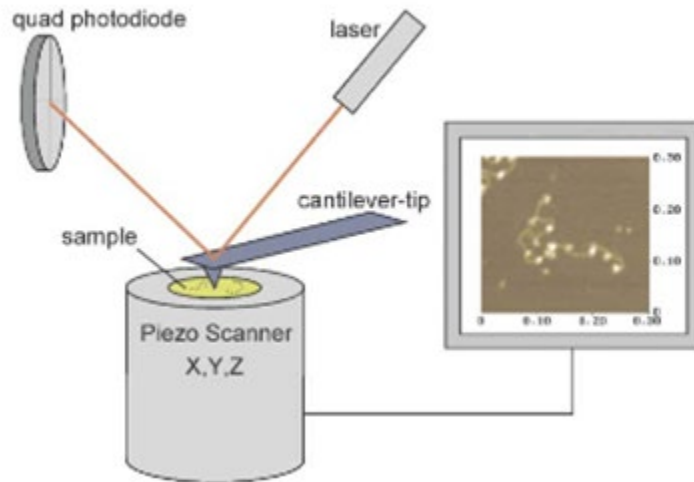


Figure 4.9: Display the force relationship between the tip to sample and distance separation. Adapted from reference [190].

In non-contact mode the tip is held at distance from the sample where the attractive forces regime is effective. In this mode the forces between the tip and sample are low and shear forces are not generated. Measuring the surface of the sample through the deflection of the cantilever is not applicable to this mode as the repulsive force is low. Instead the measurement of the cantilever is dependant on the vibration of the frequency just above to its resonant frequency. The range of frequency is typically from 100 to 400 kHz with distance between the samples of 10 to 100 Å. The oscillating cantilever resonance frequency and amplitude is decreased as the surface of the sample approached. This is due to the long-range force extending along the surface and van der-Waals interactions. These types of forces are very low compared to repulsive forces in the contact mode described earlier. The advantage of the non-contact mode is that tip has less potential for damage and contamination, and therefore a long lifetime. Also, if mapping a soft or delicate sample surface is advantageous to use non-contact mode to avoid contamination and damage of the sample as well as the tip.

The data presented in this project is being collected by using a Park Systems XE-150 AFM. The XE-150 was used with non-contact mode to obtained topographic image for the surface of the graphene.

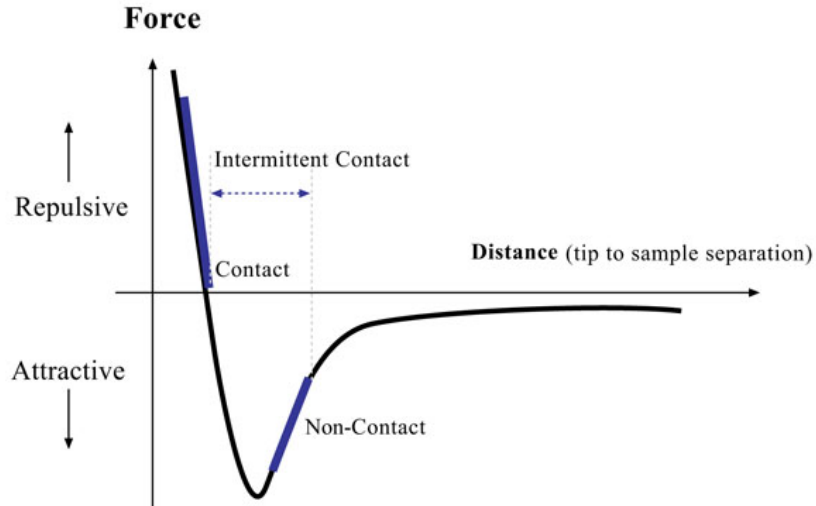


Figure 4.10: Display the force relationship between the tip to sample and distance separation. Adapted from reference [191].

### 4.3.2 Raman Spectroscopy

Raman spectroscopy is a useful tool to characterise atomic-scale structural and chemical modification of nanomaterials (graphene). It provides information about the material by measuring the shift in the scattered photon energy under illumination of monochromatic light. Raman is a type of visible light spectroscopy; it relies upon the scattering effect of the re-emitted photon energy.

Raman spectroscopy works by sending a beam of monochromatic light (laser) to illuminate the sample. Scattering occurs when the light interacts with the material of sample, and the energy shift of the scattered photon can provide information on the material. Figure 4.11. is an energy level diagram for Raman spectra representation of elastic (Rayleigh) and inelastic scattering. The wavelength of the re-emitted light after the interaction with the sample is the same energy as the incident light during elastic scattering, and will shift either up or down for Stokes and anti-Stokes during inelastic scattering. The shift occurs due to the incident photon's interaction with the material leading to photons receiving or losing the energy, which results in energy shifts down (Stokes) or up (anti-Stokes) for the scattered photons. The change in energy is related to the energy of the scattered photons. The intensity of the scattered light relevant to the Raman shift is measured by the Raman spectrometer, and described as wavenumbers ( $\text{cm}^{-1}$ ). The intensity of the scattered light presents the spectrum as a function of the monochromatic light wavenumbers.

Raman spectroscopy is a powerful tool for studying the quality of graphene, as it detects the missing Carbon (vacancy defect) within the graphene sheet [192-197]. Also, the absence of the band gap in graphene enhances the resonance of the incident photons. Which then provide high quality information of Raman spectra about the graphene atomic structure and electronic properties [192]. In addition, as single layer graphene is one atom thick, the entire graphene layer is measured under illumination [198]. By measuring the different phonon Raman spectra features, multiple different types of information can be extracted from the sample. Namely G, D, and 2D identify the quality of the graphene. The shape and intensity of G and 2D peaks change with the graphene layers [195, 199, 200]. The intensity of the G peak is increased relative to 2D with increasing number of graphene layers. On the other hand, the 2D peak is very sensitive to the graphene layer as its intensity decreases with the number of the graphene layer. The ratio of  $I_{2D}/I_G$  decreases with increasing numbers of layers. It is at a maximum of,



Figure 4.11: Demonstrates the three Raman scattering processes of Rayleigh, Stokes, and Anti-Stokes under the light-material interaction. The upward and downward shift in energy is due to obtaining or losing energy from a phonon to a phonon or unsteady state in the material.

typically, 1:2, for monolayer graphene [201-203]. Figure 4.12. represents a) the structure of the single layer graphene, b) the phonon dispersion relationship calculated of graphene by using Born-von Karman model, c) graphene spectra showing the characteristics of D, G, 2D, and D', respectively, and d) the defect activation by impurities for D and D' peaks [200]. All the processes for the Raman feature in graphene are presented in Figure 4.12.d. The  $I_D/I_G$  ratio changes with the defect percentage of the CVD graphene, as demonstrated in Figure 4.13. The D peak is generated from the breathing mode of the hexagonal ring and requires the defect to

be activated. Within this study, we approximate the oxygen defect to the point defect, and therefore, as the oxygen increases the D peak increases as a result of more defects being generated on the graphene. Therefore, the ratio of  $I_D/I_G$  is proportional to the defect. The G peak is generated from a single high-frequency phonon from the graphene in a hexagonal ring of atoms. Also, the 2D peak is generated from two phonon processes and no defect is needed for the activation. The pristine graphene G peak appears at approximately  $1580\text{ cm}^{-1}$  on Raman spectra. The defect D peak presents at around  $1350\text{ cm}^{-1}$ , and 2D presents at about  $2670\text{ cm}^{-1}$  with a laser excitation wavelength of  $532\text{ nm}$  [195, 199, 200].

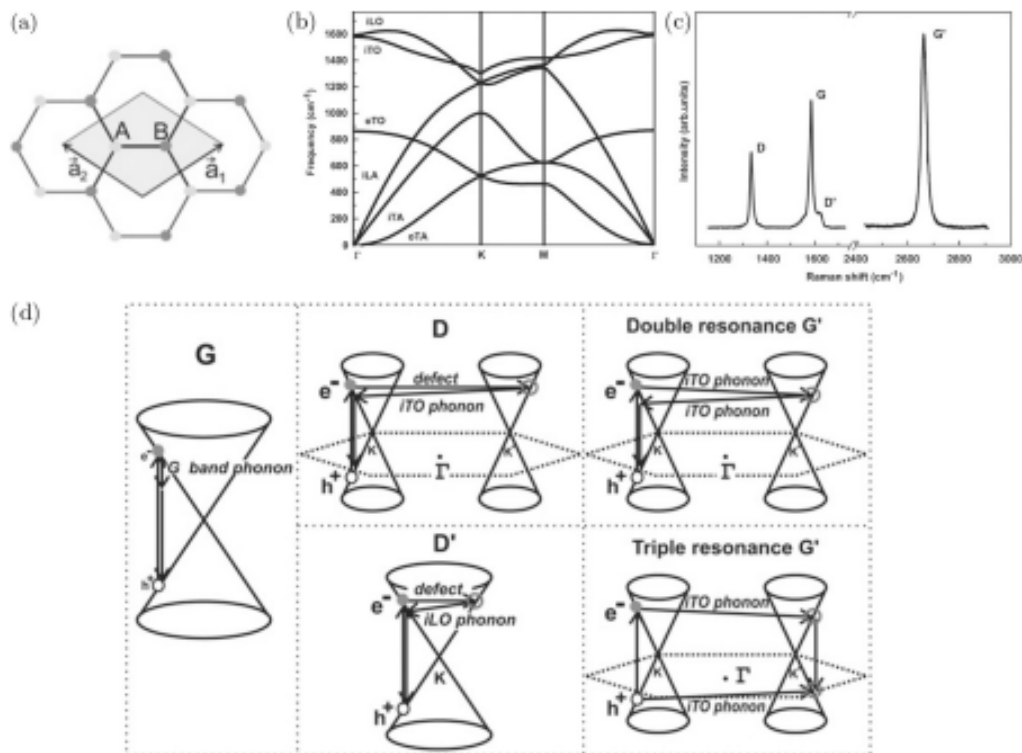


Figure 4.12: a) Shows a single-layer graphene structure, b) a measured dispersion phonon relation, and Raman spectra taken from the edge of graphene showing the characteristic D, G, 2D, D', Raman peaks. d) represent the photon-phonon interactions which give most of the spectral peaks on Raman spectroscopy. Adapted from reference [200].

Raman spectroscopy confirms the growth quality of the graphene, helps study the effect of the polymer on graphene and shows the influence of the  $\text{SO}_2/\text{Si}$  substrate on graphene. Raman spectroscopy will also be used on graphene after exposing it to an oxidising agent to study the amount of defect induced in the graphene. In this project, Raman spectroscopy measurements were collected using a Horiba Jobin Yvon HR800 UV. The incident laser power was  $4\text{ mW}$  at room temperature, the laser excitation wavelength was  $532\text{ nm}$ , and the laser beam diameter was  $0.70\text{ }\mu\text{m}$ . An acquisition time was set to  $5\text{ s}$  per measurement for spectra records. The

Raman signals depend on the excitation wavelength laser as it gets more robust with a shorter wavelength. For this reason, the laser citation energy kept similar to the excitation energy used in the literature for fair measurement comparisons.

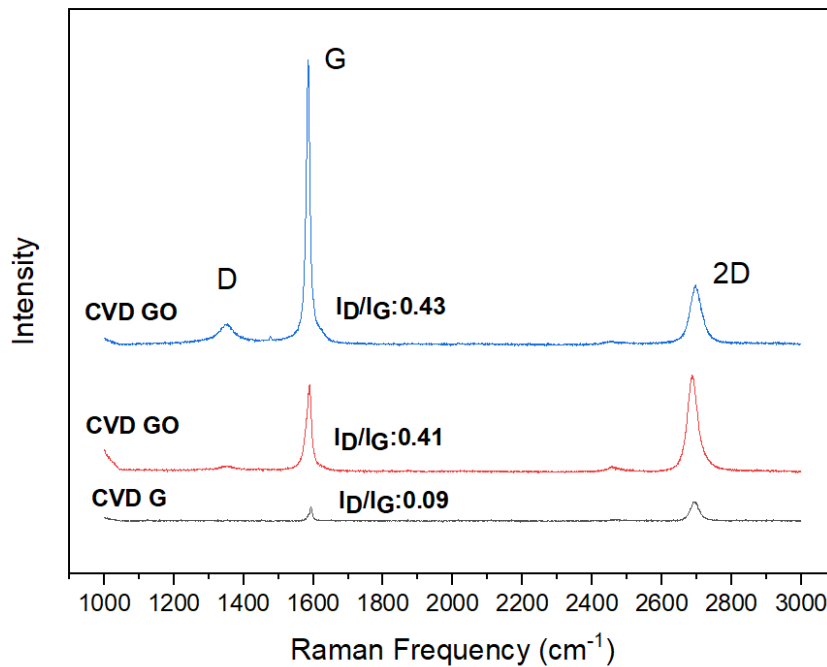


Figure 4.13: Represents  $I_D/I_G$  ratio for CVD graphene, CVD graphene with low oxidation level and CVD graphene with higher oxidation as presented on red and blue graphs, respectively.

### 4.3.3 X-Ray Photoelectron Spectroscopy

X-ray photoelectron spectroscopy (XPS) is a surface analysis technique, it provides information about the chemical elements on the surface of the sample, and details about the

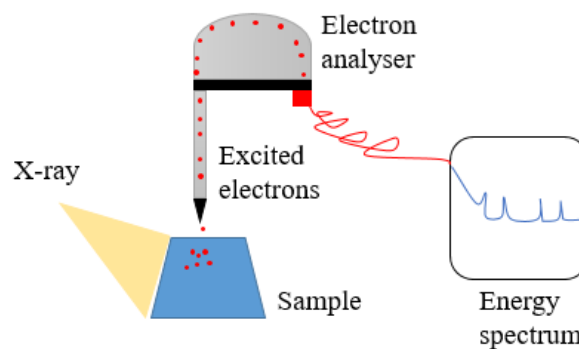


Figure 4.14: Represent a diagram of XPS.

chemical bonding between these elements. A diagram of the XPS instrument is presented in Figure 4.14 [204].

XPS measurement works by sending a monochromatic x-ray to the sample surface. Electrons in the sample are excited from their specific bond state and escape from the core levels [205]. The energy from the emitted electrons is measured by an electron analyser which then creates an intensity of spectrum as a function of energy. The measurement of atom's energy is determined by Equation 4.5:

$$E_B = E_{Ph} - (E_K + \phi) \quad (4.5)$$

Where  $E_B$  is the binding energy,  $E_{Ph}$  is the energy of the X-rays used by the spectrum,  $E_K$  is the kinetic energy of the escaped electron from the sample, and  $\phi$  is the work function of the sample. In solids, photoelectrons are only generated at the surface of the sample due to their short mean free path close to  $\sim 4$  nm [206].

XPS has an advantage in revealing information about the entire sample composition of 2D materials. Electrons escaping from a different state within the sample will have different energies, which allow XPS to determine the sample composition and measure the characteristics of just the target layer. XPS has different energy spectrum peaks corresponding to a specific element, such as Carbon (C) and Oxygen (O) peaks at 284.6 eV and 532.5 eV respectively, as demonstrated in Figure 4.15. Furthermore, the amount of each element present in the sample can be determined by the intensity of the peaks.

The measurement of XPS is performed under high vacuum conditions ( $\sim 10^{-9}$  mbar), meaning evacuation of the XPS chamber prior to measurements of XPS can take hours. This is important to ensure that the escaped electron reaches the electron analyser without any energy loss due to collision with atmospheric particles.

In this project, XPS data was collected at the EPSRC National Facility for XPS ("HarwellXPS"). The data was collected using monochromatic Al K $\alpha$  (1486.69 eV), X-rays were at 15 mA emission and 12 kV HT (180W). The spot size per analysis area was  $700 \times 300$   $\mu\text{m}$ . Spectra of the high resolution were conducted using a pass energy of 20 eV, and the pressure base was below  $5 \times 10^{-8}$  Torr at a room temperature of 294 K.

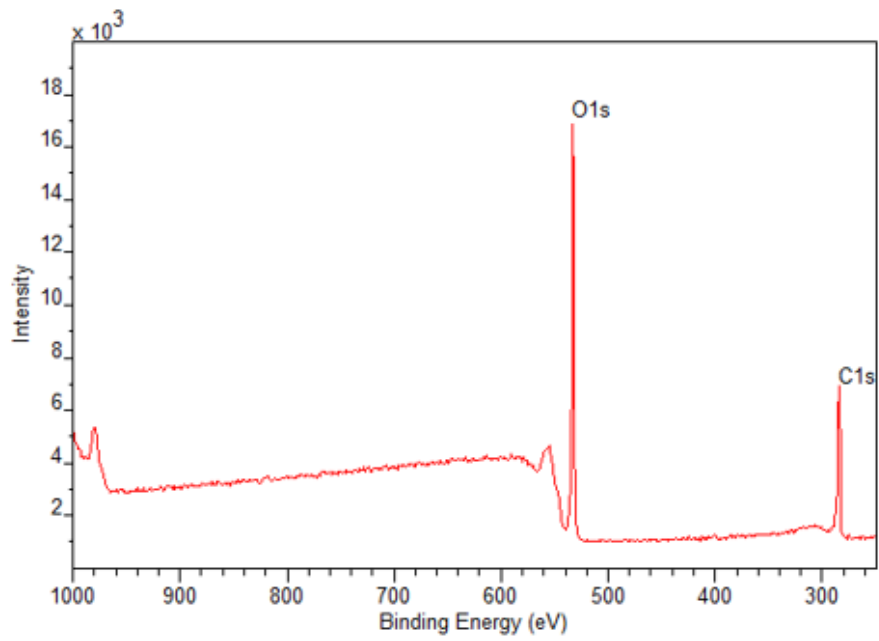


Figure 4.15: Shows the XPS result for the binding energies of Carbon and Oxygen and their intensity which relate to the atomic percentage of each element in the sample.

## Chapter 5

### 5 Pristine Graphene Gas Sensors

In this chapter, the graphene gas sensing device, built based on the graphene field effect transistor (GFET). Graphene has been investigated as a gas sensor material due to its ultimately high surface area to volume ratio [54], low carrier density, and low electrical noise [55, 56, 207]. Graphene can operate as a sensor at room temperature, which greatly reduces energy consumption compared to other key sensing technologies, such as metal oxide gas sensors [57]. In addition, graphene has high carrier mobility [207]. The distinctive features of graphene are its high surface area to volume ratio and atomic thickness, which means that any physisorbed gas molecules on the surface will interact with the entire channel thickness. Additionally, due to graphene's low carrier density near its neutral point, any charge interaction with adsorbed species should cause a measurable resistance change, even at low gas concentrations [77, 79]. This means that graphene should interact and show resistance change with its surrounding gases in the ambient.

However, the growth and transferring process can affect the quality of graphene gas sensors [208-210]. There have been many reports [80, 211-214] about the graphene gas sensors with low quality, such as lack of obtaining a large area of single-layer graphene, high polymer residues, wrinkling, tears, and fold, which results in poor electric mobility and sensitivity [215]. Also, graphene gas sensors can sense all the adsorbates on its surface, making it even more sensitive to the contamination introduced during the fabrication process [210, 216]. To overcome this problem, many ways are used to obtain the large area of graphene layer with low defects, such as exfoliation of graphite via mechanical exfoliation, Liquid phase exfoliation, epitaxial growth on silicon carbide, and CVD on transition-metal films [71, 120, 121, 128, 136]. Also, many different transferring processes are used to reduce the amount of contamination and wrinkling introduced to graphene during the transferring process using a supporting layer, which is polymethylmethacrylate (PMMA) [141, 217], rosin [218], polycyclic aromatic hydrocarbon (PAH) [219], paraffin [220], and nitrocellulose [177].

Within this chapter, we will use the best graphene transfer procedure available to us and explore sensor response in the context of literature and best practice. The GFETs used within this work demonstrate behaviour similar to reported graphene sensors [64, 77-80]. In addition, the GFETs response percentage compared to the response in the literature is presented.

## 5.1 GFET Device Cleanliness

To confirm the quality of the CVD graphene used in this work, multiple chemically sensitive spectroscopic techniques are used to evaluate the graphene quality. The samples are prepared by transferring CVD grown graphene on copper to Si substrate copped with 295 nm SiO<sub>2</sub> as described in the Methods Chapter (4.1.2). The techniques used to investigate the contamination introduced to the graphene during the transferring process are: scanning electron microscope (SEM), atomic force microscope (AFM), Raman spectroscopy, and X-Ray Photon Spectroscopy (XPS). In addition, electrical transfer curve measurements are used to evaluate the doping type on graphene and to calculate the charge-carrier mobility.

### 5.1.1 Higher Resolution Microscopy and SEM

Higher Resolution Microscopy and SEM are useful for investigating the graphene quality after transferring process. The high resolution microscopy provides a rapid method for assessing the general cleanliness and continuity of the graphene film. SEM can also provide an image which contains information about the residues, tears, and wrinkling on the transferred graphene surface [221].

In this section, high-resolution microscopy and SEM have been used to evaluate the cleanliness of graphene sheet after transferred to SiO<sub>2</sub>/Si, and to show that the transferred graphene has low amount of residues, tears, and wrinkles. SEM operates by sending a beam of electrons to the surface of a sample. The electrons will interact with the sample resulting in secondary electrons ejected from the sample, which are then collected by a secondary electron detector to provide a sample topography.

Figure 5.1: a and c) demonstrates the high-resolution microscopic images for the CVD graphene after it transfers to (295 nm) SiO<sub>2</sub>/Si substrate to see if any damage was introduced to the graphene sheet during the process with a black, blue, red, and green arrow pointing to folding graphene, residues, tear, and multilayer graphene, respectively. The images show that the graphene is continuous with full coverage after transfer to SiO<sub>2</sub>/Si. Residues, tears, and wrinkles are visible in the image corresponding to the arrows. In addition, a very low multilayer graphene [222, 223] is observed close to the transfer sheet's edge. Figures 5.1: b and d) show the same images as Figures 5.1: a and c), respectively, with dark field images to visualise the residues of nitrocellulose and dirt on graphene after transfer. Dark field

microscopy is able to show residuals by enhancing contrast and selectively detecting scattering light caused by residuals.

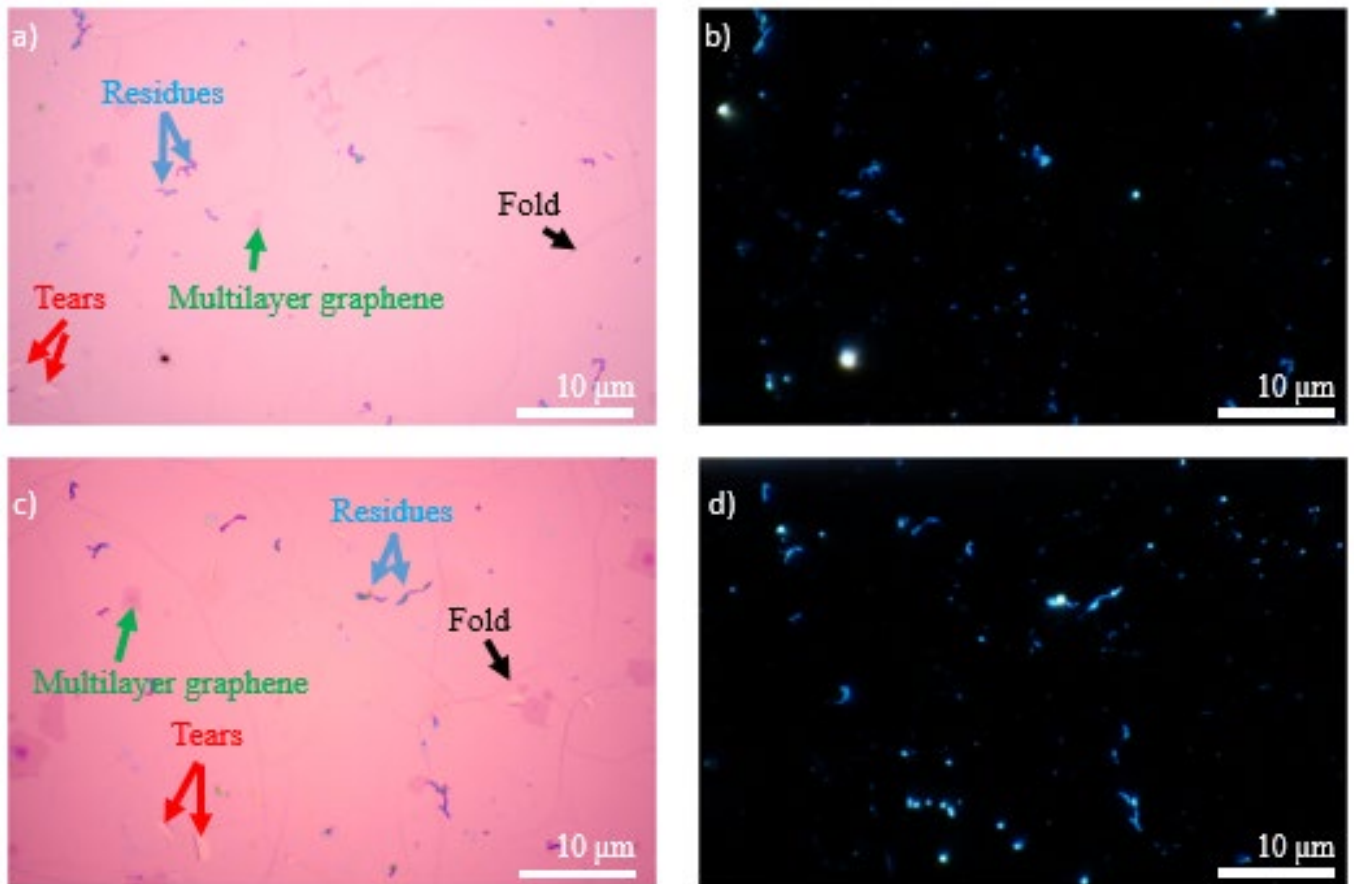


Figure 5.1: Images displaying the graphene sheet after being transferred to  $\text{SiO}_2/\text{Si}$  substrate, a and c), show the  $10\ \mu\text{m}$  area of the middle of the graphene sheet and edge of the graphene sheet, respectively, with a black, blue, red, and green arrow pointing to folding, residues, tear, and multilayer graphene, respectively. b and d), the same images of a and c) after converting the dark field for residues analysed.

Figures 5.2: a and b) Demonstrate SEM images of graphene after transfer to  $\text{SiO}_2/\text{Si}$  with red, blue, black, and orange arrow pointing to tears, residuals, fold, and back side graphene, respectively. The different thermal expansion coefficients between graphene and copper cause the wrinkles presented on the graphene surface during the growth. Also, the residuals result from the wet transfer process of graphene onto a  $\text{SiO}_2/\text{Si}$  substrate.

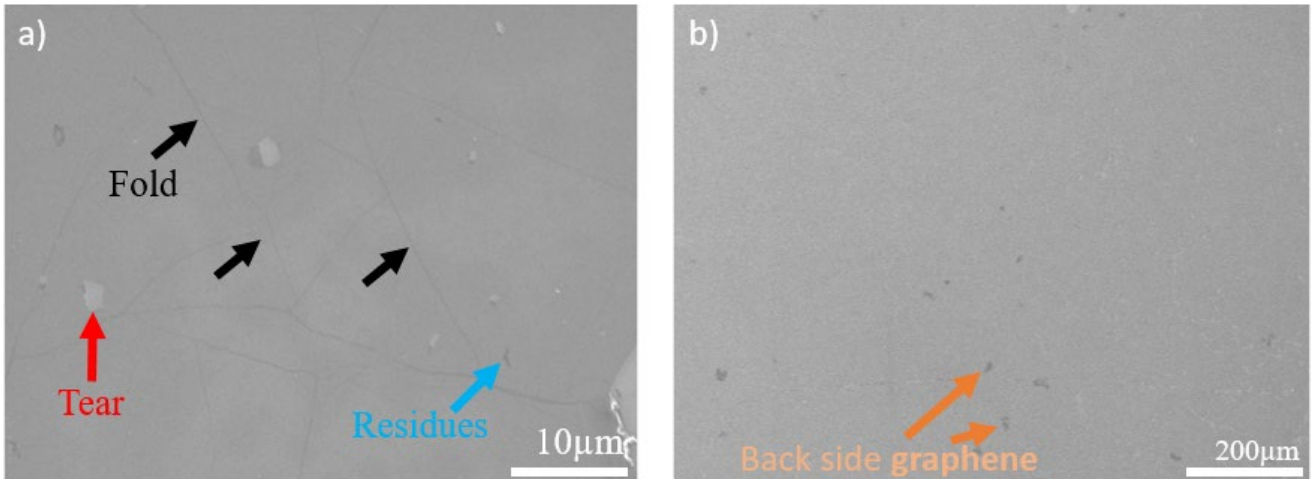


Figure 5.2: a and b) Represent the SEM image that has been taken for the graphene sheet after transfer to SiO<sub>2</sub>/Si with red, blue, black, and orange arrow pointing to tears, residuals, fold, and back side graphene, respectively. The transfer handling procedure causes a large tear on the bottom right side of Figure a) with a tweezer.

### 5.1.2 AFM

AFM is useful for characterising the quality and micro-cleanliness of graphene sheets. It provides a high-resolution image that can distinguish the single atomic layers on SiO<sub>2</sub>/Si substrate. AFM images also contain information about roughness and morphology.

Figure 5.3. displays a non-contact AFM scan of a graphene surface after transferral to SiO<sub>2</sub>/Si. The coloured arrows with blue, black, and yellow indicate the residues, wrinkles, and dirt, respectively. The image shows the low folding area originates from the CVD graphene transfer process, with low density of residues on the graphene surface. However, tears or gaps on graphene only observed at the edge of the graphene sheets indicating the continuous graphene layer growth. From the high-resolution microscope, SEM, and AFM scans, graphene has some residues resulting from the transferring process and this could lead to some doping to the graphene [224, 225]. In addition, the amount of defects on the transferred graphene is low compared to reported values [226, 227] indicating that using nitrocellulose as supporting layer during the transfer is introducing lower residues than PMMA [177]. The amount of wrinkles on the transferred graphene is low, which means that the stress on the graphene is low. This should result in the electrical conductance being high, which is suitable for electronic transportation on the performance of the graphene-based device [228-230]. If a high amount of wrinkles and gaps were observed, this could lead to isolating the graphene into isolated islands, which deteriorates the graphene's electronic

transformation [228, 230]. The transferred graphene presented within this work shows lower defect density and tears compared to the published literature [221, 231, 232].

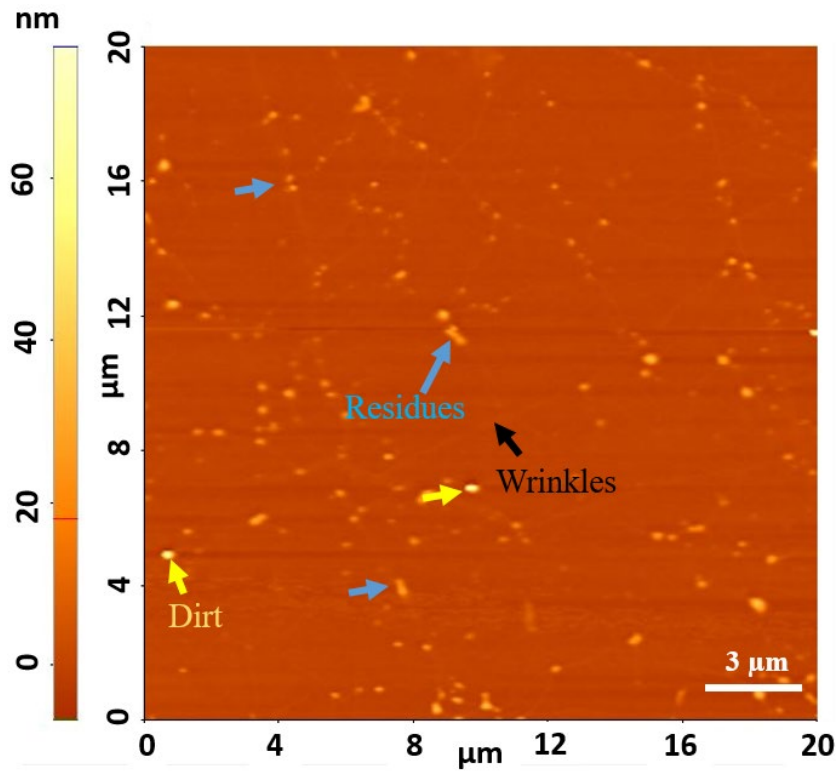


Figure 5.3: Shows an AFM image of transferred graphene to SiO<sub>2</sub>/Si substrate with blue, black, and yellow pointed to residues, wrinkles, and dirt, respectively.

### 5.1.3 Raman Spectroscopy

Raman spectroscopy is a useful tool to characterise atomic-scale structural and chemical modification of graphene. To evaluate the number of graphene layers and defect introduced to the graphene, the Raman spectrum is used. It has three major peaks used to characterise the graphene quality: G, D, and 2D. The intensity of the G peak is increased relative to the 2D peak with an increasing number of graphene layers. In addition, the shape and intensity of G and 2D peaks change with the graphene layers [195, 199, 200]. The ratio of  $I_G/I_{2D}$  can be used to estimate the number of layers of graphene [192, 196, 201, 233]. Moreover, the D peak is generated from the breathing mode of the hexagonal ring and requires a defect to be activated. Also, the intensity ratio of  $I_D/I_G$  is used to evaluate the defect density of the graphene [193].

Raman measurements have been taken for all the samples to investigate the quality of graphene. G and 2D peaks are visible, and the  $I_{2D}/I_G$  ratio of 1.97 indicates monolayer graphene [201-203]. The defect density ( $n_D$ ) can be calculated using Equation 5.1 [193].

$$n_D = \frac{1.8 \pm 0.5 \times 10^{22}}{\lambda_L^4} \cdot \left(\frac{I_D}{I_G}\right) \quad (5.1)$$

Where  $\lambda_L$  is the wave length of the illuminating laser light,  $I_D$ , and  $I_G$  are the intensity of the D and G peaks, respectively.

The amount of impurities on the graphene is very low and cannot be seen, as there is no sign of the D peak presented as it is below the noise level on the Raman spectrum, as represented in Figure 5.4. The  $I_D/I_G$  ratio is 0.038, which is smaller than the reported ratio values [89, 234-238] for pristine graphene that ranges between 0.07 to 0.98. This is due to the low amount of defects in the graphene sheet. In order to calculate an upper boundary to the number of defects density, the peak-to-peak noise amplitude was taken, and the defect density of  $1.3 \times 10^{10} \text{ cm}^{-2}$  was found. The small defect density of graphene is attributed to polymer residues and some oxygen groups. The presence of oxygen groups will be evaluated by XPS measurement in the following section.

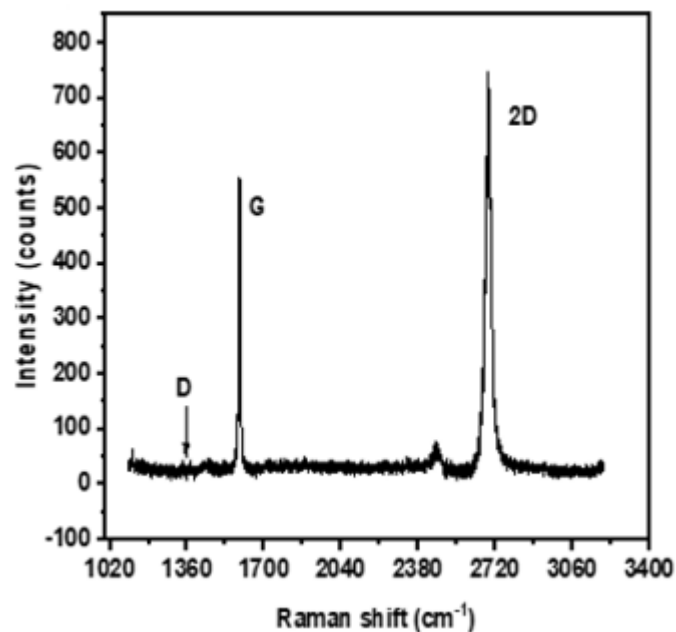


Figure 5.4: Demonstrates the Raman spectra for the graphene where G and 2D peaks are presented at  $1580 \text{ cm}^{-1}$  and  $2670 \text{ cm}^{-1}$ , respectively. The laser excitation wavelength is 532 nm.

#### 5.1.4 XPS

As Raman spectroscopy does not provide information about the type of chemical elements and bonding between these elements compound, XPS is another technique used to investigate the graphene after transfer to Si substrate coated with 295 nm SiO<sub>2</sub> and to determine the atomic percentage of the C-C bond. XPS data were collected at the EPSRC National Facility for XPS (“HarwellXPS”). XPS was acquired using Kratos Axis SUPRA using an X-ray source of monochromated Al K $\alpha$  with an energy of 1486.7 eV. The measurements were collected with a spot size/analysis area of 700  $\mu\text{m}$   $\times$  300 $\mu\text{m}$  using Kratos Axis SUPRA. The high-resolution spectra were collected by passing energy of 20 eV with step size and sweep time of 0.1 eV and 60s, respectively. All the data were collected at room temperature with a pressure set of below  $5 \times 10^{-8}$  Torr. Core-level spectra were recorded around the C1s binding energy. This energy was selected as the oxygen groups contamination presence is observable due to carbon-oxygen bonding. Figure 5.5. displays the C1s core-level spectra collected from the pristine CVD graphene after being transferred using nitrocellulose (NC) to SiO<sub>2</sub>/Si. The graphene samples spectra fitted by Casa XPS Software for carbon-to-carbon bonding (C-C), hydroxyl bonding (C-OH), epoxy bonding (C-O-C) and carbonyl bonding (C=O) peaks at 284.4 eV, 285 eV, and 286.3 eV, respectively [239]. The atomic percentage of C-C for the sample is 70.04%, comparable to the published results [64, 83, 240], which have a C-C percentage of 70 to 79%. In addition, the presence of oxygen group on pristine graphene from C1s core-level spectra is found to be 17.53% and 12.43% for C-OH or C-O-C and C=O, respectively. This is generated by transferring CVD graphene to SiO<sub>2</sub>/Si, which is known to introduce some polymer residues even after cleaning, as shown by the high-resolution microscope and AFM in the previous section [241, 242].

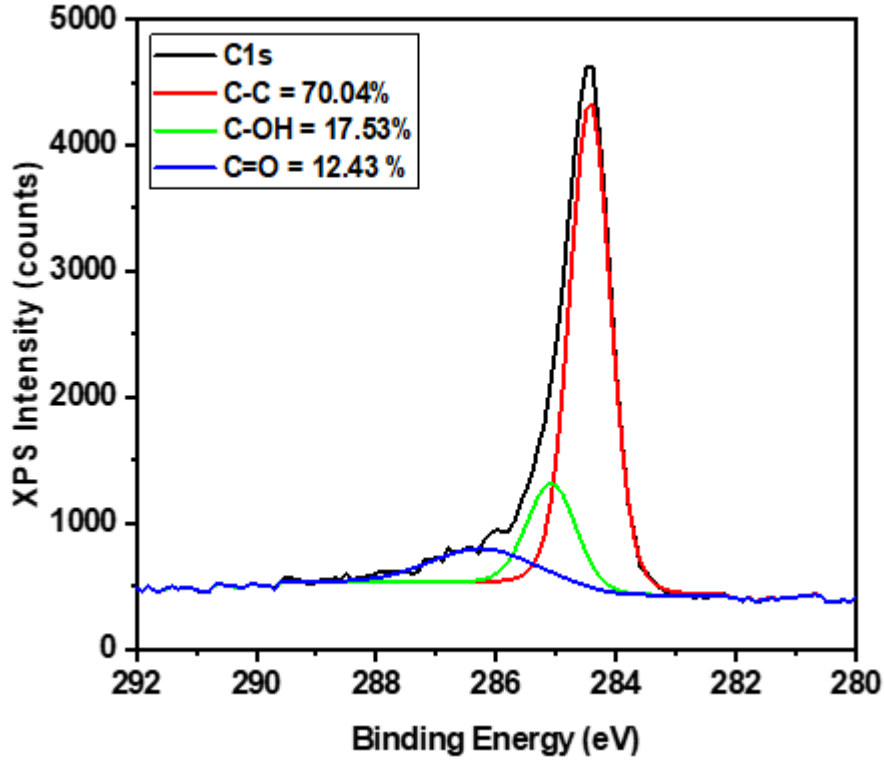


Figure 5.5: C1s core-level XPS spectrum recorded from graphene on Si substrate coated with 295 nm SiO<sub>2</sub>.

### 5.1.5 Electric Characterisation

The electric characterisation of GFETs is used to provide information about the graphene type. It also can be used to estimate the charge carrier concentration on the graphene and mobility. Also, the residual of the unintentional doping introduced to the graphene during the transferring process can be calculated using Equation 4.1.

$$n_0 = \frac{(V_g - V_{Dirac}) \cdot C_{ox}}{e} \quad (4.1)$$

Where  $n_0$  is the carrier density of the graphene device,  $V_g$  is the gate voltage,  $V_{Dirac}$  is the Dirac point voltage,  $C_{ox}$  is the capacitance for the dielectric layer per cm<sup>2</sup> (11.7 nF cm<sup>-2</sup> for 295 nm SiO<sub>2</sub>), and  $e$  is the electron charge.

The fabricated GFET device has 11 channels, and electrical measurements are taken from all channels after annealing in a vacuum at 100°C for 1 hour. The FET measurement is taken for all the channels in the device, and Figure 5.6. shows the result obtained from the device. The

plot shows a typical transfer curve of the graphene field effect transistor. The Dirac point for the forward sweep for all the 11 channels ranges between 35-37 V, and for the backward sweep range between 61-64V. In addition, the hysteresis between forward sweep and backward sweep is due to the electron trapped in water trapped between graphene and substrate following the transfer procedure and polymer [186, 243, 244]. Furthermore, the result indicates as transferred CVD graphene is p-type as the Dirac point is located at a positive voltage. Also, XPS measurement shows oxygen presence on the graphene, which may increase the hole concentration in graphene as oxygen will take electrons from graphene [70, 81, 85]. The mobility for electron and hole have been calculated for the devices using Eq. (4.4). and found to be range between 1258 – 2018 cm<sup>2</sup>/V.s and 2277- 3487 cm<sup>2</sup>/V.s, respectively, as presented in Table 5.1. Compared with published results for GFET mobility, which range from 10.15 to 3000 cm<sup>2</sup>/V.s, [58, 72, 80, 92, 245] our devices show mobility comparable with the upper end of published GFET mobility for similarly processed devices. The average electron and hole mobilities for every device vary from device to device within this work, as in Table 5.1; this variation is attributed to the quality of the transferred graphene. As the presence of residues, wrinkles and tears affect the mobility of graphene, it is important to control them in order to obtain high mobility [229, 246, 247]. The growth of CVD graphene on copper and transfer technique to SiO<sub>2</sub>/Si substrate helps reduce the wrinkles on graphene and enhance mobility [229, 247].

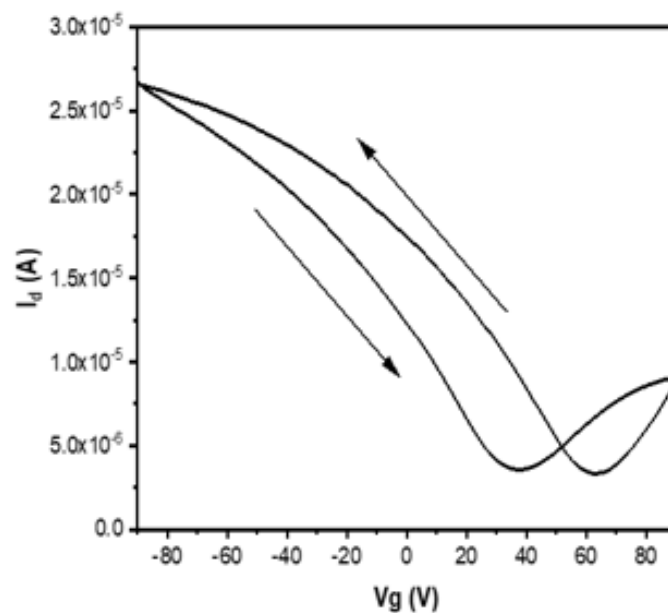


Figure 5.6: Shows typical transfer curve of graphene field effect transistor. Dirac point on the forward sweep locate at 35 V and on the backward sweep at 62V.

The GFETs presented within this work show low wrinkles, tears, and residues, as discussed in section 5.1.1. These lead to high graphene quality, which preserves graphene's electric performance. However, the low amount of residues (nitrocellulose and water trapped under the graphene sheet) and the SiO<sub>2</sub> substrate still induce some charge doping to the graphene, as was determined using Eq 4.1 and found to be  $2.18 \times 10^{12} \text{ cm}^{-2}$ . In addition, the carbon vacancy density in the graphene sheet was determined by Raman measurement and found to lie below the minimum detectable value of  $1.37 \times 10^{10} \text{ cm}^{-2}$ . The Raman defect measurement and electric measurement show that a small amount of defect of  $1.37 \times 10^{10} \text{ cm}^{-2}$  correlates to  $n_0$  of  $2.18 \times 10^{12} \text{ cm}^{-2}$ . The variation in both measurements is due to Raman being only sensitive to certain types of defects that cause changes in a vibrational mode in the lattice, such as point defects. In contrast, electric measurement is sensitive to all types of defects that affect the electrical properties of the material, including defects that Raman does not detect. Also, from the electric measurement, the residual charge carrier density is attributed to holes as the Dirac point located at positive voltage [186].

Table 5.1: Represent the average electron and hole mobility for field-effect transistor devices.

Device	Electron field effect mobility (cm <sup>2</sup> /V.s)	Hole field effect mobility (cm <sup>2</sup> /V.s)
1	1585	2927
2	2018	3472
3	1904	3487
4	1258	2277
5	1310	2747
6	1853	3160

## 5.2 NO<sub>2</sub> Sensor Characteristics

The graphene gas sensor device presented in this work based on the field effect transistor (GFET). Graphene is atomic thinness [71], low noise [248, 249] and low density of state near to the Dirac point [71, 183] which means that any interaction between the graphene and gas species through physical adsorption will have a measurable change in resistance response. P-doped graphene shows an increase in resistance upon exposure to reducing gas species and a decrease in resistance upon exposure to oxidising gas species. While for the n-doped graphene, the opposite behaviour is expected when electrons become the charge majority

carrier. The graphene has a low defect density of impurities, which act as active sites in the graphene basal plane, the NO<sub>2</sub> gas molecules are expected to be adsorbed on the graphene through the physisorption interaction. As discussed in DFT in the previous section, the oxidising gas, such as NO<sub>2</sub>, is strongly doping pristine graphene by  $-0.1e$  as its lowest unoccupied molecular orbital (LUMO) position is located below the Dirac point [73]. On the other hand, the charge transfer from NH<sub>3</sub> to the graphene surface is about  $0.03e$  in the highest occupied molecular (HOMO) orbital orientation [73]. We can see from the magnitude of these charge exchanges that GFET gas sensors should react more strongly to NO<sub>2</sub> than to NH<sub>3</sub>.

In this work, graphene devices have been investigated for their sensitivity to NO<sub>2</sub> gas via physisorption. The surface coverage of adsorbed molecules was calculated by fitting the first-order rate equation to gas-sensing saturation measurements, and to identify the maximum resistance change devices reach before saturation at given gas concentrations. This is then used to evaluate the number of sensing events the device does upon exposure to different NO<sub>2</sub> concentrations in a short period of time (3 min) before saturation is reached. The GFETs used in this work demonstrate resistance change behaviour upon NO<sub>2</sub> exposure compatible with published results [60, 69, 77-80, 250, 251]. A comparison of response percentage between device sensitivity used within this work and reported values are presented. In addition, the limit of detection for devices and recovery are compared with the literature.

### 5.2.1 NO<sub>2</sub> Saturation Measurement

A saturation test was performed to study the response behaviour of the device under long-time (1 h) exposure to NO<sub>2</sub> gas. This is then used to estimate how the device can operate in cycle events for NO<sub>2</sub> detection before reaching saturation. The experiment was carried out at room temperature inside the gas chamber. The device was left under a high vacuum overnight before the test was performed to remove molecules adsorbed on the graphene surface [25]. The gas rate during the measurement was controlled by mass flow controllers (MFCs). The change in resistance was recorded by The Keithley 2450 Sourcemeter. The sensitivity of the device was investigated by measuring the change in resistance using a four-terminal configuration method across the graphene channel during the gas exposure to NO<sub>2</sub> and N<sub>2</sub>. The N<sub>2</sub> is used in the sensitivity measurement as a reference or baseline gas in the sensitivity test for comparison and evaluating the device's response to NO<sub>2</sub>. The measurements were performed by flowing N<sub>2</sub> for 10 minutes, followed by 1000 ppb of NO<sub>2</sub> follow for 1 h and

then N<sub>2</sub> for 2 h. During the measurements, the sensing chamber pressure was kept at 799.9 mbar by the pressure modulator, and V<sub>ds</sub> was maintained at 10 mV by the sourcemeter across the graphene channel. As the device was exposed to NO<sub>2</sub> gas in different time steps, the response of the device was analysed as the relative change in resistance and can be calculated using Equation 5.2 [60].

$$S = \frac{R_0 - R_g}{R_0} \times 100\% \quad (5.2)$$

Where R<sub>0</sub> is the initial resistance and R<sub>g</sub> is the resistance after the gas has been introduced. Figures 5.7: a) and b) represent the response for the graphene devices D1 and D2 that is transferred using NC as a supporting layer to graphene, which is explained in section 2.1.2. The resistance of the devices decreases upon exposure to 1000 ppb of NO<sub>2</sub> gas for 1 h. As the electric measurement shows that the device is initially p-doped, the extracted electron from the graphene surface to NO<sub>2</sub> molecules increases the hole concentration in the graphene film, leading to a decrease in resistance [73]. In addition, the rate of resistance decrease is observed during the exposure with respect to time. Only for device D1 saturation was reached after 2329s of exposure to 1000 ppb of NO<sub>2</sub>. While for device D2 the saturation was not reached even for 1 h exposure time. The response to NO<sub>2</sub> for devices D1 and D2 were 2.2% and 2.4%, respectively.

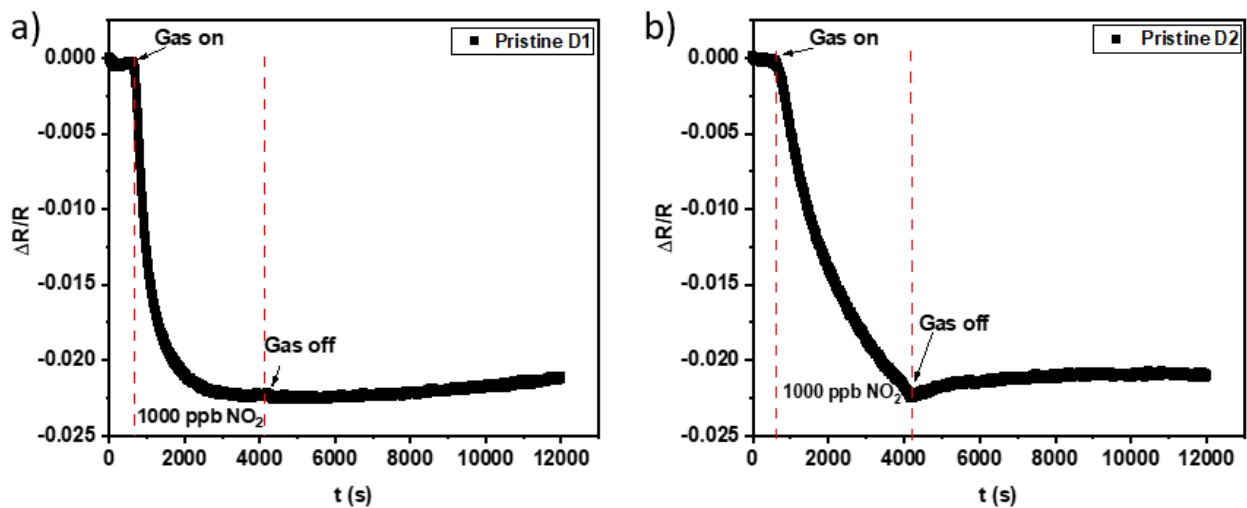


Figure 5.7: a and b) Response of graphene device D1 and D2 for 1000 ppb of NO<sub>2</sub> gas, respectively. Graphene in devices D1 and D2 were transferred using NC as a supporting layer. The measurement is done at room temperature with a flow of N<sub>2</sub> during the recovery process.

During the recovery process, none of the graphene sensors recovered to their initial resistance even after more than 2 h with N<sub>2</sub> flow. However, when the devices are left under high vacuum overnight, the sensors recover to 95% of the initial resistance. The same recovery issue for the graphene sensors has been reported within the literature, and was resolved variously by illuminating the graphene sensors with an Infra-Red (IR) light source [250, 251], or with UV light source [252] to improve the sensor baseline recovery process. Nevertheless, both our devices demonstrate slow recovery, lower than those reported in the literature [250-252]. In addition, some other sensors demonstrated recovery of up to 100 % at room temperature in short time [80, 89]. Importantly however, the aforementioned devices reported in the literature were measured without a preceding overnight vacuum conditioning step, while in our case both devices were under-vacuum overnight before the test was performed. The overnight vacuum step resulted in removing all adsorbents from the graphene surface. The effect of using vacuum on the devices before the test will be discussed later in section 5.2.4.

The rate of the adsorption and desorption of the NO<sub>2</sub> gas species on graphene can be calculated using Equation 5.3 [253].

$$\theta = \frac{K_1}{K_2} (1 - e^{-K_2 t}) \quad (5.3)$$

Where  $\theta$  is the gas molecule total coverage of the surface on the device relating to  $K_1$  and  $K_2$ .

$$K_1 = K_a P_{gas} \quad (5.4)$$

and

$$K_2 = K_1 - K_d \quad (5.5)$$

Where  $K_a$  [ $ppb^{-1}s^{-1}$ ] and  $K_d$  [ $s^{-1}$ ] are the constant of adsorption and desorption, respectively.  $P_{gas}$  is the partial pressure of the detecting gas.

Figures 5.8: a) and b) illustrates the rate equation fitting to the data obtained from devices D1 and D2. From the fitted data, the  $\frac{K_1}{K_2}$  is equal to a and  $K_2$  is equal to b.

The equation shows the resistance response during the adsorption of the NO<sub>2</sub> gas before the saturation is reached, and the exponent can be determined by fitting the equation as demonstrated in Figures 5.8: a) and b). The adsorption increases at the beginning of the cycle for devices D1 and D2 during exposure at 1000 ppb NO<sub>2</sub>. From the plotted curves of the

resistance, the adsorption  $K_a$  and the desorption  $K_d$  values can be obtained using Equations 5.4 and 5.5. For the pristine graphene device D1 the  $k_a$  and  $k_d$  found to be  $4.316 \times 10^{-6} \text{ppb}^{-1} \text{s}^{-1}$  and  $2.36 \times 10^{-3} \text{s}^{-1}$ , respectively. While for pristine graphene device D2 the  $k_a$  and  $k_d$  found to be  $1.352 \times 10^{-6} \text{ppb}^{-1} \text{s}^{-1}$  and  $8.26 \times 10^{-3} \text{s}^{-1}$ , respectively. Device D1 shows a higher adsorption rate than device D2. In contrast, device D2 demonstrate a higher desorption rate than device D1. However, the adsorption and desorption constant rates of  $\text{NO}_2$  is low on the pristine graphene, and this could be attributed to the low availability of the adsorption sites [254]. Using Equation 5.3 allows determining the  $K_a$  and  $K_d$  constant rates for both devices in this work. It could be used with functionalised graphene to study the effect of increasing the adsorption sites on graphene sensitivity.

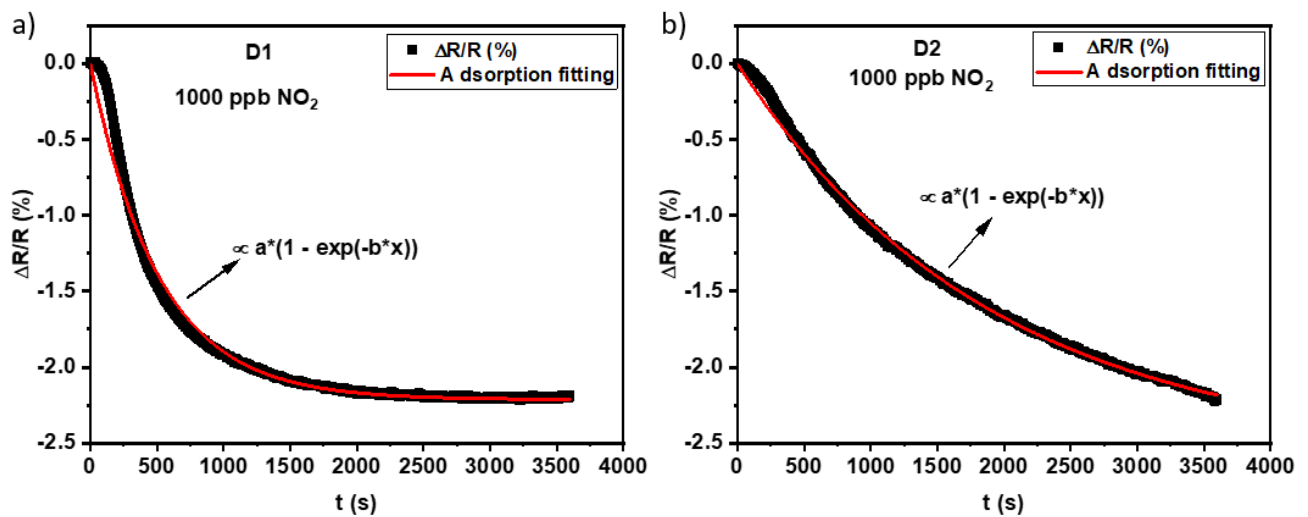


Figure 5.8: a and b) Show the rate fitting curves for the exposure curves for 1000 ppb of  $\text{NO}_2$ .

## 5.2.2 $\text{NO}_2$ Repeatability Measurement

The devices are tested under a repeatable cycle with the same gas concentration to study the reliability of the device. Figures 5.9: a) and b) represent the three cycles response of the sensors for 1000 ppb of  $\text{NO}_2$  gas from the pristine graphene. All the sensors' responses presented in this work were tested at different times for the repeatability and reproducibility of the devices. The sensors were tested for three cycles of response and recovery. The sensors were left under vacuum overnight prior to the cycle test to remove all the gas adsorbed on the sensor surface prior to testing. After that, the test cycles started with a 600s flow of  $\text{N}_2$  followed by 180s of 1000 ppb of  $\text{NO}_2$  and repeated three times. From Figure 5.7, the 180s were chosen based on the saturation measurement, as the sensor response changed 50% of

their final response. The sensitivity of the devices degraded with repeated exposure to  $\text{NO}_2$ . This is due to the repeated gas exposure causing the device to reach saturation, which is a well-known issue for graphene gas sensors [60]. It was also found that the recovery of the devices was very slow under a flow of  $\text{N}_2$  at room temperature. Therefore, as the sensors have to sense events many times, it suggests the need for shorter sensing events, which then will resolve the issue of the sensors reaching saturation. Figures 5.9: c) and d) represent the resistance response as a function of sequence, which is extracted from the data plotted in Figures 5.9: a) and b). As can be seen from the sequence response to 1000 ppb of  $\text{NO}_2$ , the sensors are able to respond multiple times. The change in resistance response was extracted for both sensors was found to be about 0.008 for D1 and 0.00175 for D2, both of which are below the saturation point as obtained earlier in the saturation test; the maximum change of resistance response was 0.022 and 0.024 for sensors D1 and D2, respectively. For the recovery to be achieved the devices were left under a high vacuum overnight to investigate the recovery and the resistance of the devices returned to 95% of the initial resistance.

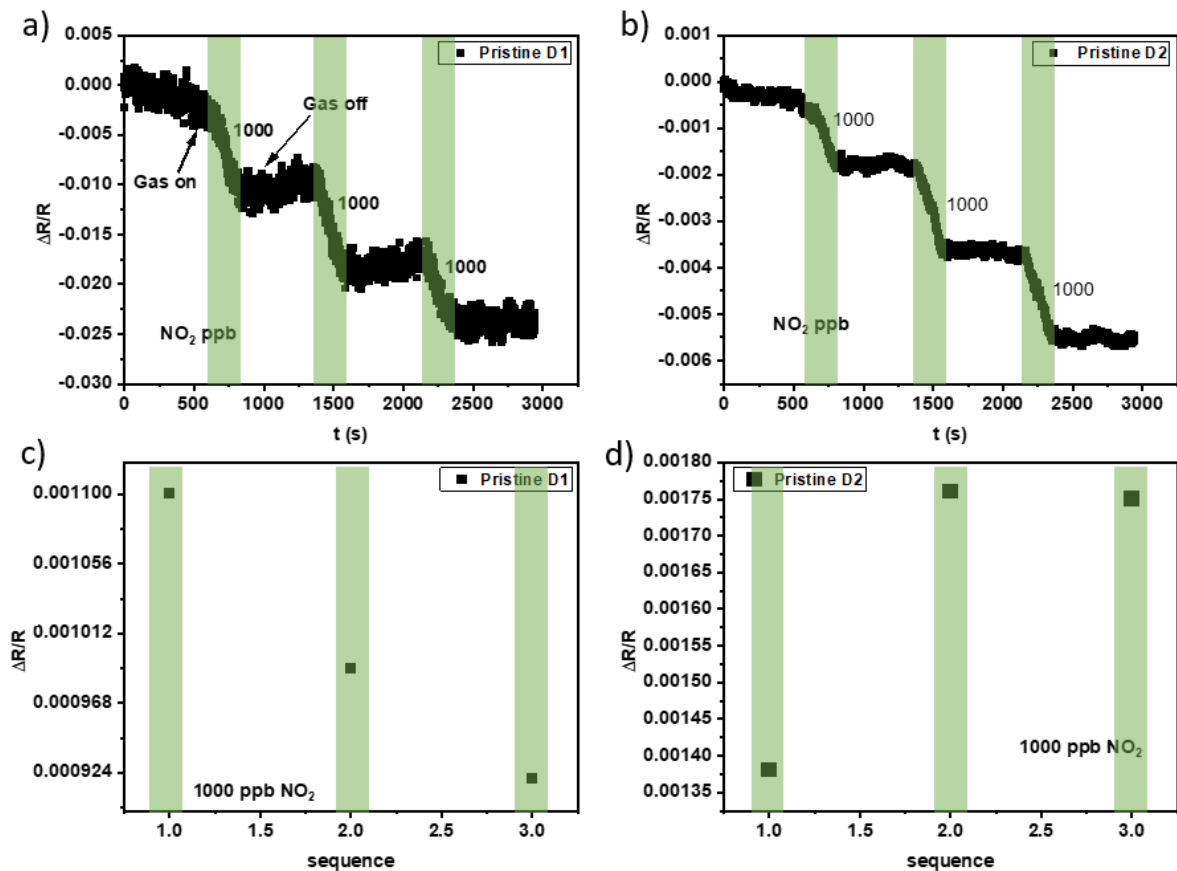


Figure 5.9: a and b) Show the repeatability of the devices for 1000 ppb of  $\text{NO}_2$  gas exposure on three cycles of 180s each at room temperature. During recovery,  $\text{N}_2$  was purged into the system. c and d) demonstrate the change in resistance response for devices D1 and D2 as a function of the sequence, obtained from Figures a and b.

### 5.2.3 NO<sub>2</sub> Cycles Measurement

Within this section, gas sensors' sensitivity response for short-time events, recovery, and limit of detection (LOD) for NO<sub>2</sub> are explored. The response time for the sensors should be as short as possible for low gas concentrations, as some gases cause an impact on health or the environment after only short exposure times. Many researchers have reported pristine graphene sensor values for the fast response, sensitivity cycles, and LOD for the pristine graphene devices upon exposure to NO<sub>2</sub>. In 2007, Schedin et al. fabricated a sensor using micromechanical cleavage of graphite for detecting NO<sub>2</sub> gas molecules at 2000 ppb with a response time of 5 minutes [77]. F. Yavari et al. successfully detected NO<sub>2</sub> at 100 ppb with a response time of 20 minutes at room temperature [79]. However, an improvement needed for the graphene sensors is rapid response to sub-ppb gas concentrations. In this work, the sensitivity of CVD graphene-based gas-sensor devices for fast response and LOD has been enhanced by obtaining high-quality CVD graphene with low residues, wrinkles, and folds.

To study the behaviour of the pristine devices under changing gas, the devices were exposed to 5 different concentrations of 200, 400, 600, 800, and 1000 ppb of NO<sub>2</sub>. The measurements were performed in the home-made gas chamber on 5 cycles for each cycle, and N<sub>2</sub> was introduced for 10 minutes before and after each NO<sub>2</sub> exposure. The exposure for NO<sub>2</sub> started from 200 ppb of concentration for 3 minutes and then increased in increments of 200 ppb as the cycles continued until the NO<sub>2</sub> concentration reached 1000 ppb. During these measurements, the sensing chamber pressure was maintained at 799.9 mbar by the pressure modulator. The potential  $V_{ds}$  was maintained at 10 mV across the graphene channel, while the change in resistance was measured.

The device was left under a high vacuum overnight, with pressure below  $1 \times 10^{-6}$  mbar, before the test was performed, to remove molecules adsorbed on the graphene surface [25]. Figures 5.10: a) and b) shows the response and recovery of the graphene devices for different concentrations of NO<sub>2</sub> at room temperature. The response of the sensors was increased with concentrations of NO<sub>2</sub>. As the graphene presented in this work is p-doped, NO<sub>2</sub> adsorption will cause a decrease in resistance as it withdraws an electron from the graphene [255]. As can be seen in Figures 5.10: a) and b), the resistance of the device decreases with increasing NO<sub>2</sub> concentration. This increase in the sensor response with concentration is attributed to

more gas molecules being adsorbed on the graphene surface, resulting in an increase in the charge transfer between gas molecules and the graphene surface [73, 255].

The recovery for the devices was very low and did not reach 1% of their baseline resistance, which is an issue for these devices. Nevertheless, even though the full recovery was not achievable, all sensors' resistance was able to change with subsequent NO<sub>2</sub> exposures. In addition, from the resistance measurements, the response upon different concentrations and the LOD was determined for the devices.

Figure 5.11. represents the response percentage of two different graphene devices to 200 – 1000 ppb NO<sub>2</sub> measured at room temperature, with black and red lines assigned to devices 1 and 2, respectively. The response increases linearly with NO<sub>2</sub> concentrations. The response percentage to NO<sub>2</sub> per ppb ranges between 0.00018 and 0.0125% for all tested devices, as presented in Table 5.2, which is consistent with the published pristine graphene response percentage results (0.00009 - 0.04 %), as shown in Table 2.1 [69, 77-80]. Figure 5.12 demonstrates the response of the pristine graphene devices presented in this work, compared to the response obtained from the literature. Also, for the comparison with the literature, all the devices' responses were calculated by taking the percentage change in the response under NO<sub>2</sub> exposure for 1min and compared with the percentage change for devices in literature with the same duration of time. The recovery of our devices was found to be about 1% for the devices at room temperature, whilst the published recovery was 70% for NO<sub>2</sub> [69, 80]. The detection limit for devices D1 and D2 was calculated and found to be 192 and 88 ppb, respectively.

Table 5.2. presents the LOD for all the devices tested within this work, with the lowest achieved LOD at 40 ppb. Devices D1, D2 and D5 were transferred using NC as a supporting layer, resulting in low residues. While D3, D4, and D6 were transferred using PMMA as a supporting layer, resulting in some contamination left on graphene and causing doping. In addition, all the devices were measured in our lab except D3, D4, and D6. Which were measured in the Universität Der Bundeswehr, München, by Dr. Kanogho Lee. As the devices did not reach saturation, the LOD was estimated using the sensing cycles. This can be compared to the literature [69, 256, 257], as the devices can operate in short-sensing events many times before saturation is reached. Compared to the low detection limit presented in Table 2.1, our devices show detection limits to NO<sub>2</sub>, close to the LOD of previously published results [69, 80]. Devices presented within this work have the ability to show responses in short sensing events (3 min) for up to 35 cycles before the response is degraded

as the sensors approach saturation. The estimation of the sensing ability was based on the change in response resistance from the saturation sensing compared to the change in response resistance from cycles sensing events with different gas concentrations.

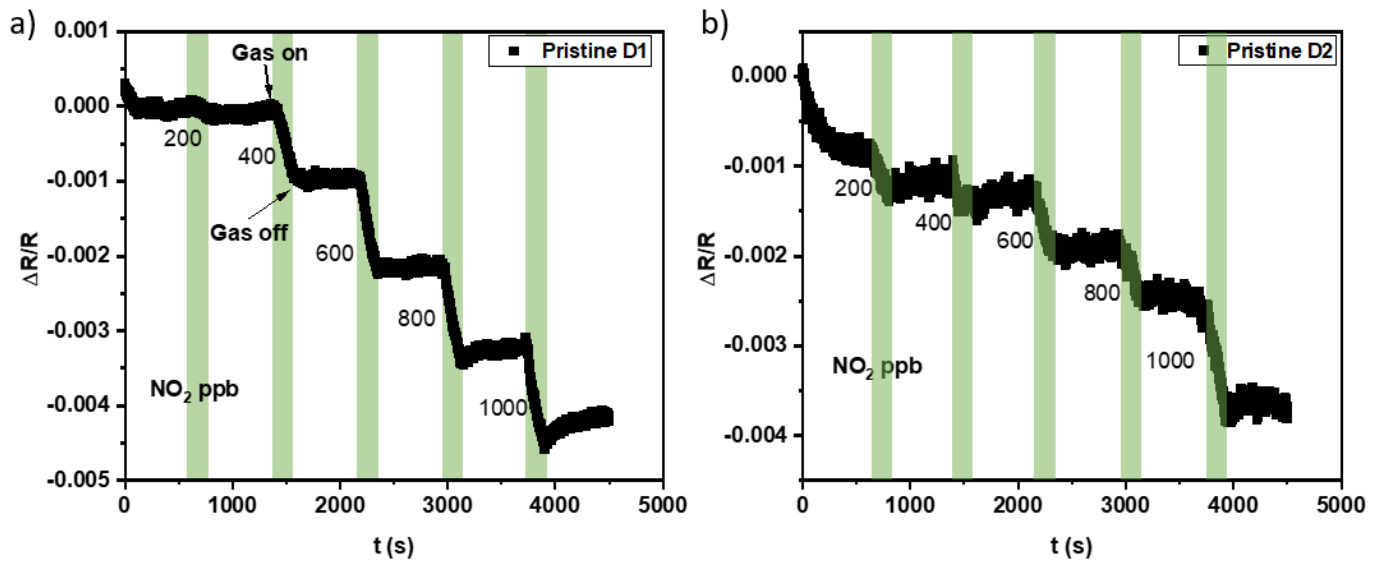


Figure 5.10: a and b) Show the sensor's response for five steps measurements under different concentrations of  $\text{NO}_2$  at room temperature. The change in resistance increase with  $\text{NO}_2$  concentration. The columns represent the time of exposure to  $\text{NO}_2$ .

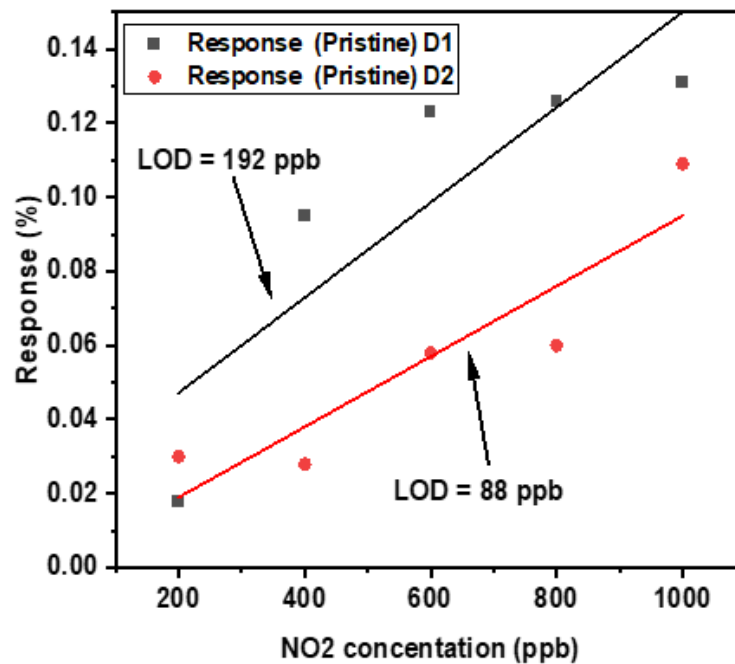


Figure 5.11: Shows the response percentage for the two devices during exposure to different  $\text{NO}_2$  concentrations. The black and red lines are related to devices 1 and 2, respectively.

Table 5.2: Represent the LOD and the response percentage for NO<sub>2</sub> for all measured devices.

Device	LOD (ppb)	Response to NO <sub>2</sub> (%)
D1	192	0.0022
D2	88	0.0024
D3	41	0.0028
D4	40	0.0028
D5	200	0.0125
D6	57	0.00018

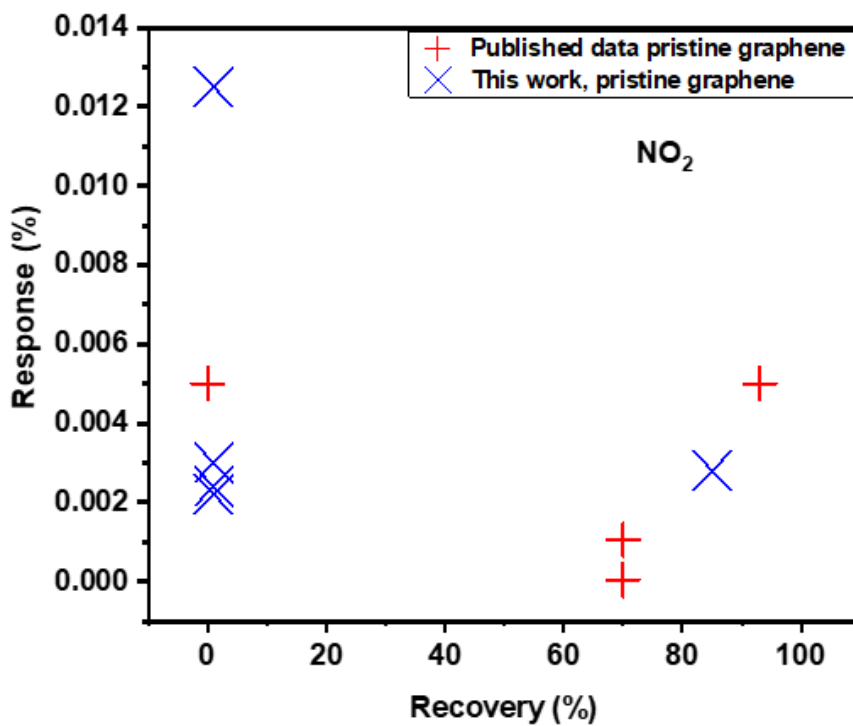


Figure 5.12: Represents the response percentage versus the recovery percentage for NO<sub>2</sub> for the pristine graphene devices presented within this work by a blue cross, compared to the pristine devices in the literature as presented by a red cross.

#### 5.2.4 Repeated Device Test after 9 Months

The device was tested after 9 months to investigate the recovery issue, as the devices presented within this project show slow recovery compared to other reported graphene sensors [78-80]. In contrast, the LOD for these devices is obtained from short detection time events (3 min) and presents LOD consistent with the best-achieved value in the literature [78-80]. As discussed in section 5.2.3, the devices were vacuum-conditioned overnight before the sensing test was performed to remove all the adsorbed molecules on the graphene surface from the surrounding environment. However, in the literature, the sensors tested without using pre-test vacuum conditions displayed improved sensor recovery. This may be due to molecules which remain adsorbed to the surface, that might change the surface energetics for the adsorption of the gases molecules and enhance the gas molecule desorption. A recent report shows that the contaminant molecules from the ambient air form a self-assembled layer on the clean graphene surface [258]. The contamination type on the graphene surface, was identified as hydrocarbons, in the form of alkanes.

In this section, the device was tested again without performing the vacuum pre-condition to see if there was any improvement in recovery. The device was stored for 9 months in ambient condition before the test. The measurements were performed similarly, as discussed in section 5.2.3. Figure 5.13 represents the resistance change for the device after preparation using vacuum conditioning before the test and after 9 months without vacuum conditioning upon exposure to different NO<sub>2</sub> concentrations. The device shows similar sensing behaviour during gas exposure steps for both tests. However, the sensitivity was found to have degraded slightly after 9 months. However, the recovery was significantly enhanced, compared to the initial measurement after the device was prepared. The aged device showed a recovery of almost 100%, while the recovery of the device after the initial test was only 1%. The enhancement in recovery could be attributed to this recently reported hydrocarbon adlayer contamination from the ambient [259, 260], which may strongly influence the desorption of the adsorbed gas. In contrast, vacuum conditioning the device removes all the contamination on the graphene surface from the ambient air, which leads to the reduced recovery behaviour. Figure 5.14 demonstrates the response of the sensors upon exposure to different NO<sub>2</sub> concentrations. The response after 9 months decreased by 80% of the original response. The reduction in sensitivity after 9 months could be attributed to the adsorbed hydrocarbon layer from the surrounding environment [64].

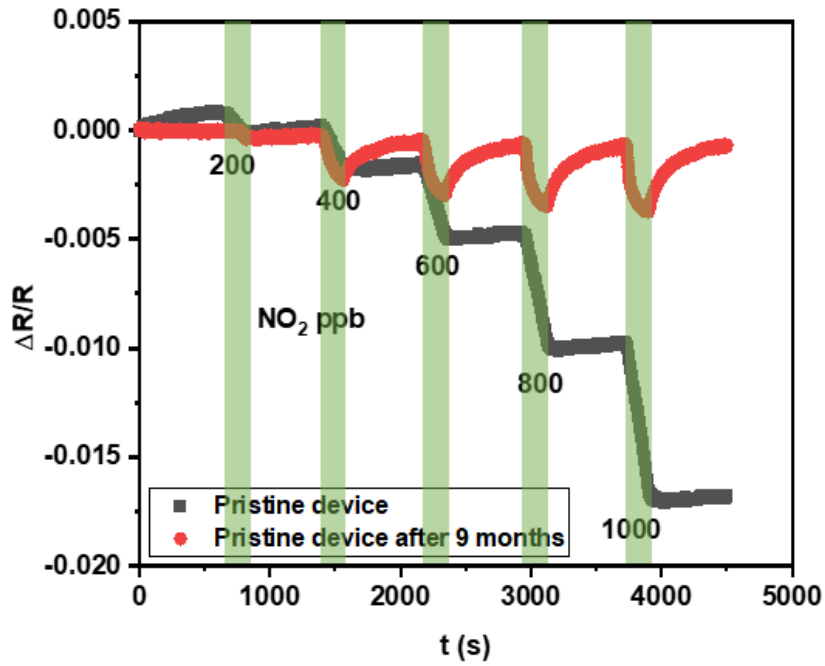


Figure 5.13: Shows both resistance response for the device after prepared and after 9 months which are presented by black and red curves, respectively. The change in resistance increase with NO<sub>2</sub> concentration. The columns represent the time of exposure to NO<sub>2</sub>.

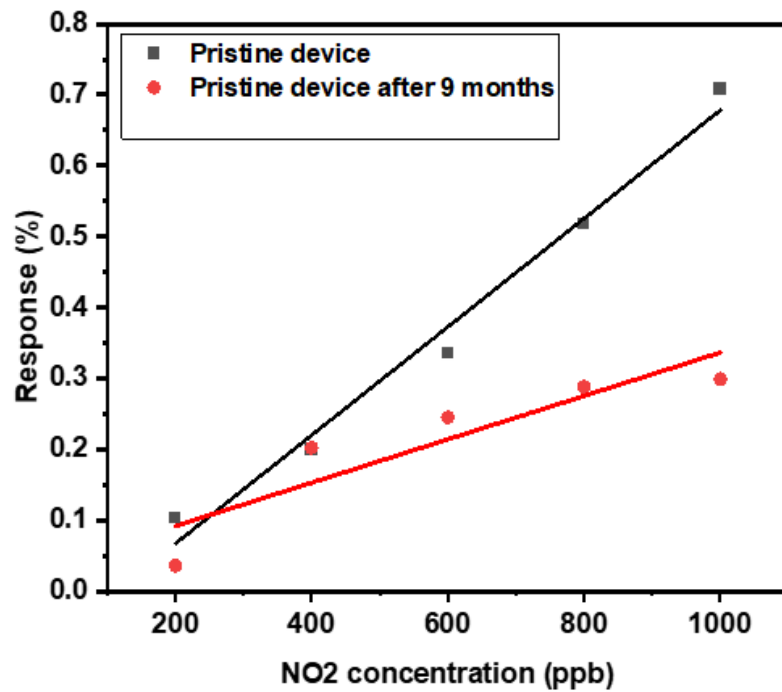


Figure 5.14: Shows the response percentage for the device before and after 9 months upon exposure to different NO<sub>2</sub> concentrations. The black and red lines are related to device measurements as prepared and after 9 months, respectively.

### 5.3 NH<sub>3</sub> Sensor Characteristics

As discussed in section 5.2, the pristine graphene device show ability to detect NO<sub>2</sub> gas. Here we are going to study the graphene device sensitivity to NH<sub>3</sub> gas. The graphene device is initially p-doped which means that the adsorbed reducing gas (NH<sub>3</sub>) will increase resistance [64, 67]. Adsorbed NH<sub>3</sub> gas molecules on the graphene surface result in electron charge transfers from NH<sub>3</sub> to graphene. This leads to an increase in the electron concentration [73], which then leads to the depletion of the hole charge carriers, creating a reduction in charge carrier density as the material is within a p-type regime, and results in an increase in resistance.

#### 5.3.1 NH<sub>3</sub> Saturation Measurement

The saturation measurement has been done to evaluate the adsorption rate for the graphene devices and to calculate the resistance response percentage. The devices were tested at room temperature under the flow of 10 ppm of NH<sub>3</sub> gas while recording the resistance for 1 h. After that, the N<sub>2</sub> was introduced for 2 h while the resistance was measured to study the recovery behaviour. Figures 5.15: a) and b) represent the response for the graphene devices D1 and D2 upon exposure to 10 ppm of NH<sub>3</sub>. The resistance of the devices decreases upon exposure to 10 ppm of NH<sub>3</sub> gas. In addition, the rate of resistance decreased during the exposure with time and did not reach saturation. The response for D1 and D2 per ppb are 0.000017% and 0.00019%, respectively. As explained, NH<sub>3</sub> is an electron donor, and it should result in an increase in resistance to the graphene device [64, 67, 73, 92]. However, these devices' characteristics show the opposite; instead of their resistance increasing, it decreased. This behaviour is not expected, as the graphene is p-doped initially.

During the recovery process, device D1 showed a recovery of 65% under the N<sub>2</sub> flow, and D2 recovery was hard to estimate as the resistance kept increasing under the N<sub>2</sub> flow. However, All the devices recovered to 95% of the original resistance after high vacuum conditions overnight. Even the devices that showed an increment in resistance returned to the baseline after high-vacuumed conditioning.

From this test, the conclusion is that gas may be contaminated with other gas types.

Therefore, mass spectrometry was employed in the following section to evaluate and confirm whether the test gas was contaminated.

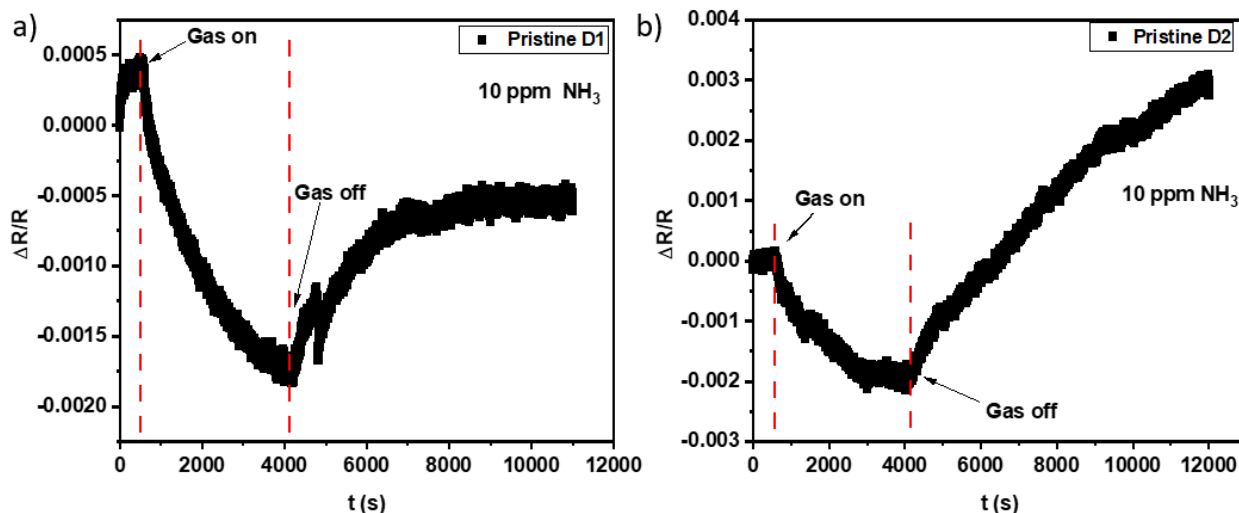


Figure 5.15: a and b) Response of graphene device D1 and D2 for 10 ppm of  $\text{NH}_3$  gas, respectively. The measurement is done at room temperature with a flow of  $\text{N}_2$  during the recovery process.

### 5.3.2 Mass Spectrometry

Mass spectrometry (MS) was carried out to investigate whether the ammonia ( $\text{NH}_3$ ) was truly ammonia or not. The testing was carried out because the sensitivity test, discussed in the previous section 5.3.1, shows the opposite response behaviour to that expected for ammonia [77, 80]. MS has the advantage of revealing the mass-to-charge ratio ( $m/z$ ) for each molecule within the sample, and displays different mass spectrum peaks corresponding to specific components of the sample. In our sample, the peaks of interest are found to correspond to nitrogen ( $\text{N}_2$ ), ammonia ( $\text{NH}_3$ ), and methanol ( $\text{CH}_3\text{OH}$ ) at 28 ( $m/z$ ), 32 ( $m/z$ ), and 39.6 ( $m/z$ ), respectively, as demonstrated in Figure 5.16. Furthermore, the amount of each component within the sample can be determined by the intensity (relative abundance) of the peaks.

Our MS analysis shows that there are no peaks of  $m/z$  that would be expected from a sample containing  $\text{NH}_3$  (17.6, 19.4, 33.6, and 39.600), presented in Figure 5.16 [261, 262], but rather, that the gas mixture was  $\text{N}_2$  and  $\text{CH}_3\text{OH}$ . The percentage of the  $\text{N}_2$  and  $\text{CH}_3\text{OH}$  was calculated from the relative abundance of  $m/z$  peaks and found to be 86% and 8.7%, respectively. This is computable with sensitivity results as methanol has a hydroxyl oxygen group (OH), which interacts with the p-type doped graphene gas sensors, as an electron withdrawing species, thereby causing a decrease in resistance response [263]. From this test, we can confirm that the tested gas was not ammonia; it was methanol.

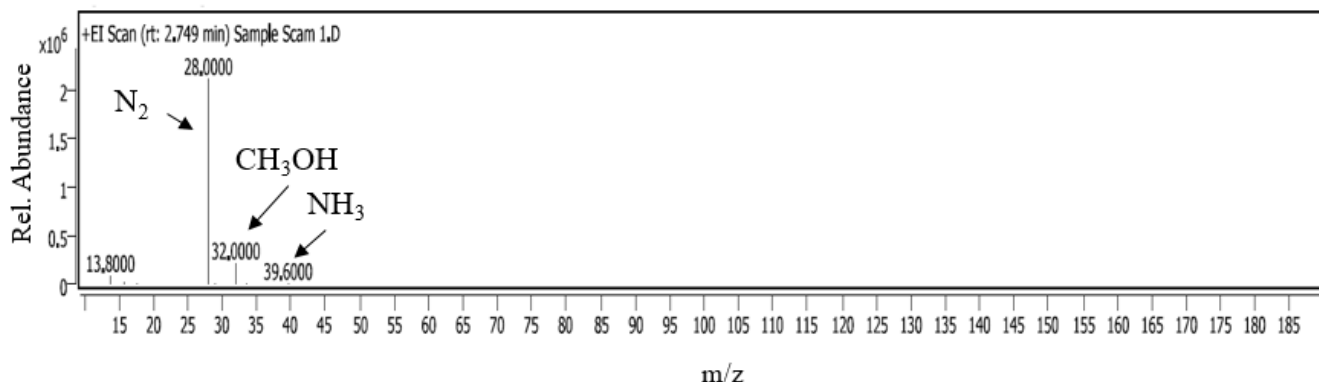


Figure 5.16: Shows the mass spectrum result of nitrogen ( $N_2$ ), methanol ( $CH_3OH$ ), and ammonia ( $NH_3$ ) gases.

#### 5.4 GFET Sensing and Field Effect Gating

Within this section, graphene devices have been fabricated based on the GFETs and sent to the Universität Der Bundeswehr, München to be tested for sensitivity for comparison with the results obtained in section 5.2.3. All devices have been characterised using Raman spectroscopy, XPS, and electric measurements, as discussed in section 5.1. Raman measurements show that all the pristine graphene devices have low point defects, as the D peak is below the noise level. The XPS test shows the presence of oxygen groups, which could be related to water trapped between the graphene film and the substrate, residue from the transferring process, and the substrate. In addition, transfer curve measurements show that the Dirac point is located at a positive voltage, indicating that graphene is p-doped. When compared with published results for GFET mobility which ranges from  $10.15$  to  $3000 \text{ cm}^2/V.s$ , [58, 92] our device mobility is found to be close to the highest published mobility as presented in Table 5.1. Also, they reported the measurement by varying the gate voltage bias; they were able to tune the GFET sensitivity.

In this work, two types of measurements have been performed to investigate the GFETs' sensitivity. First, the devices were tested under gas exposure while monitoring the change in resistance before and after gas exposure. The second test is a gate sweep measurement while recording the Dirac point shift upon exposure to the gases.

### 5.4.1 NO<sub>2</sub> Cycles Measurement

The device sensing tests were performed at the Universität Der Bundeswehr, München, by Dr. Kanogho Lee. N<sub>2</sub> was continuously flowed at 100 sccm in the chamber during the sensing test while chamber pressure was maintained at 0.9 mbar. The potential was fixed at  $V_{ds} = 5\text{mV}$  while recording the resistance. NO<sub>2</sub> was introduced into the chamber in cycles of 5 minutes on and 5 minutes off. The cycle started by introducing a concentration of 800 ppb and then reduced by 100 for each following cycle. In addition, devices were vacuum annealed at 100 °C for 1 h at a pressure of  $9 \times 10^{-6}$  mbar before loading into the chamber, which assists with the removal of ambient adsorbates [25, 264, 265].

As discussed in section 5.1.3, our graphene devices are initially p-doped, and should show a decrease in the channel resistance upon NO<sub>2</sub> adsorption [73]. Figures 5.17: a) and b) demonstrate a plot of devices D3 and D4 response upon exposure to different concentrations of NO<sub>2</sub>. The resistance response changed with NO<sub>2</sub> concentration, and the highest response was achieved at an exposure of 800 ppb with a relative resistance decrease of 0.014. Both devices display the same response behaviour. However, the resistance during the recovery keeps increasing even after reaching the baseline resistance. Figure 5.18 represents the response percentage and the detection limit of devices D3 and D4. The response increases linearly with NO<sub>2</sub> concentration. The limit of detection is 41 and 40 ppb for D3 and D4, respectively. The response for both devices was 2.3% at 800 ppb of NO<sub>2</sub> exposure, as presented in Figure 5.18.

The device's response per ppb discussed in this section exhibits the same response for the devices presented in sections 5.2.3 and 5.2.4, which is reported in Table 5.2. The response for all devices ranges between 0.0125 and 0.00018%. Devices D3 and D4 show recovery of about 95%, while devices D1 and D2 did not show recovery during the measurements.

However, when tested at Munchen, the devices presented in this section showed no sensitivity to NH<sub>3</sub> upon exposure to different concentrations ranging from 1 to 10 ppm. Additionally, the devices discussed in section 5.3.1 show the opposite response behaviour to NH<sub>3</sub> as that described within the literature [64, 67, 73, 92]. As mentioned above, this is believed to be because the NH<sub>3</sub> gas at Newcastle contained other gaseous species. This was investigated using mass spectrometry, and it was found that the tested gas was not NH<sub>3</sub>.

The devices discussed within this section show higher response than the aged device, which is discussed in section 5.2.4. Nevertheless, the recovery for the aged device was higher than for devices D3 and D4. In addition, the devices presented in this section show the lowest detection limits compared to those presented in the previous section (5.2.3).

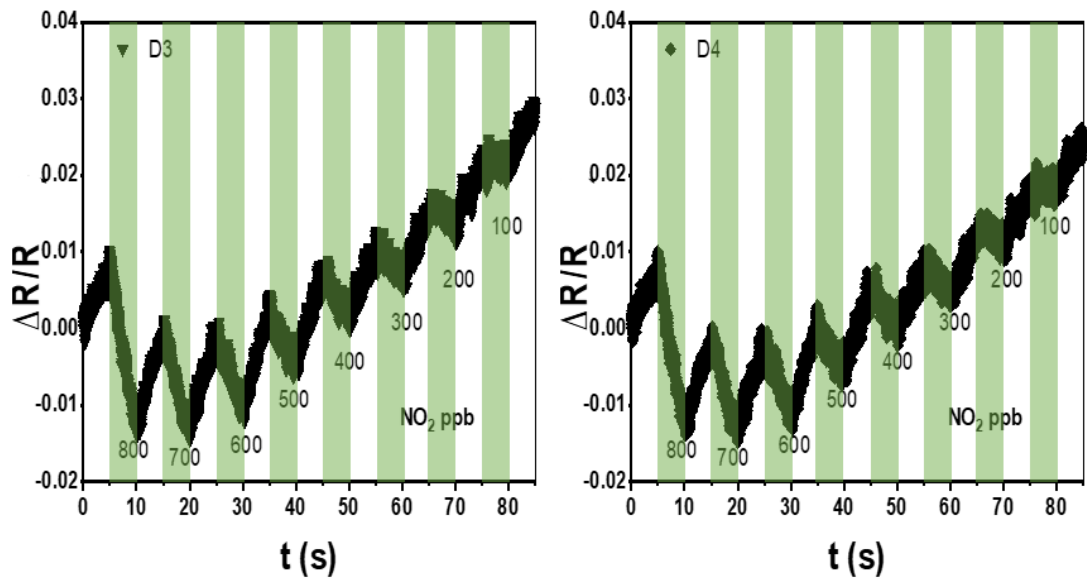


Figure 5.17: Shows both resistance response for the devices D3 and D4 which are presented by black and red curves, respectively. The change in resistance increase with  $\text{NO}_2$  concentration. The columns represent the time of exposure to  $\text{NO}_2$ .

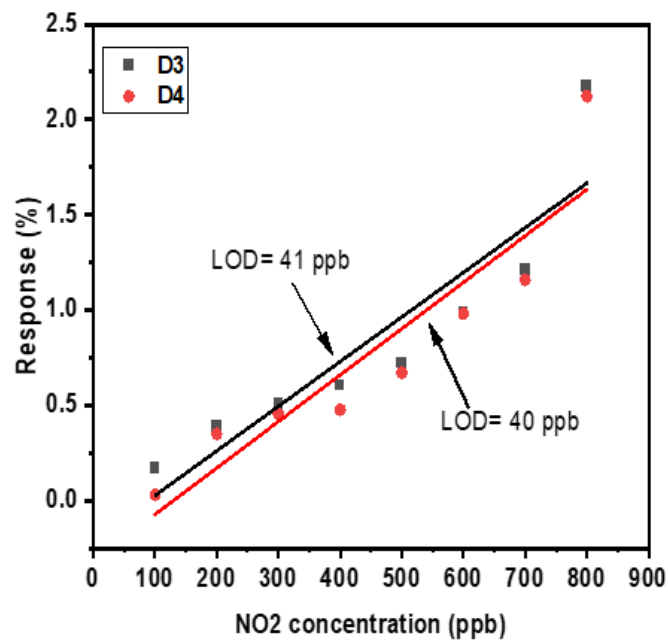


Figure 5.18: shows the response percentage for the device D3 and D4 upon exposure to different  $\text{NO}_2$  concentrations. The black and red lines are related to device measurements of D3 and D4, respectively.

### 5.4.2 Gating Sensitivity Test

Having successfully demonstrated that the resistance of GFET is sensitive to  $\text{NO}_2$  and  $\text{NH}_3$  exposure, the sensing characteristics of pristine graphene by Dirac point shifts are investigated upon gas exposure. Studying the change in graphene FET's electrical properties upon the gas's adsorption is usually done by characterising the change in the electric resistance of the graphene. Here we will show that the change of the charge carrier density and the field effect mobility of graphene can be used to reveal the type of gas adsorbed on graphene [149, 266]. For example, the  $\text{NO}_2$  molecule adsorbed on the GFET can act as a dopant by withdrawing partial electron charge per molecule [73], and thus decrease the graphene resistance by increasing the hole carrier concentration. Meanwhile, the negatively charged  $\text{NO}_2$  molecule, after withdrawing  $\sim 0.1e$  from graphene, can behave as a spatially charged impurity sitting on the surface of pristine graphene, which will act as a scattering centre for charge carriers and modify the mobility of GFET [149]. These two affect the graphene's electrical resistance and give information about the physiochemical effect of gas differentiation [266].

The mobility of the GFET at room temperature is limited by the charged impurities, which act as scattering centres for the charge carriers through the Coulomb effect. When gas species are adsorbed on the graphene surface, they become such charged centres, altering the sensor channel mobility. This effect can be used to differentiate between different gas molecule types [266].

There are two significant behaviours after a gas molecule adsorbes on the graphene surface and becomes charged impurity on graphene. The first one is the Coulomb scattering ; long-range scattering resulting from graphene's low carrier density. At the same time, the second one is the short-range scattering, which results from the graphene's high carrier density. Therefore, the number of carriers in the graphene affects the charge impurity behaviour.

In this work, we will show the ability of the GFET to distinguish between  $\text{NO}_2$  and  $\text{NH}_3$  gases by measuring the change in carrier density of graphene, which is relative to the shift in the Dirac point voltage upon gas exposure and the mobility of the GFET which is related to conductance as explained in section 4.2.1. All the GFET measurements were carried out at room temperature.

The sensing characteristics of pristine graphene by Dirac point shifts are investigated for device D3 and D4. The sensing measurement were performed by Dr. Kangho Lee at the Universität Der Bundeswehr München. During the measurement the device was annealed at 100 C for 1 h in high vacuum down to  $2.6 \times 10^{-5}$  mbar and then tested in the vacuum ( $\sim 800$  mbar) by sweeping the gate from -80V to +80V at  $V_{ds} = 2$  mV. The sensing cycle starts from measuring the conductance versus gate voltage before and after each exposure of the gases concentrations. The device was exposed for 30 minutes to the each gas concentration before sweeping the gate voltage. From the plotting of the conductance versus the gate voltage, Dirac point shift was taken to calculate the mobility and the carrier density. Each device was exposed to NO<sub>2</sub> with concentration range from 0.1 to 1 ppm, followed by testing under exposure to NH<sub>3</sub> with concentration range from 0.5 to 10 ppm.

These results demonstrate the pristine CVD graphene sensors' sensitivity toward NO<sub>2</sub> and NH<sub>3</sub> gas. Figures 5.19 a) and b) display the change in conductance versus gate voltage of GFETs measurements upon the exposure of different concentrations of NO<sub>2</sub> and NH<sub>3</sub>, respectively. The solid black curve is related to the normal state of the device (before exposure to the gas), and the dashed lines are related to the doped states after exposure to the gas. NO<sub>2</sub> is known to be electron acceptor which will take an electron from the graphene, leading to increase the hole density and therefore the Dirac point shifts toward positive voltage as  $\Delta V_{g,Dirac}(t)/\Delta t > 0$  as shown in Figure 5.19.a. The Dirac point shifts to more positive as the concentration of the NO<sub>2</sub> increases from 0.10 ppm to 1 ppm. On the other hand, NH<sub>3</sub> is electron donor which will donate electron to the graphene leading to increase of the electron density and that result on the Dirac point shifts toward negative voltage as  $\Delta V_{g,Dirac}(t)/\Delta t < 0$  as in Figure 5.19.b) as the concentration of NH<sub>3</sub> increases from 1 ppm to 10 ppm, the Dirac point shifts to more negative voltage.

Figure 5.19 c) represents the change in the carrier charge density upon exposure to a different concentration of NO<sub>2</sub>. The carrier charge density increases linearly for the smaller concentration of NO<sub>2</sub>. This is attributed to the number of available sites for adsorption on graphene. As the concentration of NO<sub>2</sub> increases, the linearity disappears. The graphene is initially p-doped, and the adsorption of NO<sub>2</sub> will increase the hole density in the graphene as the concentration of NO<sub>2</sub> increases leading to more hole creation in graphene. This then leads to increasing the surface coverage of the sensor toward the saturation with increasing concentration of NO<sub>2</sub>. Figure 5.19 d) shows the change in the carrier density with exposure to different concentrations of NH<sub>3</sub>. The adsorption of NH<sub>3</sub> on the graphene increases the

electron density, which depletes the hole density. Therefore, the overall charge carrier density decreases as more electrons are donated to graphene by  $\text{NH}_3$ . The change in charge carrier density with increasing  $\text{NH}_3$  follows the opposite behaviour described for  $\text{NO}_2$ . The charge carrier density is estimated using Eq.(4.1). In this work,  $V_g$  Dirac was calculated from the electric measurements for each gas concentration.

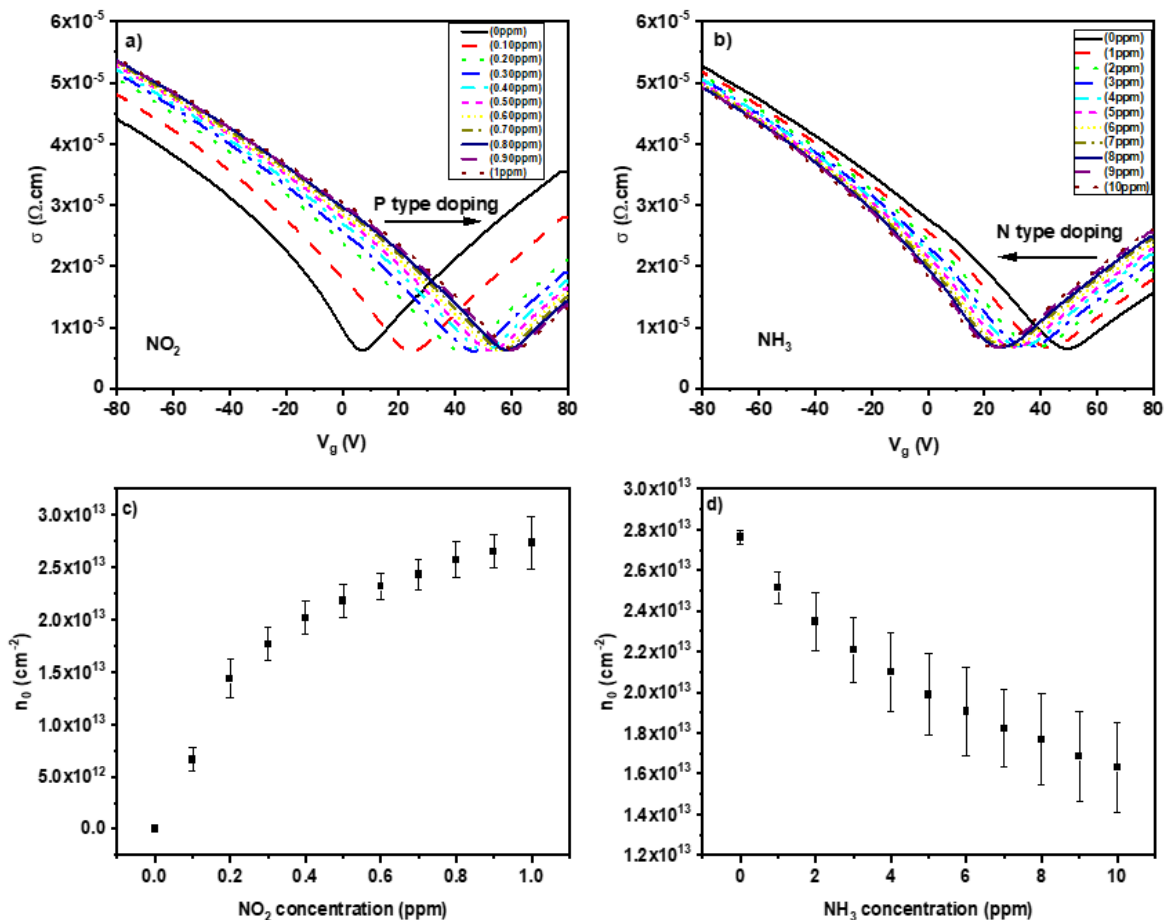


Figure 5.19: a and b) Demonstrate the conductance vs gate voltage under different concentration of  $\text{NO}_2$  and  $\text{NH}_3$ , respectively. c) the carrier charge density increase with  $\text{NO}_2$  adsorption, and d) the carrier charge density decrease with  $\text{NH}_3$  adsorption.

Figures 5.20 a) and b) represent the calculated Dirac point shift upon exposure to different concentrations of  $\text{NO}_2$  and  $\text{NH}_3$ , respectively. As can be seen, the shift in Dirac point was observed to be increased toward high positive voltage with  $\text{NO}_2$  concentration. While for  $\text{NH}_3$ , the Dirac point shift is observed to increase with  $\text{NH}_3$  concentration toward negative voltage. Figure 5.20 c) shows the resistance response for the devices decreased with exposure to  $\text{NO}_2$  until a concentration of 0.5 ppm, and then the change was very slow due to the device reaching saturation. The devices are initially p-doped, meaning if the oxidising gas ( $\text{NO}_2$ ) is

adsorbed on the graphene surface, electrons will transfer to  $\text{NO}_2$ , increasing hole concentration density. Which then results in a decrease in the graphene resistance [58, 80, 267]. However, the adsorption of reducing gas ( $\text{NH}_3$ ) leads to electron transfer to graphene, which increases the electron concentration on graphene and reduces holes [58, 92, 267]. Therefore, this results in a resistance increase, as demonstrated in Figure 5.20.d.

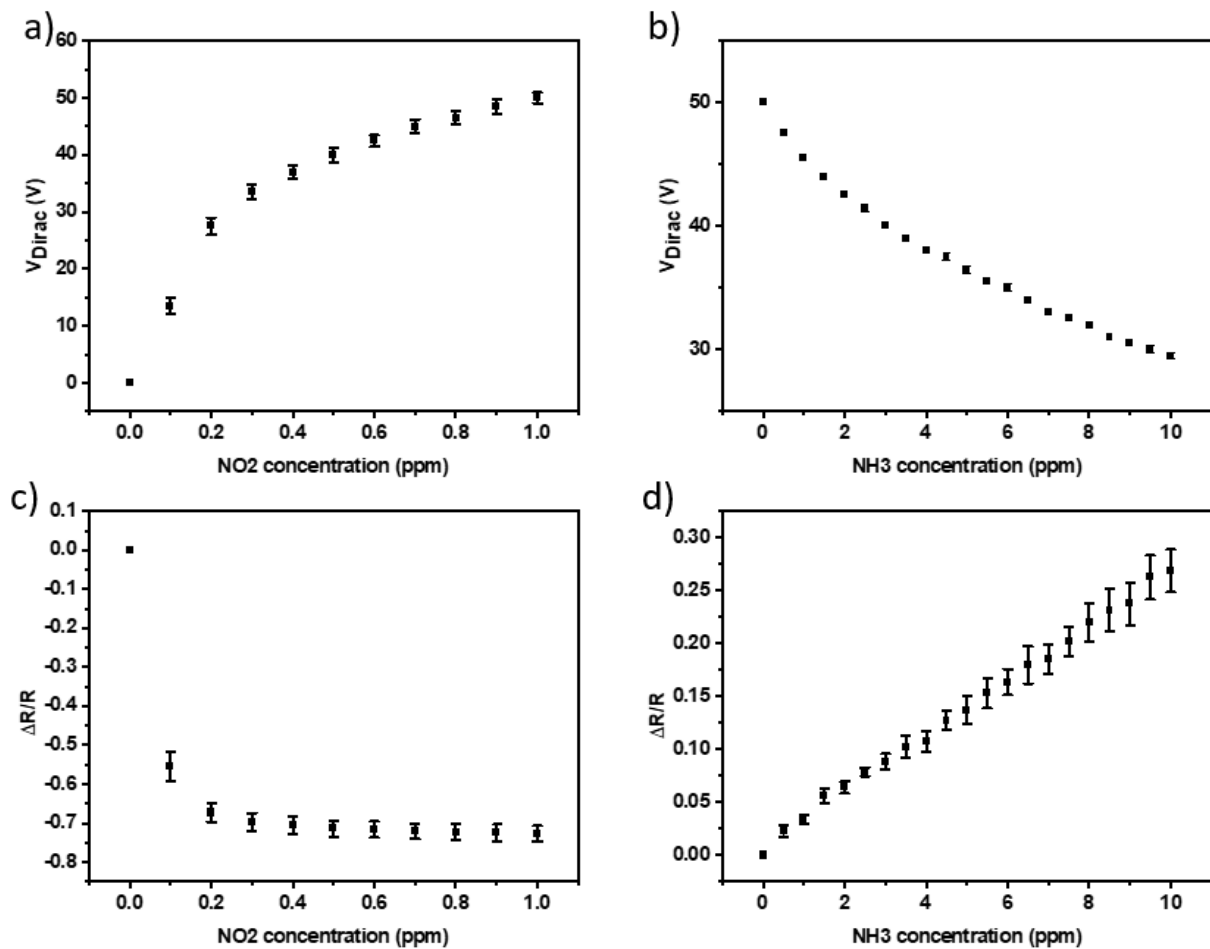


Figure 5.20: a and b) Demonstrate the Dirac point shift vs gas concentration of  $\text{NO}_2$  and  $\text{NH}_3$ , respectively. a and c) the resistance response upon  $\text{NO}_2$  and  $\text{NH}_3$  adsorption, respectively.

From the electric measurement we can calculate the long range scattering limited mobility from the field effect mobility  $\mu_{e/h,c} = \mu_{e/h}(V_g)$  where  $V_g$  is chosen to be at the Dirac point and from this we can drive the range of the scattering mobility for hole and electron [266]. The scattering regime for the scattering potential goes to the short regime when the applied gate voltage is away from the Dirac point. Also, the maximum change in carrier density after the Dirac point shifted in the two cases upon exposure to 1 ppm of  $\text{NO}_2$  and 10 ppm of  $\text{NH}_3$  can be computed as  $2.74 \times 10^{13}$  and  $1.63 \times 10^{13} \text{ cm}^{-2}$ , respectively

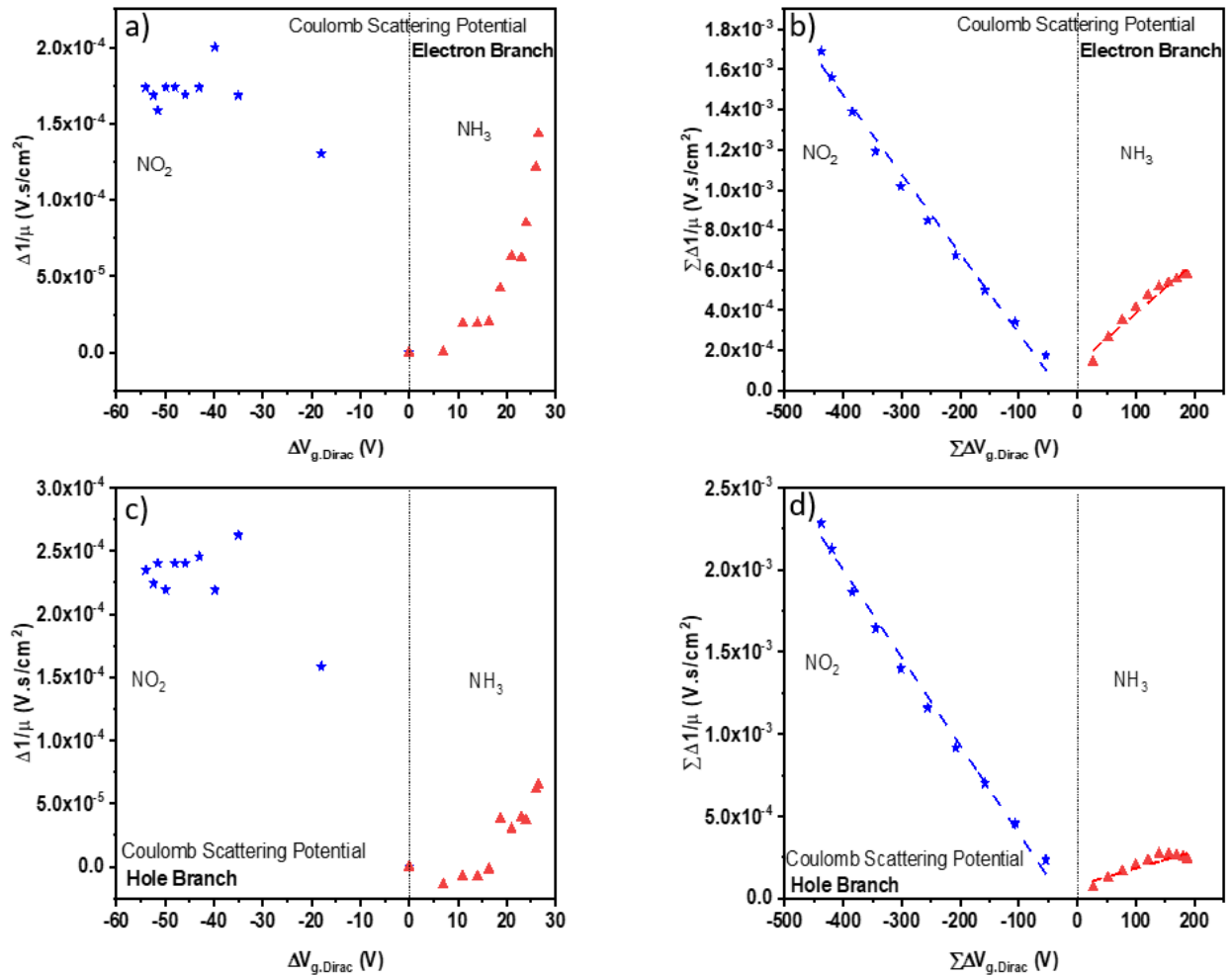


Figure 5.21: a and c) Represent the linear factor calculated from inverse of mobility versus gate voltage. b and d) the summation of the linear factor versus the summation of gate voltage.

Figures 5.21 a) and c) demonstrates the inverse of calculated real-time from the field effect mobility upon exposure to NO<sub>2</sub> and NH<sub>3</sub> versus the Dirac point voltage for electron and hole regimes, respectively. Each data point obtained from GFET gas exposure time measurement shows the exact time exposure for a particular gas. The measurement did not show the linearity dependence between the inverse of mobility and the Dirac point, as expected. This is because of the noise in the testing system and measurement errors. Therefore, a summation of the inverse mobility and the Dirac point is taken to improve the linearity dependence. Figures 5.21 b) and d) represent the summation results, which have linearity dependence better than the presented in Figures 5.20 a) and c). In addition, the linear factor for real-time gas exposure is different between NO<sub>2</sub> and NH<sub>3</sub> gases.

Table 5.3: Represent the data obtained from the linear factor fitting.

Gas	Hole Regime $\times 10^{-6}(\text{cm}^2/\text{V.s})^{-1}$ (norm of residuals)	Electron Regime $\times 10^{-6}(\text{cm}^2/\text{V.s})^{-1}$ (norm of residuals)
NO <sub>2</sub>	-5.35 (0.0025)	-3.95 (0.0018)
NH <sub>3</sub>	1.04 (0.00036)	2.51 (0.00074)

The linear fitting for each gas exposure is done on the data presented in Figures 5.4 b) and d). Table 5.3. shows the data obtained from the linear fitting and the norm of residuals for NO<sub>2</sub> and NH<sub>3</sub>. The norm of residuals for NO<sub>2</sub> in the hole regime is larger than the residuals in the other regime, and this is due to the hole increases with NO<sub>2</sub> adsorption. Meanwhile, the electron residuals are larger than other regimes due to the electron donation to the graphene by NH<sub>3</sub> gas. Therefore, characterising the linear factor from the real time-measurements of GFET measurements can be used to differentiate between different types of gas.

## Chapter 6

### 6 Functionalised Graphene Gas Sensors

The aim of this chapter is to introduce sensing specificity and improve the sensitivity of the graphene sensors introduced in Chapter 5. Many different methods to achieve this aim have been explored within the literature (see chapter 2); to achieve high sensitivity, recovery, and selectivity in a simple way, we have chosen to introduce a low concentration of oxygen-based defect into the pristine CVD graphene lattice via a chemical method.

Oxygen groups on graphene (C-OH, C-O, C=O) have high bonding energies which are more favourable for gas adsorption than the low bonding energy of pristine graphene (C-C) [67, 69]. Oxidising graphene has been investigated widely for improving the sensitivity, recovery and the selectivity [64, 69]. In 2015, Y. R. Choi et al. demonstrated a high sensitivity of GO sensors to 550 ppb for NO<sub>2</sub> at room temperature [64]. The enhancement in sensitivity is due to the increased bonding strength for oxygen groups, causing larger electron transfer from adsorbates. In graphene oxide, the high-oxygen concentration on graphene provides bonding sites with higher energy, which increases the chemisorption of the adsorbates, leading to low recovery for the device. Therefore, reducing oxygen concentration on graphene should provide high bonding-energy sites without sacrificing too much recovery behaviour. For example, G. Lu et al. reported high sensitivity of reduced graphene oxide (rGO) sensors to 400 ppb for NO<sub>2</sub> at room temperature [81]. The enhancement over GO is attributed to the removing some functional oxygen groups, which increases electrical mobility. Oxidising CVD graphene by the chemical method has been investigated recently, and it found that the amount of introduced oxygen can be controlled during the oxidation process [68].

This chapter shows that the controlled oxidisation of CVD graphene via chemical methods demonstrates high sensitivity compared to the pristine graphene device. The optimal level of oxidation for achieving high sensitivity was found to be 60 minutes of exposure to 3.6 mol sulphuric acid (H<sub>2</sub>SO<sub>4</sub>). The mechanisms for gas sensing behaviour are investigated based on physisorption and chemisorption. The GFETs used within this work demonstrate behaviour similar to reported graphene sensors [64, 65, 69, 70, 84, 85, 89]. In addition, the GFETs response percentage compared to the response within the literature is presented and is found to be comparable, improved.

## 6.1 Functionalised GFET Device

To confirm the oxidation of the CVD graphene used in this work, multiple chemically sensitive spectroscopic techniques are used to evaluate the oxidation percentage of graphene. The samples are prepared by transferring graphene grown on copper via CVD, to a Si substrate copped with 295 nm SiO<sub>2</sub>, as described in the previous section. Then oxygen groups are introduced to CVD graphene by immersing in 3.6 mol of H<sub>2</sub>SO<sub>4</sub> for different durations of time (30, 60, 90, and 120 minutes), and after each time of oxidation, the device is characterised. The techniques used to investigate the oxygen groups that are introduced to the graphene after the oxidation process are Raman spectroscopy and X-Ray Photon Spectroscopy (XPS). In addition, transfer curve measurements are used to evaluate the graphene's doping type, and calculate the mobility before and after each oxidation step. Furthermore, the transfer curve measurement, plus Raman and XPS, determine the number of defects, the introduction of carriers and the chemical configuration of defects before and after each oxidation step.

### 6.1.1 High Resolution Microscope

In this section, a high-resolution microscope has been used to evaluate the damage introduced to the graphene sheet after oxidation. Figure 6.1) demonstrate the high-resolution microscopic images for the CVD graphene a) before and b) after being immersed in 3.6 mol of H<sub>2</sub>SO<sub>4</sub> for 120 minutes with a black, blue, red, and green arrow pointing to folding graphene, residues, tear, and multilayer graphene, respectively. The amount of dirt and polymer residues reduced after oxidation, as seen in Figure 6.1 c). The residues estimation before and after oxidation was done by taking the residues ratio to the clean area from the dark field images in Figures 6.1: b) and d). The percentage coverage of the dirt and residues was estimated from the high-resolution microscope images and found to be 0.204% for pristine graphene and 0.024% for oxidised graphene. This reduction is attributed to the acid removal of dirt and residues from graphene surface [70, 268]. Figure 6.1:c) shows no obvious optically visible damage caused to the graphene sheet after oxidation. Small areas of multilayer (2,3 and 4 layers) graphene are visible, which is expected from CVD graphene growth. The lack of observable gaps within the graphene film indicate full graphene coverage and homogeneous transfer of the CVD graphene film. Figures 6.1: b and d) shows the same images as Figures 6.1: a and c), with dark field images to visualise the residues of nitrocellulose and dirt on graphene before and after oxidation. The remaining particles are

identified as rolled-up backside graphene, which adhered themselves to the graphene film during transfer.

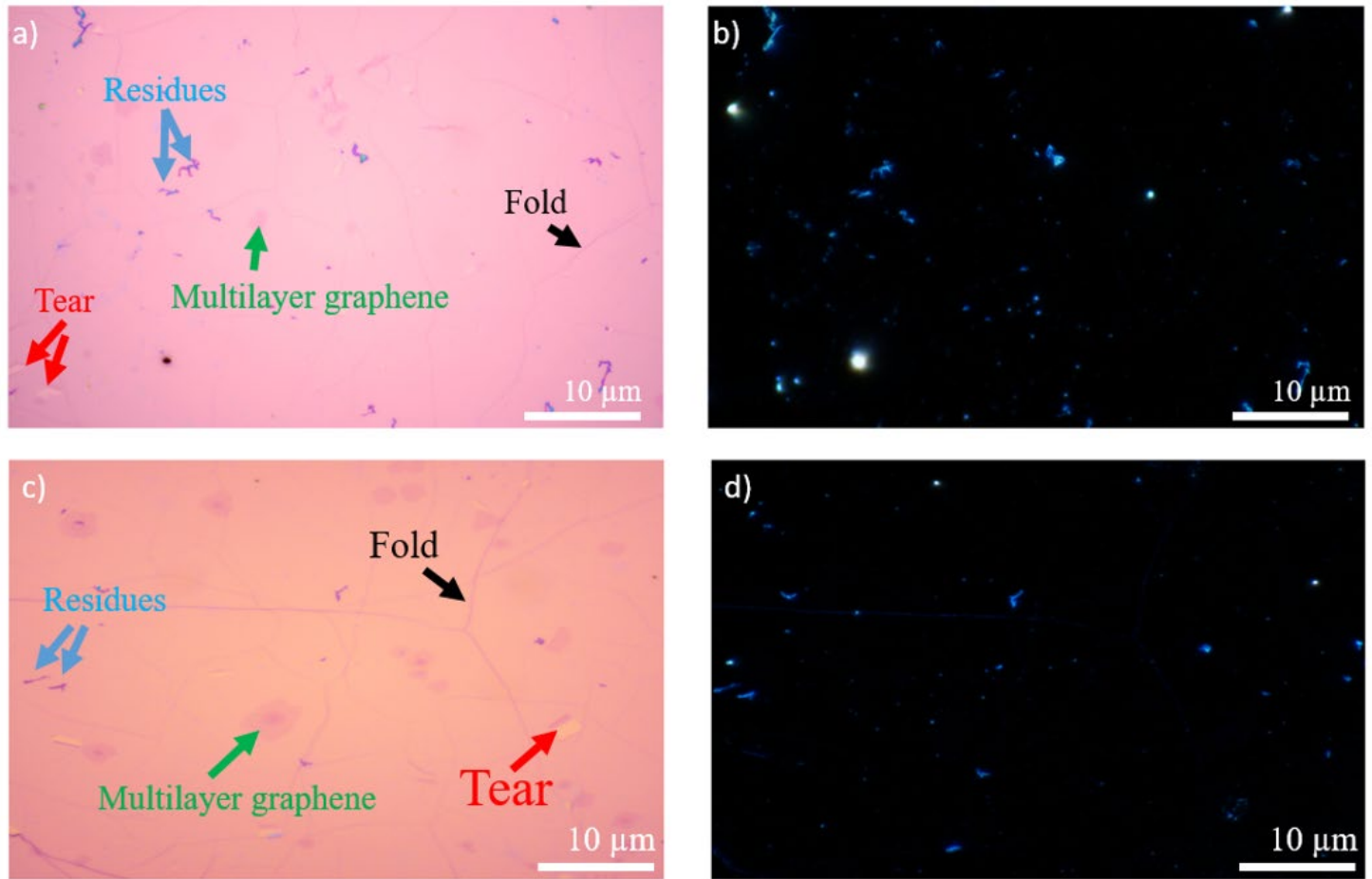


Figure 6.1: Images displaying the graphene sheet before a) and after being immersed in 3.6 mol of sulphuric acid ( $H_2SO_4$ ) for 120 minutes c). a and c) show the 10  $\mu m$  area of the graphene sheet with a black, blue, red, and green arrow pointing to folding, residues, tear, and multilayer graphene, respectively. b and d) the same image after converting to the dark field for residue analysing.

### 6.1.2 Raman Spectroscopy

Raman spectroscopy is a useful tool to characterise atomic-scale structural and chemical modification of graphene. To evaluate the number of graphene layers and defects introduced (oxygen groups) after the oxidation process, the Raman spectrum is used. It has three major peaks used to study the graphene quality: G, D, and 2D. The intensity of the G peak is increased relative to 2D with an increasing number of graphene layers. Also, the shape and intensity of G and 2D peaks change with the graphene layers and strain [195, 199, 200]. The ratio of  $I_G/I_{2D}$  can be used to estimate the number of layers of graphene [192, 196, 201, 233]. The D peak is generated from the breathing mode of the hexagonal ring and requires a defect to be activated, meaning that the intensity ratio of  $I_D/I_G$  can be used to evaluate the defect density of the graphene [193].

Raman spectroscopy measurements were collected using a Horiba Jobin Yvon HR800. The incident laser power was 4 mW at room temperature, and the laser beam diameter was 0.70  $\mu\text{m}$ . An acquisition time was set to 5 s per measurement for spectral windows. For each oxidation step, Raman measurements have been taken for devices to evaluate the defect (oxygen groups) introduced to the graphene. Raman spectra are presented in Figure 6.2.a) for all peaks G, D, and 2D. Both G and 2D peaks are visible for all oxidation steps. In addition, the  $I_{2D}/I_G$  ratio for the pristine graphene is 1.97, which indicates monolayer graphene [201-203]. Figure 6.2.b) demonstrates the D peak region, which indicate no observable D peak for pristine graphene while a D-peak can be observed for all the oxidised graphene samples. The D peak intensity increases as the time of exposure to  $\text{H}_2\text{SO}_4$  increases. This is due to the oxygen covalent bond and substitution of a carbon atom by oxygen atom in to the graphene lattice. In Figure 6.3.a), a linear increase of  $I_D/I_G$  with exposure time is observed, until a critical point, which lies between 90 and 120 minutes. At that point, the D/G ratio increases substantially. Either this is due to increased reaction beyond a certain point, or too much graphene damage. Therefore loss of graphene rings and G-peak intensity. The change in  $I_D/I_G$  ratio after exposure to  $\text{H}_2\text{SO}_4$  for 0, 30, 60, 90, and 120 minutes increased by 0.038, 0.058, 0.085, 0.1, and 0.26, respectively. In the literature [68, 269, 270], the  $I_D/I_G$  ratio for GO ranges between 0.11 to 2.5, consistent with the ratio detected within this project. The concentration of introduced oxygen groups has been estimated by calculating defect density using Equation 5.1 and plotted in Figure 6.3.b). The calculated result suggests that more defects (oxygen groups) are formed on the graphene with increasing exposure to  $\text{H}_2\text{SO}_4$ . It is calculated that the defect density of

pristine graphene, at the very most, is  $1.3 \times 10^{10} \text{ cm}^{-2}$  (D-peak intensity is below the measurable limit) increases to  $6.1 \times 10^{10} \text{ cm}^{-2}$  for highly oxidised graphene, with 120 minutes of oxidation. The increase in the defect density is attributed to the increase in oxygen groups concentration (C-OH, C-O-C, and C=O) [271, 272]. The oxidation recipe presented within this work is controllable and repeatable by controlling the time of exposure to  $\text{H}_2\text{SO}_4$ , as all the oxides samples show comparable defect densities (oxygen groups) introduced across samples as indicated by Raman defect density calculation.

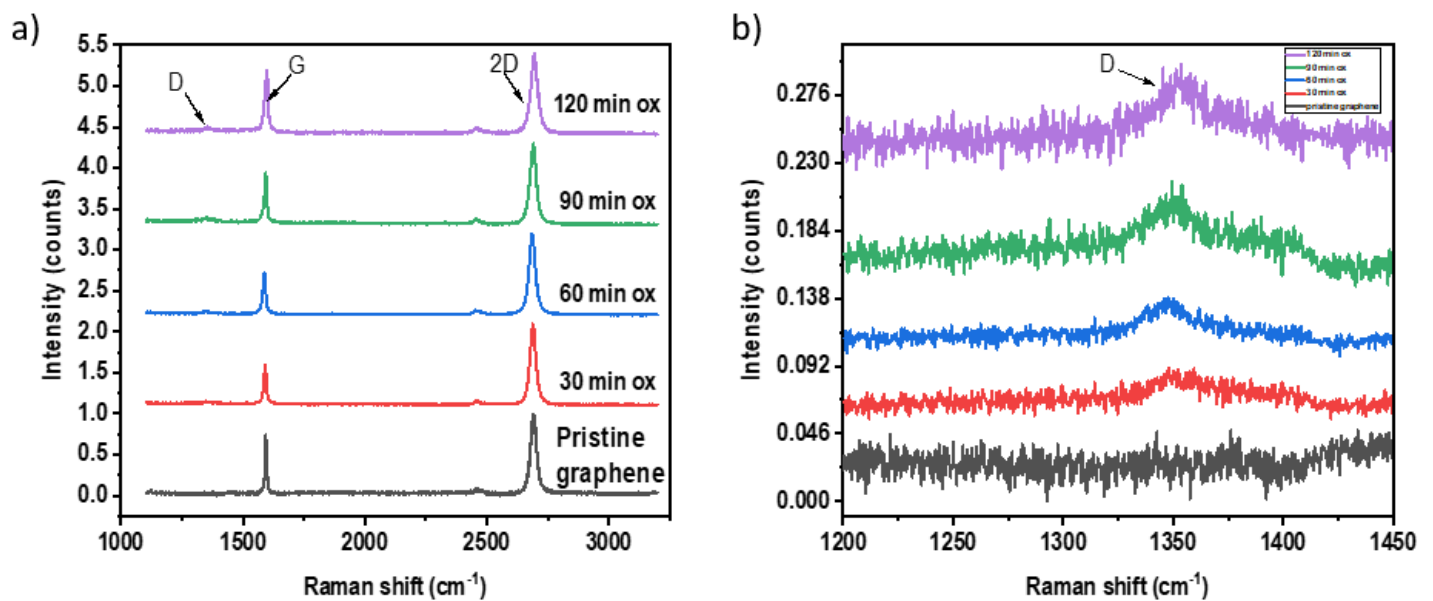


Figure 6.2: a) Raman spectra taken from CVD graphene before and after oxidation for 0, 30, 60, 90, and 120 as indicated by black, red, blue, green, and grey spectra, respectively. b) magnified view of the D peak before and after oxidation.

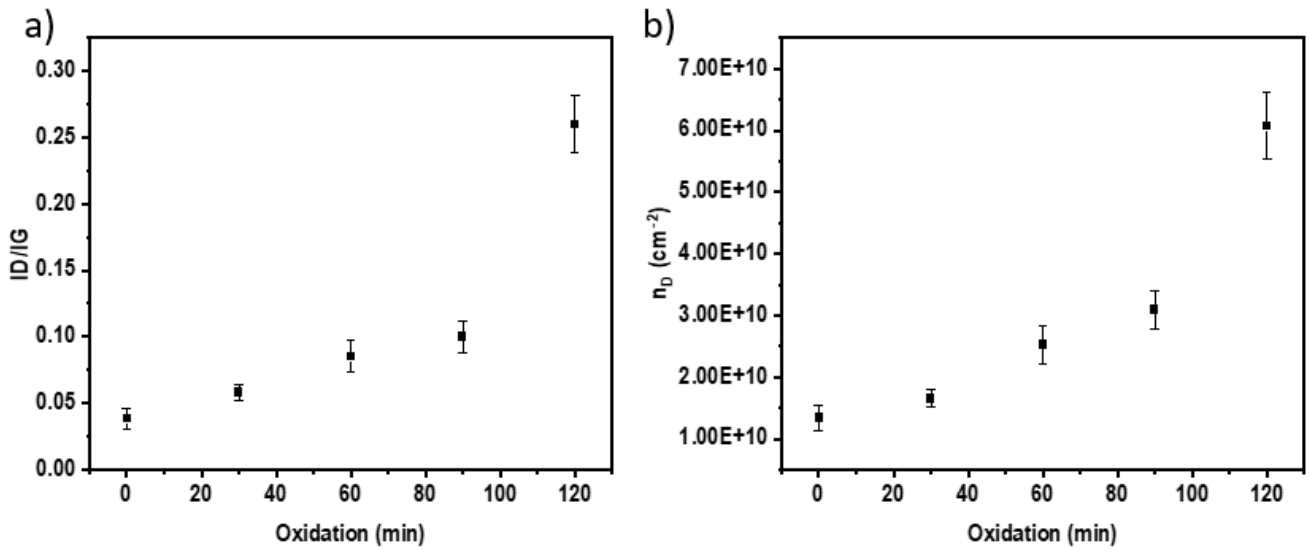


Figure 6.3: a) Demonstrate the intensity ratio  $I_D/I_G$  as the function of time of exposure  $\text{H}_2\text{SO}_4$ . b) The calculated defect density as the function of the time of exposure. Both intensity ration and defect intensity increases linearly with time of oxidation.

### 6.1.3 XPS

As the Raman spectroscopy measurements indicated, the formation of defects in the graphene lattice after oxidation does not provide information about the type of chemical elements, and the bonding between these elements and compounds. XPS is used to determine the atomic percentage before and after the oxidation for the C-C bond, C-OH bond, and C-O-C bond on graphene.

XPS data was collected at the EPSRC National Facility for XPS (“HarwellXPS”). XPS was acquired using Kratos Axis SUPRA using an X-ray source of monochromated  $\text{Al } K\alpha$  with an energy of 1486.7 eV. The measurements were collected with a spot size/analysis area of  $700 \mu\text{m} \times 300 \mu\text{m}$  using Kratos Axis SUPRA. The high-resolution spectra were collected by passing energy of 20 eV with step size and sweep time of 0.1 eV and 60s, respectively.

Figure 6.4. Shows all the data were collected at room temperature with a pressure set of below  $5 \times 10^{-8}$  Torr. Core-level spectra was recorded around the C1s binding energy. This energy was selected as the oxygen groups contamination presence is observable due to carbon-oxygen bonding.

Figure 6.4: displays the C1s core-level spectra collected from the pristine CVD graphene after transferred using NC to  $\text{SiO}_2/\text{Si}$ . Casa XPS Software is used to fit the graphene XPS

spectra for carbon-to-carbon bonding (C-C), hydroxyl bonding (C-OH), epoxy bonding (C-O-C) and carbonyl bonding (C=O), with peaks at 284.4 eV, 285 eV, and 286.3 eV, respectively. The atomic percentage of C-C for the sample is 70.04 %. In addition, the presence of oxygen group on pristine graphene from C1s core-level spectra is thought to be related to the polymer residues containing C-C and C-O groups.

Figure 6.5.a) represents the C1s core-level spectra for graphene sample oxidised for 30 minutes in H<sub>2</sub>SO<sub>4</sub>, whilst Figure 6.5. b) demonstrates the C1s core-level spectra for graphene sample oxidised for 120 minutes. The C-C peak is observed to decrease in intensity for both oxidised samples, when compared with the pristine graphene spectrum, whilst the intensity of the C-OH and C=O intensities increase. This indicates that the atomic percentages for C-OH and C=O increases as the oxidation time increase whilst the percentage of C-C bonding decreases. The atomic percentage of C-C after oxidation decreases after 30 and 120 minutes of oxidation to 60.47% and 49.63%, respectively, as presented in Figure 6.6. Also, the atomic percentages of C-OH increase with oxidation from 26.36% to 43.26%, respectively. In contrast, the percentage of C=O decreased from 12.43% for pristine graphene to 7.11% after 120 minutes of oxidation, and this could be because the C=O signal originated from the transfer residues in that case. Overall, the oxygen group percentage increases with oxidation time from 30% for pristine CVD graphene to 50% for highly oxidised CVD graphene by H<sub>2</sub>SO<sub>4</sub>. While the carbon-to-carbon bonding decreased from 70% to 50% as the oxidation time in sulphuric acid increased. XPS measurements show a large increment in oxygen groups of C-OH with oxidation time. The percentage of introduced oxygen groups (C-OH) on graphene is comparable to XPS results published for GO and reduced GO [64, 89, 90], which range between 11.29 to 35%. XPS measurement confirmed the formation of the oxygen groups on the graphene, suggesting that the Raman defect density measurements can be used to indirectly determine the amount of oxidation of the graphene sheet.

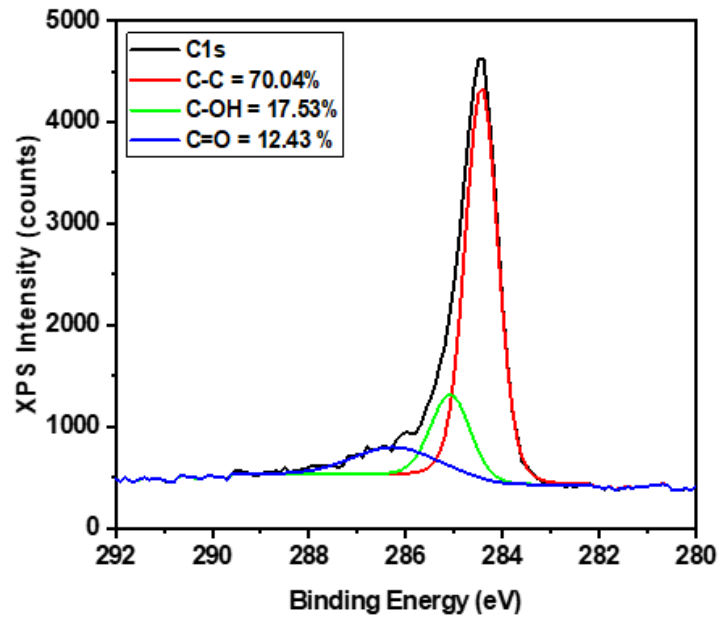


Figure 6.4: Demonstrates C1s core-level XPS spectrum collected from pristine CVD graphene.

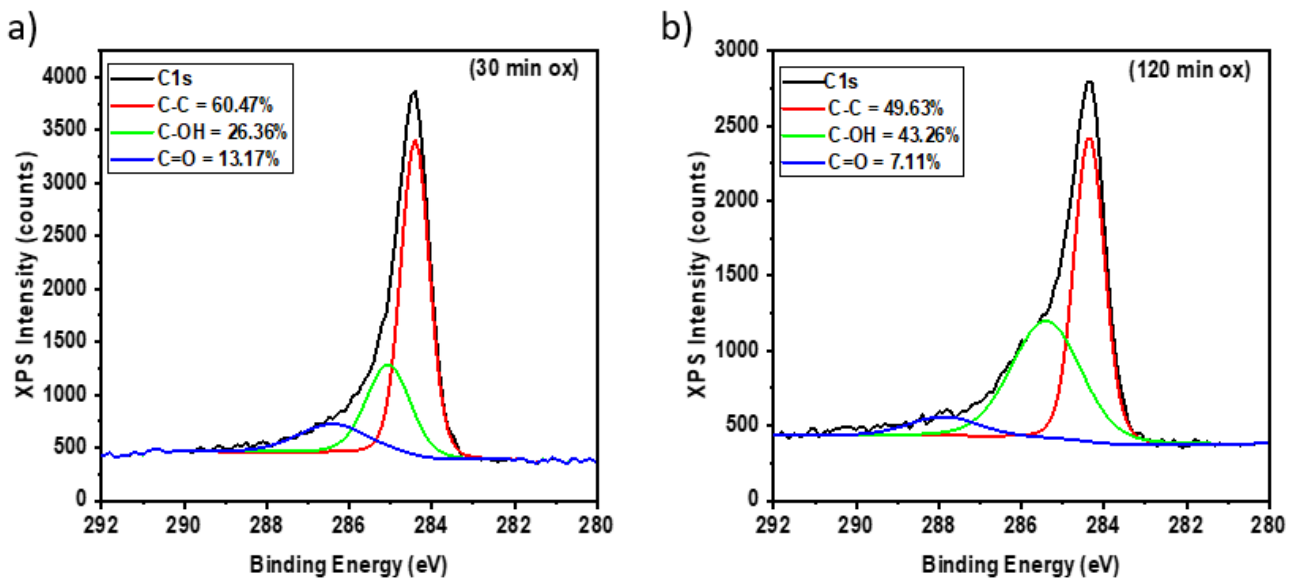


Figure 6.5: Demonstrates C1s core-level XPS spectrum collected from oxidised CVD graphene. a) oxidised sample for 30 min in H<sub>2</sub>SO<sub>4</sub> and b) oxidised sample for 120 min in H<sub>2</sub>SO<sub>4</sub>.

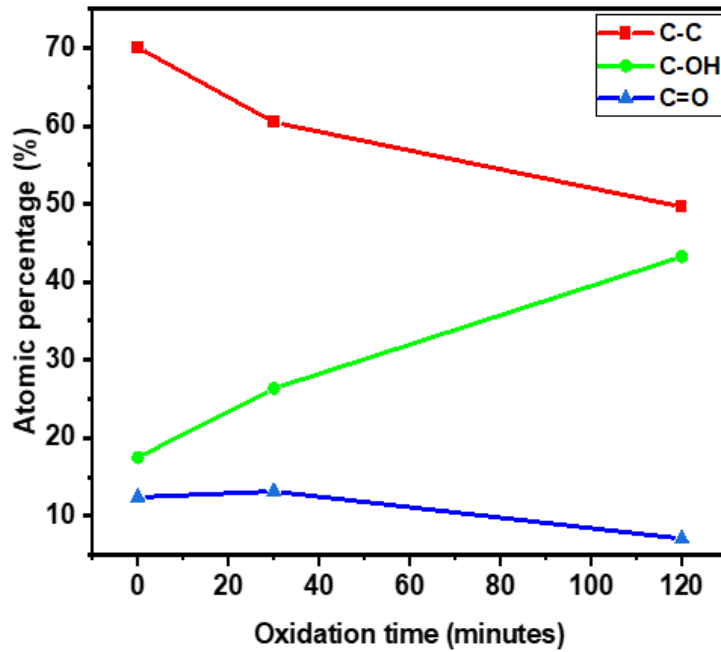


Figure 6.6: Shows the atomic percentage of carbon-to-carbon bonding (C-C), carbon-to-hydroxyl or epoxy oxygen bonding (C-OH, C-O), and carbon-to-carbonyl bonding (C=O) plotted versus the oxidation time.

#### 6.1.4 Electric Measurements for Functionalised Graphene FET (GFET)

The electric characterisation of GFETs is used to provide information about the graphene doping before and after the oxidation. It also used to estimate the charge carrier concentration of the graphene and the mobility before and after each oxidation step. Additionally, the residual of the charge carrier density introduced to the graphene during the oxidation process can be calculated using Equation 4.1.

$$n_0 = \frac{(V_g - V_{Dirac}) \cdot C_{ox}}{e} \quad (4.1)$$

Where  $n_0$  is the carrier density of the graphene device,  $V_g$  is the gate voltage,  $V_{Dirac}$  is the Dirac point voltage,  $C_{ox}$  is the capacitance for the dielectric layer per  $\text{cm}^2$  ( $11.7 \text{ nF cm}^{-2}$  for  $295 \text{ nm SiO}_2$ ), and  $e$  is the electron charge.

The fabricated GFET devices have 11 channels, and electrical measurements are taken from all channels for pristine devices and after each oxidation step. Figure 6.7.a) shows the result obtained from one measured device before and after each oxidation step. The plot shows a typical transfer curve of the graphene field effect transistor before and after exposure to the  $\text{H}_2\text{SO}_4$  for 30, 60, 90, and 120 minutes, respectively. The solid black curve is related to the

pristine graphene device (before oxidation), and the dashed lines are related to the doped graphene after the oxidation. The Dirac point for the pristine graphene is located at 4 V which indicates that the graphene device is initially p-doped. This initial doping assigned to the polymer residue and water molecules trapped between the graphene sheet and the substrate [186, 243, 244]. Upon exposure to H<sub>2</sub>SO<sub>4</sub>, the Dirac point was observed to shift towards a more positive voltage, and the shift increased with the time of exposure. The Dirac point shifted after exposure to H<sub>2</sub>SO<sub>4</sub> for 0, 30, 60, 90, and 120 minutes to 4, 9, 10.5, 13.8, and 14V, respectively. The result indicates that H<sub>2</sub>SO<sub>4</sub> is doping graphene with holes [244]. This agrees with the XPS measurements indicating that H<sub>2</sub>SO<sub>4</sub> introduces oxygen groups to graphene, and the concentration of oxygen groups increases as the exposure time increases to H<sub>2</sub>SO<sub>4</sub>. Therefore, hole concentration in graphene increases as oxygen increases, resulting in larger electron transfer from the graphene lattice to the oxygen groups [70, 81, 85]. Electrons and holes mobility were calculated by Eq (4.4) for the devices before exposure to the H<sub>2</sub>SO<sub>4</sub>, and the average holes and electron mobility are displayed in Figure 6.7.b), which is consistent with reported GFET mobility [58, 72, 80, 92, 245]. After the device exposure to H<sub>2</sub>SO<sub>4</sub> for the different durations of time, the electrons and holes mobility calculated for each time duration for all 11 channels and the average result is plotted in Figure 6.7.b). From Figure 6.7.b) both electrons and holes mobility decrease with increasing the time of exposure to the H<sub>2</sub>SO<sub>4</sub> resulting from the increased defect density scattering. Also, as the time of exposure to H<sub>2</sub>SO<sub>4</sub> increases, the carrier charge density increases as in Figure 6.8. This increase is due to the charge impurities induced to graphene by oxygen groups. The average hole concentration was calculated using Eq 4.1 for the pristine graphene and found to be  $2.2 \times 10^{12} \text{ cm}^{-2}$ . Also, for 30, 60, 90, and 120 minutes of oxidation, the average charge impurities are 4.81, 5.5, 7.22, and  $7.74 \times 10^{12} \text{ cm}^{-2}$ , respectively. The doping densities calculated from the devices are similar to the published graphene devices on SiO<sub>2</sub> substrate [186, 273-275].

The oxidation process presented in this work shows an increase in the defect density and charge residual carrier (oxygen groups) with oxidation on the graphene sheet, as calculated from Raman measurements and electric measurements presented in Table 6.1. The defect density is increases as the time of oxidation increases, resulting in a greater concentration of oxygen groups being introduced to graphene. Therefore, the charge residual increases as the oxygen concentration increase on the graphene as presented in Table 6.1. As can be seen, for 60 minutes of oxidation, Raman-measured defects  $n_D = 2.52 \times 10^{10} \text{ cm}^{-2}$  correlates to  $n_0$  of  $5.5 \times 10^{12} \text{ cm}^{-2}$  charged residues. These results show that Raman defect quantification

possibly underestimates the number of defects. This is because the equation used was determined for use with native point defects.

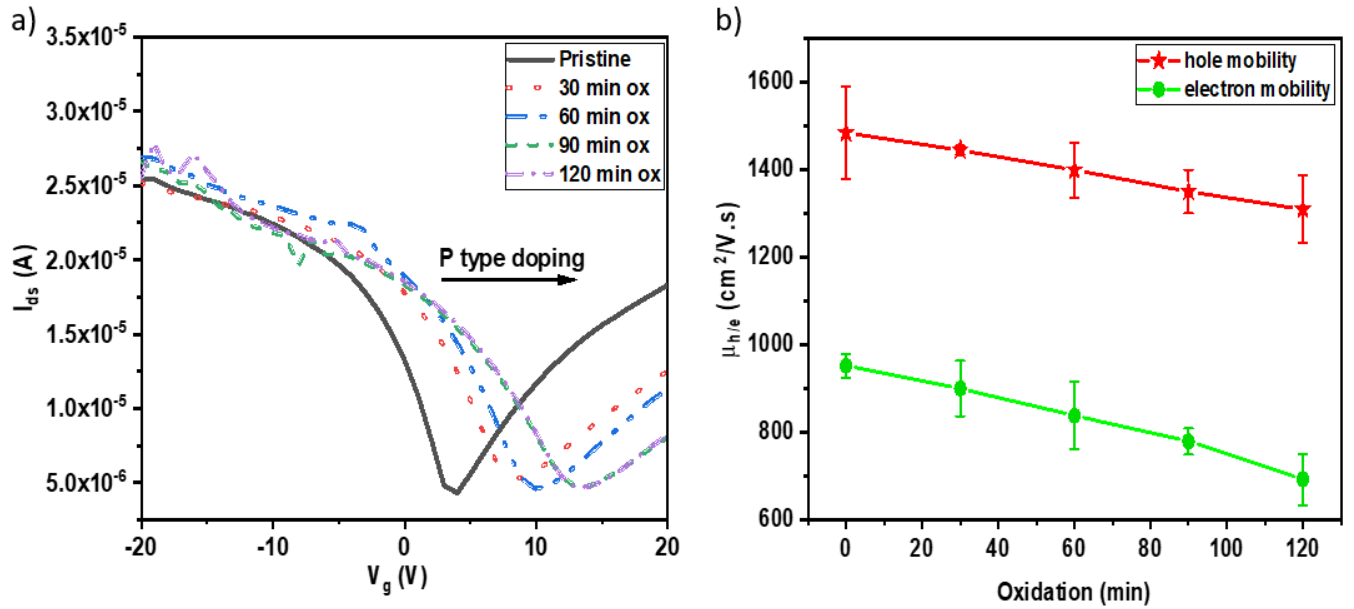


Figure 6.7: a) Shows the Dirac point shifted toward positive voltage as the time of exposure to the  $\text{H}_2\text{SO}_4$  increases. Dirac point before exposure to the  $\text{H}_2\text{SO}_4$  located at 4 V. After 30, 60, 90, and 120 minutes of exposure to the  $\text{H}_2\text{SO}_4$ , Dirac point shifted to 9, 11, 13.8, and 14 V respectively. b) Shows both holes and electrons mobility as a function of time of exposure.

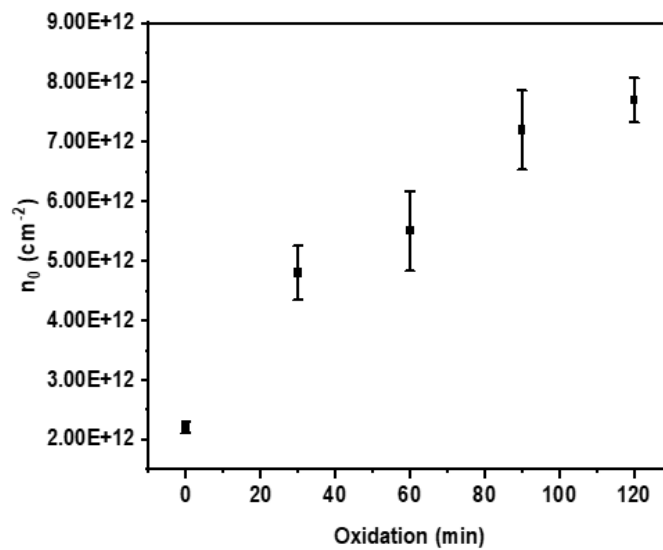


Figure 6.8: Shows the carrier charge density increase with increasing the exposure time to  $\text{H}_2\text{SO}_4$ .

Table 6.1: Represent the average Raman defect and charge residual carrier before and after each oxidation step for field-effect transistor devices.

Oxidation (min)	Defect density ( $n_D$ ) ( $\times 10^{10} \text{ cm}^{-2}$ )	Residual carrier density ( $n_0$ ) ( $\times 10^{12} \text{ cm}^{-2}$ )
0	1.3	2.2
30	1.65	4.8
60	2.52	5.5
90	3.09	7.2
120	6.07	7.7

## 6.2 NO<sub>2</sub> Functionalised Sensor Characteristics

The graphene gas sensor devices presented in this work are based on the graphene field effect transistor (GFET). Graphene has atomic thinness [71], low electrical noise [248, 249] and a small density of states close to the Dirac point [71, 183] which means that any interaction between the graphene and gas species through physical adsorption will have a measurable change in resistance response. Graphene has been used as a gas sensor and shows sensitivity to both oxidising and reducing gases [72, 77, 79]. Pristine graphene has a low density of defects, which act as active sites in the graphene basal plane for the gas adsorption [64, 69]. As a result, pristine graphene does not favour gas adsorption as it has fewer chemically active sites, meaning that any sensing is predominantly due to physisorption interactions between gases and graphene sensors [64, 69]. Therefore, variations on pristine graphene gas sensors have been introduced to increase graphene-gas interactions. Introducing oxygen groups on CVD graphene (CVD GO) has been widely investigated to improve sensitivity and selectivity [68, 69, 87-90].

In this work, graphene oxide devices have been investigated for their sensitivity to NO<sub>2</sub> gas via physisorption and chemisorption by studying the response behaviour, which follows two regimes of fast and slow response, due to the physisorption and chemisorption, respectively [276]. The saturation measurement was performed to identify the maximum resistance change devices reach before saturation and detection limit. This is then used to evaluate the number of sensing events the device can achieve upon exposure to different NO<sub>2</sub> concentrations in a short period of time (3 min) before saturation is reached. The CVD GO devices used within this work demonstrate behaviour compatible with published results [69,

70, 84, 85, 87-89]. A comparison of response percentage between device sensitivity used within this work and reported values are presented. In addition, the detection limit of devices (LOD) and recovery are compared with the literature.

### 6.2.1 NO<sub>2</sub> Saturation Measurement

A saturation test was performed to study the response behaviour of the device before and after each oxidation step under long-time (1 h) exposure to NO<sub>2</sub> gas. This is then used to estimate how the device can operate in cyclic events for NO<sub>2</sub> detection before reaching saturation, which is then used to estimate the best oxidation time for obtaining a high device response.

The device's oxidation was done in steps, and sensitivity measurements were performed after each oxidation step. The oxidation of the device was done by immersing the graphene sensors in H<sub>2</sub>SO<sub>4</sub> in four steps of 30, 60, 90, and 120 minutes. At the same time, the sensitivity measurement was carried out at room temperature inside the gas chamber before and after each oxidation step. The device was left under a high vacuum overnight before the test was performed to remove molecules adsorbed on the graphene surface [25]. The gas rate during the measurement was controlled by mass flow controllers (MFCs). The change in resistance was recorded by a Keithley 2450 Sourcemeater. The sensitivity of the device was investigated by measuring the change in resistance, using a four-terminal configuration method across the graphene channel during the gas exposure to NO<sub>2</sub> and N<sub>2</sub>. The measurements were performed by flowing N<sub>2</sub> for 10 minutes, followed by 1000 ppb of NO<sub>2</sub> follow for 1 h and then N<sub>2</sub> for 2 h. During the measurements, the sensing chamber pressure was kept at 799.9 mbar by the pressure modulator, and V<sub>ds</sub> was maintained at 10 mV across the graphene channel. As the device was exposed to NO<sub>2</sub> gas in different time steps, the response of the device was analysed as the relative change in resistance and calculated using Equation 5.2.

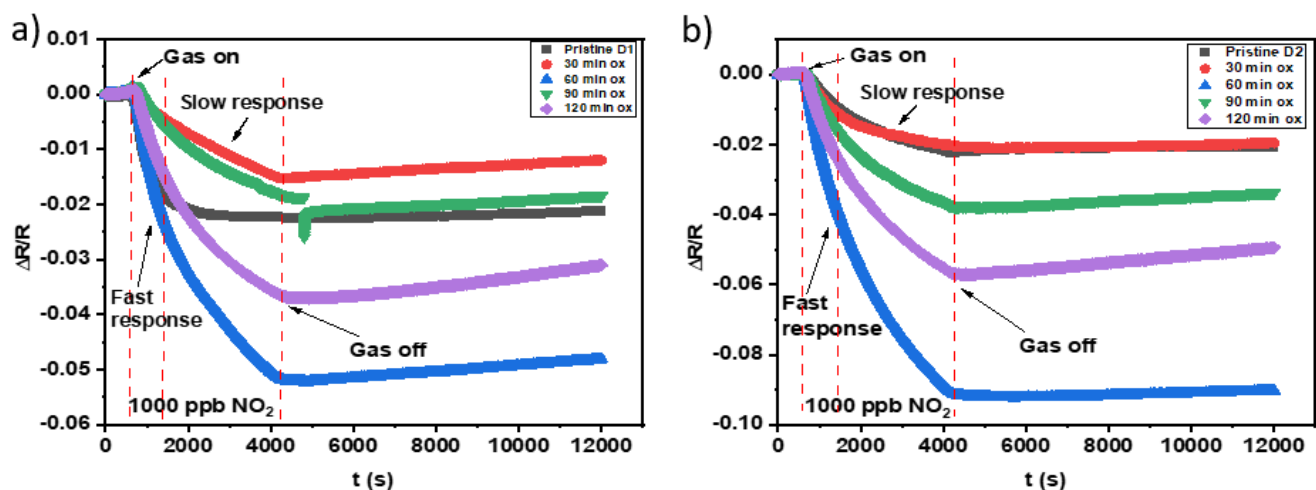


Figure 6.9: a and b) Response of graphene device D1 and D2 for 1000 ppb of  $\text{NO}_2$  gas before and after each oxidation step, respectively. The black, red, blue, green, and grey curves represent the response result obtained from device after 0, 30, 60, 90, and 120 minutes of oxidation, respectively. The measurement is done at room temperature with a flow of  $\text{N}_2$  during the recovery process.

Figures 6.9: a) and b) represent the response (sensitivity) for the graphene devices D1 and D2 exposed to 1000 ppb of  $\text{NO}_2$  gas for 1h and left to recover under  $\text{N}_2$  flow for 2 h before and after each oxidation time while the change in resistance recorded. The pristine device results were discussed in section 5.2.1. As presented on Figure 6.9, the response of the device upon exposure to 1 ppm  $\text{NO}_2$  increases more as the oxidation time increases up to 60 min and then decreases as the oxidation time increases to 120 min for all the devices. The black, red, blue, green, and grey curves represent the response for devices after 0, 30, 60, 90, and 120 min of oxidation, respectively. Saturation changes with oxidation and is not even reached after 1h of exposure time to  $\text{NO}_2$ . This is attributed to the increases in the interaction between the gas molecules and oxygen groups on the graphene surface [164]. However, the oxidation first removed polymer residue reduces the conductivity and therefore reduces the response after the first step of oxidation for 30 min. After that, oxidation rapidly improves the response by introducing oxygen sites. This leads to two response rates in the saturation curves: the first rate represents the fast change in resistance response upon the  $\text{NO}_2$  exposure, and the second is the slow change in resistance response, as seen in Figure 6.9, which is consistent with the reported results [164, 276]. The fast rate of response is attributed to the  $\text{NO}^+$  molecular adsorption on C-C low binding energy sites, while the slow rate response to the high-energy binding sites (C-OH, C=O)[164]. For the fast rate response, the change in response for the device reaches 50% of the total change in response after 13min, while the other 50% of the

response change takes 47min to be reached in the slow response regime. Furthermore, beyond a certain threshold, the interaction of oxygen groups is more damaging to the transport than beneficial to the sensing, and the response goes down as the oxidation time increases from 60 to 120min, as presented in Figures 6.9. a) and b) and is consistent with reported GO sensors' behaviour [64, 67, 276, 277]. The maximum change in response to NO<sub>2</sub> was observed for the sensors that oxidised for 60 minutes which ranged between 5.5% and 9%. This is a 100% improvement in response compared to the pristine graphene devices (2.2% and 2.4%).

During the recovery process, all the graphene sensors before and after the oxidation did not recover to the initial resistance even after more than 2 h with N<sub>2</sub> flow. However, when the devices are left under high vacuum overnight, the sensors recover to 95% of the initial resistance. In contrast, the reported graphene oxide sensors [69, 70, 81, 87, 88] show up to 80 % recovery at room temperature. The improvement in recovery might be because they did not vacuum condition the sensors before performing the sensing test, as discussed in section 5.2.4, and show that recovery was good for devices that were not vacuumed condition before the sensitivity test.

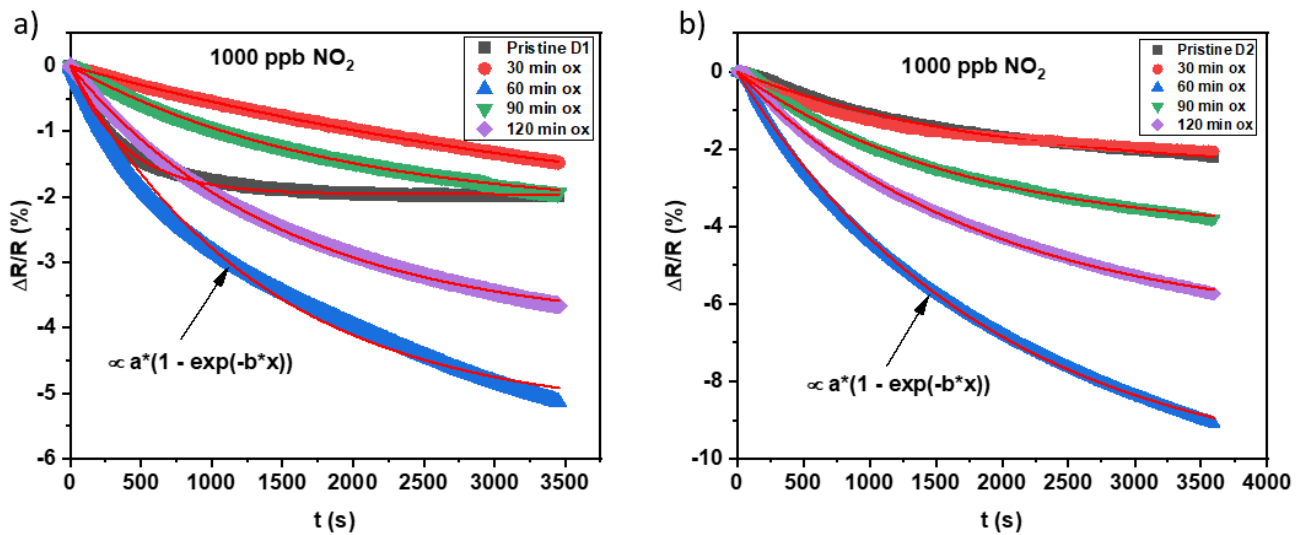


Figure 6.10: a and b) Show the rate fitting curves of device D1 and D2 for the exposure curves for 1000 ppb of NO<sub>2</sub> before and after each oxidation steps. The black, red, blue, green, and grey curves represent the response result obtained from device after 0, 30, 60, 90, and 120 minutes of oxidation, respectively.

Figures 6.10: a) and b) illustrate the rate fitting from the data obtained from devices D1 and D2. From the fitted data, the  $\frac{K_1}{K_2}$  is equal to  $a$  and  $K_2$  is equal to  $b$ . The equation 5.3 shows the resistance response change during the adsorption of the NO<sub>2</sub> gas before the saturation is

reached, and the exponent can be determined by fitting the equation as demonstrated in Figures 5.10: a) and b). The equation used is for a single rate and is valid for a pristine graphene device. However, as the two rates fitting did not work for our data, the single rate equation was used just to give a notion of the change in adsorption after oxidation, with the error percentage being high from the fitting quality. The adsorption increases at the beginning of the cycle for devices D1 and D2 during exposure at 1000 ppb NO<sub>2</sub>. From the plotted curves of the resistance, the adsorption K<sub>a</sub> and the desorption K<sub>d</sub> values can be obtained using Equations 5.4 and 5.5.

Table 6.2. Represent all the values of K<sub>a</sub> and K<sub>d</sub> extracted from the plot before and after the oxidation steps. The extracted data show that both constants, relating to adsorption and desorption rates, increase with oxidation. However, the highest constant rate of adsorption and desorption was observed for both devices after 60 min of oxidation. The enhancement in both constant rates is attributed to the introduced oxygen groups, which provide a more active site for gas adsorption and desorption and, therefore, enhance the device sensitivity. In comparison between the K<sub>a</sub> and K<sub>d</sub> values taken before and after oxidation steps within this work, these are useful for evaluating the effect of introducing various concentrations of oxygen groups on the graphene with regards to sensing performance.

Table 6.2: Represent both constant of adsorption (k<sub>a</sub>) and desorption(k<sub>d</sub>) rates extracted from fitted curves for devices D1 and D2 before and after oxidation.

D1 oxidation (min) <sup>-1</sup>	K <sub>a</sub> (ppb.s) <sup>-1</sup>	K <sub>d</sub> (s) <sup>-1</sup>	D2 oxidation (min) <sup>-1</sup>	K <sub>a</sub> (ppb.s) <sup>-1</sup>	K <sub>d</sub> (s) <sup>-1</sup>
0	4.316 × 10 <sup>-6</sup>	2.36 × 10 <sup>-3</sup>	0	1.352 × 10 <sup>-6</sup>	8.26 × 10 <sup>-4</sup>
30	5.911 × 10 <sup>-7</sup>	3.966 × 10 <sup>-4</sup>	30	1.866 × 10 <sup>-6</sup>	9.712 × 10 <sup>-4</sup>
60	3.391 × 10 <sup>-6</sup>	2.808 × 10 <sup>-3</sup>	60	5.520 × 10 <sup>-6</sup>	4.996 × 10 <sup>-3</sup>
90	9.187 × 10 <sup>-7</sup>	5.746 × 10 <sup>-4</sup>	90	2.476 × 10 <sup>-6</sup>	1.892 × 10 <sup>-3</sup>
120	2.216 × 10 <sup>-6</sup>	2.216 × 10 <sup>-3</sup>	120	3.511 × 10 <sup>-6</sup>	2.980 × 10 <sup>-3</sup>

### 6.2.2 NO<sub>2</sub> Repeatability Measurement

In this work, all the sensors' responses were tested individually for the sake of repeatability and reproducibility. All sensors were left under vacuum overnight (below  $1 \times 10^{-6}$  mbar) prior to the cycle test. After that, the test cycles started with a 600s flow of N<sub>2</sub> followed by 180s of 1000 ppb of NO<sub>2</sub> and repeated three times. The devices were tested under a repeatable cycle with the same gas concentration to study the reliability of the device before and after the oxidation step. Figures 6.11: a) and b) represent the three cycles response of the sensors for 1000 ppb of NO<sub>2</sub> gas from all sensors before and after each oxidation step. The response for the sensors with each time of 0, 30, 60, 90, and 120 minutes of oxidation is presented by black, red, blue, green, and grey curves, respectively. The sensitivity of the devices degraded with repeated exposure to NO<sub>2</sub> cycles. This is due to the repeated gas exposure, causing the device to reach saturation, which is a known issue for graphene gas sensors [60]. Also, the recovery of the devices was very slow within a flow of N<sub>2</sub> at room temperature. Therefore, as the sensors have to sense events many times, it suggests the need for shorter sensing events or better recovery mechanisms, such as integrated heater or LED. Figure 6.11: c) and d) represent the resistance response as a function of sequence, which is obtained from the data plotted in Figures 6.11: a) and b) as seen from the sequence response to 1000 ppb of NO<sub>2</sub>, the sensors are able to respond multiple times. The change in resistance response for both sensors upon NO<sub>2</sub> exposure is enhanced after 60 minutes of oxidation. Even though the response degraded with repeated cycles, it can still show a response with repeated cycles up to 20 times before reaching saturation. All the devices show similar repeatable response behaviour. The sensors' response increases with an oxidation time of 30 and 60 minutes and then degrades as the oxidation time increases to 90 and 120 minutes. In addition, the recovery of the devices was very slow at a flow of N<sub>2</sub> at room temperature and did not improve after oxidation; however, full recovery was achieved after leaving sensors under a high vacuum overnight.

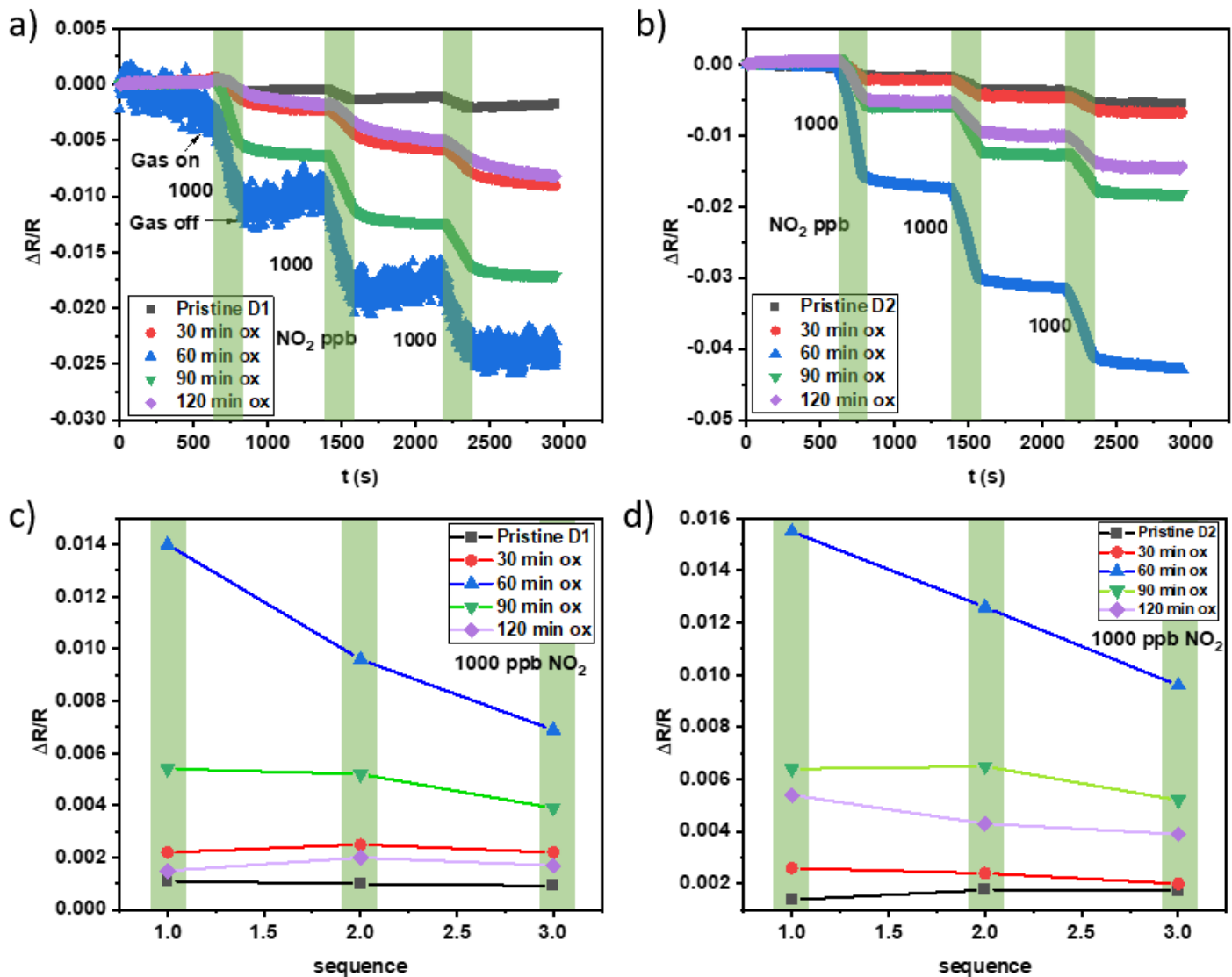


Figure 6.11: a and b) Show the repeatability of the devices for 1000 ppb of NO<sub>2</sub> gas exposure on three cycles before and after oxidation steps at room temperature. During recovery, N<sub>2</sub> was purged into the system. The black, red, blue, green, and grey curve represent the response obtained from devices after 0, 30, 60, 90, and 120 minutes of oxidation, respectively. c and d) demonstrate the change in resistance response for devices D1 and D2 as a function of the sequence obtained from Figures a and b.

### 6.2.3 NO<sub>2</sub> Cycles Measurement

Within this section, gas sensors' sensitivity response for short-time events, recovery, and LOD for NO<sub>2</sub> are explored. The response time for the sensors should be as short as possible, as some gases cause an impact on health or the environment in short exposure times. Many researchers have reported GO, rGO, and CVD GO sensor values for the fast response, sensitivity cycles, and LOD for the oxidised graphene devices upon exposure to NO<sub>2</sub>. In 2015, Y. R. Choi et al. fabricated a sensors using rGO sensors for detecting NO<sub>2</sub> gas molecules at 1000 ppb with response time of 15 minutes [64]. M. G. Chung et al. successfully detected NO<sub>2</sub>

at 200 ppb with a response time of 15 minutes at room temperature [69]. However, an improvement is needed for the graphene oxide sensors by controlling the oxidation level in order to achieve a faster response in a shorter time with a LOD. In this work, the sensitivity of an oxidised CVD graphene-based gas sensors device for fast response and LOD has been enhanced by controlling the concentration of introduced oxygen groups on CVD graphene.

To study the behaviour of the devices under changing the gas concentrations for sensing in short time cycles without reaching saturation. The devices were exposed to 5 different concentrations of 200, 400, 600, 800, and 1000 ppb of NO<sub>2</sub>. The measurements were performed in the gas chamber on 5 cycles, and for each cycle, N<sub>2</sub> was introduced for 10 minutes before and after the NO<sub>2</sub> exposure. During the measurements, the sensing chamber pressure is kept at 799.9 mbar by the pressure modulator. The potential V<sub>ds</sub> were maintained at 10 mV across the graphene channel, while the change in resistance by using a four-terminal configuration method was measured.

The device was left under a high vacuum overnight before the test was performed to remove molecules adsorbed on the graphene surface from the ambient [25]. The vacuum was kept at below  $1 \times 10^{-6}$  mbar overnight. Figures 6.12: a) and b) show the resistance response and recovery for each oxidation time of the graphene devices with NO<sub>2</sub> concentration. The black, red, blue, green, and grey curves represent the response obtained from devices after 0, 30, 60, 90, and 120 minutes of oxidation, respectively. All the sensors' responses increased with an increasing concentration of NO<sub>2</sub> from 200 to 1000 ppb. In addition, the change in response to NO<sub>2</sub> exposure was enhanced after device oxidation. The biggest change in response was observed for both devices at 60 minutes of oxidation, as presented in Figures 6.12: a) and b). The increase in the response is attributed to the increased bonding strength for oxygen groups, which causes larger electron transfers from adsorbates [69]. However, the device's response decreased as the oxidation time increased to 90 and 120 minutes, respectively, as indicated by green and grey curves in Figures 6.12; a) and b). This is a result of introducing a high amount of oxygen functional groups on GO, reducing the conductivity, which reduces the response [65, 67, 81].

The recovery for the devices was very low and did not exceed 1% of their baseline before and after oxidation steps, which is an issue for these devices. Nevertheless, even though the recovery was not achievable during the measurement, all sensors' resistance was able to change with NO<sub>2</sub> concentrations in a short time of exposure (3 min). Also, devices show full

recovery after NO<sub>2</sub> exposure under vacuum conditioning overnight at room temperature, suggesting that NO<sub>2</sub> is physisorbed rather chemisorbed.

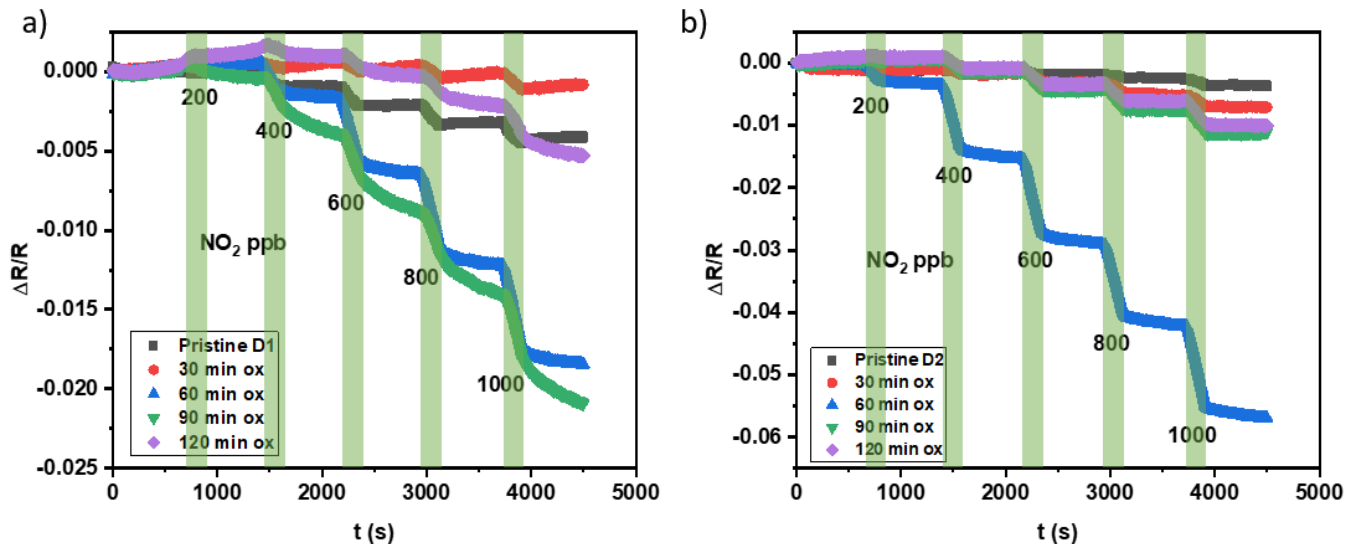


Figure 6.12: a and b) Show the sensor's response for five steps measurements under 200, 400, 600, 800, and 1000 ppb of NO<sub>2</sub> at room temperature. All the measurements were taken for each step of 0, 30, 60, 90, and 120 minutes of oxidation. The black, red, blue, green, and grey curves represent the response obtained from device D1 and D2 after 0, 30, 60, 90, and 120 minutes of oxidation, respectively.

Figures 6.13: a) and b) represents the response percentage obtained from device D1 and D2, respectively, after each oxidation step. The black, red, blue, green, and grey lines are related to the response percentage obtained from the sensor after each oxidation step of 0, 30, 60, 90, and 120 minutes, respectively. The response to NO<sub>2</sub> is increased with increased oxidation by H<sub>2</sub>SO<sub>4</sub>. Both devices show the highest sensitivity to NO<sub>2</sub> after oxidation for 60 minutes, while as the oxidation time rises above 60 minutes, the sensitivity decreases. The increase in response for 30 and 60 minutes of oxidised devices was 12x and 25x, respectively, compared to pristine devices. However, for highly oxidised devices with oxidation time of 90 and 120 minutes, the sensitivity was 6x and 5x, respectively, compared to pristine devices. Table 6.3 presents the response percentage per ppb for all devices tested in this work. The response percentage per ppb was found to be 0.0022%, 0.0015%, 0.0051%, 0.0018%, and 0.0036% for the pristine device, 30 min oxide device, 60 min oxide device, 90 min oxide device, and 120 min oxide device, respectively. Also, the LOD was calculated for all the devices before and after oxygen groups were introduced to the graphene, and the results are presented in Table 6.4.

The good sensitivity and LOD were achieved for device D1 and D2 after 60 minutes of oxidation. As the devices did not reach saturation, the LOD was estimated using the sensing cycles. Overall, devices show a LOD with the highest response in ppb after 60 minutes of oxidation compared to pristine devices. This can be compared to the literature, as the devices can operate in short-sensing events many times before saturation is reached. Compared to the LOD range between 100 to 1000 ppb presented in Table 2.1, our devices show detection limits to NO<sub>2</sub>, close to the most sensitive published LOD results.

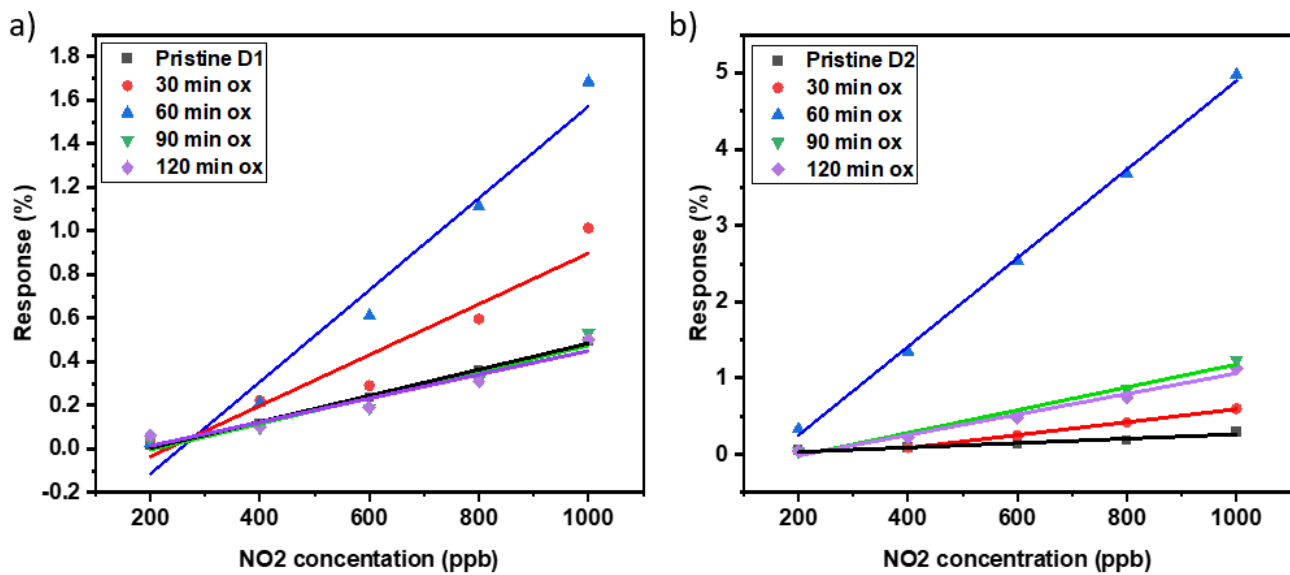


Figure 6.13: Shows the response percentage for four device measurements taken after each oxidation step to the devices during exposure to different NO<sub>2</sub> concentrations. The black, red, blue, green, and grey lines are related to the data obtained from device after oxidation of 0, 30, 60, 90, and 120 minutes, respectively.

Figure 6.14. demonstrates the response of the oxidised graphene devices presented within this work (0.0048 – 0.0102%), compared to the response obtained from the literature (0.00009-0.078%) [64, 65, 69, 70, 81, 82, 84-86, 89]; our devices show a higher response percentage per ppb for 1 minutes of NO<sub>2</sub> exposure compared to all the reported values. However, the recovery was about 1% for the devices at room temperature, whilst the published recovery was between 20 and 85% for NO<sub>2</sub> [69, 82, 84, 85]. Nevertheless, oxide devices for 60 minutes with introducing a low concentration of oxygen groups ( $2.52 \times 10^{10} \text{ cm}^{-2}$ ) presented within this work have the ability to show responses in short sensing events (3 min) for up to 25 cycles before the response is degraded as the sensors approach saturation. The estimation of the sensing ability was based on the change in response resistance from the saturation sensing compared to the change in response resistance upon 400 ppb exposure for

3 minutes. This leads to the importance of controlling the concentration of oxygen groups on the graphene to achieve highest sensitivity.

In conclusion, the measurements shows that the introduction of the relatively low oxygen-group concentration of  $2.52 \times 10^{10} \text{ cm}^{-2}$  results in a charge carrier of  $5.5 \times 10^{12} \text{ cm}^{-2}$  after 60 minutes of oxidation, which enhanced the sensitivity of the GFET gas sensors by 25x. The XPS result confirms that hydroxyl and epoxy groups (C-OH and C-O-C) increased after 30 min of oxidation from 17.53% to 26.36% and for C=O from 12.43% to 13.17%, which is consistent with increased defect after oxidation detected by Raman. The increase in sensitivity could be related to the increase of the C-OH group as it provides active sites for NO<sub>2</sub> adsorption. Similar behaviour of increased sensitivity of oxide graphene toward NO<sub>2</sub> was attributed to C-OH groups [64, 70, 277, 278]. However, the Raman defect measurement of increased oxygen concentration was significantly increased after 120 minutes of oxidation. The oxygen concentration was found to be  $6.07 \times 10^{10} \text{ cm}^{-2}$  with induced charge carriers of  $7.7 \times 10^{12} \text{ cm}^{-2}$ , reducing the sensitivity of the devices. At the same time, the XPS result shows that the increase in oxygen groups with oxidation time is nonlinear and, after 120 minutes of oxidation, found to be 43.26% of C-OH and 7.11% of C=O. It shows that the concentration of the carbonyl group decreases at higher oxidation time, and the C-OH and C-O-C concentration increases. Compared with Raman defect results, which show a high increase, Raman measurement underestimates the oxygen introduced at this oxidation level. However, according to the literature, as the oxygen groups of C-O-C increase, the sensitivity to NO<sub>2</sub> decrease due to the epoxy groups not being energetically favourable for NO<sub>2</sub> adsorption [64, 70, 277]. The epoxy groups have negative binding energy, repulsing the NO<sub>2</sub> from the graphene oxide surface and reducing the sensitivity [277]. From the XPS result, it is hard to distinguish between C-OH and C-O-C, as they both exist at the same binding energy peak. But from the device's response behaviour, we can speculate that epoxy groups increase rather than hydroxyl groups compared to the reported device's behaviour [64, 70, 277]. The reduction in sensitivity could be attributed to the increases in the epoxy groups at higher oxidation times while the hydroxyl groups decrease or stay unchanged. Overall, the oxidised CVD graphene presented within this project demonstrated similar behaviour of reduced graphene oxide type [67, 81-86].

Table 6.3: Summary of pristine and oxidised graphene gas sensors response percentage for NO<sub>2</sub>.

Device	Response to NO <sub>2</sub> (%) Oxidation (0 min)	Response to NO <sub>2</sub> (%) Oxidation (30 min)	Response to NO <sub>2</sub> (%) Oxidation (60 min)	Response to NO <sub>2</sub> (%) Oxidation (90 min)	Response to NO <sub>2</sub> (%) Oxidation (120 min)
D1	0.0022	0.0015	0.0051	0.0018	0.0036
D2	0.0024	0.0019	0.0090	0.0037	0.0056
D3	0.0030	0.0019	0.0102	0.0032	0.0070
D4	0.0024	0.008	0.0048	0.0026	0.00002

Table 6.4: Summary of the detection limit for the devices with different oxidation times for NO<sub>2</sub>.

Device	LOD (ppb) (0 min oxidation)	LOD (ppb) (30 min oxidation)	LOD (ppb) (60 min oxidation)	LOD (ppb) (90 min oxidation)	LOD (ppb) (120 min oxidation)
D1	192	41	160	206	174
D2	88	300	156	212	212
D3	330	217	178	204	196
D4	310	150	120	178	189

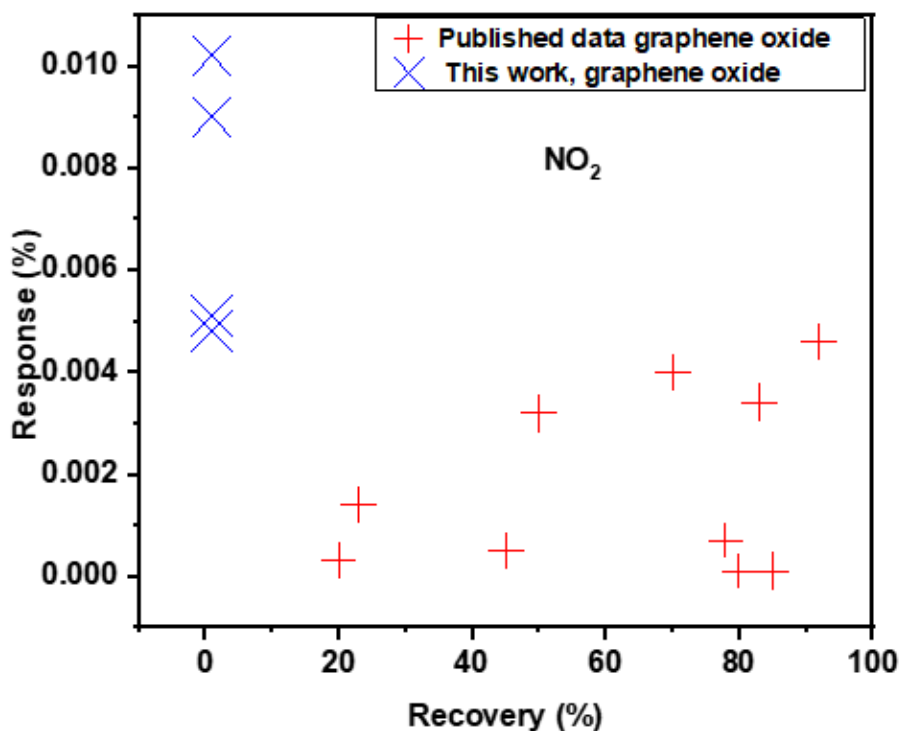


Figure 6.14: Shows the response percentage per ppb for the oxidise devices for 60 minutes presented in this work, which is presented by the blue cross, and the response percentage data from the published oxidise devices data presented by the red cross.

#### 6.2.4 Repeated Device Test without Vacuum Condition

Having successfully demonstrated that pristine graphene device recovery improved after performing sensitivity test without vacuum conditioning as discussed in Chapter 5. In this section, a highly-oxidised graphene device (120 minutes of oxidation) was tested using vacuum conditions overnight before the sensing test was performed, and then the test was repeated without using vacuum conditions before the test to investigate the recovery behaviour of the device. The measurements were performed similarly, as discussed in section 5.2.4. Figure 5.15 represents the resistance change for the device after preparation using vacuum conditioning before the test and without vacuum conditioning upon exposure to different NO<sub>2</sub> concentrations. The device shows similar behaviour for both tests. However, the sensitivity degraded for the device tested without using a vacuum condition. In addition, the recovery was improved compared to the measurement using vacuum conditions. The device showed a recovery of about 100 % after tests without using the vacuum condition, while the recovery of the device tested after the vacuum condition was only 1%. The enhancement in recovery could be attributed to the hydrocarbon add layer contamination from the ambient, which has been reported recently [259, 260]. This may lead to strongly influencing the desorption of the adsorbed gas. In contrast, vacuum conditioning the device removes all the contamination on the graphene surface from the ambient air, which reduces the recovery behaviour. Figure 5.16 demonstrates the response of the sensors upon exposure to different NO<sub>2</sub> concentrations. The response for the device after testing without vacuum condition decreased by 80% compared to the response after vacuum condition. The reduction in sensitivity for the device test without vacuum condition could be attributed to the adsorbent species from the surrounding environment [64].

The vacuum condition of the device before the sensing test dramatically increases the sensitivity as the vacuum condition removes all the adsorbent from the ambient but results in low recovery. While devices tested without using vacuum conditioning shows reduced sensitivity with complete recovery. However, even though the vacuum-conditioned device shows low recovery, it can sense up to 25 cycles in short events of 3 minutes before the sensitivity degrades with a low detection limit of 156 ppb. This is important for gas detection as some gas causes severe harm in low exposure time.

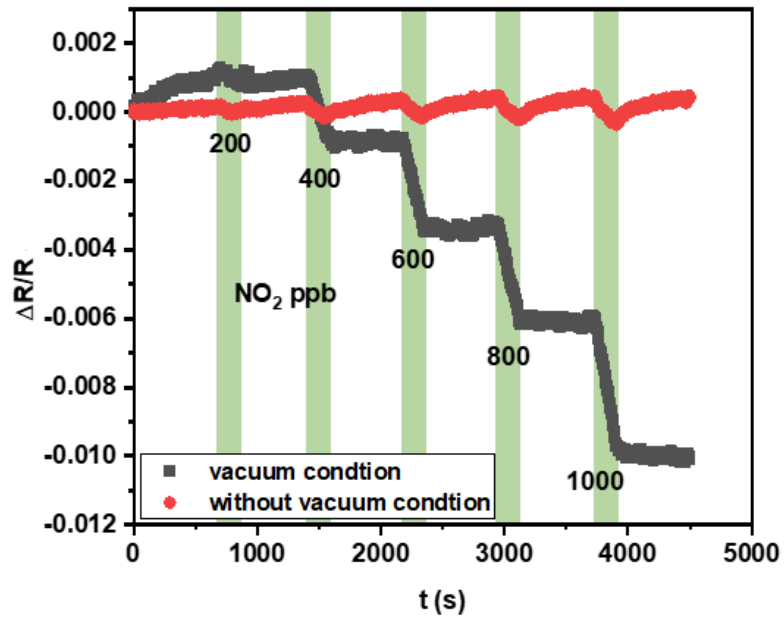


Figure 6.15: Shows both resistance responses for the device with the vacuumed condition and without vacuumed condition, which are presented by black and red curves, respectively. The change in resistance increase with  $\text{NO}_2$  concentration, and the columns represent the time of exposure to  $\text{NO}_2$ .

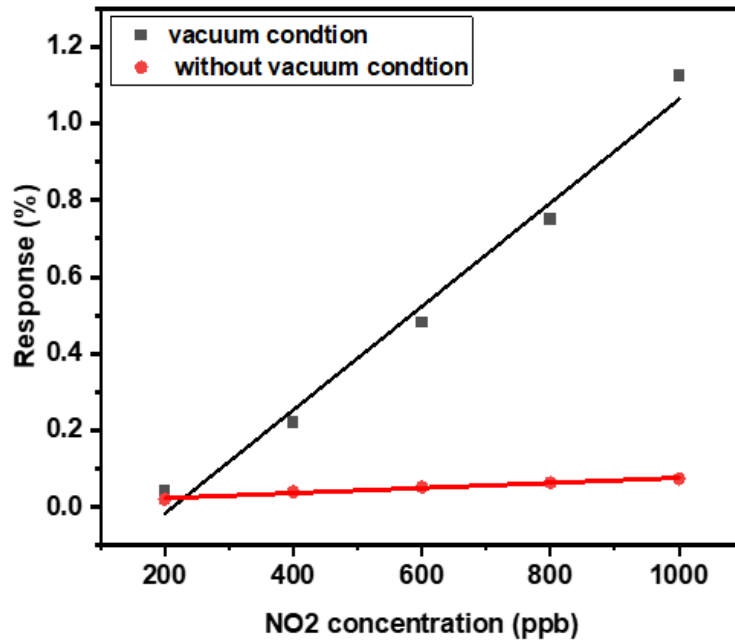


Figure 6.16: Shows the response percentage for the device with the vacuumed condition and without vacuumed condition up on exposure to different  $\text{NO}_2$  concentrations. The black and red lines are related to measurements for the device with vacuum conditions and without vacuum conditions, respectively.

### 6.2.5 Specificity Measurement

Detailed spectroscopy from section 5.3.2 has shown that the specialist gas obtained for ammonia testing did not contain ammonia. Instead, significant quantities of methanol ( $\text{CH}_3\text{OH}$ ) were detected along with the nitrogen carrier gas. While it was not possible to obtain an accurate concentration for methanol we are at least able to present results for methanol sensing in the following section. Many studies have been done on reduced graphene oxide and graphene oxide composite with polymer to detect  $\text{CH}_3\text{OH}$  gas [279-281].  $\text{CH}_3\text{OH}$  acts as an electron-withdrawing species, which should cause the resistance for the p-type graphene sensors to decrease during exposure [279].

One example of oxygen functionalisation of graphene sensors used a sensors based on reduced graphene oxide/conjugated polymer composite for detecting  $\text{CH}_3\text{OH}$  [279]. The sensors show high sensitivity to 1000 ppb of  $\text{CH}_3\text{OH}$  with a response of 1%. Another publication reported graphene-oxide-coated graphene-foam sensors with sensitivity to  $\text{CH}_3\text{OH}$  with a response of 8% [280]. The enhancement in sensitivity for both devices is attributed to the increase of active sites via the addition of oxygen groups and the composite material, which causes larger charge transfer from adsorbates.

Figures 6.17: a) and b) shows the sensing response for devices D1 and D2 during and after a 60 minutes exposure to the methanol nitrogen mixture. The black, red, blue, green, and grey curves represent the response for devices after 0, 30, 60, 90, and 120 minutes of oxidation, respectively. The response for the pristine sensors shows a small sensing signal, approximately reaching saturation after the 60 minutes dose duration. Following the methanol/nitrogen exposure the device recovers. When the same devices have been oxidised the response to the methanol mixture is suppressed for increasing oxidation up to an oxidation level of 60- or 90-minutes oxidation. Beyond this the sensitivity increases.

A further feature of the sensitivity for oxidised graphene samples to the methanol mixture is a continuous increasing tendency in the resistivity of the devices. Interestingly, this increase continues even after the end of the dosing of the analyte mixture.

Despite the unknown actual composition of the analyte mixture, we may make a few meaningful comments about the sensitivity of the oxidised sensors to a methanol analyte:

The first point is that the sensitivity towards methanol is decreased after oxidation with respect to sensitivity to  $\text{NO}_2$ . This is interesting as both of the analytes from this thesis  $\text{NO}_2$  and methanol are electron withdrawing, but we have introduced a symmetric response indication

that the specific chemistry of the analyte with the substrate is important for the introduction of sensor specificity.

The second point of interest is, that when observing the sensitivity of oxygen functionalised sensor at this low level of response, we have been able to identify a trend for continuous change in signal level during and after the methanol dose. Give that both the analyte and recovery mixture both contain nitrogen it would seem obvious that the oxidised graphene sensors are responding to nitrogen. However, the lack of this behaviour for the other testing carried out in this chapter suggest that there is maybe more at play, and possibly some other unknown component of the methanol/nitrogen mixture. While tantalizing this observation must ultimately be relegated to future work.

Recovery behaviour of the devices, post-oxidation, was difficult to estimate, as the resistance kept increasing under the N<sub>2</sub> flow. However, all the devices recovered to 95% of the original resistance after high vacuum conditions overnight.

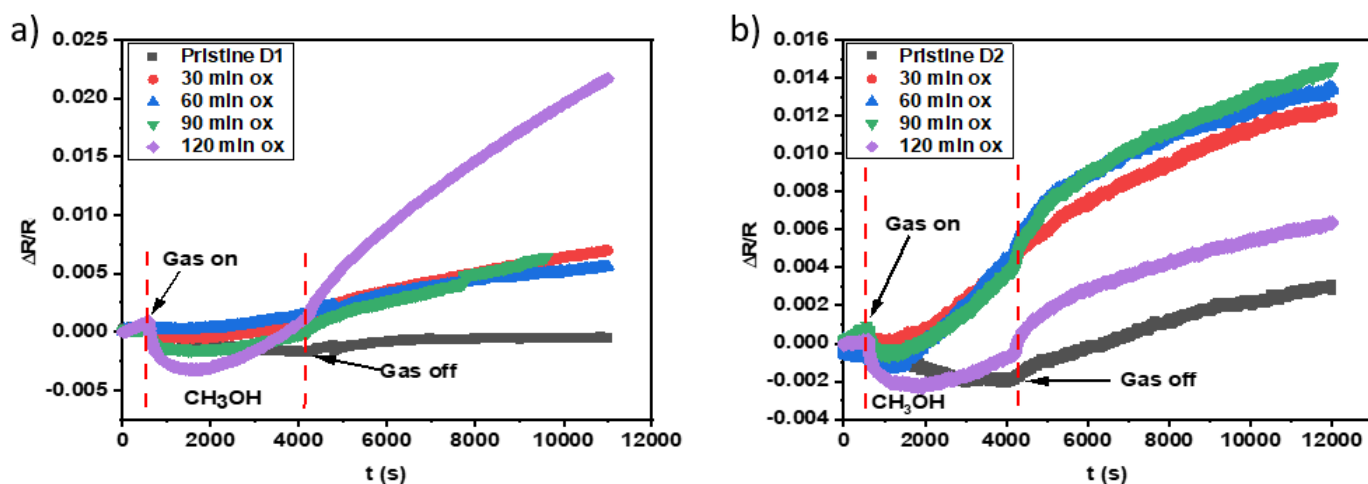


Figure 6.17: a and b) Response of graphene device D1 and D2 for CH<sub>3</sub>OH gas before and after each oxidation step, respectively. The black, red, blue, green, and grey curves represent the response result optioned from device after 0, 30, 60, 90, and 120 minutes of oxidation, respectively. The measurement is done at room temperature with a flow of N<sub>2</sub> during the recovery process.

This test concludes that the oxidised graphene device sensitivity increased to the maximum toward NO<sub>2</sub> after 60 minutes, as discussed earlier, while it decreased toward CH<sub>3</sub>OH. This shows that the selectivity for the sensors is improved after oxidation. In addition, the enhanced selectivity could be attributed to the increase of the hydroxyl groups (-OH) present

on the graphene sheet, which is favoured for the NO<sub>2</sub> adsorption, while the -OH is not favoured energetically for the CH<sub>3</sub>OH adsorption [282, 283]. Furthermore, at a higher oxidation time of 120 minutes, the sensitivity to CH<sub>3</sub>OH increased, which could be attributed to the increase of epoxy group (C-O) and carbonyl group (C=O) on the graphene sheet, which is favoured for CH<sub>3</sub>OH adsorption [282]. The take-home point of this study is that the sweet spot of oxidation to achieve high sensitivity and improve selectivity toward NO<sub>2</sub> is 60 minutes of oxidation. Whilst it seems that selectivity can be tuned towards methanol through more intensive oxidisation of the graphene sheet.

## Chapter 7

### 7 Conclusion and Future Work

This work was intended to improve CVD graphene-based sensors technology.

The absence of active sites on pristine graphene sensors limits their uses as gas sensors, as they have low sensitivity and selectivity. In addition, improving the graphene sensors by functionalising with nanoparticles is not applicable without breaking its planar  $sp^2$ -hybridization. Therefore, functionalising graphene by covalently adding functional oxygen groups is important as it disrupts its  $sp^2$  and provides active sites for gas adsorption. However, controlling the percentage of oxygen groups is important for retaining the high performance of graphene whilst providing simple chemical functional groups, and if it is useful, we might put other simple chemical functional groups rather than resorting to more complex functional groups or non-covalent functionalisation.

The research presented within this work addresses four areas which we believe are important for those interested in moving CVD graphene sensors to an industrial operation. Firstly, we have used the linear factor method for gas selectivity. As each gas molecule adsorbed on GFET donates a unique amount of charge, which will result in increasing the charge density of  $h/e$  and therefore changing the mobility of the GFET and shifting the Dirac point. We have demonstrated that linear factor from the inverse of mobility versus gate voltage ratio to differentiate between gases as introduced in Chapter 5.

Secondly, a path for functionalising CVD graphene with oxygen groups using  $H_2SO_4$  has been identified, which should be suitable for all the CVD graphene sensors. The recipes presented in this work are applicable for introducing low concentrations of oxygen groups on CVD graphene. In addition, the introduced oxygen percentage on CVD graphene is comparable to the lowest percentage achieved by highly reduced graphene oxide. The oxidation percentage could be controlled by controlling the exposure time to  $H_2SO_4$ .

Thirdly, the improved sensitivity and selectivity of functionalised GFETs with oxygen groups toward  $NO_2$ . The GFETs used in this work were initially doped by polymer residues that result from the polymer-assisted graphene-transfer process and show a limit of detection of 192 ppb of  $NO_2$ . The use of oxidation to GFETs was shown to increase the hydroxyl groups (-OH), which was believed to enhance the sensitivity to  $NO_2$  rather than  $NH_3$ . The oxidised sensors were shown to have an improvement of approximately 20% in sensitivity of up to

156 ppb of NO<sub>2</sub> after 60 minutes of oxidation. However, the NH<sub>3</sub> sensitivity test is not available due to the tested gas being found to be CH<sub>3</sub>OH rather than NH<sub>3</sub>.

As the test gas was CH<sub>3</sub>OH, the GFETs were tested for selectivity toward different oxidising agents and found to have high sensitivity toward NO<sub>2</sub>, while the sensitivity to CH<sub>3</sub>OH is reduced dramatically after 60 minutes of oxidation. However, the sensitivity to NO<sub>2</sub> is reduced after 120 minutes of oxidation and is increased for CH<sub>3</sub>OH. This adds to the selectivity being improved after oxidation, which is very important as the gas sensors need to be able to detect a certain type of gas in the gas mixture. Furthermore, the oxidised GFETs presented in this work show a higher response per ppb compared to all the reported values.

The fourth was the investigation of the impact of the vacuum conditioning on the device sensitivity and recovery. It was found that vacuum conditioning improved the sensitivity of the GFETs by 80%, compared with devices that did not undergo vacuum pre-conditioning, whilst the absence of vacuum pre-conditioning improved the recovery behaviour of GFET devices, reducing recovery times from 8 h to 9 minutes. The enhanced recovery time was attributed to a thin self-assembled hydrocarbon layer on top of the GFET devices, which originated from the ambient atmosphere.

## 7.1 Future Work

Multiple functional groups are used in sensors, as either electronic nose (e-nose) types arrays of sensors or by introducing multiple cross-sensitivities in a single sensor. The fingerprinting technique in Chapter 5 shows that there was scope for this. In-situ gating of samples is important for this, especially since that can be done in a very short time span. Therefore, the future work is to improve the sensing sensitivity for graphene FET sensors by using multiple devices in the same substrate and gate each device separately for a selective and fast sensor response by characterizing the data using Dirac point shifts and changes in mobility.

Many researchers use oxygen functional groups on graphene as a baseline for adding other materials (nanoparticles) to enhance sensitivity and selectivity. The fingerprinting results in Chapter 6 show that there was a baseline for this as oxidation does not sacrifice the graphene sensors' performance, as the amount of introduced oxygen is very low and comparable to the lowest amount of oxygen on reduced graphene oxide. Therefore, the future work of this research aims to enhance the sensitivity and selectivity by adding nanoparticles to the oxidised graphene. The growth and control of nanoparticles such as TiO<sub>2</sub> and ZnO on

oxidised graphene could lead to the combination of the flavour of the oxygen groups and nanoparticle material sensitivities. Therefore, this may result in a considerable improvement in sensors' sensitivity toward-detected gas type.

A further aim is to improve the sensitivity and selectivity by coating CVD graphene with graphene oxide to achieve high sensitivity. In addition, we aim to synthesise sulfur-doped oxidised graphene by evaporating sulfur powder on the oxidised graphene surface.

## Reference

- [1] B.-J. Kim and J.-S. Kim, "Gas sensing characteristics of MEMS gas sensor arrays in binary mixed-gas system," *Materials Chemistry and Physics*, vol. 138, no. 1, pp. 366-374, 2013.
- [2] R. Fuller *et al.*, "Pollution and health: a progress update," *The Lancet Planetary Health*, 2022.
- [3] J. Lee *et al.*, "High-performance gas sensor array for indoor air quality monitoring: The role of Au nanoparticles on WO<sub>3</sub>, SnO<sub>2</sub>, and NiO-based gas sensors," *Journal of Materials Chemistry A*, vol. 9, no. 2, pp. 1159-1167, 2021.
- [4] G. Sberveglieri, *Gas sensors: principles, operation and developments*. Springer Science & Business Media, 2012.
- [5] G. Korotcenkov and B. Cho, "Instability of metal oxide-based conductometric gas sensors and approaches to stability improvement (short survey)," *Sensors and Actuators B: Chemical*, vol. 156, no. 2, pp. 527-538, 2011.
- [6] T. C. Bond, G. D. Cole, L. L. Goddard, and E. M. Behymer, "Photonic MEMS for NIR in-situ Gas Detection and Identification," in *SENSORS, 2007 IEEE, 2007: IEEE*, pp. 1368-1371.
- [7] B. Bott and T. Jones, "A highly sensitive NO<sub>2</sub> sensor based on electrical conductivity changes in phthalocyanine films," *Sensors and Actuators*, vol. 5, no. 1, pp. 43-53, 1984.
- [8] T. Shukla, "Synthesis of tin oxide thick film and its investigation as a LPG sensor at room temperature," 2012.
- [9] J.-H. Kim, A. Mirzaei, H. W. Kim, and S. S. Kim, "Extremely sensitive and selective sub-ppm CO detection by the synergistic effect of Au nanoparticles and core-shell nanowires," *Sensors and Actuators B: Chemical*, vol. 249, pp. 177-188, 2017.
- [10] B. Sharma, A. Sharma, and J.-S. Kim, "Recent advances on H<sub>2</sub> sensor technologies based on MOX and FET devices: A review," *Sensors and Actuators B: Chemical*, vol. 262, pp. 758-770, 2018.
- [11] A. Maity and B. Ghosh, "Fast response paper based visual color change gas sensor for efficient ammonia detection at room temperature," *Scientific reports*, vol. 8, no. 1, pp. 1-10, 2018.
- [12] M. Shaik, V. Rao, M. Gupta, K. Murthy, and R. Jain, "Chemiresistive gas sensor for the sensitive detection of nitrogen dioxide based on nitrogen doped graphene nanosheets," *RSC advances*, vol. 6, no. 2, pp. 1527-1534, 2016.
- [13] S. Xue, S. Cao, Z. Huang, D. Yang, and G. Zhang, "Improving gas-sensing performance based on MOS nanomaterials: A review," *Materials*, vol. 14, no. 15, p. 4263, 2021.
- [14] M. Donarelli *et al.*, "Graphene oxide for gas detection under standard humidity conditions," *2D Materials*, vol. 2, no. 3, p. 035018, 2015.
- [15] Z. Li *et al.*, "A fast response & recovery H<sub>2</sub>S gas sensor based on  $\alpha$ -Fe<sub>2</sub>O<sub>3</sub> nanoparticles with ppb level detection limit," *Journal of hazardous materials*, vol. 300, pp. 167-174, 2015.
- [16] J. Zhang, X. Liu, G. Neri, and N. Pinna, "Nanostructured materials for room-temperature gas sensors," *Advanced materials*, vol. 28, no. 5, pp. 795-831, 2016.
- [17] Y. Han *et al.*, "Construction of MoS<sub>2</sub>/SnO<sub>2</sub> heterostructures for sensitive NO<sub>2</sub> detection at room temperature," *Applied Surface Science*, vol. 493, pp. 613-619, 2019.
- [18] Z. Yuan, E. Han, F. Meng, and K. Zuo, "Detection and identification of volatile organic compounds based on temperature-modulated ZnO sensors," *IEEE Transactions on Instrumentation and Measurement*, vol. 69, no. 7, pp. 4533-4544, 2019.
- [19] T. Wang, S. Liu, P. Sun, Y. Wang, K. Shimano, and G. Lu, "Unexpected and enhanced electrostatic adsorption capacity of oxygen vacancy-rich cobalt-doped In<sub>2</sub>O<sub>3</sub> for high-sensitive MEMS toluene sensor," *Sensors and Actuators B: Chemical*, vol. 342, p. 129949, 2021.
- [20] X. Yang, X. Yu, M. Jing, W. Song, J. Liu, and M. Ge, "Defective Mn<sub>x</sub>Zr<sub>1-x</sub>O<sub>2</sub> Solid Solution for the Catalytic Oxidation of Toluene: Insights into the Oxygen Vacancy Contribution," *ACS applied materials & interfaces*, vol. 11, no. 1, pp. 730-739, 2018.

- [21] Y. Zou *et al.*, "Generating oxygen vacancies in MnO hexagonal sheets for ultralong life lithium storage with high capacity," *ACS nano*, vol. 13, no. 2, pp. 2062-2071, 2019.
- [22] T. Li *et al.*, "The combination of two-dimensional nanomaterials with metal oxide nanoparticles for gas sensors: a review," *Nanomaterials*, vol. 12, no. 6, p. 982, 2022.
- [23] X. Wang *et al.*, "Ultrathin In<sub>2</sub>O<sub>3</sub> nanosheets with uniform mesopores for highly sensitive nitric oxide detection," *ACS applied materials & interfaces*, vol. 9, no. 19, pp. 16335-16342, 2017.
- [24] M. Epifani *et al.*, "The role of oxygen vacancies in the sensing properties of SnO<sub>2</sub> nanocrystals," in *SENSORS, 2008 IEEE*, 2008: IEEE, pp. 110-113.
- [25] H. Fei *et al.*, "Enhanced NO<sub>2</sub> sensing at room temperature with graphene via monodisperse polystyrene bead decoration," *ACS omega*, vol. 4, no. 2, pp. 3812-3819, 2019.
- [26] G. Williams and G. S. Coles, "NO<sub>x</sub> response of tin dioxide based gas sensors," *Sensors and Actuators B: Chemical*, vol. 16, no. 1-3, pp. 349-353, 1993.
- [27] P. Mitra, A. Chatterjee, and H. S. Maiti, "Chemical deposition of ZnO films for gas sensors," *Journal of Materials science: materials in electronics*, vol. 9, no. 6, pp. 441-445, 1998.
- [28] S. Yang, C. Jiang, and S.-h. Wei, "Gas sensing in 2D materials," *Applied Physics Reviews*, vol. 4, no. 2, p. 021304, 2017.
- [29] J.-L. Hou, T.-J. Hsueh, S.-Y. Fang, and S.-W. Kuo, "Gold Nanoparticles Decorated Copper Oxide Nanosheets Sensor for Hydrogen Sulfide Gas Sensing at Room Temperature," *Journal of The Electrochemical Society*, vol. 169, no. 8, p. 087510, 2022.
- [30] C. Zhang, Y. Luo, J. Xu, and M. Debligny, "Room temperature conductive type metal oxide semiconductor gas sensors for NO<sub>2</sub> detection," *Sensors and Actuators A: Physical*, vol. 289, pp. 118-133, 2019.
- [31] H. Choi, H. Y. Jeong, D.-S. Lee, C.-G. Choi, and S.-Y. Choi, "Flexible NO<sub>2</sub> gas sensor using multilayer graphene films by chemical vapor deposition," *Carbon letters*, vol. 14, no. 3, pp. 186-189, 2013.
- [32] J. W. Fergus, "Materials for high temperature electrochemical NO<sub>x</sub> gas sensors," *Sensors and Actuators B: Chemical*, vol. 121, no. 2, pp. 652-663, 2007.
- [33] A. Azad, S. Akbar, S. Mhaisalkar, L. Birkefeld, and K. Goto, "Solid-state gas sensors: A review," *Journal of the Electrochemical Society*, vol. 139, no. 12, p. 3690, 1992.
- [34] A. Dey, "Semiconductor metal oxide gas sensors: A review," *Materials Science and Engineering: B*, vol. 229, pp. 206-217, 2018.
- [35] T.-V. Dinh, I.-Y. Choi, Y.-S. Son, and J.-C. Kim, "A review on non-dispersive infrared gas sensors: Improvement of sensor detection limit and interference correction," *Sensors and Actuators B: Chemical*, vol. 231, pp. 529-538, 2016.
- [36] J. Zhang, Z. Qin, D. Zeng, and C. Xie, "Metal-oxide-semiconductor based gas sensors: screening, preparation, and integration," *Physical Chemistry Chemical Physics*, vol. 19, no. 9, pp. 6313-6329, 2017.
- [37] R. Alrammouz, J. Podlecki, P. Abboud, B. Sorli, and R. Habchi, "A review on flexible gas sensors: From materials to devices," *Sensors and Actuators A: Physical*, vol. 284, pp. 209-231, 2018.
- [38] T. Lin, X. Lv, S. Li, and Q. Wang, "The morphologies of the semiconductor oxides and their gas-sensing properties," *Sensors*, vol. 17, no. 12, p. 2779, 2017.
- [39] A. Kumar, M. Kumar, R. Kumar, R. Singh, B. Prasad, and D. Kumar, "Numerical model for the chemical adsorption of oxygen and reducing gas molecules in presence of humidity on the surface of semiconductor metal oxide for gas sensors applications," *Materials Science in Semiconductor Processing*, vol. 90, pp. 236-244, 2019.
- [40] S. G. Chatterjee, S. Chatterjee, A. K. Ray, and A. K. Chakraborty, "Graphene-metal oxide nanohybrids for toxic gas sensor: a review," *Sensors and Actuators B: Chemical*, vol. 221, pp. 1170-1181, 2015.

- [41] M. Al-Hashem, S. Akbar, and P. Morris, "Role of oxygen vacancies in nanostructured metal-oxide gas sensors: a review," *Sensors and Actuators B: Chemical*, vol. 301, p. 126845, 2019.
- [42] M. E. Franke, T.J. Koplin, and U. Simon, "Metal and metal oxide nanoparticles in chemiresistors: does the nanoscale matter?," *small*, vol. 2, no. 1, pp. 36-50, 2006.
- [43] Y. Liu *et al.*, "Magnetic-Induced-Piezopotential Gated MoS<sub>2</sub> Field-Effect Transistor at Room Temperature," *Advanced Materials*, vol. 30, no. 8, p. 1704524, 2018.
- [44] N. A. M. Tran *et al.*, "Graphene field effect transistor scaling for ultra-low-noise sensors," *Nanotechnology*, vol. 32, no. 4, p. 045502, 2020.
- [45] C.-O. Park, J. Fergus, N. Miura, J. Park, and A. Choi, "Solid-state electrochemical gas sensors," *Ionics*, vol. 15, no. 3, pp. 261-284, 2009.
- [46] R. Hanafi, R. D. Mayasari, Masmui, Agustanhakri, J. Raharjo, and R. Nuryadi, "Electrochemical sensor for environmental monitoring system: A review," in *AIP Conference Proceedings*, 2019, vol. 2169, no. 1: AIP Publishing LLC, p. 030007.
- [47] M. El Achhab and K. Schierbaum, "Gas sensors based on plasma-electrochemically oxidized titanium foils," *Journal of sensors and sensor systems*, vol. 5, no. 2, pp. 273-281, 2016.
- [48] T. Aldhafeeri, M.-K. Tran, R. Vrolyk, M. Pope, and M. Fowler, "A review of methane gas detection sensors: Recent developments and future perspectives," *Inventions*, vol. 5, no. 3, p. 28, 2020.
- [49] P. Yáñez-Sedeno, J. M. Pingarrón, J. Riu, and F. X. Rius, "Electrochemical sensing based on carbon nanotubes," *TrAC Trends in Analytical Chemistry*, vol. 29, no. 9, pp. 939-953, 2010.
- [50] P. Krebs and A. Grisel, "A low power integrated catalytic gas sensor," *Sensors and Actuators B: Chemical*, vol. 13, no. 1-3, pp. 155-158, 1993.
- [51] A. Austin, "Comparing catalytic vs. infrared gas monitors: each proven technology has its pros and cons for monitoring combustible gases in the workplace. A site-specific analysis will reveal the best approach.(Environmental Manager)," *Chemical Engineering*, vol. 109, no. 1, pp. 75-79, 2002.
- [52] D. Gibson and C. MacGregor, "A novel solid state non-dispersive infrared CO<sub>2</sub> gas sensor compatible with wireless and portable deployment," *Sensors*, vol. 13, no. 6, pp. 7079-7103, 2013.
- [53] Y. Xing, B. Urasinska-Wojcik, and J. W. Gardner, "Plasmonic enhanced CMOS non-dispersive infrared gas sensor for acetone and ammonia detection," in *2018 IEEE International Instrumentation and Measurement Technology Conference (I2MTC)*, 2018: IEEE, pp. 1-5.
- [54] J. Y. Chong, B. Wang, P. C. Sherrell, F. M. Pesci, C. Mattevi, and K. Li, "Fabrication of Graphene-Covered Micro-Tubes for Process Intensification," *Advanced Engineering Materials*, vol. 21, no. 11, p. 1900642, 2019.
- [55] S. S. Varghese, S. H. Varghese, S. Swaminathan, K. K. Singh, and V. Mittal, "Two-dimensional materials for sensing: graphene and beyond," *Electronics*, vol. 4, no. 3, pp. 651-687, 2015.
- [56] N. Alzate-Carvajal and A. Luican-Mayer, "Functionalized graphene surfaces for selective gas sensing," *ACS omega*, vol. 5, no. 34, pp. 21320-21329, 2020.
- [57] D. Sun, Y. Luo, M. Debliquy, and C. Zhang, "Graphene-enhanced metal oxide gas sensors at room temperature: A review," *Beilstein journal of nanotechnology*, vol. 9, no. 1, pp. 2832-2844, 2018.
- [58] J. Wei, B. Liang, Q. Cao, H. Ren, Y. Zheng, and X. Ye, "Understanding asymmetric transfer characteristics and hysteresis behaviors in graphene devices under different chemical atmospheres," *Carbon*, vol. 156, pp. 67-76, 2020.
- [59] W. Tian, X. Liu, and W. Yu, "Research progress of gas sensor based on graphene and its derivatives: A review," *Applied Sciences*, vol. 8, no. 7, p. 1118, 2018.
- [60] M. Gautam and A. H. Jayatissa, "Gas sensing properties of graphene synthesized by chemical vapor deposition," *Materials Science and Engineering: C*, vol. 31, no. 7, pp. 1405-1411, 2011.
- [61] H. Liu *et al.*, "AC phase sensing of graphene FETs for chemical vapors with fast recovery and minimal baseline drift," *Sensors and Actuators B: Chemical*, vol. 263, pp. 94-102, 2018.

- [62] A. K. Geim and K. S. Novoselov, "The rise of graphene," *Nature materials*, vol. 6, no. 3, pp. 183-191, 2007.
- [63] G. R. Bhimanapati *et al.*, "Recent advances in two-dimensional materials beyond graphene," *ACS nano*, vol. 9, no. 12, pp. 11509-11539, 2015.
- [64] Y. R. Choi *et al.*, "Role of oxygen functional groups in graphene oxide for reversible room-temperature NO<sub>2</sub> sensing," *Carbon*, vol. 91, pp. 178-187, 2015.
- [65] A. G. Bannov, J. Prášek, O. Jašek, and L. Zajíčková, "Investigation of pristine graphite oxide as room-temperature chemiresistive ammonia gas sensing material," *Sensors*, vol. 17, no. 2, p. 320, 2017.
- [66] D. Shahdeo, A. Roberts, N. Abbineni, and S. Gandhi, "Graphene based sensors," in *Comprehensive Analytical Chemistry*, vol. 91: Elsevier, 2020, pp. 175-199.
- [67] X. Huang, N. Hu, L. Zhang, L. Wei, H. Wei, and Y. Zhang, "The NH<sub>3</sub> sensing properties of gas sensors based on aniline reduced graphene oxide," *Synthetic metals*, vol. 185, pp. 25-30, 2013.
- [68] Y. Wang *et al.*, "Structural evolution in CVD graphene chemically oxidized by sulphuric acid," *Journal of Raman Spectroscopy*, vol. 46, no. 3, pp. 283-286, 2015.
- [69] M. G. Chung *et al.*, "Highly sensitive NO<sub>2</sub> gas sensor based on ozone treated graphene," *Sensors and Actuators B: Chemical*, vol. 166, pp. 172-176, 2012.
- [70] J. Park, Y. Kim, S. Y. Park, S. J. Sung, H. W. Jang, and C. R. Park, "Band gap engineering of graphene oxide for ultrasensitive NO<sub>2</sub> gas sensing," *Carbon*, vol. 159, pp. 175-184, 2020.
- [71] K. S. Novoselov *et al.*, "Electric field effect in atomically thin carbon films," *science*, vol. 306, no. 5696, pp. 666-669, 2004.
- [72] T. Wehling *et al.*, "Molecular doping of graphene," *Nanoletters*, vol. 8, no. 1, pp. 173-177, 2008.
- [73] O. Leenaerts, B. Partoens, and F. Peeters, "Adsorption of H<sub>2</sub>O, NH<sub>3</sub>, CO, NO<sub>2</sub>, and NO on graphene: A first-principles study," *Physical Review B*, vol. 77, no. 12, p. 125416, 2008.
- [74] S. Tang and Z. Cao, "Adsorption of nitrogen oxides on graphene and graphene oxides: Insights from density functional calculations," *The Journal of chemical physics*, vol. 134, no. 4, p. 044710, 2011.
- [75] E. C. Mattson *et al.*, "Exploring adsorption and reactivity of NH<sub>3</sub> on reduced graphene oxide," *The Journal of Physical Chemistry C*, vol. 117, no. 20, pp. 10698-10707, 2013.
- [76] Y. Peng and J. Li, "Ammonia adsorption on graphene and graphene oxide: a first-principles study," *Frontiers of Environmental Science & Engineering*, vol. 7, no. 3, pp. 403-411, 2013.
- [77] F. Schedin *et al.*, "Detection of individual gas molecules adsorbed on graphene," *Nature materials*, vol. 6, no. 9, pp. 652-655, 2007.
- [78] S. Novikov, N. Lebedeva, A. Satrapinski, J. Walden, V. Davydov, and A. Lebedev, "Graphene based sensor for environmental monitoring of NO<sub>2</sub>," *Sensors and Actuators B: Chemical*, vol. 236, pp. 1054-1060, 2016.
- [79] F. Yavari, E. Castillo, H. Gullapalli, P. M. Ajayan, and N. Koratkar, "High sensitivity detection of NO<sub>2</sub> and NH<sub>3</sub> in air using chemical vapor deposition grown graphene," *Applied Physics Letters*, vol. 100, no. 20, p. 203120, 2012.
- [80] A. Singh *et al.*, "Electrically tunable molecular doping of graphene," *Applied Physics Letters*, vol. 102, no. 4, p. 043101, 2013.
- [81] G. Lu, L. E. Ocola, and J. Chen, "Gas detection using low-temperature reduced graphene oxide sheets," *Applied Physics Letters*, vol. 94, no. 8, p. 083111, 2009.
- [82] S. A. Evlashin *et al.*, "Ambient condition production of high quality reduced graphene oxide," *Advanced Materials Interfaces*, vol. 5, no. 18, p. 1800737, 2018.
- [83] N. Hu *et al.*, "Ultrafast and sensitive room temperature NH<sub>3</sub> gas sensors based on chemically reduced graphene oxide," *Nanotechnology*, vol. 25, no. 2, p. 025502, 2013.

- [84] X. Wang, X. Li, Y. Zhao, Y. Chen, J. Yu, and J. Wang, "The influence of oxygen functional groups on gas-sensing properties of reduced graphene oxide (rGO) at room temperature," *RSC advances*, vol. 6, no. 57, pp. 52339-52346, 2016.
- [85] Y. Zhou *et al.*, "Impact of further thermal reduction on few-layer reduced graphene oxide film and its np transition for gas sensing," *Sensors and Actuators B: Chemical*, vol. 235, pp. 241-250, 2016.
- [86] Y. J. Yun *et al.*, "A 3D scaffold for ultra-sensitive reduced graphene oxide gas sensors," *Nanoscale*, vol. 6, no. 12, pp. 6511-6514, 2014.
- [87] H. Li, A. Singh, A. S. Childress, and G. Koley, "Sensing Characteristic Enhancement of Oxygen Plasma Treated Graphene," in *2018 IEEE 13th Nanotechnology Materials and Devices Conference (NMDC)*, 2018: IEEE, pp. 1-4.
- [88] H. Wu *et al.*, "A gas sensing channel composited with pristine and oxygen plasma-treated graphene," *Sensors*, vol. 19, no. 3, p. 625, 2019.
- [89] Q. Li *et al.*, "Highly sensitive graphene ammonia sensor enhanced by concentrated nitric acid treatment," *Applied Surface Science*, vol. 586, p. 152689, 2022.
- [90] R. Singla and A. Kottantharayil, "Stable hydroxyl functionalization and p-type doping of graphene by a non-destructive photo-chemical method," *Carbon*, vol. 152, pp. 267-273, 2019.
- [91] A. Butko *et al.*, "Detection of lysine molecular ions in solution gated field effect transistors based on unmodified graphene," *Journal of Applied Physics*, vol. 128, no. 21, p. 215302, 2020.
- [92] H. E. Romero *et al.*, "Adsorption of ammonia on graphene," *Nanotechnology*, vol. 20, no. 24, p. 245501, 2009.
- [93] M. Gautam and A. H. Jayatissa, "Ammonia gas sensing behavior of graphene surface decorated with gold nanoparticles," *Solid-State Electronics*, vol. 78, pp. 159-165, 2012.
- [94] S. Chen *et al.*, "Adsorption/desorption and electrically controlled flipping of ammonia molecules on graphene," *New Journal of Physics*, vol. 12, no. 12, p. 125011, 2010.
- [95] A. Calvi, A. Ferrari, L. Sbuelz, A. Goldoni, and S. Modesti, "Recognizing physisorption and chemisorption in carbon nanotubes gas sensors by double exponential fitting of the response," *Sensors*, vol. 16, no. 5, p. 731, 2016.
- [96] A. K. Geim, "Graphene: status and prospects," *science*, vol. 324, no. 5934, pp. 1530-1534, 2009.
- [97] B. Y.-K. Hu, E. Hwang, and S. D. Sarma, "Density of states of disordered graphene," *Physical Review B*, vol. 78, no. 16, p. 165411, 2008.
- [98] W. Yuan and G. Shi, "Graphene-based gas sensors," *Journal of Materials Chemistry A*, vol. 1, no. 35, pp. 10078-10091, 2013.
- [99] E. W. Hill, A. Vijayaraghavan, and K. Novoselov, "Graphene sensors," *IEEE Sensors Journal*, vol. 11, no. 12, pp. 3161-3170, 2011.
- [100] A. D. Smith *et al.*, "Graphene-based CO<sub>2</sub> sensing and its cross-sensitivity with humidity," *RSC advances*, vol. 7, no. 36, pp. 22329-22339, 2017.
- [101] T. Wang *et al.*, "A review on graphene-based gas/vapor sensors with unique properties and potential applications," *Nano-Micro Letters*, vol. 8, pp. 95-119, 2016.
- [102] J. R. Lima, "Controlling the energy gap of graphene by Fermi velocity engineering," *Physics Letters A*, vol. 379, no. 3, pp. 179-182, 2015.
- [103] A. C. Neto, F. Guinea, N. M. Peres, K. S. Novoselov, and A. K. Geim, "The electronic properties of graphene," *Reviews of modern physics*, vol. 81, no. 1, p. 109, 2009.
- [104] P. R. Wallace, "The band theory of graphite," *Physical review*, vol. 71, no. 9, p. 622, 1947.
- [105] K. I. Bolotin *et al.*, "Ultrahigh electron mobility in suspended graphene," *Solid state communications*, vol. 146, no. 9-10, pp. 351-355, 2008.
- [106] N. Lindvall, *Towards graphene-based devices: Fabrication and characterization*. Chalmers Tekniska Hogskola (Sweden), 2012.

- [107] S. Sahu and G. Rout, "Band gap opening in graphene: a short theoretical study," *International Nano Letters*, vol. 7, no. 2, pp. 81-89, 2017.
- [108] N. K. Chowdhury and B. Bhowmik, "Role of graphene-metal oxide composite for performance improvement of chemical sensor: Study for various analytes," in *AIP Conference Proceedings*, 2021, vol. 2341, no. 1: AIP Publishing LLC, p. 040011.
- [109] A. Chauhan *et al.*, "Enhancement of the carrier mobility of conducting polymers by formation of their graphene composites," *RSC advances*, vol. 7, no. 20, pp. 11913-11920, 2017.
- [110] L. S. Hui, E. Whiteway, M. Hilke, and A. Turak, "Synergistic oxidation of CVD graphene on Cu by oxygen plasma etching," *Carbon*, vol. 125, pp. 500-508, 2017.
- [111] W. S. Hummers Jr and R. E. Offeman, "Preparation of graphitic oxide," *Journal of the American Chemical Society*, vol. 80, no. 6, pp. 1339-1339, 1958.
- [112] D. C. Marcano *et al.*, "Improved synthesis of graphene oxide," *ACS nano*, vol. 4, no. 8, pp. 4806-4814, 2010.
- [113] S. Stankovich *et al.*, "Synthesis of graphene-based nanosheets via chemical reduction of exfoliated graphite oxide," *carbon*, vol. 45, no. 7, pp. 1558-1565, 2007.
- [114] F. Ye, B. Zhao, R. Ran, and Z. Shao, "Facile mechanochemical synthesis of nano SnO<sub>2</sub>/graphene composite from coarse metallic Sn and graphite oxide: an outstanding anode material for lithium-ion batteries," *Chemistry—A European Journal*, vol. 20, no. 14, pp. 4055-4063, 2014.
- [115] G. Lee, B. Lee, J. Kim, and K. Cho, "Ozone adsorption on graphene: ab initio study and experimental validation," *The Journal of Physical Chemistry C*, vol. 113, no. 32, pp. 14225-14229, 2009.
- [116] J. Simmons *et al.*, "Effect of ozone oxidation on single-walled carbon nanotubes," *The journal of physical chemistry B*, vol. 110, no. 14, pp. 7113-7118, 2006.
- [117] S. Pei and H.-M. Cheng, "The reduction of graphene oxide," *Carbon*, vol. 50, no. 9, pp. 3210-3228, 2012.
- [118] F. Bonaccorso, A. Lombardo, T. Hasan, Z. Sun, L. Colombo, and A. C. Ferrari, "Production and processing of graphene and 2d crystals," *Materials today*, vol. 15, no. 12, pp. 564-589, 2012.
- [119] X. Liang, Z. Fu, and S. Y. Chou, "Graphene transistors fabricated via transfer-printing in device active-areas on large wafer," *Nano letters*, vol. 7, no. 12, pp. 3840-3844, 2007.
- [120] M. Bhuyan, S. Alam, M. Uddin, M. Islam, F. A. Bipasha, and S. S. Hossain, "Synthesis of graphene," *International Nano Letters*, vol. 6, no. 2, pp. 65-83, 2016.
- [121] A. G. Kelly *et al.*, "All-printed thin-film transistors from networks of liquid-exfoliated nanosheets," *Science*, vol. 356, no. 6333, pp. 69-73, 2017.
- [122] C.-J. Shih, S. Lin, M. S. Strano, and D. Blankshtein, "Understanding the stabilization of liquid-phase-exfoliated graphene in polar solvents: molecular dynamics simulations and kinetic theory of colloid aggregation," *Journal of the American Chemical Society*, vol. 132, no. 41, pp. 14638-14648, 2010.
- [123] D. Parviz, F. Irin, S. A. Shah, S. Das, C. B. Sweeney, and M. J. Green, "Challenges in liquid-phase exfoliation, processing, and assembly of pristine graphene," *Advanced Materials*, vol. 28, no. 40, pp. 8796-8818, 2016.
- [124] T. Chen *et al.*, "High throughput exfoliation of graphene oxide from expanded graphite with assistance of strong oxidant in modified Hummers method," in *Journal of Physics: Conference Series*, 2009, vol. 188, no. 1: IOP Publishing, p. 012051.
- [125] R. Mas-Balleste, C. Gomez-Navarro, J. Gomez-Herrero, and F. Zamora, "2D materials: to graphene and beyond," *Nanoscale*, vol. 3, no. 1, pp. 20-30, 2011.
- [126] Y. Hernandez, V. Nicolosi, M. Lotya, F. Blighe, and Z. Sun, "S. de, IT McGovern, B," *Holland, M. Byrne, YK Gun'ko, JJ Boland, P. Niraj, G. Duesberg, S. Krishnamurthy, R. Goodhue, J. Hutchison, V. Scardaci, AC Ferrari, JN Coleman, High-yield production of graphene by liquid-phase exfoliation of graphite. Nat. Nanotechnol*, vol. 3, pp. 563-568, 2008.

- [127] X. Wu *et al.*, "Growth of continuous monolayer graphene with millimeter-sized domains using industrially safe conditions," *Scientific reports*, vol. 6, no. 1, pp. 1-7, 2016.
- [128] N. Mishra, J. Boeckl, N. Motta, and F. Iacopi, "Graphene growth on silicon carbide: A review (Phys. Status Solidi A 9/ 2016)," *Physica Status Solidi (A) Applications and Materials Science*, 2016.
- [129] M. Choucair, P. Thordarson, and J. A. Stride, "Gram-scale production of graphene based on solvothermal synthesis and sonication," *Nature nanotechnology*, vol. 4, no. 1, pp. 30-33, 2009.
- [130] M. Ruan *et al.*, "Epitaxial graphene on silicon carbide: Introduction to structured graphene," *Mrs Bulletin*, vol. 37, no. 12, pp. 1138-1147, 2012.
- [131] K. Emtsev, F. Speck, T. Seyller, L. Ley, and J. D. Riley, "Interaction, growth, and ordering of epitaxial graphene on SiC {0001} surfaces: A comparative photoelectron spectroscopy study," *Physical review B*, vol. 77, no. 15, p. 155303, 2008.
- [132] J. Hass *et al.*, "Structural properties of the multilayer graphene/4H-SiC (000 1<sup>-</sup>) system as determined by surface x-ray diffraction," *Physical Review B*, vol. 75, no. 21, p. 214109, 2007.
- [133] N. Archer, "Chemical vapour deposition," *Physics in Technology*, vol. 10, no. 4, p. 152, 1979.
- [134] B. Deng, Z. Liu, and H. Peng, "Toward mass production of CVD graphene films," *Advanced Materials*, vol. 31, no. 9, p. 1800996, 2019.
- [135] L. Lin, H. Peng, and Z. Liu, "Synthesis challenges for graphene industry," *Nature materials*, vol. 18, no. 6, pp. 520-524, 2019.
- [136] S. Chaitoglou and E. Bertran, "Effect of temperature on graphene grown by chemical vapor deposition," *Journal of Materials Science*, vol. 52, no. 13, pp. 8348-8356, 2017.
- [137] A. Guermoune *et al.*, "Chemical vapor deposition synthesis of graphene on copper with methanol, ethanol, and propanol precursors," *Carbon*, vol. 49, no. 13, pp. 4204-4210, 2011.
- [138] Z. Sun, Z. Yan, J. Yao, E. Beitler, Y. Zhu, and J. M. Tour, "Growth of graphene from solid carbon sources," *Nature*, vol. 468, no. 7323, pp. 549-552, 2010.
- [139] R. B. McLellan, "The solubility of carbon in solid gold, copper, and silver," *Scripta Metallurgica*, vol. 3, no. 6, pp. 389-391, 1969.
- [140] G. López and E. Mittemeijer, "The solubility of C in solid Cu," *Scripta Materialia*, vol. 51, no. 1, pp. 1-5, 2004.
- [141] X. Li, W. Cai, L. Colombo, and R. S. Ruoff, "Evolution of graphene growth on Ni and Cu by carbon isotope labeling," *Nano letters*, vol. 9, no. 12, pp. 4268-4272, 2009.
- [142] M. Losurdo, M. M. Giangregorio, P. Capezzuto, and G. Bruno, "Graphene CVD growth on copper and nickel: role of hydrogen in kinetics and structure," *Physical Chemistry Chemical Physics*, vol. 13, no. 46, pp. 20836-20843, 2011.
- [143] X. Li *et al.*, "Large-area synthesis of high-quality and uniform graphene films on copper foils," *science*, vol. 324, no. 5932, pp. 1312-1314, 2009.
- [144] Y. Hao *et al.*, "The role of surface oxygen in the growth of large single-crystal graphene on copper," *Science*, vol. 342, no. 6159, pp. 720-723, 2013.
- [145] X. Xu *et al.*, "Ultrafast growth of single-crystal graphene assisted by a continuous oxygen supply," *Nature nanotechnology*, vol. 11, no. 11, pp. 930-935, 2016.
- [146] P. Braeuninger-Weimer, B. Brennan, A. J. Pollard, and S. Hofmann, "Understanding and controlling Cu-catalyzed graphene nucleation: the role of impurities, roughness, and oxygen scavenging," *Chemistry of materials*, vol. 28, no. 24, pp. 8905-8915, 2016.
- [147] I. Meric, M. Y. Han, A. F. Young, B. Ozyilmaz, P. Kim, and K. L. Shepard, "Current saturation in zero-bandgap, top-gated graphene field-effect transistors," *Nature nanotechnology*, vol. 3, no. 11, pp. 654-659, 2008.
- [148] J.-H. Chen, C. Jang, S. Xiao, M. Ishigami, and M. S. Fuhrer, "Intrinsic and extrinsic performance limits of graphene devices on SiO<sub>2</sub>," *Nature nanotechnology*, vol. 3, no. 4, pp. 206-209, 2008.

- [149] S. Adam, E. Hwang, V. Galitski, and S. Das Sarma, "A self-consistent theory for graphene transport," *Proceedings of the National Academy of Sciences*, vol. 104, no. 47, pp. 18392-18397, 2007.
- [150] J. Martin *et al.*, "Observation of electron-hole puddles in graphene using a scanning single-electron transistor," *Nature physics*, vol. 4, no. 2, pp. 144-148, 2008.
- [151] J.-H. Chen, C. Jang, S. Adam, M. Fuhrer, E. D. Williams, and M. Ishigami, "Charged-impurity scattering in graphene," *Nature physics*, vol. 4, no. 5, pp. 377-381, 2008.
- [152] K. I. Bolotin, K. J. Sikes, J. Hone, H. Stormer, and P. Kim, "Temperature-dependent transport in suspended graphene," *Physical review letters*, vol. 101, no. 9, p. 096802, 2008.
- [153] X. Du, I. Skachko, A. Barker, and E. Y. Andrei, "Approaching ballistic transport in suspended graphene," *Nature nanotechnology*, vol. 3, no. 8, pp. 491-495, 2008.
- [154] F. Schwierz and J. J. Liou, "RF transistors: Recent developments and roadmap toward terahertz applications," *Solid-State Electronics*, vol. 51, no. 8, pp. 1079-1091, 2007.
- [155] A. Khakifirooz and D. A. Antoniadis, "Transistor performance scaling: The role of virtual source velocity and its mobility dependence," in *2006 International Electron Devices Meeting, 2006: IEEE*, pp. 1-4.
- [156] M. Łuszczek, M. Turzyński, and D. Świsulski, "Modelling of Graphene Field-Effect Transistor for electronic sensing applications," *Przeegląd Elektrotechniczny*, vol. 91, no. 10, pp. 170-172, 2015.
- [157] Y. Zhang, E. E. Mendez, and X. Du, "Mobility-dependent low-frequency noise in graphene field-effect transistors," *ACS nano*, vol. 5, no. 10, pp. 8124-8130, 2011.
- [158] M. Donarelli and L. Ottaviano, "2D materials for gas sensing applications: a review on graphene oxide, MoS<sub>2</sub>, WS<sub>2</sub> and phosphorene," *Sensors*, vol. 18, no. 11, p. 3638, 2018.
- [159] G. Neri, "First fifty years of chemoresistive gas sensors," *Chemosensors*, vol. 3, no. 1, pp. 1-20, 2015.
- [160] K.-S. Kim *et al.*, "Chemical vapor deposition-grown graphene: the thinnest solid lubricant," *ACS nano*, vol. 5, no. 6, pp. 5107-5114, 2011.
- [161] R. Muller, T. Kamins, and M. Chan, "Device Electronics for Integrated Circuits 3rd edn John Wiley & Sons," ed: Inc, 2003.
- [162] R. Ghosh, A. Midya, S. Santra, S. K. Ray, and P. K. Guha, "Chemically reduced graphene oxide for ammonia detection at room temperature," *ACS applied materials & interfaces*, vol. 5, no. 15, pp. 7599-7603, 2013.
- [163] P. Tiwary, S. Chatterjee, S. Singha, R. Mahapatra, and A. K. Chakraborty, "Room temperature ethanol sensing by chemically reduced graphene oxide film," *FlatChem*, vol. 30, p. 100317, 2021.
- [164] J. T. Robinson, F. K. Perkins, E. S. Snow, Z. Wei, and P. E. Sheehan, "Reduced graphene oxide molecular sensors," *Nano letters*, vol. 8, no. 10, pp. 3137-3140, 2008.
- [165] L. Guo *et al.*, "Improved NO<sub>2</sub> gas sensing properties of graphene oxide reduced by two-beam-laser interference," *Scientific reports*, vol. 8, no. 1, pp. 1-7, 2018.
- [166] V. Dua *et al.*, "All-organic vapor sensor using inkjet-printed reduced graphene oxide," *Angewandte Chemie International Edition*, vol. 49, no. 12, pp. 2154-2157, 2010.
- [167] T. V. Khai, M. Prachuporn, and K.-B. Shim, "NO<sub>2</sub> gas sensing based on graphene synthesized via chemical reduction process of exfoliated graphene oxide," *Journal of the Korean Crystal Growth and Crystal Technology*, vol. 22, no. 2, pp. 84-91, 2012.
- [168] S. Drewniak, M. Procek, R. Muzyka, and T. Pustelny, "Comparison of Gas Sensing Properties of Reduced Graphene Oxide Obtained by Two Different Methods," *Sensors*, vol. 20, no. 11, p. 3175, 2020.
- [169] C. R. Minitha, V. S. Anithaa, V. Subramaniam, and R. T. Rajendra Kumar, "Impact of oxygen functional groups on reduced graphene oxide-based sensors for ammonia and toluene detection at room temperature," *ACS omega*, vol. 3, no. 4, pp. 4105-4112, 2018.

- [170] S. Zhu, H. Sun, X. Liu, J. Zhuang, and L. Zhao, "Room-temperature NH<sub>3</sub> sensing of graphene oxide film and its enhanced response on the laser-textured silicon," *Scientific reports*, vol. 7, no. 1, pp. 1-8, 2017.
- [171] F. Khurshid, M. Jeyavelan, T. Hussain, M. S. L. Hudson, and S. Nagarajan, "Ammonia gas adsorption study on graphene oxide based sensing device under different humidity conditions," *Materials Chemistry and Physics*, vol. 242, p. 122485, 2020.
- [172] N. Sharma, V. Sharma, S. Sharma, and K. Sachdev, "Gas sensing behaviour of green synthesized reduced graphene oxide (rGO) for H<sub>2</sub> and NO," *Materials Letters*, vol. 236, pp. 444-447, 2019.
- [173] W. Li *et al.*, "Reduced graphene oxide electrically contacted graphene sensor for highly sensitive nitric oxide detection," *ACS nano*, vol. 5, no. 9, pp. 6955-6961, 2011.
- [174] J. M. Kay and R. M. Nedderman, *Fluid mechanics and transfer processes*. CUP Archive, 1985.
- [175] H. Arjmandi-Tash, N. Lebedev, P. M. van Deursen, J. Aarts, and G. F. Schneider, "Hybrid cold and hot-wall reaction chamber for the rapid synthesis of uniform graphene," *Carbon*, vol. 118, pp. 438-442, 2017.
- [176] P. Blake *et al.*, "Making graphene visible," *Applied physics letters*, vol. 91, no. 6, p. 063124, 2007.
- [177] T. Hallam, N. C. Berner, C. Yim, and G. S. Duesberg, "Strain, bubbles, dirt, and folds: a study of graphene Polymer-Assisted transfer," *Advanced Materials Interfaces*, vol. 1, no. 6, p. 1400115, 2014.
- [178] L. Anzi *et al.*, "Ultra-low contact resistance in graphene devices at the Dirac point. 2D Mater," 2018.
- [179] B. W. Scott and J.-P. Leburton, "Modeling of the output and transfer characteristics of graphene field-effect transistors," *IEEE transactions on Nanotechnology*, vol. 10, no. 5, pp. 1113-1119, 2011.
- [180] W. Shockley, "A unipolar" field-effect" transistor," *Proceedings of the IRE*, vol. 40, no. 11, pp. 1365-1376, 1952.
- [181] J. Yang, K. Jia, Y. Su, Y. Chen, and C. Zhao, "Hysteresis analysis of graphene transistor under repeated test and gate voltage stress," *Journal of Semiconductors*, vol. 35, no. 9, p. 094003, 2014.
- [182] F. Urban, G. Lupina, A. Grillo, N. Martucciello, and A. Di Bartolomeo, "Contact resistance and mobility in back-gate graphene transistors," *Nano Express*, vol. 1, no. 1, p. 010001, 2020.
- [183] K. S. Novoselov *et al.*, "Two-dimensional gas of massless Dirac fermions in graphene," *nature*, vol. 438, no. 7065, pp. 197-200, 2005.
- [184] Y.-W. Tan *et al.*, "Measurement of scattering rate and minimum conductivity in graphene," *Physical review letters*, vol. 99, no. 24, p. 246803, 2007.
- [185] F. Crowne, "Classical Gradual-Channel Modeling of Graphene Field-Effect Transistors (FETs)," ARMY RESEARCH LAB ADELPHI MD, 2010.
- [186] P. Joshi, H. Romero, A. Neal, V. Toutam, and S. Tadigadapa, "Intrinsic doping and gate hysteresis in graphene field effect devices fabricated on SiO<sub>2</sub> substrates," *Journal of Physics: Condensed Matter*, vol. 22, no. 33, p. 334214, 2010.
- [187] J. Ryu *et al.*, "Fast synthesis of high-performance graphene films by hydrogen-free rapid thermal chemical vapor deposition," *ACS nano*, vol. 8, no. 1, pp. 950-956, 2014.
- [188] G. Binnig, C. F. Quate, and C. Gerber, "Atomic force microscope," *Physical review letters*, vol. 56, no. 9, p. 930, 1986.
- [189] R. Garcia and R. Perez, "Dynamic atomic force microscopy methods," *Surface science reports*, vol. 47, no. 6-8, pp. 197-301, 2002.
- [190] J. H. Hafner, C.-L. Cheung, A. Woolley, and C. M. Lieber, "Structural and functional imaging with carbon nanotube AFM probes," *Progress in biophysics and molecular biology*, vol. 77, no. 1, pp. 73-110, 2001.

- [191] S. Maghsoudy-Louyeh, M. Kropf, and B. Tittmann, "Review of progress in atomic force microscopy," *The Open Neuroimaging Journal*, vol. 12, no. 1, 2018.
- [192] A. C. Ferrari and D. M. Basko, "Raman spectroscopy as a versatile tool for studying the properties of graphene," *Nature nanotechnology*, vol. 8, no. 4, pp. 235-246, 2013.
- [193] L. G. Cançado *et al.*, "Quantifying defects in graphene via Raman spectroscopy at different excitation energies," *Nano letters*, vol. 11, no. 8, pp. 3190-3196, 2011.
- [194] Z. H. Ni *et al.*, "Probing charged impurities in suspended graphene using Raman spectroscopy," *ACS nano*, vol. 3, no. 3, pp. 569-574, 2009.
- [195] L. Malard, M. A. Pimenta, G. Dresselhaus, and M. Dresselhaus, "Raman spectroscopy in graphene," *Physics reports*, vol. 473, no. 5-6, pp. 51-87, 2009.
- [196] A. C. Ferrari, "Raman spectroscopy of graphene and graphite: Disorder, electron-phonon coupling, doping and nonadiabatic effects," *Solid state communications*, vol. 143, no. 1-2, pp. 47-57, 2007.
- [197] N. Kovalchuk, K. Nigirish, M. Mikhailik, N. Kargin, I. Komissarov, and S. Prischepa, "Possibility of determining the graphene doping level using Raman spectra," *Journal of Applied Spectroscopy*, vol. 84, no. 6, pp. 995-998, 2018.
- [198] A. C. Ferrari *et al.*, "Raman spectrum of graphene and graphene layers," *Physical review letters*, vol. 97, no. 18, p. 187401, 2006.
- [199] E. M. Ferreira *et al.*, "Evolution of the Raman spectra from single-, few-, and many-layer graphene with increasing disorder," *Physical Review B*, vol. 82, no. 12, p. 125429, 2010.
- [200] P. Yin, Q. Lin, and Y. Duan, "Applications of Raman spectroscopy in two-dimensional materials," *Journal of Innovative Optical Health Sciences*, vol. 13, no. 05, p. 2030010, 2020.
- [201] A. Das, B. Chakraborty, and A. Sood, "Raman spectroscopy of graphene on different substrates and influence of defects," *Bulletin of Materials Science*, vol. 31, no. 3, pp. 579-584, 2008.
- [202] M.-S. Kim, J.-M. Woo, D.-M. Geum, J. Rani, and J.-H. Jang, "Effect of copper surface pre-treatment on the properties of CVD grown graphene," *Aip Advances*, vol. 4, no. 12, p. 127107, 2014.
- [203] D. Basko, "Calculation of the Raman G peak intensity in monolayer graphene: role of Ward identities," *New Journal of Physics*, vol. 11, no. 9, p. 095011, 2009.
- [204] F. A. Stevie and C. L. Donley, "Introduction to x-ray photoelectron spectroscopy," *Journal of Vacuum Science & Technology A: Vacuum, Surfaces, and Films*, vol. 38, no. 6, p. 063204, 2020.
- [205] J. Chastain and R. C. King Jr, "Handbook of X-ray photoelectron spectroscopy," *Perkin-Elmer Corporation*, vol. 40, p. 221, 1992.
- [206] !!! INVALID CITATION !!! .
- [207] G. Song, M. Ranjbar, and R. A. Kiehl, "Operation of graphene magnetic field sensors near the charge neutrality point," *Communications Physics*, vol. 2, no. 1, p. 65, 2019.
- [208] K. Toda, R. Furue, and S. Hayami, "Recent progress in applications of graphene oxide for gas sensing: A review," *Analytica chimica acta*, vol. 878, pp. 43-53, 2015.
- [209] D. Dutta *et al.*, "Performance of a CVD grown graphene-based planar device for a hydrogen gas sensor," *Measurement Science and Technology*, vol. 26, no. 11, p. 115104, 2015.
- [210] Y. Dan, Y. Lu, N. J. Kybert, Z. Luo, and A. C. Johnson, "Intrinsic response of graphene vapor sensors," *Nano letters*, vol. 9, no. 4, pp. 1472-1475, 2009.
- [211] J. D. Fowler, M. J. Allen, V. C. Tung, Y. Yang, R. B. Kaner, and B. H. Weiller, "Practical chemical sensors from chemically derived graphene," *ACS nano*, vol. 3, no. 2, pp. 301-306, 2009.
- [212] W. Choi, I. Lahiri, R. Seelaboyina, and Y. S. Kang, "Synthesis of graphene and its applications: a review," *Critical Reviews in Solid State and Materials Sciences*, vol. 35, no. 1, pp. 52-71, 2010.

- [213] L. G. De Arco, Y. Zhang, A. Kumar, and C. Zhou, "Synthesis, transfer, and devices of single- and few-layer graphene by chemical vapor deposition," *IEEE Transactions on Nanotechnology*, vol. 8, no. 2, pp. 135-138, 2009.
- [214] J. D. Wood *et al.*, "Annealing free, clean graphene transfer using alternative polymer scaffolds," *Nanotechnology*, vol. 26, no. 5, p. 055302, 2015.
- [215] X. Langston and K. E. Whitener Jr, "Graphene transfer: a physical perspective," *Nanomaterials*, vol. 11, no. 11, p. 2837, 2021.
- [216] R. Rautela *et al.*, "Mechanistic insight into the limiting factors of graphene-based environmental sensors," *ACS applied materials & interfaces*, vol. 12, no. 35, pp. 39764-39771, 2020.
- [217] S. Kim *et al.*, "Robust graphene wet transfer process through low molecular weight polymethylmethacrylate," *Carbon*, vol. 98, pp. 352-357, 2016.
- [218] Z. Zhang *et al.*, "Rosin-enabled ultraclean and damage-free transfer of graphene for large-area flexible organic light-emitting diodes," *Nature communications*, vol. 8, no. 1, p. 14560, 2017.
- [219] H. H. Kim *et al.*, "Clean transfer of wafer-scale graphene via liquid phase removal of polycyclic aromatic hydrocarbons," *ACS nano*, vol. 9, no. 5, pp. 4726-4733, 2015.
- [220] W. S. Leong *et al.*, "Paraffin-enabled graphene transfer," *Nature communications*, vol. 10, no. 1, p. 867, 2019.
- [221] G. Capote Mastrapa and F. L. Freire, "Plasma-treated CVD graphene gas sensor performance in environmental condition: The role of defects on sensitivity," *Journal of Sensors*, vol. 2019, pp. 1-7, 2019.
- [222] E. Mikmeková, L. Frank, I. Müllerová, B. W. Li, R. S. Ruoff, and M. Lejeune, "Study of multi-layered graphene by ultra-low energy SEM/STEM," *Diamond and Related Materials*, vol. 63, pp. 136-142, 2016.
- [223] J. Xie and J. P. Spallas, "Different contrast mechanisms in SEM imaging of graphene," *Agil. Technol*, 2012.
- [224] C. Deng *et al.*, "Reversible charge-transfer doping in graphene due to reaction with polymer residues," *The Journal of Physical Chemistry C*, vol. 118, no. 25, pp. 13890-13897, 2014.
- [225] W. Choi, M. A. Shehzad, S. Park, and Y. Seo, "Influence of removing PMMA residues on surface of CVD graphene using a contact-mode atomic force microscope," *RSC advances*, vol. 7, no. 12, pp. 6943-6949, 2017.
- [226] M. Lobet, N. Reckinger, L. Henrard, and P. Lambin, "Robust electromagnetic absorption by graphene/polymer heterostructures," *Nanotechnology*, vol. 26, no. 28, p. 285702, 2015.
- [227] K. S. Park *et al.*, "Wafer-scale single-domain-like graphene by defect-selective atomic layer deposition of hexagonal ZnO," *Nanoscale*, vol. 7, no. 42, pp. 17702-17709, 2015.
- [228] Z. Li *et al.*, "Deformation of wrinkled graphene," *Acs Nano*, vol. 9, no. 4, pp. 3917-3925, 2015.
- [229] S. Deng and V. Berry, "Wrinkled, rippled and crumpled graphene: an overview of formation mechanism, electronic properties, and applications," *Materials Today*, vol. 19, no. 4, pp. 197-212, 2016.
- [230] B. Vasić, A. Zurutuza, and R. Gajić, "Spatial variation of wear and electrical properties across wrinkles in chemical vapour deposition graphene," *Carbon*, vol. 102, pp. 304-310, 2016.
- [231] S. Zhao, S. P. Surwade, Z. Li, and H. Liu, "Photochemical oxidation of CVD-grown single layer graphene," *Nanotechnology*, vol. 23, no. 35, p. 355703, 2012.
- [232] M. Ahmad, S. A. Han, D. H. Tien, J. Jung, and Y. Seo, "Local conductance measurement of graphene layer using conductive atomic force microscopy," *Journal of Applied Physics*, vol. 110, no. 5, p. 054307, 2011.
- [233] M. Dresselhaus, A. Jorio, A. Souza Filho, and R. Saito, "Defect characterization in graphene and carbon nanotubes using Raman spectroscopy," *Philosophical Transactions of the Royal*

- Society A: Mathematical, Physical and Engineering Sciences*, vol. 368, no. 1932, pp. 5355-5377, 2010.
- [234] M. Zubair, J. Jose, A. H. Emwas, and M. A. Al-Harhi, "Effect of modified graphene and microwave irradiation on the mechanical and thermal properties of poly (styrene-co-methyl methacrylate)/graphene nanocomposites," *Surface and Interface Analysis*, vol. 46, no. 9, pp. 630-639, 2014.
- [235] S. Eigler, C. Dotzer, and A. Hirsch, "Visualization of defect densities in reduced graphene oxide," *Carbon*, vol. 50, no. 10, pp. 3666-3673, 2012.
- [236] J.-H. Zhong *et al.*, "Quantitative correlation between defect density and heterogeneous electron transfer rate of single layer graphene," *Journal of the American Chemical Society*, vol. 136, no. 47, pp. 16609-16617, 2014.
- [237] Z. Ni, Y. Wang, T. Yu, and Z. Shen, "Raman spectroscopy and imaging of graphene," *Nano Research*, vol. 1, pp. 273-291, 2008.
- [238] S. Gupta, P. Joshi, and J. Narayan, "Electron mobility modulation in graphene oxide by controlling carbon melt lifetime," *Carbon*, vol. 170, pp. 327-337, 2020.
- [239] J. B. McManus, A. Hennessy, C. P. Cullen, T. Hallam, N. McEvoy, and G. S. Duesberg, "Controlling defect and dopant concentrations in graphene by remote plasma treatments," *physica status solidi (b)*, vol. 254, no. 11, p. 1700214, 2017.
- [240] W. Zhang, L. Zhang, H. Zhang, L. Song, Q. Ye, and J. Cai, "Synthesize monolayer graphene on SiO<sub>2</sub>/Si substrate with copper-vapor-assisted CVD method," *Materials Research Express*, vol. 5, no. 12, p. 125601, 2018.
- [241] G. Cunge *et al.*, "Dry efficient cleaning of poly-methyl-methacrylate residues from graphene with high-density H<sub>2</sub> and H<sub>2</sub>-N<sub>2</sub> plasmas," *Journal of Applied Physics*, vol. 118, no. 12, p. 123302, 2015.
- [242] G. Piccinini *et al.*, "Deterministic direct growth of WS<sub>2</sub> on CVD graphene arrays," *2D Materials*, vol. 7, no. 1, p. 014002, 2019.
- [243] E. Vianello *et al.*, "Explanation of the charge trapping properties of silicon nitride storage layers for NVMs—Part II: Atomistic and electrical modeling," *IEEE Transactions on Electron Devices*, vol. 58, no. 8, pp. 2490-2499, 2011.
- [244] H. Wang, Y. Wu, C. Cong, J. Shang, and T. Yu, "Hysteresis of electronic transport in graphene transistors," *ACS nano*, vol. 4, no. 12, pp. 7221-7228, 2010.
- [245] V. Blechta, M. Mergl, K. Drogowska, V. Valeš, and M. Kalbáč, "NO<sub>2</sub> sensor with a graphite nanopowder working electrode," *Sensors and Actuators B: Chemical*, vol. 226, pp. 299-304, 2016.
- [246] P. Zomer, S. Dash, N. Tombros, and B. Van Wees, "A transfer technique for high mobility graphene devices on commercially available hexagonal boron nitride," *Applied Physics Letters*, vol. 99, no. 23, p. 232104, 2011.
- [247] D. Zhang *et al.*, "The anisotropy of field effect mobility of CVD graphene grown on copper foil," *Small*, vol. 10, no. 9, pp. 1761-1764, 2014.
- [248] V. Nagareddy *et al.*, "Detection of polar chemical vapors using epitaxial graphene grown on SiC (0001)," *Applied Physics Letters*, vol. 102, no. 17, p. 173103, 2013.
- [249] D. Kuzum *et al.*, "Transparent and flexible low noise graphene electrodes for simultaneous electrophysiology and neuroimaging," *Nature communications*, vol. 5, no. 1, pp. 1-10, 2014.
- [250] B. Pradhan, K. Setyowati, H. Liu, D. H. Waldeck, and J. Chen, "Carbon nanotube–polymer nanocomposite infrared sensor," *Nano letters*, vol. 8, no. 4, pp. 1142-1146, 2008.
- [251] S. A. McDonald *et al.*, "Solution-processed PbS quantum dot infrared photodetectors and photovoltaics," *Nature materials*, vol. 4, no. 2, pp. 138-142, 2005.
- [252] T.-C. Chen, Y.-C. Yang, H.-L. Liu, C.-M. Yang, M. Meyyappan, and C.-S. Lai, "The effect of monolayer graphene on the UV assisted NO<sub>2</sub> sensing and recovery at room temperature," *Multidisciplinary Digital Publishing Institute Proceedings*, vol. 1, no. 4, p. 461, 2017.

- [253] R. R. Kumar, T. Murugesan, T.-W. Chang, and H.-N. Lin, "Defect controlled adsorption/desorption kinetics of ZnO nanorods for UV-activated NO<sub>2</sub> gas sensing at room temperature," *Materials Letters*, vol. 287, p. 129257, 2021.
- [254] Y. You *et al.*, "On the mechanism of gas adsorption for pristine, defective and functionalized graphene," *Physical Chemistry Chemical Physics*, vol. 19, no. 8, pp. 6051-6056, 2017.
- [255] Q. He, S. Wu, Z. Yin, and H. Zhang, "Graphene-based electronic sensors," *Chemical Science*, vol. 3, no. 6, pp. 1764-1772, 2012.
- [256] C. Lee, J. Ahn, K. B. Lee, D. Kim, and J. Kim, "Graphene-based flexible NO<sub>2</sub> chemical sensors," *Thin Solid Films*, vol. 520, no. 16, pp. 5459-5462, 2012.
- [257] C.-M. Yang, T.-C. Chen, Y.-C. Yang, and M. Meyyappan, "Annealing effect on UV-illuminated recovery in gas response of graphene-based NO<sub>2</sub> sensors," *RSC advances*, vol. 9, no. 40, pp. 23343-23351, 2019.
- [258] A. Pálincás *et al.*, "The composition and structure of the ubiquitous hydrocarbon contamination on van der Waals materials," *Nature Communications*, vol. 13, no. 1, p. 6770, 2022.
- [259] A. Pálincás *et al.*, "The composition and structure of the ubiquitous hydrocarbon contamination on van der Waals materials," *Nature Communications*, vol. 13, no. 1, pp. 1-10, 2022.
- [260] E. Khestanova, F. Guinea, L. Fumagalli, A. Geim, and I. Grigorieva, "Universal shape and pressure inside bubbles appearing in van der Waals heterostructures," *Nature communications*, vol. 7, no. 1, pp. 1-10, 2016.
- [261] J. Wu and C. Wesdemiotis, "Cu (NH<sub>3</sub>)<sub>1-2</sub> complexes: formation and characterization in the gas phase by neutralization-reionization mass spectrometry," *Chemical physics letters*, vol. 303, no. 1-2, pp. 243-247, 1999.
- [262] J.-H. Beynon, A. Fontaine, and G. Lester, "Mass spectrometry: the mass spectrum of methanol. Part I. Thermochemical information," *International Journal of Mass Spectrometry and Ion Physics*, vol. 1, no. 1, pp. 1-24, 1968.
- [263] Y. Liu *et al.*, "An AC sensing scheme for minimal baseline drift and fast recovery on graphene FET gas sensor," in *2017 19th International Conference on Solid-State Sensors, Actuators and Microsystems (TRANSDUCERS)*, 2017: IEEE, pp. 230-233.
- [264] W. Xie, L.-T. Weng, K. M. Ng, C. K. Chan, and C.-M. Chan, "Clean graphene surface through high temperature annealing," *Carbon*, vol. 94, pp. 740-748, 2015.
- [265] K. Kumar, Y.-S. Kim, and E.-H. Yang, "The influence of thermal annealing to remove polymeric residue on the electronic doping and morphological characteristics of graphene," *Carbon*, vol. 65, pp. 35-45, 2013.
- [266] Y. Liu, *Room Temperature Gas Sensing using Graphene FET*. eScholarship, University of California, 2017.
- [267] A. Di Bartolomeo, F. Giubileo, S. Santandrea, F. Romeo, R. Citro, and T. Schroeder, "Charge transfer and trapping as origin of a double dip in the transfer characteristics of graphene based field-effect transistors," *arXiv preprint arXiv:1102.2308*, 2011.
- [268] H. Park *et al.*, "Optimized poly (methyl methacrylate)-mediated graphene-transfer process for fabrication of high-quality graphene layer," *Nanotechnology*, vol. 29, no. 41, p. 415303, 2018.
- [269] S. Claramunt, A. Varea, D. Lopez-Diaz, M. M. Velázquez, A. Cornet, and A. Cirera, "The importance of interbands on the interpretation of the Raman spectrum of graphene oxide," *The Journal of Physical Chemistry C*, vol. 119, no. 18, pp. 10123-10129, 2015.
- [270] X. Díez-Betriu *et al.*, "Raman spectroscopy for the study of reduction mechanisms and optimization of conductivity in graphene oxide thin films," *Journal of Materials Chemistry C*, vol. 1, no. 41, pp. 6905-6912, 2013.
- [271] A. Y. Lee *et al.*, "Raman study of D\* band in graphene oxide and its correlation with reduction," *Applied surface science*, vol. 536, p. 147990, 2021.

- [272] M. R. Karim *et al.*, "Effect of interlayer distance and oxygen content on proton conductivity of graphite oxide," *The Journal of Physical Chemistry C*, vol. 120, no. 38, pp. 21976-21982, 2016.
- [273] S. Goniszewski, M. Adabi, O. Shaforost, S. Hanham, L. Hao, and N. Klein, "Correlation of p-doping in CVD Graphene with Substrate Surface Charges," *Scientific reports*, vol. 6, no. 1, pp. 1-9, 2016.
- [274] G. Yang, B.-J. Kim, K. Kim, J. W. Han, and J. Kim, "Energy and dose dependence of proton-irradiation damage in graphene," *RSC Advances*, vol. 5, no. 40, pp. 31861-31865, 2015.
- [275] S. W. Schmucker, C. D. Cress, J. C. Culbertson, J. W. Beeman, O. D. Dubon, and J. T. Robinson, "Raman signature of defected twisted bilayer graphene," *Carbon*, vol. 93, pp. 250-257, 2015.
- [276] G. Lu *et al.*, "Toward practical gas sensing with highly reduced graphene oxide: a new signal processing method to circumvent run-to-run and device-to-device variations," *ACS nano*, vol. 5, no. 2, pp. 1154-1164, 2011.
- [277] L. Guo *et al.*, "Improved NO<sub>2</sub> gas sensing properties of graphene oxide reduced by two-beam-laser interference," *Scientific reports*, vol. 8, no. 1, p. 4918, 2018.
- [278] T. Han, S. Gao, Z. Wang, T. Fei, S. Liu, and T. Zhang, "Investigation of the effect of oxygen-containing groups on reduced graphene oxide-based room-temperature NO<sub>2</sub> sensor," *Journal of Alloys and Compounds*, vol. 801, pp. 142-150, 2019.
- [279] H. J. Cheon, S. Y. Shin, V. Van Tran, B. Park, H. Yoon, and M. Chang, "Preparation of conjugated polymer/reduced graphene oxide nanocomposites for high-performance volatile organic compound sensors," *Chemical Engineering Journal*, vol. 425, p. 131424, 2021.
- [280] S. Aslam, T. H. Bokhari, T. Anwar, U. Khan, A. Nairan, and K. Khan, "Graphene oxide coated graphene foam based chemical sensor," *Materials Letters*, vol. 235, pp. 66-70, 2019.
- [281] K. Phasukom, W. Prissanaroon-Ouajai, and A. Sirivat, "A highly responsive methanol sensor based on graphene oxide/polyindole composites," *RSC advances*, vol. 10, no. 26, pp. 15206-15220, 2020.
- [282] I. Maity, H. Rahaman, and P. Bhattacharyya, "DFT Based Simulation for Predicting Alcohol Adsorption on Oxygenated Functional Group Containing GO and rGO Based Gas Sensor Devices," in *2020 International Symposium on Devices, Circuits and Systems (ISDCS)*, 2020: IEEE, pp. 1-6.
- [283] M. D. Esrafil and L. Dinparast, "The selective adsorption of formaldehyde and methanol over Al- or Si-decorated graphene oxide: A DFT study," *Journal of Molecular Graphics and Modelling*, vol. 80, pp. 25-31, 2018.